



PhD Thesis

Ana Villalba Requena

**The role of the synaptic protein SV2B
in embryonic development of
the cerebral cortex**

Programa de doctorado en Neurociencias

Instituto de Neurociencias

Universidad Miguel Hernández-CSIC

Thesis supervisor:

Víctor Borrell



INSTITUTO DE NEUROCIENCIAS



THE ROLE OF THE SYNAPTIC PROTEIN SV2B IN EMBRYONIC DEVELOPMENT OF THE CEREBRAL CORTEX

Doctoral Thesis presented by
Ana Villalba Requena

- 2020 -

Thesis Director:

Víctor Borrell

PhD Program in Neuroscience

Instituto de Neurociencias – UMH-CSIC



San Juan de Alicante, 3 of February 2020

To whom it may concern:

The doctoral thesis developed by myself, Ana Villalba Requena, entitle "*The role of Synaptic vesicle Sv2b in embryonic development of the cerebral cortex*", is presented in a conventional format. It is based on experimental studies undertaken at the Neuroscience Institute of Alicante during the PhD program in Neuroscience of the Miguel Hernández University.

Yours sincerely,

ANA|
VILLALBA|
REQUENA

Firmado digitalmente por ANA|
VILLALBA|REQUENA
Nombre de reconocimiento (DN):
cn=ANA|VILLALBA|REQUENA,
serialNumber=53602498D,
givenName=ANA, sn=VILLALBA
REQUENA, ou=CIUDADANOS,
o=ACCV, c=ES
Fecha: 2020.07.28 12:42:01
+02'00'

Ana Villalba Requena

San Juan de Alicante, 14 of February 2020

To whom it may concern:

The doctoral thesis entitle "*The role of Synaptic vesicle Sv2b in embryonic development of the cerebral cortex*", has been developed by myself, Ana Villalba Requena presented in a conventional format. This thesis includes the following publication(s), of which I am second and fourth author respectively. I declare that the publication has not been used and will not be used in any other thesis in agreement with my thesis director Víctor Borrell:

- Cárdenas A, Villalba A, de Juan Romero C, Picó E, Kyrousi C, Tzika AC, Tessier-Lavigne M, Ma L, Drukkler M, Cappello S, Borrell V. 2018. Evolution of Cortical Neurogenesis in Amniotes Controlled by Robo Signaling Levels. *Cell*. 174-3, pp.590-606.e21.
- del Toro D, Ruff T, Cederfjäll E, Villalba A, Seyit-Bremer G, Borrell V, Klein R.. 2017. Regulation of Cerebral Cortex Folding by Controlling Neuronal Migration via FLRT Adhesion Molecules. *Cell*. 169-4, pp.621-635.e16.

Yours sincerely,

ANA|
VILLALBA|
REQUENA

Firmado digitalmente por ANA|
VILLALBA|REQUENA
Nombre de reconocimiento (DN):
cn=ANA|VILLALBA|REQUENA,
serialNumber=53602498D,
givenName=ANA, sn=VILLALBA
REQUENA, ou=CIUDADANOS,
o=ACCV, c=ES
Fecha: 2020.07.28 12:40:40 +02'00'

Firmado por BORRELL FRANCO VICTOR -
DNI 52211395S el día 28/07/2020 con un
certificado emitido por AC Administración
Pública

Ana Villalba Requena

Dr. Víctor Borrell

A QUIEN CORRESPONDA:

Dr. Víctor Borrell Franco, investigador científico del Consejo Superior de Investigaciones Científicas,

Autoriza la presentación de la Tesis Doctoral titulada "*The role of Synaptic vesicle Sv2b in embryonic development of the cerebral cortex* ", realizada por D.^a Ana Villalba Requena (DNI 53602498D) bajo su inmediata dirección y supervisión en el Instituto de Neurociencias de Alicante, Centro Mixto de la Universidad Miguel Hernández-UMH y la Agencia Estatal Consejo Superior de Investigaciones Científicas-CSIC, y que presenta para la obtención del grado de Doctor por la Universidad Miguel Hernández.

Para que así conste, y a los efectos oportunos, firma el presente Certificado en San Juan de Alicante, a 14 de Febrero de 2020.

Firmado por BORRELL FRANCO
VICTOR - DNI 52211395S el día
28/07/2020 con un certificado emitido
por AC Administración Pública

Fdo: Dr. Víctor Borrell Franco

A QUIEN CORRESPONDA:

Prof. Miguel Valdeolmillos López, Catedrático y Coordinador del Programa de Doctorado en Neurociencias del Instituto de Neurociencias, Centro Mixto de la Universidad Miguel Hernández-UMH y la Agencia Estatal Consejo Superior de Investigaciones Científicas (CSIC),

CERTIFICA:

Que la Tesis Doctoral titulada "*The role of Synaptic vesicle Sv2b in embryonic development of the cerebral cortex*" ha sido realizada por D.^a Ana Villalba Requena (DNI 53602498D) bajo la dirección del Dr. Víctor Borrell Franco y da su conformidad para que sea presentada a la Comisión de Doctorado de la Universidad Miguel Hernández.

Para que así conste a los efectos oportunos, firma el presente certificado en San Juan de Alicante a 14 de Febrero de 2020.

MIGUEL
ANGEL|
VALDEOLMIL
LOS|LOPEZ

Firmado digitalmente
por MIGUEL ANGEL|
VALDEOLMILLOS|
LOPEZ
Fecha: 2020.07.28
13:08:14 +02'00'

Fdo: Miguel Valdeolmillos

A QUIEN CORRESPONDA:

La Tesis Doctoral "*The role of Synaptic vesicle Sv2b in embryonic development of the cerebral cortex*" realizada por Ana Villalba Requena (DNI 53602498D) en el Instituto de Neurociencias de Alicante, Centro Mixto de la Universidad Miguel Hernández-UMH y la Agencia Estatal Consejo Superior de Investigaciones Científicas-CSIC ha sido desarrollada bajo la financiación del programa de Ayudas para contratos predoctorales Severo Ochoa 2014 (SVP-2014-068671) y EMBO Short-Term Fellowship Number 8025, 2018.

Para que así conste a los efectos oportunos, firma el presente certificado en San Juan de Alicante a 14 de Febrero de 2020.

**ANA|
VILLALBA|
REQUENA**

Firmado digitalmente por ANA|
VILLALBA|REQUENA
Nombre de reconocimiento (DN):
cn=ANA|VILLALBA|REQUENA,
serialNumber=53602498D,
givenName=ANA, sn=VILLALBA
REQUENA, ou=CIUDADANOS,
o=ACCV, c=ES
Fecha: 2020.07.28 12:41:17 +02'00'

Fdo: Ana Villalba Requena

ACKNOWLEDGEMENTS

"El secreto, querida Alicia, es rodearte de personas
que te hagan sonreír el corazón. Es entonces,
solo entonces, que estarás en el País de las Maravillas"

- Lewis Carroll, Alicia en el país de las maravillas

En los inicios de esta aventura decía que iba a "casa" cuando volvía a Valencia, actualmente cuando digo que "voy a casa" me refiero a mi piso en San Juan, y es que después de estos años he acabado sintiéndome en un nuevo hogar y en gran parte ha sido gracias a toda la gente maravillosa que ha estado en mi vida en ese tiempo. A la vista está en mi muro de post-its que este camino no lo he recorrido ni mucho menos sola, todo esto no habría sido posible sin ellos y me gustaría agradecerélos a todos los que han puesto su granito de arena. Desde ya pido perdón si me dejo a alguien en el tintero, pero he tenido la suerte de que seáis muchos los implicados y este apartado no puede ser más largo que la propia tesis ^^'.

Tuve la suerte de pasar esta aventura en un laboratorio con un ambiente genial. Por lo que al primero que quiero dar gracias es a mi jefe, Víctor. Primero de todo gracias por darme la oportunidad, por confiar en mí y mi criterio para proyectos tan bonitos. Realmente me siento orgullosa de haber podido pertenecer a tu equipo. Gracias por permitirme aprender mil cosas, por las discusiones científicas que me han enseñado tanto; pero también, por el apoyo en momentos complicados, por los croassans de chocolate, por la comprensión, por preocuparte, por el positivismo cuando a mí me faltaba, por el entusiasmo, por escuchar siempre. Muchas gracias por todo porque he estado tan a gusto en esta familia científica que será muy duro marchar.

En esta familia siempre hay gente yendo y viniendo, pero no por eso dejan huellas menos profundas. Por ello, quiero empezar por los que cambiaron de aires pero cuya esencia nunca se marchó. La primera en recibirme fue la gran Esther Picó. Picó, gracias por ese humor negro cargado de preocupación por nosotros, gracias por tus consejos siempre tan acertados, por tus "escuchameee", por todo lo que me enseñaste y porque oye, a veces estábamos mal... pero "peor es ser p*". Trini, gracias por tu salero infinito, por tus sonrisas que son el verdadero quitapenas, por toda tu sabiduría compartida, por el cariño que le entregas a todo y todos, por transmitir tanta pasión por la ciencia y por tus mil anécdotas. Cos, tu paso por el lab fue breve pero intenso. Gracias por animarme a aprovechar esta oportunidad y por todo tu apoyo en el camino previo del máster. Sabes que me encantas y que aunque, de uvas a peras, siempre tendrás un hueco en mi agenda.

Luego están esas personitas con las que conviví prácticamente toda la tesis y que aunque ya no están en este equipo han sido parte importante de ella. Caminin, en seguida me acogiste y me enseñaste todas las maravillas de la molecular. Gracias por toda tu paciencia al enseñarme, por todos tus truquis, por tus consejos siempre tan acertados, por los ánimos cuando todo se complicaba, por las risas, por los favores, por sacarme a respirar cuando todo se desbordaba, por las fiestas vividas y sobre todo por impulsarme siempre a ir más allá.

Virginia cuando te fuiste empezó a hacerse real que este lindo periodo no era para siempre. Eres maravillosa y desde el primer momento sentí como si te conociera desde toda la vida. Me encanta tu locura (TOC incluido) y he reído hasta doler contigo. Gracias por tu positivismo, tu alegría, por contar conmigo sin dudas, por el salimos de

tranquis que se alarga hasta el amanecer, por toda tu ayuda, por ser tan linda, por seguir siendo tan detallista incluso en la distancia, por tu apoyo infinito y todo tu cariño. Se nota tu ausencia.

La otra compañera de fatigas como estudiantes de doctorado fue Cris. Bonica mía, gracias por las cervezas para celebrar, por las cervezas para olvidar y por las cervezas porque sí. Gracias por tus recomendaciones gourmet, por tus súper audios que enganchan como una miniserie, por los cantos Disney en días largos, por estar pendiente, por apreciar las pequeñas cosas, por tu ayuda, por tus detalles y por todos los momentos memorables que compartimos.

Ahora la que se va del labo soy yo y dejo atrás un equipo de gente genial al que voy a echar muchísimo de menos. Jorge, eres un crack, aún recuerdo cuando empezamos a indagar en las cirugías de las huronas adultas en el 139. Gracias por enseñarnos un ámbito nuevo desconocido, por tus visitas, por preguntar cada vez cómo va todo, por tu ayuda y tu buen humor. Gracias también por ampliar la familia con gente tan genial como Arturo y Pablo. Ambos sois unos grandes, gracias por todos los ánimos y las risas. Pep, muchísimas gracias por tu ayuda, por tu genial humor, tu mermelada casera y tus consejos de manitas! Kaviya, thanks for your kindness, for your smile and your patience. Good luck with the small way left. Salma sweetie, meeting you was the hallmark to be even more interested about Egypt that I already was. Thanks for your wonderful expressions, your fashion advices, your powerful energy, your confident words when I fall and your sweets. "Despacito" and "Latinoamérica" will never be the same. Thanks for allow me to be forever link to your first contact with the snow. It is a great example of these small things that we shared and made me laugh sincerely by your side. My most sincere encouragement, I know you will achieve whatever you porpoise, cause, come on...you're Egyptian! El siguiente fichaje fue Lucía compañera de penurias de los hurones, mucha suerte con ellos, gracias por estar ahí, por tu paciencia y tu calma. Yuki, having you here was super nice, you are a very kind and funny person. Thank you for being so helpful and dedicated. すべてに感謝します. Álex, primero de todo, te perdono por arrebatarme el título de más joven del labo. Aún así gracias por las geniales recomendaciones de todo tipo, por el estupendo vino de tu pueblo, por ser un maravilloso compañero, por estar siempre dispuesto a echar una mano y por tu buen humor. A la más novatilla del grupo, Anna, gracias por estar siempre dispuesta a ayudar con una sonrisa. Recuerda no tener prisa, que es un camino duro pero maravilloso y seguro que te irá genial. Me hubiera gustado tener más tiempo para compartir contigo, aún así, mil gracias por los almuerzos de los sábados, por los paseos a casa, por los mimos de Milka, por los dulces para subir el ánimo y por las conversaciones de patio.

Esther, mi punto ácido del labo, mi reina del aquelarre. No te puedes imaginar todo lo que he aprendido y disfrutado a tu lado, desde playa con niños a noches de fiesta. Gracias por escucharme, por unirme a mi causa cuando me quemaba la vida, por los cotilleos geniales, por los almuerzos con y sin pincho, por las confesiones, por los abrazos (cortitos), por preocuparte por mí al mínimo signo de que algo haya cambiado,

por ayudarme dentro y fuera del lab. Los días de lluvia no serán lo mismo sin tu pelo bufado, ni las comidas sin agonías, ni los té sin terapia, ni la rutina sin ti.

Pon una Bea en tu vida, lo digo y lo diré siempre, y es que tus virtudes van desde asistente legal que se asegura de que no acabemos en la cárcel hasta planificadora de viajes profesional, pasando por personal shopper, make-up assistance, consejera de hacienda y profesora de idiomas. Bea, mil gracias por cada una de tus facetas, por todo lo que has hecho por mí dentro y fuera del trabajo. Gracias por ser tan detallista, tan cariñosa y tan bonita en general. Gracias por compartir mil momentos, preocupaciones, depresiones, cenas, fiestas y viajes. Eres una compañera estupenda de trabajo y de vida. Tengo suerte de tenerte como amiga y sabes que allá donde acabe tienes un hueco para visitas y viajes. Por todo esto, puse una Bea en mi vida y no quiero imaginármela sin ella ahí.

A mi compi de bancada, ese que ha tenido que lidiar con el elefante en una cacharrería desde el minuto uno hasta el tiempo de descuento. Adri, eres una persona increíble y te admiro muchísimo tanto como científico como persona. Hemos vivido mucho en esta convivencia así que muchísimas gracias por aguantarme incluso con café, gracias por las postcomidas con discusiones científicas trascendentales, por ayudarme a pensar críticamente, por enseñarme tantísimo (y no solo del laboratorio), por los pinchos y las cervezas, por compartir música y conciertos, por apoyarme siempre, por ver más allá de una maraña de nervios, por hacerme entender que a veces las cosas que no son mi p* problema deberían sudarme la p*, por hacerme despertar cuando ando perdida, por fomentar mis pasiones, por abrazarme cuando lo necesito aunque no te gusten los abrazos, por creer tanto en mí incluso cuando yo no podía, por confiar plenamente en mí y por ayudarme a crecer tanto. GRACIAS por ser tan tú conmigo. Realmente no sabes todo lo que te echaré de menos.

Además de todos los borrelianos he tenido la suerte de compartir edificio con personas maravillosas. Esto se alargaría enormemente por mencionaros a todos y me siento muy afortunada por ello. En breve, muchas gracias al team Canals por acogerme como una más de la familia siempre con vuestra escandalosa alegría y vuestras ricas comidas; a los Herrerianos por ser nuestros hermanitos más cercanos en esta rara familia, gracias por vuestro apoyo y por los geniales momentos compartidos; a las Carmenas por estar siempre dispuestas a echar una mano ya sea con la ciencia o despotricando un poco y a todos los servicios del INA por hacer nuestro trabajo mucho más fácil, siempre dispuestos a adaptarse sea cual sea nuestra petición y con una sonrisa. De corazón, muchísimas gracias a todos.

Mi estancia en Alicante también ha dado para conocer a gente estupenda fuera de la ciencia, donde entra gente como Lau. "Pila", gracias por los té de cazo, los litros de helado, los mate de viaje, por soportar mis agobios sin juzgar, por estar fuera de lo convencional y fomentar mis rarezas. Gracias por ser ese aire fresco en un pueblo pequeño y por nuestras conversaciones filosóficas a cualquier hora. Me llevo conmigo muchas de tus lecciones, porque a veces solo pasa "La viiiida", y los que te quieren "no

se preocupan, se ocupan" y a veces simplemente, "la vida es más sencilla". Gracias por lidiar con mis *quilombos*, por bajarme de las nubes cuando mis preocupaciones no me dejaban centrarme y por llevarme bailando a otro universo donde desconectar.

No me podía olvidar de esa dosis de locura que tan bien me sienta. Moimoi, gracias por ser esa inagotable energía llena de ilusión de curiosidad y ansia por vivir. Gracias por apoyarme incondicionalmente aunque no comprendieras cómo vivo mi pasión por mi trabajo. Gracias por inundarme de chocolate para endulzar las horas extra y por llevarme a vivir mil aventuras. Gracias por empujarme a ver el mundo de otro modo, por enseñarme a relativizar las cosas, por hacerme creer que era toda una percherona, por impulsarme a combatir mis miedos y expresar mis pasiones. Gracias por todos tus detalles y tu fresca locura que siempre me sienta tan bien. Fuiste un descubrimiento casual increíble que espero conservar siempre.

No solo cuentan estos últimos 5 años, en el camino hasta aquí también tengo mucho que agradecer a mi pequeña tribu, esta familia no de sangre que se elige y te acompaña siempre por mucho que cambien las cosas. Y es que aunque pase el tiempo y crezcan las distancias, ellos son mi estabilidad en el cambio y un servicio salvavidas al que siempre regresar con los brazos abiertos. Agrelo, gracias por tu salero único capaz de hacernos olvidar cualquier desdicha, por tu energía arrolladora, por todo tu cariño, por preocuparte por todos, por cuidarnos y por encima de todo, por haber metido a Mary en nuestras vidas. Mary, gracias por ser tan atenta, tan cercana y cariñosa, gracias por dar tanto sin dudarlo, gracias por querernos desde el minuto uno y gracias por ser una más. Jaime, mi grandullón que todo lo que tiene de grande lo tiene de buenazo. Gracias por estar siempre presente incluso en tu discreción, por ser tan detallista, por tu generosidad, por tus chuches, por entenderme tan bien, por escuchar, por apuntarte a un bombardeo y sobre todo por tu comprensión y tu cariño. Lucas, durante mucho tiempo fuiste mi gran apoyo y he de agradecerte mucho en el camino que me ha llevado a donde estoy y soy. Gracias por entenderme como nadie, por hacerme creer en la magia y fomentar mi humor negro, por acudir cuando lo necesito por muy inapropiado que sea, por seguir ahí a pesar de las dificultades y las riñas, por las conversaciones a deshora, por tus consejos sin prejuicio, por seguir queriéndome a pesar de todo.

Pocos pueden decir que han estado tanto tiempo en mi vida como ella, y es que mi Trasto ¡ya son más de 27 años! Mara, mi aparentemente despreocupada aventurera, gracias por ser mi compañera de juegos durante tanto tiempo, por cuidarme tanto, por equilibrarme, por reír y vivir aventuras juntas, por apoyarme siempre aunque fuera desde la distancia, por evolucionar conmigo, por seguir queriéndonos tal y como somos. En definitiva, gracias por seguir creciendo a mi lado.

A mi niña de grandes rizos. Poder tenerte tan cerca todo este tiempo ha sido maravilloso, ¿quién iba a decir que pasaríamos juntas por tanto? Eres la definición gráfica de buen rollito y tienes el poder de hacer reír incluso cuando se llora. Gracias por estar siempre ahí aunque fuera para quitar los pelos de mi cepillo (pocas cosas reflejan mejor la confianza entre dos amigas). Gracias por las cervezas que se hacen

comidas que se hacen meriendas, por transmitir siempre esa alegría infinita que desprendes, por darme tantos abrazotes (y quesos) llenos de cariño, por haberme apoyado en cada uno de los retos que podían conmigo incluso cuando ya podían hasta contigo, gracias por ser una persona tan única y especial, gracias por escucharme y aconsejarme sin juzgar nunca, por las risas (incluso las crueles), gracias por todo mi niña bonita. Gracias por estar siempre, porque no se qué sería de mí sin una loca como tú a mi lado. Te quiero mucho mi niña bonita.

Por último, gracias a la última incorporación en mi vida, al valiente que se atrevió a convivir con una neurótica en un bucle terrible de ansiedad... gracias por soportarme, por ser mi compañero de equipo, por apoyarme en todos mis retos, por no dejar que me sintiera sola ni en la distancia, por mimarme, por cuidarme, por apreciar todas mis taritas, por hacerme la vida más fácil, por aguantar mis lloros y frustraciones para cambiarlos por una sonrisa (siempre, incluso cuando no toca), por celebrar mis pequeñas batallas como grandes conquistas, por tus detalles, por abrirte a mí, por animarme hasta cuando no quedan fuerzas (hasta cuando no te quedan fuerzas)... Gracias por anteponerme, porque sin ti a mi lado no habría sobrevivido a este periodo. Gracias por compartir alegrías y miedos conmigo, por tener ganas de compartir mil experiencias más y hacerlas únicas a tu lado. Espero que acabes dándome esa prórroga... gracias por estar hecho a mi medida, por quererme tanto. Te quiero Cristian.

No puedo acabar esta sección sin mencionar a mis personajes principales, mis mayores guías, mis padres. Papá, gracias por empujarme siempre más alto, por transmitirme la competitividad (muy a pesar de algunos), por la sensatez en tus consejos, por enseñarme a pensar lógicamente y apreciar el arte. Mamá, gracias por tu fortaleza, por tu humor en los momentos más difíciles (*dientes dientes que es lo que les j**), por enseñarme a ser meticulosa y atenta con los demás, por demostrarme que hay que enfrentarnos a las cosas aunque muramos de miedo, por enseñarme que con fuerza de voluntad todo se puede. Papá, mamá; gracias por transmitirme vuestra creatividad, vuestro cariño, vuestra dedicación, vuestra tolerancia, vuestra sed de vivir experiencias, vuestra confianza y vuestro total apoyo SIEMPRE. Gracias por haberme ayudado a convertirme en la persona que soy. Espero que podáis estar casi tan orgullosos de mí como yo lo estoy de ser vuestra hija. Os quiero muchísimo.

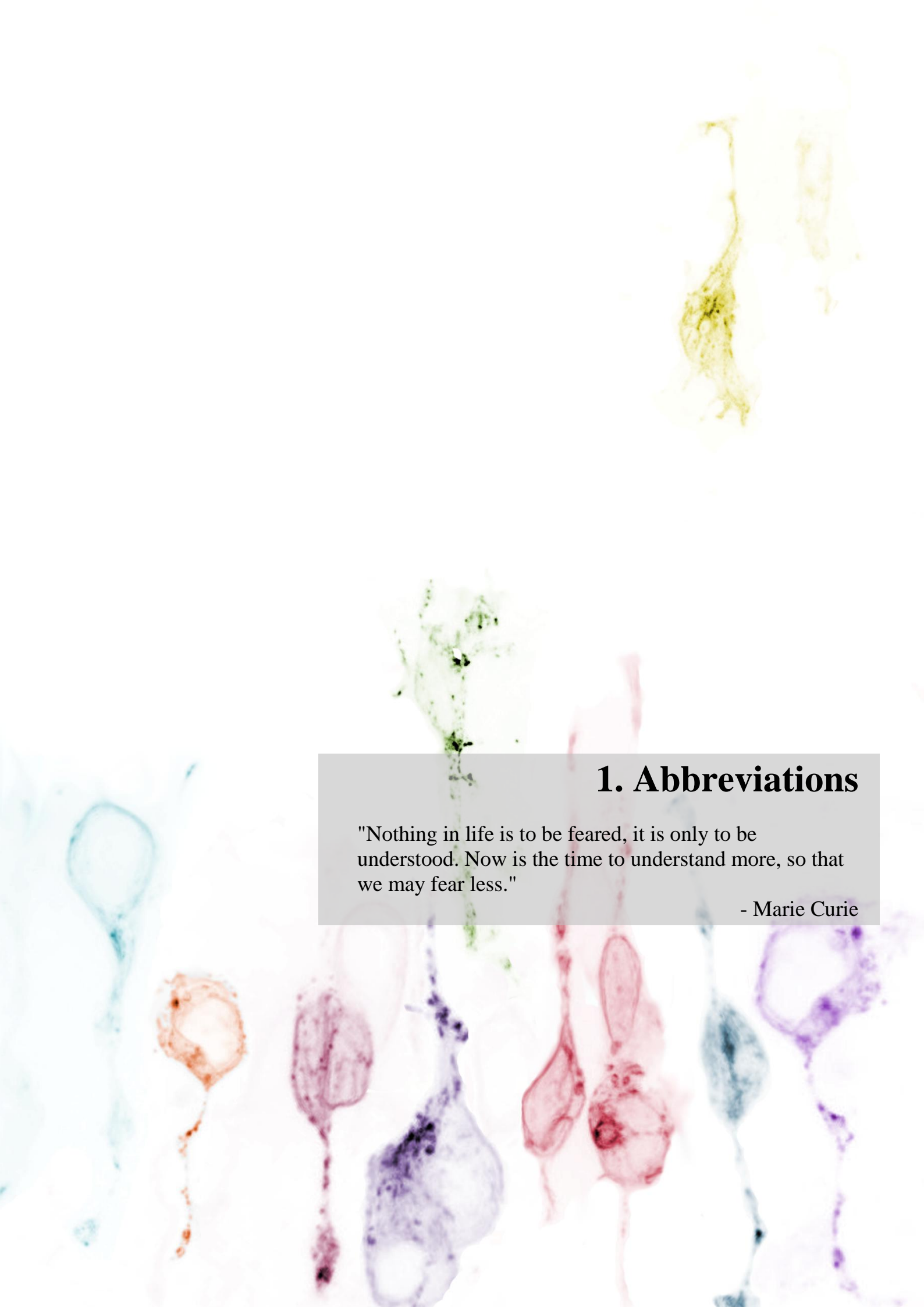
A los que ya no están,
pero nunca se irán del todo.

INDEX

1. Abbreviations	27
2. Abstract/Resumen	35
3.Introduction	43
3.1 Development of the mammalian nervous system	45
3.1.1 Ontogeny of the CNS.....	45
3.1.2 Phylogenic classification of cortical regions	47
3.2 Organization of the cerebral cortex	49
3.2.1 Radial organization.....	49
3.2.2 Tangential organization	52
3.3 Cellular composition of the neocortex	54
3.3.1 Excitatory neurons	54
3.3.2 Inhibitory neurons.....	54
3.3.3 Cajal-Retzius cells	55
3.3.4 Glial cells	56
3.4 Development of the mammalian cerebral cortex	56
3.4.1 Germinal layers.....	57
3.4.2 Neural progenitors: features and dynamics.....	59
3.4.3 Cell cycle and Interkinetic Nuclear Migration.....	64
3.4.4 Types of division	66
3.5 Cerebral cortex: factors underlying neurogenesis and cortical folding	68
3.5.1 Primary factors.....	68
3.5.2 Secondary factors.....	73
3.6 Synaptic Vesicle proteins 2 (SV2)	79
3.6.1 General features	79
3.6.2 SV2 structure	82
3.6.3 SV2 expression patterns.....	83
3.6.4 Sv2 Knockout mice	85
3.6.5 SV2 functions	87
3.6.6 SV2 and pathology.....	95
3.6.7 SV2 mutations	98
3.6.8 Regulation of Sv2 expression.....	98
4. Objectives	101
5. Materials and Methods	105

6.Results	123
Part 1. Overexpression of SV2B in embryonic mouse telencephalon leads to alterations in progenitor cell adhesion, cell cycle and proliferation	125
Characterization of <i>Sv2a</i> and <i>Sv2b</i> endogenous expression in mice	127
SV2B overexpression causes delayed neuronal migration and disruption of the VZ	129
SV2B overexpression disrupts the apical adherens junction belt and the position of aRGCs.....	132
SV2B overexpression alters cell cycle, interkinetic nuclear migration and cell division	134
SV2B+ vesicles are highly motile along the apical process	137
SV2B overexpression leads to a bulge formation.....	140
Part 2. <i>Sv2b</i> is expressed in ferret germinal layers and its genetic modification in ferret leads to alterations in progenitor cell proliferation	143
<i>Sv2a</i> and <i>Sv2b</i> are highly expressed in germinal layers of the developing ferret cortex	145
Subcellular characterization of SV2B in ferret.....	148
SV2B overexpression in ferret reduces neural production and regular migration.....	150
SV2B ablation in ferrets induces an increase in basal mitosis.....	153
Part 3. SV2B expression in human cells and its role in embryonic development ...	157
SV2B is distributed along the exocytic and endocytic pathways in human RPE-1 cells.....	159
SV2B overexpression in human cerebral organoids does not induce changes in apical lamina, ventricular surface integrity or cell delamination.....	159
SV2B overexpression in human cerebral organoids tends to decrease mitotic activity and apical progenitors.....	161
7. Discussion	163
8. Conclusions/Conclusiones	181
9. Annex. Author's published scientific contributions	187
Annex 1 . Evolution of Cortical Neurogenesis in Amniotes Controlled by Robo Signaling Levels	189
Annex 2. Regulation of Cerebral Cortex Folding by Controlling Neuronal Migration via FLRT Adhesion Molecules	231
10. References	265





1. Abbreviations

"Nothing in life is to be feared, it is only to be understood. Now is the time to understand more, so that we may fear less."

- Marie Curie

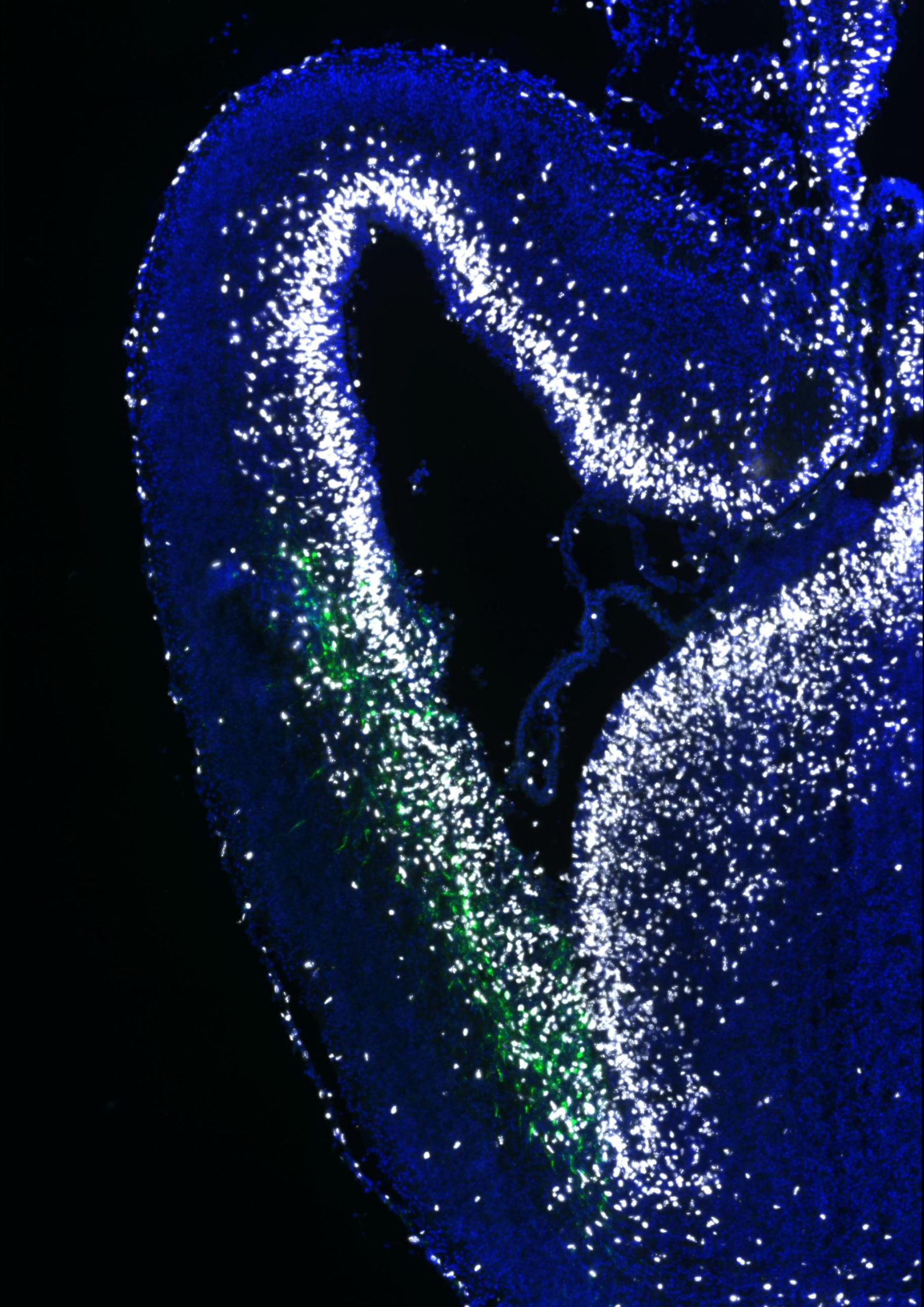
a	Apical
A1	Auditory primary cortical area
AIPs	Apical Intermediate Progenitors
Ap	Apical process
aPCs	Apical Progenitor Cells
aPKC	Atypical Protein Kinase C
aRGCs	Apical Radial Glia Cells
Arl13b	ADP-ribosylation factor-like protein 13B
ATP	Adenosine Triphosphate
BCIP	5-bromo-4-chloro-3-indolyl phosphate
bIPs	Basal Intermediate Progenitors
BLBP	Brain Lipid Binding Protein
BMPs	Bone Morphogenetic Proteins:
BoNT	Botulinum Neurotoxins
Bp	Basal process
bPCs	Basal Progenitor Cells
BrdU	Bromodeoxyuridine
bRGCs	Basal Radial Glia Cells
Cas9	CRISPR associated protein 9
Casp3	Caspase 3
<i>C. elegans</i>	<i>Caenorhabditis elegans</i>
CC	Cortico-cortical Connection
Cdh1	Cadherin 1
CMV	Citomegalovirus promotor
CNS	Central Nervous System
COUP-TF1	COUP Transcription Factor 1
CP	Cortical Plate
CRISPR	Clustered Regularly Interspaced Short Palindromic Repeats
CSF	Cerebrospinal Fluid
cSv2b	CRISPR guides against Sv2b gene
Cux1	Cut Like Homeobox 1
d	Days

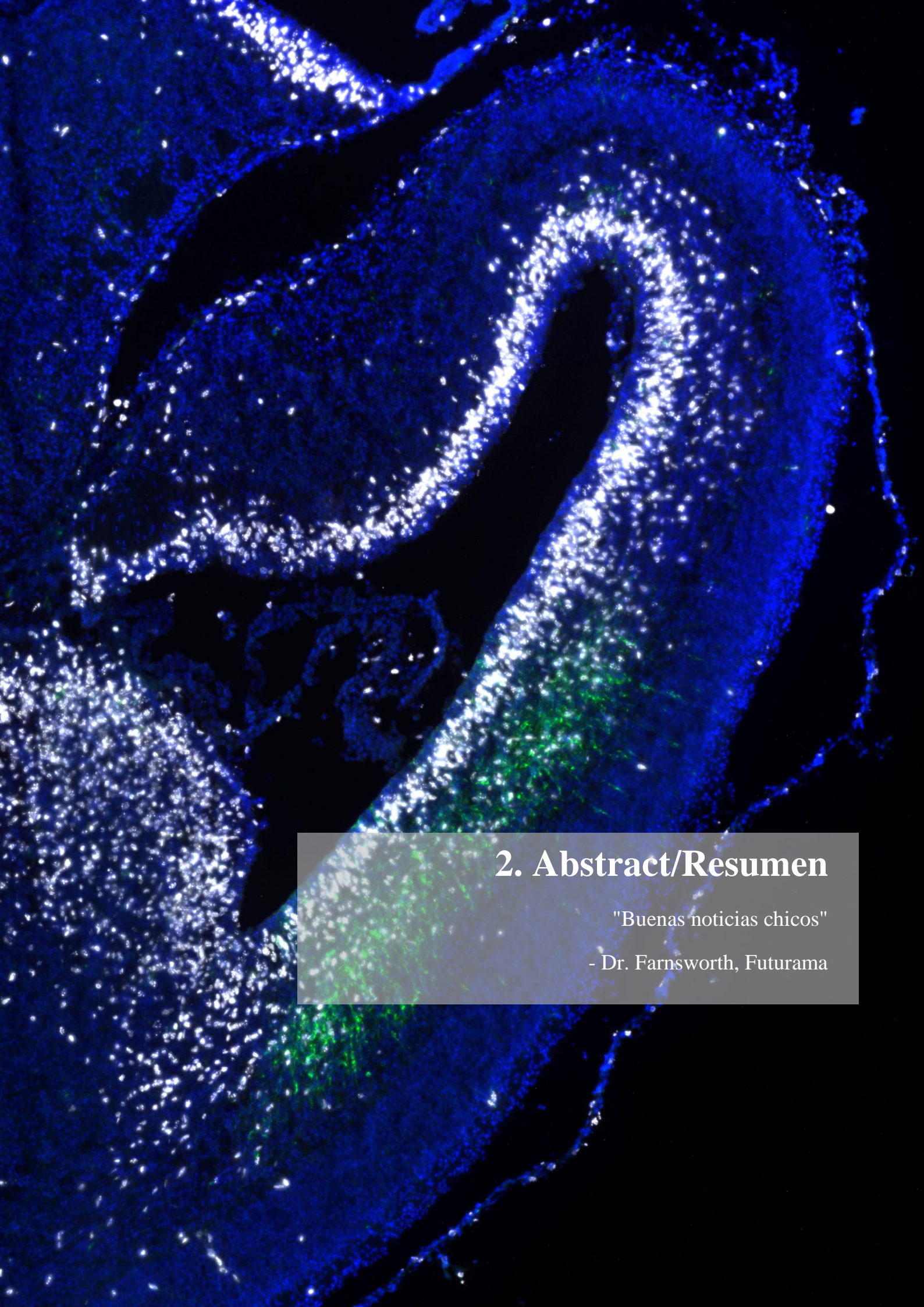
DAPI	4',6-diamidino-2-phenylindole
DCX	Doublecortin
DNA	Deoxyribonucleic Acid
E(X)	Embryonic day (x)
ECM	Extracellular Matrix
EEA1	Early Endosome-Associated Protein
Emx2	Empty Spiracles Homeobox 2
F	Ferret
fc	Fold-change
FGF	Fibroblast Growth Factor
FLRT1/3	Leucine-Rich Repeat Protein 1/3
Fw	Foward
GABA	γ -aminobutyric-acid
GFAP	Glial Fibrillary Acidic Protein
GFP	Green Fluorescent Protein
GLAST	Astrocyte-Specific Glutamate Transporter
Glut1	Human Glucose Transporter 1
GRASP65	Golgi Reassembly-Stacking Protein of 65 kDa
gRNA	Guide RNA
H	Human
HA	Hyaluronic Acid
HAPLN1	Hyaluronan And Proteoglycan Link Protein 1
HE	Heterozygous
Hipp	Hippocampus
HO	Homozygous
HSFY1	Heat Shock transcription Factor Y-linked 1
IFL	Inner Fiber Layer
INM	Interkinetic Nuclear Migration
ISVZ	Inner Subventricular Zone
IPCs	Intermediate Progenitor Cells
IZ	Intermediate Zone
KO	Knockout
Lam	Laminin

LAMB1	Laminin β 1
LAMP1	Lysosomal-Associated Membrane Protein 1
L-DOPA	L-3,4 Dihydroxifenilalanina
LEV	Levetiracetam
LGE	Lateral Ganglionic Eminences
LS	Lateral Sulcus
loxP	Locus of X-over P1
MA	Monoamine
MFS or MF	Major Facilitator Superfamily
MGE	Medial Ganglionic Eminences
mIPSCs	Miniature Inhibitory Postsynaptic Currents
miRNA	microRNA
MN	Migrating Neuron
mRNA	Messenger RNA
Ms	Mouse
MUNCs	Mammalian Uncoordinated proteins
MZ	Marginal Zone
N	Nucleus
NAD	Nicotinamide Adenine Dinucleotide
NB	Nucleus Basalis
NBT	Nitroblue Tetrazolium
NE	Neuroepithelium
NECs	Neuroepithelial Cells
NeuN	Neuronal Nuclei protein
NeuroD2	Neuronal Differentiation 2 protein
ns	Non significant
Ntn1	Netrin1
OSVZ	Outer Subventricular Zone
P(X):	Postnatal day (x)
Par3	Partitioning defective 3
Pax6	Paired box 6
PH3	Phospho-Histone 3
PhVim	Phospho Vimentin

PNS	Peripheral Nervous System
Prom1	Prominin 1
Rab6	Ras-related protein 6
Rab7	Ras-related protein 7
RNA	Ribonucleic Acid
Rv	Reverse
Rv:	Retrovirus
S1	Somatosensory primary cortical area
sa	Subapical
SAPs	Subapical Progenitors
Shh	Sonic hedgehog
sIPSCs	Spontaneous Inhibitory Postsynaptic Currents
SNAP25	Synaptosome Associated Protein 25
SNARE	SNAP Receptor
SG	Splenic Gyrus
SP	Subplate
SV2	Synaptic Vesicle Glycoprotein 2
SVOP	SVtwO-related Protein
SVOPL	SVOP-like protein
SVZ	Subventricular Zone
SYT1	Synaptotagmin 1
Tbr2	T-box transcription factor 2
TeNT	Tetanus Neurotoxins
TMR	Transmembrane Region
TR	Thalamic Radiation
Trnp1	TMF regulated nuclear protein 1
Tub	Tubulin
Tuj1	Neuron-specific class III beta-tubulin
V	Varicosity
V1	Visual primary cortical area
VAMP	Vesicle-Associated Membrane Protein
Vim	Vimentin
VZ	Ventricular Zone

WB	Western Blot
WT	Wild Type





2. Abstract/Resumen

"Buenas noticias chicos"

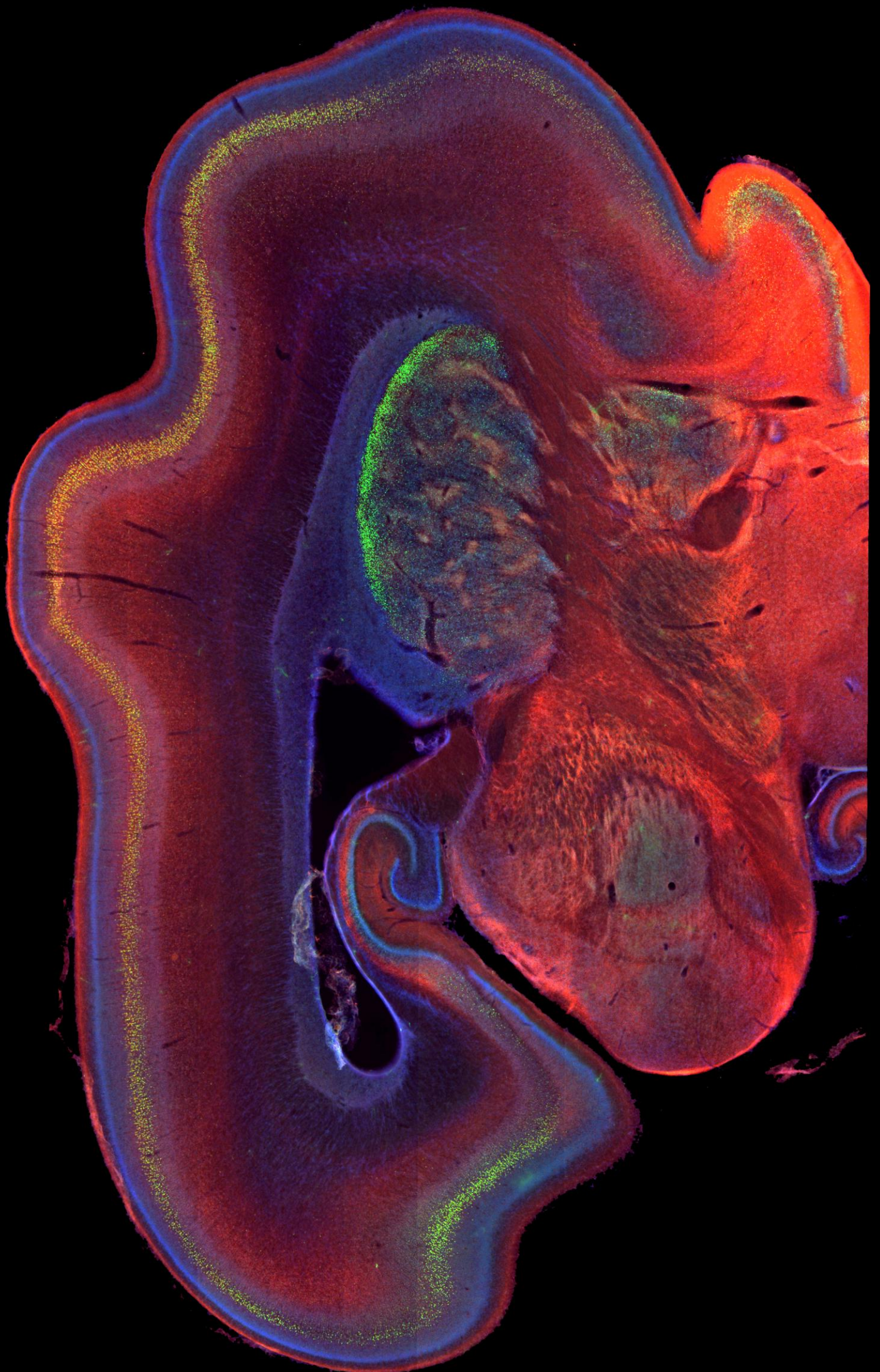
- Dr. Farnsworth, Futurama

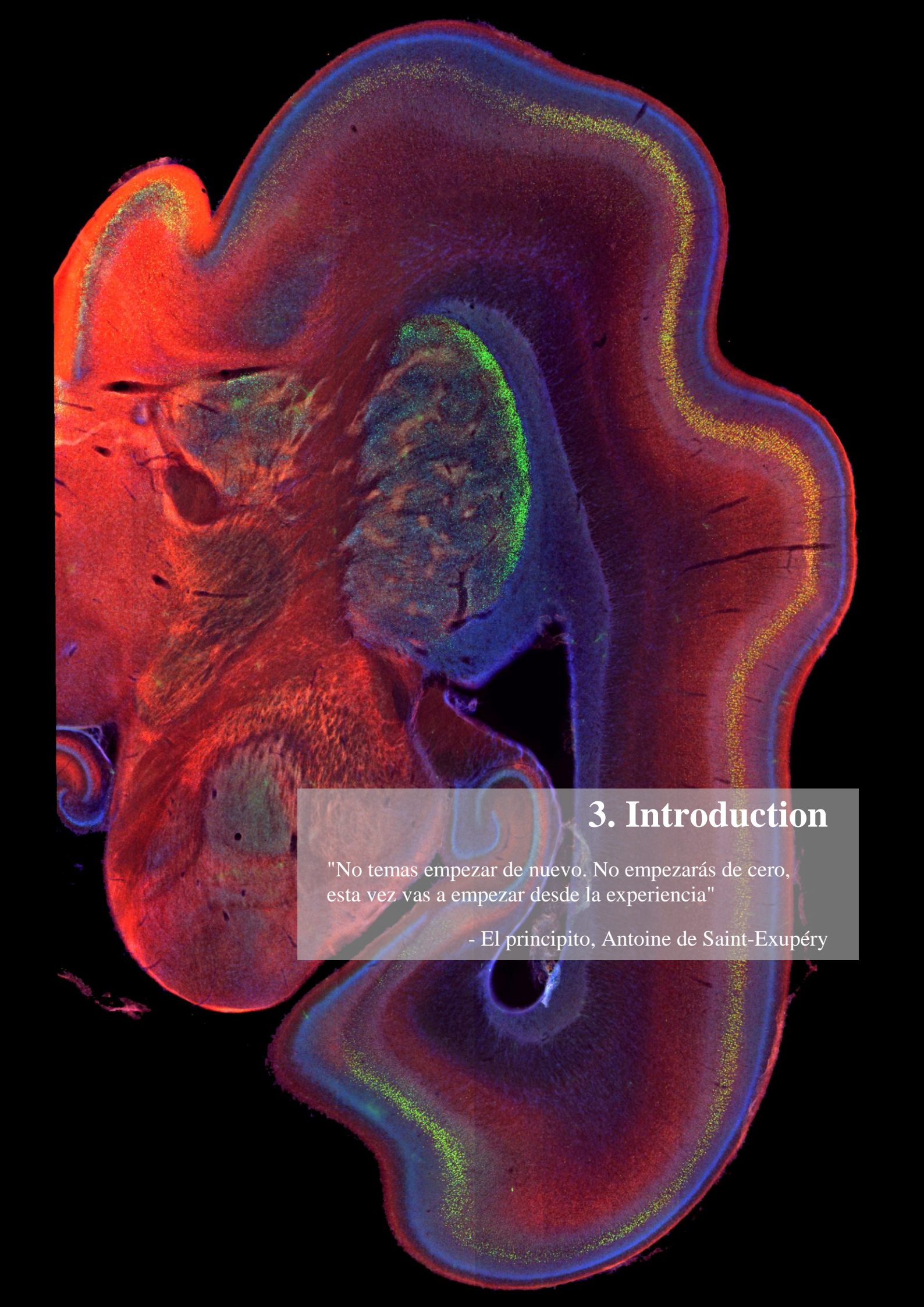
The mammalian cerebral cortex experienced an extraordinary expansion during evolution, concomitant with an increase in complexity and cognitive capacities. The increase in cortical surface area appeared along with folding, which allowed including a large cortical surface within a limited cranial volume. This evolutionary process is recapitulated during embryonic development, where the activity of progenitor cells determines the final brain conformation. Apical Radial Glia Cells (aRGCs) are the main type of progenitor cells in the cerebral cortex, forming the Ventricular Zone (VZ). aRGCs give rise to Intermediate Progenitor Cells (IPCs) and basal Radial Glia Cells (bRGCs), that populate the Subventricular Zone (SVZ). In gyrencephalic species, with a folded cortex as ferrets or humans, the SVZ is dramatically enlarged and subdivided into inner and outer domains (ISVZ and OSVZ), densely populated by bRGCs and playing critical roles in cortex expansion and folding. In ferret, aRGCs switch from amplificative divisions to produce massive amounts of bRGCs during a brief period, which will establish the OSVZ. Disruptions in bRGC production profoundly impair OSVZ formation, altering normal folding. In the ferret VZ several genes change their expression levels during development, in parallel with the dynamics of aRGCs forming bRGCs and the emergence of the OSVZ. These genes are promising candidates to regulate this process and, therefore, cortical folding. One of these candidates is *Sv2b*, which encodes for the Synaptic Vesicle Glycoprotein 2B, with not known function in progenitor cells or cerebral cortex development. In this thesis, we show that in the small and smooth mouse cortex, with very few bRGCs, *Sv2b* is not expressed in germinal layers. In contrast, in the big and folded ferret brain *Sv2b* is highly expressed in germinal layers, dynamically changing its expression before, during and after the critical period for bRGCs generation. *Sv2b* is downregulated during the critical period and later on upregulated. Moreover, when bRGCs are being massively produced, *Sv2b* is more expressed in the SVZ than the VZ. We have found that SV2B accumulates in subcellular compartments of aRGCs, including varicosities of the processes and the end-feet. By gain- and loss-of-function experiments in mouse and ferret, we have found that SV2B is involved in the laminar organization of the VZ, the delamination of aRGCs to basal positions, and their proliferation. At mid-term, these alterations lead to folding of the cortex. Experimental overexpression of SV2B in ferret during the critical period, when endogenous *Sv2b* expression is low, causes a reduction in proliferation and neurogenesis. Conversely, *Sv2b* removal from aRGCs induces an increase in proliferation and basal mitoses. Thus, levels of *Sv2b* expression regulate the

proliferative activity of aRGCs and the production of bRGCs during cerebral cortex development.

La corteza cerebral de los mamíferos experimentó una expansión extraordinaria a lo largo de la evolución, paralelamente a un aumento de la complejidad y las capacidades cognitivas. Este aumento en el área de la superficie cortical surgió de la mano del plegamiento cerebral, lo que permitió incluir una gran superficie cortical dentro de un volumen craneal limitado. Este proceso evolutivo se recapitula durante el desarrollo embrionario, donde la actividad de las células progenitoras determina la conformación cerebral final. Las células gliales radiales apicales (aRGCs) son el principal tipo de células progenitoras en la corteza cerebral, formando la zona ventricular (VZ). Las aRGC dan lugar a las células progenitoras intermedias (IPC) y a las células gliales radiales basales (bRGC), alojadas en la zona subventricular (SVZ). En especies girencefálicas, con una corteza plegada como la de los hurones o los humanos, la SVZ se amplía y subdivide en dominios interno y externo (ISVZ y OSVZ). Éstas están densamente pobladas por bRGCs y desempeñan papeles críticos en la expansión y plegamiento de la corteza. En hurón, las aRGC cambian de divisiones amplificativas a automermantes para producir cantidades masivas de bRGC durante un breve período de tiempo estableciendo la OSVZ. Las alteraciones en la producción de bRGC deterioran profundamente la formación de la OSVZ, alterando el plegamiento cortical normal. Se han identificado varios genes en la VZ de hurón cuyos niveles de expresión cambian durante el desarrollo, de forma paralela a la dinámica de aRGC para formar bRGC y la aparición de OSVZ. Por lo tanto, estos genes son prometedores candidatos para regular este proceso y, de este modo, el plegamiento cortical. Uno de estos genes candidatos es *Sv2b*, el cual codifica la *Synaptic Vesicle Glycoprotein 2B*, sin función conocida en las células progenitoras o en el desarrollo de la corteza cerebral. En esta tesis, mostramos que en la pequeña y lisa corteza de ratón, con muy pocos bRGCs, *Sv2b* no se expresa en capas germinales. En contraste, en cerebros de hurón grandes y plegados, *Sv2b* se expresa mucho en las capas germinales y cambia dinámicamente su expresión antes, durante y después del período crítico para la generación de bRGC. El mentado gen se regula negativamente durante el período crítico y luego aumenta de nuevo su expresión. Además, en este momento crucial para la producción masiva de bRGC, *Sv2b* se expresa más en la SVZ respecto a la VZ. Hemos descrito que SV2B se acumula en varios compartimentos subcelulares de las aRGCs, incluidas las varicosidades del proceso basal y los pies. Mediante experimentos de ganancia y pérdida de función en ratón y hurón, hemos descubierto que *Sv2b* está involucrado en la organización laminar de la VZ, la delaminación de las aRGC a posiciones basales y su proliferación. A medio

plazo, estas alteraciones conducen al plegamiento de la corteza en el área electroporada. La sobreexpresión de SV2B en hurón durante el período crítico, cuando la expresión endógena de *Sv2b* es baja, provoca una reducción de la proliferación y la neurogénesis. Por el contrario, la eliminación de *Sv2b* en las aRGCs induce un aumento en la proliferación y mitosis basales. Por lo tanto, los niveles de *Sv2b* regulan la actividad de las aRGC y la producción de bRGC durante el desarrollo de la corteza cerebral.





3. Introduction

"No temas empezar de nuevo. No empezarás de cero, esta vez vas a empezar desde la experiencia"

- El principito, Antoine de Saint-Exupéry

In the course of development, one of the first systems initiating its formation is the complex nervous system. Interestingly, this ensemble of organs is also the last in being completely formed after birth. The nervous system is divided into two major parts: the central (CNS) and the peripheral nervous system (PNS). The latter receives all the information from the peripheral organs and sends it to the CNS. It is composed of spinal and cranial nerves, while the CNS is mainly formed by the brain and spinal cord.

In particular, the nervous system reaches its maximum in terms of complexity with the brain. Although it has always been an important subject of interest, there are still features that remain obscure. The brain acts as the central controller of the body. This organ is in charge of collecting the information from our surroundings, processing, combining and storing it to respond accordingly, controlling all the organs, including itself. Vast knowledge about the brain is continuously generated at different levels and, integrating it, would derive in a coherent understanding about its formation, organization, function and alteration in disorders.

Within the animal kingdom, the mammalian brain is considered the pinnacle of the nervous system ever developed. Immense interconnected numbers of cells in an incredibly intricate wire form the brain. As an example of a highly complex structure, it has been predicted that in the human brain around 100 billion neurons form over 100 trillion estimated connections, called synapses (Purves, 2011). When facing this fascinating achievement of brain evolution, it is unavoidable to wonder how this complexity is formed during development and how the disruption of this process can lead to significant abnormalities.

3.1 Development of the mammalian nervous system

3.1.1 Ontogeny of the CNS

To understand how this incredibly complex structure functions, it is essential to know how it forms. The entire nervous system arises from one germ layer, the neuroectoderm, that folds inwards forming a closed tube. The neural tube is formed by neural stem cells able to give rise to all different kinds of neural cells. It is filled with liquid, and the walls thicken and expand during development to form the different brain structures,

while leaving cavities in the interior called ventricles (Fig. 1A). The prosomeric model attempts to compile the developmental brain structures with evolutionary conserved genetic boundaries and adult neuroanatomy (Puelles et al., 2013; Purves, 2011).

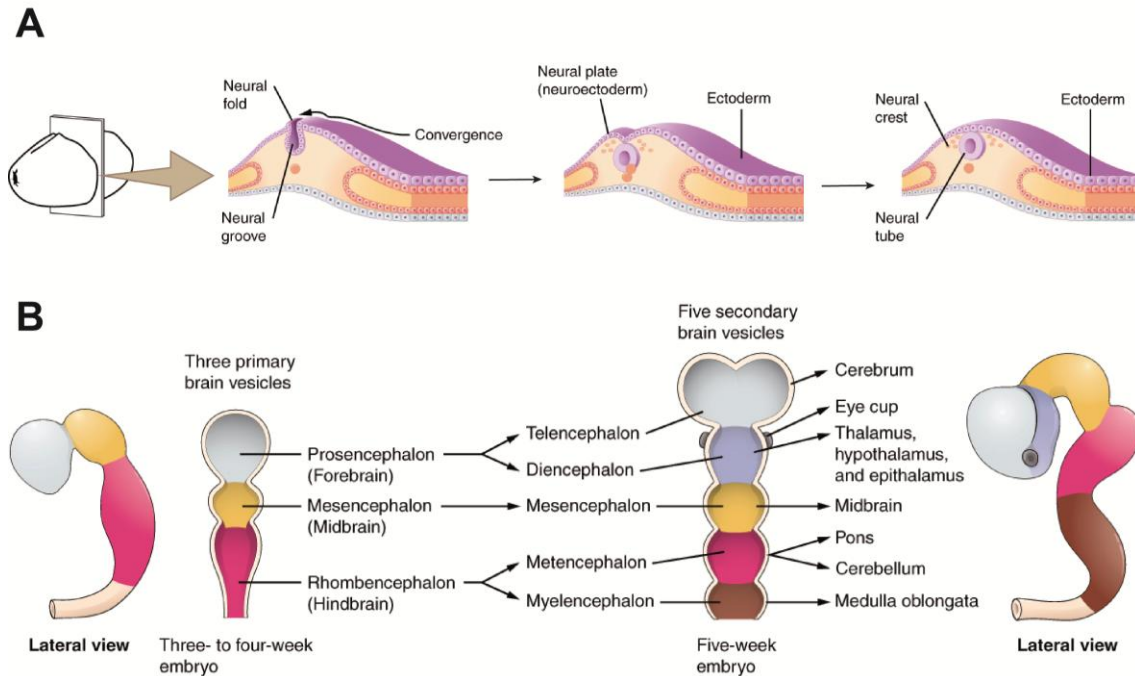


Figure 1. Early development of the nervous system. (A) The neuroectoderm folds inwards to form the neural tube. Below lies the ectoderm. The brain will rise from the anterior part of the neural tube while the posterior part will become the spinal cord. (B) Regionalization of the mouse embryonic central nervous system from E8.5 to E12.5. We can observe the enlargement and increase in complexity of the embryonic neural tube. Adapted from Gordon Betts, 2017.

According to this model, the neural primordium tube is subdivided in forebrain, midbrain, hindbrain and the spinal cord. The forebrain gives rise to the prosencephalon and diencephalon. Subsequently, these are subdivided in caudal secondary prosencephalon and rostral secondary prosencephalon and prosomeres 1-3. The midbrain is further differentiated in mesomeres 1-3. Then, in the hindbrain, we can recognize the prepontine hindbrain, the pontine hindbrain, the pontomedullary hindbrain and the medullary hindbrain, that will further generate the isthmus and rhombomeres 1-11. Together with the first rhombomere, the dorsal isthmus forms the cerebellum (Puelles et al., 2013; Purves, 2011) (Fig. 1B).

As complementary divisions, the alar-basal boundary further differentiates the central nervous system. Mainly, the alar lamina belongs to the dorsal part of the neural tube and the basal to the ventral part. Particular gene expression profiles precisely draw the subdivisions across the whole brain as *Sonic hedgehog (Shh)*, *Netrin1 (Ntn1)*, *Pax6*, *Pax3*, *Pax7*, *NK2 homeobox 1 (Nkx2.1)*, among others. In this scenario, we can further delimit the forebrain into the telencephalon and the preoptic telencephalon as alar formations; and the terminal hypothalamus and the peduncular hypothalamus as basal formations. Besides, the prosomeres form respectively the pretectum, thalamus and prethalamus. They are further subdivided in the ventral part into prethalamic tegmentum, thalamic tegmentum, pretectal tegmentum, the midbrain tegmentum and preisthmic tegmentum. The alar lamina of the midbrain generates the main midbrain tectum and the preisthmic tectum. In the spinal cord, the first one is conformed of mainly sensory neurons, while the second one would be composed of motor neurons (Puelles et al., 2013; Purves, 2011) (Fig. 1B).

As the next level of hierarchical subdivisions, within the telencephalon we can distinguish the pallium and subpallium (dorsal and ventral area respectively). The pallium gives rise to the cerebral cortex, the hippocampus and the olfactory bulb. The subpallium gives rise to the pallidum, the striatum, the preoptic area and the basal forebrain area (Puelles et al., 2013; Purves, 2011).

3.1.2 Phylogenic classification of cortical regions

Within the forebrain, the mammalian cerebral cortex is generally divided into three differentiated parts: the lateral paleocortex, the medial archicortex and, in between them, the isocortex or neocortex (Fig. 2).

3.1.2.1 Archicortex

In mammals, around 10% of the cortex corresponds to the allocortex which encompasses the archicortex and the paleocortex. archicortex (from *archi*, early) is the phylogenetically older cortex. It corresponds to the hippocampal formation, composed of three layers. The archicortex belongs to the limbic system, so it is mainly involved in memory formation and retrieval (Insausti, 1993; Purves, 2011).

3.1.2.2 Paleocortex

Phylogenetically, the paleocortex or olfactory piriform cortex would emerge during evolution in a mid-time between archicortex and neocortex. It is composed by four or five layers, depending on the information processing capabilities and proportionally to the phylogenetic age (Caroline Crosby and Humphrey, 1939; Insausti, 1993; Purves, 2011).

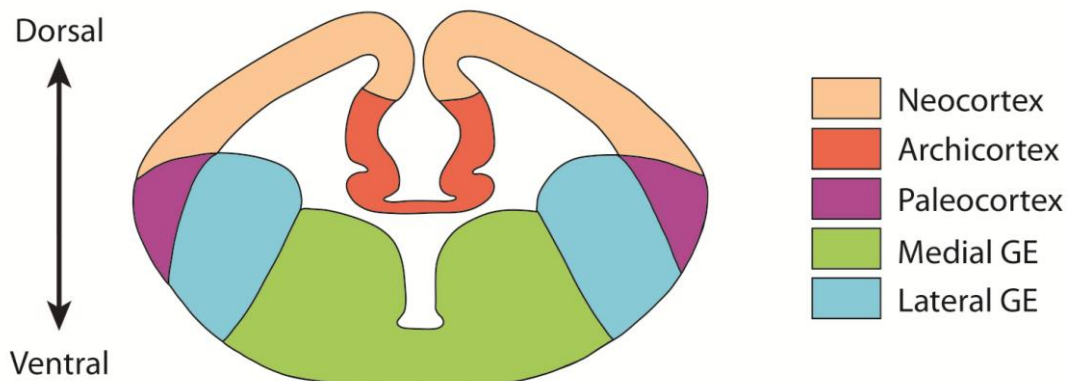


Figure 2. Schematic coronal section of an embryonic mouse brain phylogenetic areas of the cortex. It is distinguishable: Archicortex (dark orange), Paleocortex (purple) and Neocortex (light orange). The Ganglionic Eminences (GE) are also shown, both medial (green) and lateral (blue). Modified from Hebert and Fishell, 2008.

3.1.2.3 Neocortex

As its name suggests, the neocortex is the evolutionary newest region. It is considered the pinnacle of nervous system evolution and the responsible for the evolution of cognitive abilities in higher mammals, such as the human mental capacities. The evolution in complexity of the neocortex has been achieved thanks to a considerable enlargement of the cortex primarily. Indeed, the surface of the neocortex in the macaque monkey and human is 100 and 1000 times bigger than the mouse cortex, while the ratio in thickness is around two. It is thought that this enlargement is mainly due to an expansion of the basal surface without being accompanied by a comparable increase in thickness. In detail, the neocortex is a cellular sheet that shows some differences between mammalian groups, such as the presence or absence of convolutions (gyrencephalic or lissencephalic brains, respectively). However, the cerebral cortex of all mammals shares a common radial and tangential organization (Rakic, 1995, 2009).

3.2 Organization of the cerebral cortex

As it has been explained until this point, the embryonic telencephalon is derived from the most anterior part of the forebrain. From furthered subdivisions, the dorsal part or pallium gives rise to what we know as the cerebral cortex. Next, I will focus on the organization of the neocortex (hereon referred to as “cortex”).

3.2.1 Radial organization

The cerebral cortex is a sheet of tissue mainly composed of excitatory or projection neurons (namely pyramidal neurons), local circuit neurons (interneurons) and glial cells (further explained below). These cells showed an arrangement in vertical columns stereotypically interconnected in the vertical dimension and share extrinsic connectivity. In general, dividing cells are placed lining the ventricular cavities, attached apically to the ventricular surface and basally to the pial surface. Cortical excitatory neurons are generated near to the ventricle surface during the first half of gestation, and from there they migrate along the basal radial processes of the progenitors through the developing cortex, to their final position in the vicinity of the cortical surface. The radial-unit hypothesis states that cortical expansion during evolution was made possible as a result of changes in proliferation that would increase the number of radial columnar units. These are cells that share the same birthplace, the migration pathway and the ontogenetic column. In that way, cortical surface size would be determined by the number of ontogenetic columns, whereas cortical thickness would be determined by the number of cells within each column. Even in a large and convoluted cerebral cortex like primates, the radial alignment seems to be largely respected (Rakic, 1972, 1988, 1995, 2009) (Fig. 3).

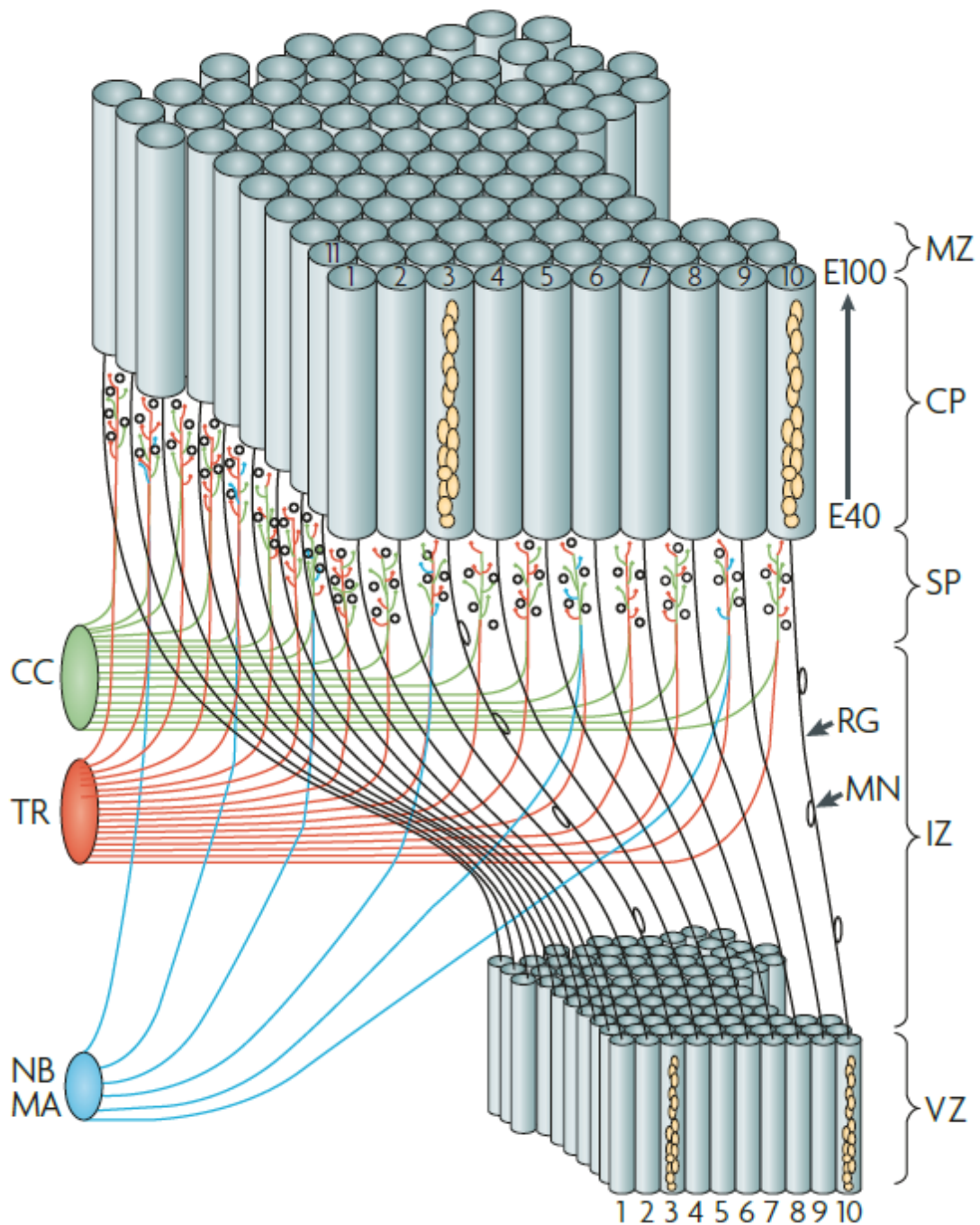


Figure 3. Columnar distribution and radial-unit hypothesis. Schematic representation of migrating neurons (MN) born from RGCs following the columnar organization through radial glia fibers (RG) in embryonic monkey cerebral cortex. Connections from other parts of the brain are shown as: cortico-cortical connection (CP - green); thalamic radiation (TR - red); monoamine nucleus basalis (MA, NB - blue). Layers of the cortex are also labeled with brackets: ventricular zone (VZ), intermediate zone (IZ), subplate (SP), cortical plate (CP) and marginal zone (MZ). Modified from Rakic, 2009.

Tangential final position of each neuron is defined by its birth time. Neurons will migrate towards the cortex traversing previous neuronal generations, and finally will be arranged in an inside-out pattern (Angevine and Sidman, 1961; Rakic, 1974). The differentiation of neurons takes place also in an inside-out manner, from deep to superficial layers. As a consequence, the neocortex is divided into six horizontal layers (Fig. 4), numbered from the pia mater to the white matter within different features (Fatterpekar et al., 2002; Kandel et al., 2012; Mountcastle, 1997; Purves, 2011):

- Layer I: also called the molecular or plexiform layer due to the absence of cell bodies. Instead, it is full of dendrites and axons from deeper layers.
- Layer II: named the external granule cell layer, it contains small packed spherical cells, the granule cells.
- Layer III: external pyramidal cell layer, it is composed of a variety of cell types. The majority of them display a pyramidal morphology, where deep cells are bigger than more superficial ones within the same layer. It also contains scattered non-pyramidal cells.
- Layer IV: usually the narrowest, it is called the internal granule cell layer. Similar to layer II, it is mainly populated by granule cells but also densely packed stellate cells.
- Layer V: also named the internal pyramidal cell layer, it is mainly occupied by pyramidal cells that are larger than those in layer III.
- Layer VI: known as the polymorphic or multiform layer, it is quite heterogeneous and it integrates with the white matter forming the inner border of the neocortex. It contains axons to and from the cortex, and spindle-shaped cells. In contrast, neurons in layers V and VI project their apical dendritic arbors to layers I and III, respectively.

This formation allows efficient distribution of the inputs that a neuron receives and sends, determining the function that each area will have. Interestingly, this basic layering schema is mostly preserved in different areas of the neocortex, but the thickness of each layer may vary. It is hypothesized that an increase in specific layers involved in intracortical information processing may have contributed to the amplification of cognitive abilities in higher mammals (Kandel et al., 2012;

Mountcastle, 1997). On the section *Cellular composition of the Neocortex* we will widely focused on neuronal types.

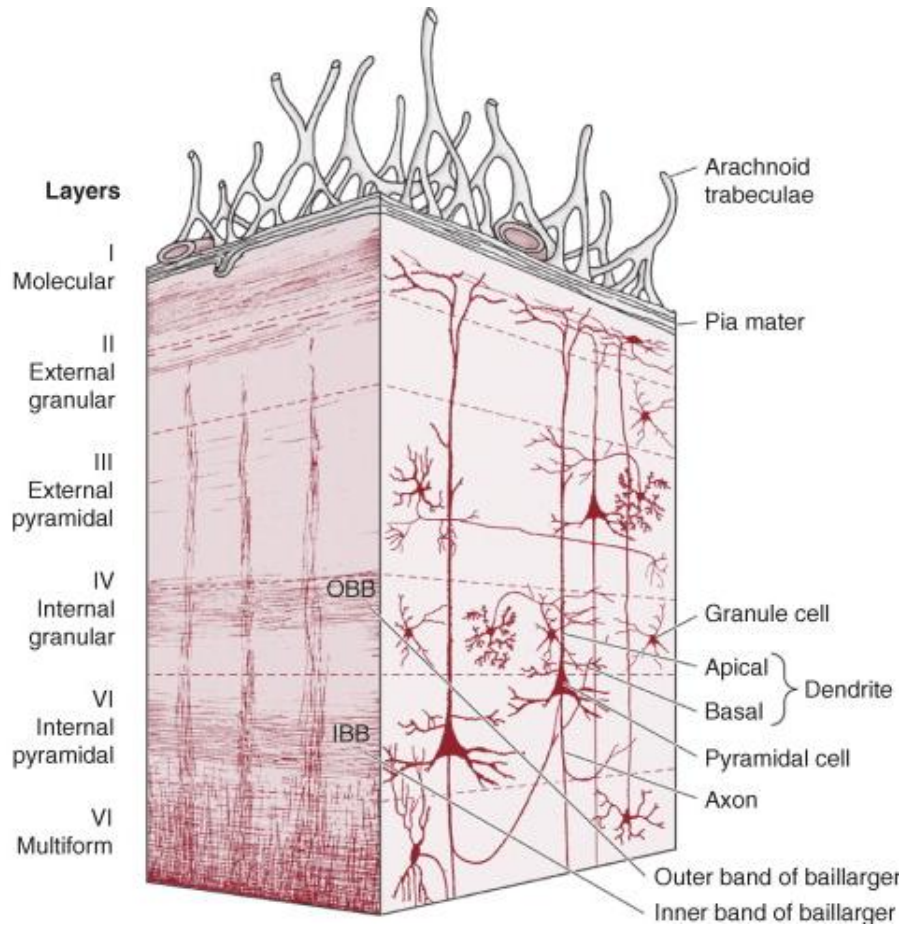


Figure 4. Radial organization and cellular composition of the cortex. Schema of the six layered cortex and the interconnections between neural cells in the coronal plane. Pyramid cells and interneurons are arranged in their final position. Scheme adapted from Krames et al., 2018.

3.2.2 Tangential organization

Functionally speaking, the cerebral cortex can be tangentially divided into several cytoarchitectonic areas. The first studies regarding the borders between cortical areas were based on distinctive cell size and packing characteristics (Brodmann, 1909). Going further, if we take into account also information about functional experiments, more distinct areas can be accurately defined (Arai and Pierani, 2014; Kandel et al., 2012; O'Leary et al., 2007).

The mammalian cerebral cortex is functionally organized around four primary areas: visual (V1), auditory (A1), somatosensory (S1) and motor (Fig. 5). These cortical

areas receive sensory inputs from the periphery and control motor output. Primary areas are connected to other areas specialized as integrating or processing centers, likely evolved later. Those centers are furthered connected with the multimodal associative cortex, where higher-order information is combined, processed and integrated. At this level, the inputs can even induce a response of conscious thinking. Along evolution not all areas expanded equally. For example, associative areas and prefrontal territories, mainly in charge of information integration, are notably expanded in the primate lineage (including humans). Interestingly, primates and carnivores with big and highly folded brains show relatively smaller areas for primary processing than for higher-order brain functions, when compared to species with small and smooth brains. These changes were accompanied by region-specific expression of gene programs (Arai and Pierani, 2014; Krubitzer, 2007).

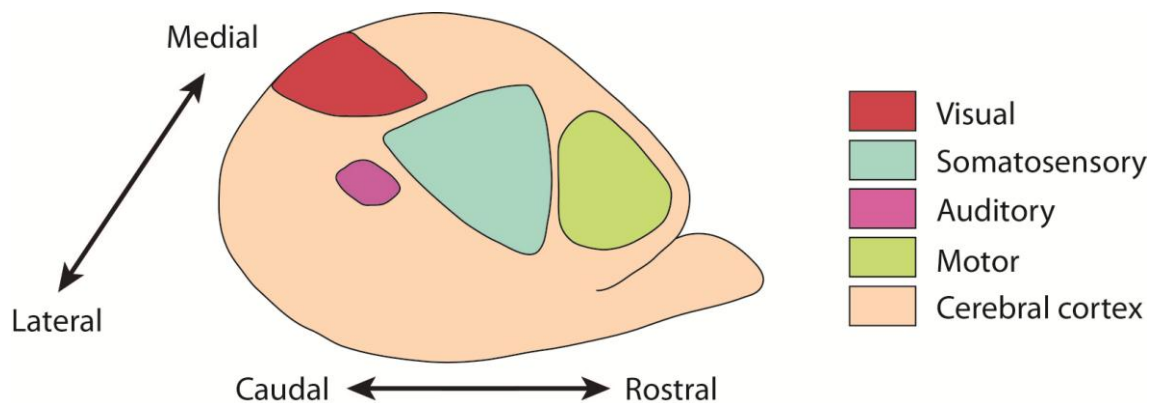


Figure 5. Arealization of the embryonic cerebral cortex. Primary area identity specification in embryonic mouse cerebral cortex: visual (red), auditory (purple), somatosensory (light blue) and motor (green). Modified from Greig et al., 2013.

Area identity starts to be specified early in development (around E12,5 in mice), when cortical progenitor cells may respond to different gradients of morphogens (such as Fgfs, Wnt, Bmps and Shh) secreted from organizing centers, that lead to differential expression of transcription factors and effectors like PAX6, EMX2, COUP-TF1 and SP8. Consequently, the dorsal telencephalon is regionalized along the anteroposterior and dorsoventral axes (Arai and Pierani, 2014; Kandel et al., 2012). In addition to the importance of the radial organization previously mentioned, external cues brought by peripheral axons arboring into cortical areas codified the ultimate determination.

3.3 Cellular composition of the neocortex

The mammalian neocortex is populated by a large number of cells and thanks to the considerable variability among them a high level of complexity can be achieved.

3.3.1 Excitatory neurons

Excitatory neurons are characterized by a pyramidal-like morphology and by containing the glutamate neurotransmitter, gaining the name of glutamatergic neurons. During development, they are mainly generated from progenitors placed in a neocortical germinal zone at the dorsolateral wall of the telencephalon, the ventricular zone (VZ), while at later stages, they are produced at the subventricular zone (SVZ), a layer at the lateral walls of the lateral ventricles. Neuronal production will be addressed in detail on section 3.4. Glutamatergic neurons are specialized in transmitting information between distant regions for what they extend axons to their intracortical, subcortical and subcerebral targets; a reason why they also deserve to be called projection neurons (Molyneaux et al., 2007; Rakic, 1974).

Attending to their morphologic features, electrophysiological properties, functions and gene expression patterns, is possible to classify them into diverse groups. They are so variable that their subdivision is complicated, but this also allows the creation of a very complex system (Migliore and Shepherd, 2005; Molyneaux et al., 2007).

3.3.2 Inhibitory neurons

Inhibitory neurons, also named cortical interneurons, are GABAergic, containing γ -aminobutyric-acid (GABA) and are locally projecting cells. The amount of these cells vary depending on the species, and less evolved cortices as in rodents contain fewer GABAergic interneurons compared to primates cortices. An excitatory-inhibitory balance is established from their interactions with glutamatergic neurons and the disruption of this equilibrium leads to severe and variable neurological disorders like schizophrenia or autism (Gelman and Marin, 2010; Jones, 2009).

These inhibitory cells are generated far from the neocortex, mainly at the medial (~60%) and caudal (~30%) ganglionic eminences of the ventral telencephalon and the preoptic area (~10%). Small populations are generated from lateral ganglionic eminence and septal area too. Interneurons migrate tangential pathways in the marginal zone and intermediate zone. To reach its final position at the cortex, they turn its pathway and migrate radially into the cortical plate. Curiously, in the human cortex, there is a subpopulation derived from progenitors that undergo, at least, its final division in the dorsal telencephalon and then migrate radially into the cortex like the glutamatergic neuronal pathway (Gelman and Marin, 2010; Jones, 2009; Molyneaux et al., 2007; Wonders and Anderson, 2006).

Each type of progenitor at the different localizations generate a distinct set of interneurons. Depending on the subset of neuropeptides that they also expressed, their morphology and their electrophysiological characteristics, we can define four main subclasses: fast-spiking Basket and Chandelier cells (parvalbumin containing); burst spiking or non-fast-spiking Somatostatin interneurons (somatostatin containing); bipolar rapidly adapting interneurons (calretinin and/or vasointestinal peptide containing) and multipolar rapidly adapting interneurons (neuropeptide Y and/or reelin containing) (Gelman and Marin, 2010).

3.3.3 Cajal-Retzius cells

This is a relatively reduced population of cortical neurons that are distributed along the marginal zone. They are required to establish the proper layering and radial migration of the neurons through the radial glia processes, and regulate progenitor cell behavior. These processes are regulated by the secretion of Reelin. Cajal-Retzius cells are born very early in development to assess such essential roles in the formation of the cortex and its organization. Cajal-Retzius cells are mainly generated at the cortical hem, from where they migrate tangentially to their final position right below the meninges. A small proportion of these cells come from other sites of the embryonic telencephalon, in the subpallium and septum (Molyneaux et al., 2007; O'Leary et al., 2007; Taverna et al., 2014).

3.3.4 Glial cells

These cells sustain a crucial role in the maintenance of the proper functioning of excitatory-inhibitory circuits. To assess such vital tasks, they are present in the brain at high numbers, achieving a 3 to 1 ratio with neurons. They also show complex processes but less prominent than glutamatergic neurons and for other purposes (Purves, 2011; Reemst et al., 2016). There are three types of glial cells in the nervous system:

- Astrocytes: restricted to the central nervous system and with a star-like morphology. These cells are principally in charge of maintaining the proper environment for circuitry transmission. In addition, several studies show a retaining of stem cell features in adult brains (Molyneaux et al., 2007; Purves, 2011).
- Oligodendrocytes: extend their membranes around some axons forming a lipid-rich wrap called myelin that allows high-speed transmission of electrical signals. Cells performing the same function but in the peripheral nervous system are named Schwann cells. Both retain mitotic capacity in response to neural injury, generating oligodendroglia or Schwann cells (Molyneaux et al., 2007; Purves, 2011).
- Microglia: mainly derived from hematopoietic precursors, fulfill a role in the CNS similar to macrophages in the rest of the body. They are mainly responsible for removing the cellular debris, resulting from injury or normal cell turnover. Moreover, microglia secrete factors to modulate inflammation and determine the cell decision between survival or death (Molyneaux et al., 2007; Purves, 2011). Lately, some studies have shown that microglia performs a much more critical role in neurogenesis regulation than what was before established in the field (Ueno and Yamashita, 2014).

3.4 Development of the mammalian cerebral cortex

Many features of the cerebral cortex are common to all mammals (i.e., organization in six layers), but the shape and surface area may differ quite dramatically. One easily identified difference is the presence or absence of convolutions within the neocortex. In that way, we can differentiate between gyrencephalic species (with a folded cerebral

cortex, like primates, ferrets and humans) and lissencephalic species (with a smooth cerebral cortex, like mice and rats). During embryonic development, neural progenitors and their derivatives are organized to produce the great variety of cortical cells that constitute the complex structure of the brain (Fig. 6). To understand the mechanisms by which the mature neocortex is built, we must study its germinal compartments.

3.4.1 Germinal layers

3.4.1.1 Ventricular Zone

In the first steps of cortical development, the neural plate and the neural tube are composed of a single layer, the neuroepithelium (NE). Primary progenitor cells are distributed lining the telencephalic ventricle surface in a false appearance of lamination (pseudostratified epithelium) due to the distribution of the cell nuclei. This monolayer of progenitor cells is later transformed into the Ventricular Zone (VZ), a primary germinal layer from which all neurons of the mature neocortex are generated (Borrell and Reillo, 2012; De Juan Romero and Borrell, 2015; Smart et al., 2002).

3.4.1.2 Subventricular Zone: Outer and Inner subdivisions

Around embryonic day 10.5 in mice, neurons start being generated and accumulate giving rise to distinct layers. Following, right basal to VZ, a secondary germinal layer forms, the subventricular zone (SVZ). This layer contains radially and tangentially migrating neurons, radial fibers and axons. It also contains basal progenitor cells, which have a central role in cortex formation (Fig. 6). The population of basal progenitors is quite heterogeneous and a major focus of this Thesis, so it will be described in further detail in the following sections.

The number of progenitor cells in SVZ increases rapidly during development in gyrencephalic compared to lissencephalic species. Indeed, the vast majority of cortical progenitor cells in human embryos are found in the SVZ, while in rodents it only contains about one third of cortical progenitor cells. The size of the SVZ correlates with the degree of folding, in agreement with its crucial role in cortical expansion during

development and evolution (Fig. 6). Moreover, a higher accumulation of mitosis is found at the SVZ of the most pronounced gyration compared to less convolved adjacent areas (Borrell and Reillo, 2012; Reillo et al., 2011; Smart et al., 2002).

In fact, in these large brains, SVZ can be divided into inner (ISVZ) and outer SVZ (OSVZ), where the first one stays apically to the second (Fig. 6). Both sublayers are distinguishable, due to the lower cell density of the OSVZ and the axonal processes that separate them (the inner fiber layer, IFL). The ISVZ is also thinner, and the OSVZ is further subdivided into inner and outer (iOSVZ and oOSVZ) (Borrell and Reillo, 2012; Smart et al., 2002).

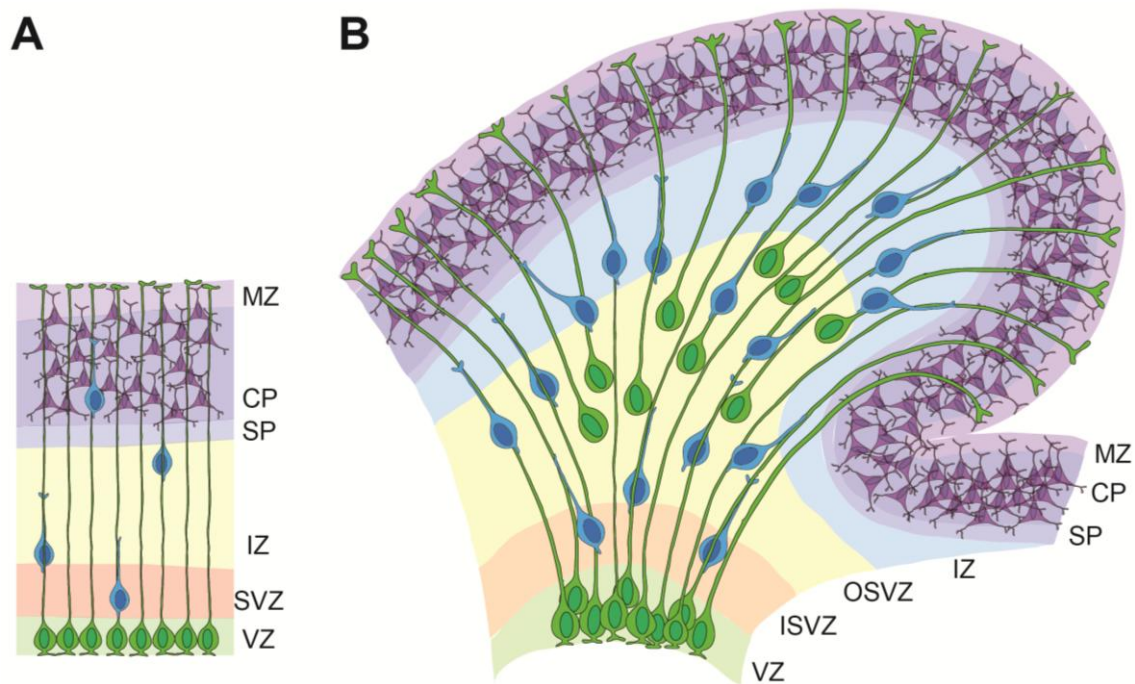


Figure 6. Tangential versus radial expansion of the cerebral cortex. (A) In lissencephalic species as mouse, radial glia fibers from RGCs (green) are parallel and migrating neurons (blue) follow those processes with parallel trajectories. (B) In gyrencephalic species, radial fibers may be parallel or divergent. These variability allows radial migration and tangential dispersion at the same time, thus, increasing the surface area and folding on cerebral cortex. Radial fibers from bRGCs intercalate between aRGCs favoring also this tangential expansion. Differentiated neurons appear in purple at the final position on the cortical plate (CP). VZ, Ventricular Zone; SVZ, Subventricular Zone; IZ, Intermediate Zone; SP, Subplate; CP: Cortical plate. Adapted from Borrell and Reillo, 2012.

3.4.2 Neural progenitors: features and dynamics

Several types of progenitor cells participate and are crucial for the formation of the cerebral cortex. As it has been reiteratively described, the neocortex displays a high degree of polarization, with an apical and a basal side (Fig. 6 and 7). According to the location of mitosis, cortical progenitor cells are classified as apical or basal (Gotz and Huttner, 2005).

3.4.2.1 Apical progenitors

This type of progenitors undergoes mitosis at the apical or ventricular surface, and their soma is located within the NE or VZ. Four different types of apical progenitor cells have been identified: Neuroepithelial Cells (NECs), apical Radial Glia Cells (aRGCs), apical Intermediate Progenitors (aIPs) and Subapical Progenitors (SAPs) (Fig. 7).

Neuroepithelial cells

In early cortical development, the neuroepithelium is formed by NECs organized in a pseudostratified manner, which retain an attachment to both apical and basal lamina. These cells are self-amplifying progenitors that expand the surface area of the telencephalic walls. Although NECs are committed to the neural lineage, they show typical epithelial features such as polarization, a belt of tight and adherent junctions at the apical site, and integrin receptors at the basal lamina (De Juan Romero and Borrell, 2015; Gotz and Huttner, 2005).

Apical Radial Glia Cells

At mid-corticogenesis, concomitantly with the formation of a layered sheet, NECs begin to downregulate some epithelial features. NECs show astroglial ultrastructural characteristics like glycogen granules and initiate the expression of astroglial molecules; like Astrocyte-Specific Glutamate Transporter (GLAST), Ca²⁺-binding protein S100 β , Vimentin, GFAP or Brain Lipid Binding Protein (BLBP). These changes sustain the

transition of NECs to another type of progenitor cells, the apical Radial Glia Cells (aRGCs) (Borrell and Reillo, 2012; De Juan Romero and Borrell, 2015; Gotz and Huttner, 2005).

aRGCs display their own specific features, showing an accumulation of Prominin-1, PAR3, PAR6, aPKC, β -catenin, N-cadherin and PAX6 (Gotz and Huttner, 2005). In spite of this transformation, aRGCs still retain neuroepithelial hallmarks as the Nestin expression, an adherent junction belt or the highly polarized morphology with the attachment to both apical and basal limits of the developing cortex. Indeed, mutations inducing detachment from the apical junction organization promote delamination of neurons and basal progenitors born from aRGCs (Kawaue et al., 2019). At the apical surface, a single cilium emerges from these progenitor cells into the cerebrospinal fluid at the ventricle. With regard the basal process, this is branched at the marginal zone where the tips formed growth cones much simpler than axonal ones and with a bulb-like structure. These endings are attached to the basal lamina, which is composed of integrins, extracellular matrix proteins and G-protein coupled receptors (De Juan Romero and Borrell, 2015; Gotz and Huttner, 2005; Takahashi et al., 1990).

In regard to subcellular compartments of aRGCs, there are still not many studies. It has been shown that the polarization of these cells is also a reflex of their distribution of mRNA, proteins and organelles, such as Golgi apparatus or centrosomes. Interestingly, some compounds change their subcellular localization depending on the cell cycle phase or progenitor type (Arai and Taverna, 2017; Taverna et al., 2016).

As development progresses and more cells are being produced, the cerebral cortex increases in thickness. Because aRGCs remain in contact with the basal lamina, their basal process increases in length, now referred to as radial fiber. Newly formed neurons need to travel through the thickness of the developing cortex to their final position near the basal surface, and use these radial fibers as a guide and scaffold. Hence, aRGCs are both generators of cortical cells and guides for radially migrating neurons (Borrell and Reillo, 2012; Rakic, 1972). Compared to NECs, aRGCs are more committed to a neural fate, and settle as the primary progenitor cells of the neocortex, giving rise to all subsequent progenitor cells and all excitatory neurons (De Juan Romero and Borrell, 2015; Gotz and Huttner, 2005).

Apical Intermediate Progenitors and Subapical Progenitors

Recent studies have described two more progenitor types similar to aRGCs. Apical Intermediate Progenitors (aIPs), also called Short neural precursors, are a small population of progenitors that, like aRGCs, present an apical-basal polarity and divide apically (Gal et al., 2006). They are also anchored to the ventricular surface, but their basal process is short and confined to the VZ. Normally, aIPs experience self-consuming divisions, generating basal progenitors or neurons (De Juan Romero and Borrell, 2015; Pilz et al., 2013).

Last but not least, Subapical progenitors (SAPs) also extend apical and basal processes but undergo mitosis at the basal half of the VZ. SAPs are included in the adherent junctions belt near the ventricular surface. Both aIPs and SAPs are capable of undergoing several rounds of division, but, at least in the mouse cortex, their relative abundance is low (De Juan Romero and Borrell, 2015; Pilz et al., 2013).

3.4.2.2 Basal progenitors

As indicated by their name, basal progenitors undergo mitosis at an abventricular localization (basal positions), principally in the SVZ. Two main classes of basal progenitors are distinguished in the embryonic cerebral cortex: basal Intermediate Progenitors (bIPs) and basal Radial Glia Cells (bRGCs) (Fig. 7).

Basal Intermediate Progenitors

Basal Intermediate Progenitors (bIPs), or Intermediate Progenitor Cells (IPCs), directly derive from aRGCs. After being born, they migrate from VZ to populate the SVZ. They retain an apical process anchored to the apical lamina by adherent junctions until their first cell cycle progression, when this is entirely detached from the apical surface. During this transition from aRGCs, IPCs begin to downregulate the aRGC marker paired-box transcription factor 6 (PAX6) and proceed to express the T-box transcription factor 2 (TBR2) (de Juan Romero et al., 2015; Gotz and Huttner, 2005).

Typically, IPCs only divide once to produce two neurons, hence duplicating the neurogenic output of each single aRGC. As a result, IPCs are the major source of glutamatergic neurons in the mouse cortical plate. Although the focus of this description is the neocortex, IPCs are also present in other parts of the developing forebrain, where they have been observed to undergo multiple rounds of self-amplifying divisions (Borrell et al., 2012; De Juan Romero and Borrell, 2015; Pilz et al., 2013).

Basal Radial Glia Cells

Basal Radial Glia Cells (bRGCs) have their soma placed in the SVZ, and thus they undergo mitosis at basal positions. bRGCs share multiple structural and molecular characteristics with aRGCs, including the expression of PAX6 and intermediate filament Vimentin, but not of TBR2. Similarly, classical bRGCs extend a long basal process attached to the basal lamina, like aRGCs, but then do not have an apical process contacting the ventricular surface, and hence they lack the expression of apical membrane proteins such as PAR3, PROM1 or aPKC. Videomicroscopy of living brain slices demonstrate a wide range of bRGCs morphologies with high degree of plasticity to dynamically change to other bRGC shape. While in aRGCs the Golgi apparatus is confined to the apical process and far from the centrosome, in bRGCs the Golgi apparatus is placed in the basal process and becomes pericentrosomal. Moreover, one of the first detectable differences in nascent bRGCs is the relocation of the cilium to an abventricular position (Arai and Taverna, 2017; Betizeau et al., 2013; De Juan Romero and Borrell, 2015; Fietz et al., 2010; Hansen et al., 2010; Taverna et al., 2016; Toda et al., 2016).

bRGCs are very scarce in the mouse cortex but extremely abundant in large cortices like ferret, macaque and human. In mice, they usually divide only once to generate two neurons in a self-consuming manner, similar to IPCs, contributing to neuron production at late stages of development. In larger and folded cortices, however, bRGCs self-amplify multiple times before producing neurons, thus massively increasing neuron production (Betizeau et al., 2013; De Juan Romero and Borrell, 2015; Gotz and Huttner, 2005; Hansen et al., 2010; Reillo and Borrell, 2012; Reillo et al., 2011). Furthermore, several previous studies reveal that the number of basal progenitors can

vary due to loss of apical adherent junctions, ultimately inducing delamination of the progenitors and early neuronal differentiation (Cappello et al., 2006; Chenn and Walsh, 2002). Interestingly, bRGCs are crucial in driving cortex folding and further details will be addressed at section *Cerebral cortex: underlying neurogenesis and cortical folding*.

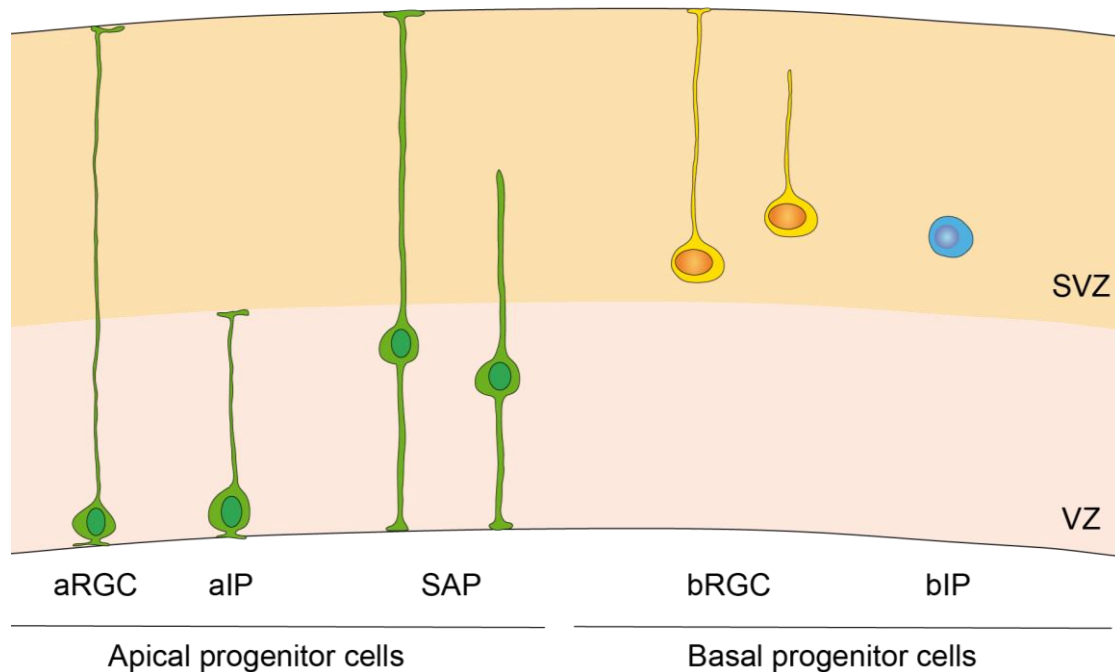


Figure 7. NPC types in the developing neocortex. NPC are classified according to the localization of their mitosis, cell polarity and the presence of apical contact. Apical progenitor cells include apical Radial Glia Cells (aRGCs), apical intermediate progenitor (aIPs) and Subapical Progenitor (SAPs). All of them undergo their mitosis on the VZ but the later one show an adventricular localization. aRGCs and SAPs present a basal contact, while aIPs show a ventricular contact. Basal progenitor cells, which mitoses take place at basal positions, comprise basal Radial Glia Cells (bRGCs) and basal Intermediate Progenitors (bIPs). Both types lack of an apical attachment but bRGCs may present a basal contact. Adapted from Florio and Huttner, 2014.

Single cell transcriptomic analyses subdivided the already presented progenitor types based on their different levels of expression of determined genes. However it is not clear enough with this data if the additional subclasses belong to progenitor cell types or different transcriptional transitional states. As an example, some studies classified as distinct groups progenitor cells and dividing progenitor cells, although the transcriptional differences just reflect two cell states of the same progenitor cell. This

variability remains relatively simple in lissencephalic species, although a broader amount of populations can be differentiated in gyrencephalic species as ferret or human (Betizeau et al., 2013; Johnson et al., 2015; Pollen et al., 2015). Thus, molecular cascades developed a critical role in formation and maintenance of stem cells and so, in cortical expansion too (Betizeau et al., 2013; De Juan Romero and Borrell, 2015; Reillo and Borrell, 2012).

3.4.3 Cell cycle and Interkinetic Nuclear Migration

As mentioned previously, neural progenitor cells in the NE and the VZ are set along the apical-basal axis in a bipolar morphology, extending two processes to each surface of the cortex (apical or basal) and the soma placed in the NE showing a pseudostratified structure with several layers of nuclei. This distribution of cell nuclei is due to their continuous apical-basal movements in a cell cycle-dependent manner (Fig. 8A and 8B), known as interkinetic nuclear migration (INM). During the G1 phase, the cell grows and the nucleus travels from the apical to the basal surface, where the synthesis of DNA (S phase) takes place. Next, during G2, the nucleus moves apically, to finally undergo mitosis (M phase) at the ventricular surface. After mitosis, if the cell re-enters the cell cycle proceeds into G1, again with the movement of the nucleus from the apical to the basal surface. This INM spans the entire thickness of the NE, but as the cortex grows in thickness this movement becomes restricted inside the boundaries of the VZ, while neurons accumulate basally between VZ and the pial surface. As development progresses, the cortex becomes thicker and the basal process of aRGCs elongates, maintaining INM within the VZ which, hence, it defines the VZ thickness (De Juan Romero and Borrell, 2015; Gotz and Huttner, 2005; Miyata et al., 2015; Reiner et al., 2012; Taverna and Huttner, 2010; Watanabe et al., 2018). Intriguingly, although INM is evolutionary conserved, the migration flow from the apical to basal surface seems to vary between species, in the same way as VZ thickness and cell density differs. For example, the straightness of the nuclear movement is higher in mice G2 phase compared to ferret, unlike G1 phase in these species (Miyata et al., 2015; Okamoto et al., 2014).

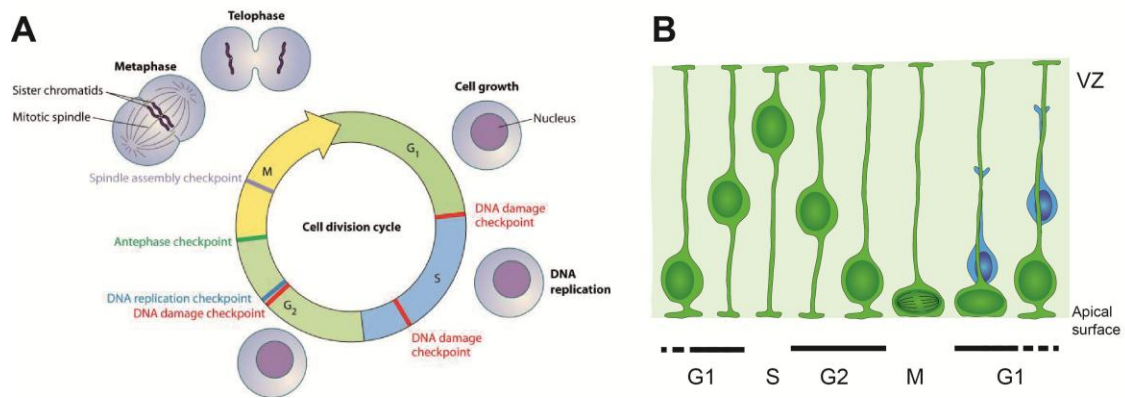


Figure 8. Cell cycle and INM. (A) Cell cycle and its checkpoints. During G₁ (green), cells grow. Then, progenitors replicate their DNA along with S phase (blue). After the G₂ phase, cells undergo mitosis (M phase; yellow), where the sister chromatids are separated into two daughter cells. In red, checkpoints for DNA damage are labeled. In G₂ phase, DNA replication (blue) and proper anaphase (green) is controlled. A final checkpoint has been suggested where the correct spindle assembly is assessed. (B) Interkinetic Nuclear Migration is represented, showing the soma dynamics along the cell cycle. In green, the progenitor cell and in blue, the newborn neuron. Modified from Chin and Yeong, 2010.

Deregulation of INM has been related to severe cortical malformations, as in human mutations for *LIS1*, where abnormal neuron migration and defects in INM produce Lissencephaly (smooth brain) (Gotz and Huttner, 2005). INM dysfunction is a consequence of several factors. Watanabe *et al.*, showed that a basal physical limitation is necessary for progenitors to undergo regular movements (Watanabe *et al.*, 2018). Interestingly, blocking INM and uncoupling it from the cell cycle does not prevent cell division. However, INM can be disrupted due to an alteration in the cell cycle (Taverna and Huttner, 2010). The cell cycle is regulated by several checkpoints to assess a proper division, where the growth of the cell, the DNA integrity and the correct segregation at mitosis are verified (Fig. 8A). When damage is identified, the response varies greatly, from cell cycle reprogramming to cell death. Classically, three checkpoints are distinguished: 1) G₁ checkpoint; 2) intra-S phase checkpoint; and 3) G₂/M checkpoint. The first and the third prevent cells from progressing into S phase or G₂ to M phase, respectively, with damage DNA from previous stages. Both can delay during hours or even arrest cell cycle as a result of post-translational modifications of effectors that drive alterations of transcriptional programs. On the other hand, the intra-S phase checkpoint causes only transient delays when sensing genotoxic insults. It inhibits the

initiation of a new replicon lagging DNA replication. Additionally, some authors include a DNA replication checkpoint close to G2/M phase, where the cell may detect unpaired DNA lesions from S phase due to inappropriate replication (Barnum and O'Connell, 2014; Chin and Yeong, 2010; Lukas et al., 2004).

Interestingly, somal movements during cell cycle seem not a unique characteristic of NECs and aRGCs. A similar process takes place in basal proliferative regions of large cortex like ferret, macaque or human, where basal progenitors (both bRGCs and SAPs) undergo nuclear translocation linked to cell division. This process has been called mitotic somal translocation, and its frequency of appearance varies between species (De Juan Romero and Borrell, 2015; Hansen et al., 2010; Taverna et al., 2014). Just prior to mitosis, and contrary to what happens with aRGCs, basal progenitor somas undergo a fast movement in the basal direction. And before nucleus movement, the cellular centrosome shifts into the basal process. Nuclear migration during the cell cycle seems to be an essential feature for proper division and in evolution. However, its functional significance remains currently unknown (Hansen et al., 2010).

3.4.4 Types of division

After presenting the variability in progenitor types and the process by which they divide, I will focus on the possible outputs of cell division. Depending on the daughter cell identity, cortical stem and progenitor cells divide symmetrically or asymmetrically. In the first case, the progeny will show the same identity, while from asymmetric division two different cells arise. Each division can either self-renew the progenitor cell or consume it, independently of the division symmetry. In self-renewing divisions, one daughter cell has the same identity of the progenitor cell but the other is different. In consumptive divisions, both cells are distinct from the mother cell. Consequently, four possible combinations of cell division may occur: asymmetric self-renewing, asymmetric consumptive, symmetric proliferative or symmetric consumptive (Fernandez et al., 2016; Gotz and Huttner, 2005; Llinares-Benadero and Borrell, 2019; Taverna et al., 2014) (Fig. 9).

The mechanisms underlying the decisions among the types of divisions are still under study, but asymmetry is shown to be related to the asymmetric physical

inheritance of specific molecules. This is highly correlated with the division plane, a cleavage plane parallel to the ventricular surface usually produce an asymmetric division because of the marked apico-basal polarity of the progenitor cells. However, a perpendicular cleavage plane derives more probably in symmetric divisions where both daughter cells inherit the same type of components (Taverna et al., 2014).

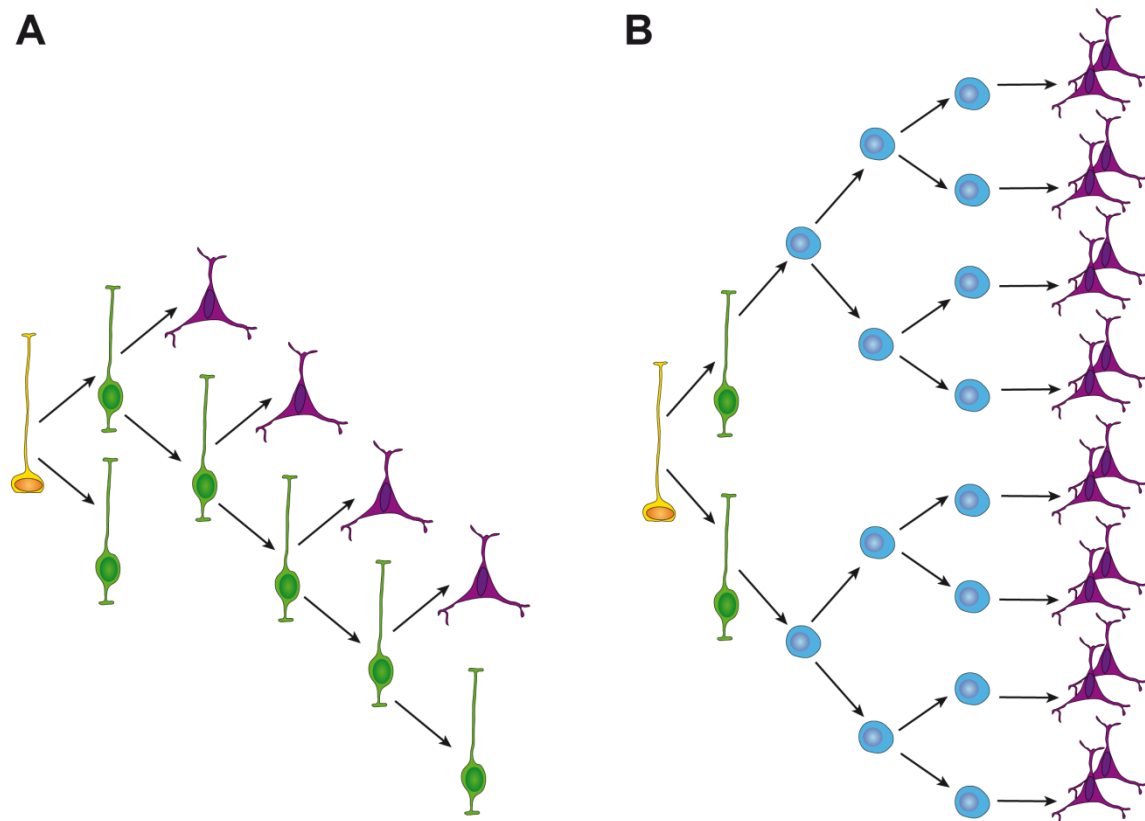


Figure 9. Types of divisions at cerebral cortex. Schematic representation of the types of progenitor divisions during cortical development. (A) Direct divisions would early deplete neural progenitors giving rise to few neurons. (B) Indirect divisions would give rise to higher amounts of neurons by IP generation and division. NE (yellow), RGCs (green), IP (blue) and neurons (purple). Adapted from Fernandez et al., 2016.

Changes on cell division modes at early developmental stages generate profound abnormalities in the mature neocortex, commonly dealing with microcephaly and macrocephaly (neurodevelopmental disorders characterized by aberrant reduction or enlarged cortex, respectively) (Sun and Hevner, 2014). As an example, some studies have reported that premature switching from asymmetric aRGCs division to symmetric proliferative division are related with microcephaly phenotypes (Fish et al., 2006;

Johnson et al., 2018). Evolutionary changes in cell division mode would also affect basal progenitor production, and then, cortical expansion (Cardenas et al., 2018). Thus, the proper number and type of cell divisions have to be carefully regulated to produce the proper populations of cells generating a well formed brain (Sun and Hevner, 2014) (Fig. 9).

3.5 Cerebral cortex: factors underlying neurogenesis and cortical folding

Humans have a very large brain-to-body weight ratio, mainly consequence of an increase in brain cell number. This increment is largely due to a high abundance of basal progenitor cells and entails primarily an increase in cortical surface rather than in thickness. However, cortical expansion and folding is not just a matter of an increased proliferation, as has been widely shown by human malformations and mouse mutations which, while forcing a massive overgrowth of the cerebral cortex (such as *WDR6*, *ASPM*, *FGFR3*, *FLN1A* and *GPR56*), are not accompanied of *bona fide* folding. Conversely, human mutations causing microcephaly, a significant reduction in cortical neuron abundance, may nonetheless display normal folding patterns. Interestingly, it has been reported that modifications in *Cdk4* expression leads to a massive production of basal progenitors in lissencephalic (mouse) and gyrencephalic (ferret) cortices, but folding was increased only in ferret. Hence, such a complicated process depends on many different features that have to be tightly coordinated and regulated (Borrell, 2018; Borrell and Reillo, 2012; Nonaka-Kinoshita et al., 2013; Smart et al., 2002). Next, I detail how proliferation and other important factors seem to underlie folding and cortical expansion.

3.5.1 Primary factors

We refer to primary factors as those that directly influence cortical folding, either by increasing progenitor cell numbers, neuronal dispersion or tissue plasticity (Fig. 10).

3.5.1.1 Regulation of apical progenitor cell proliferation

The abundance of NECs is greater in gyrencephalic species compared to lissencephalic species. The NE, and later the VZ, are larger and have a greater ventricular surface compared to lissencephalic species. Consequently, the telencephalic vesicles are much greater in size, suggesting a direct relationship between NECs abundance and expanded cortex (Fernandez et al., 2016; Reillo et al., 2011; Sauerland et al., 2018; Smart et al., 2002).

In addition, progenitor lineage dynamics is also critical in the final neuron production. Progenitor cells continuously have to decide whether directly producing neurons or intermediate progenitor cells, which amplify their neuronal output. Interestingly, the genetic mechanisms that control this choice seem to be well evolutionary conserved, and changes in expression levels of these genes modify the balance of basal progenitor production (Cardenas et al., 2018). The proliferative potential of progenitor cells is also related to cell cycle length. While shorter cell cycles are related to the generation of more stem cells, longer cell cycle promotes the production of differentiated cells. This seems to be largely due to the shortening of S-phase in neurogenic aRGCs and bIP, thus reducing DNA repairing time (Betizeau et al., 2013; Borrell and Calegari, 2014; Pilz et al., 2013; Taverna et al., 2014; Turrero Garcia et al., 2016). Hence, evolutionary alterations on cell cycle length influence the proliferative potential. Moreover, even while the cell cycle is longer in species like macaque, ferret and human, their period of neurogenesis is also much longer, allowing for more time to undergo several additional rounds of division compared to rodents, thus allowing an increase in neuronal production (Borrell and Calegari, 2014; Fernandez et al., 2016; Reillo and Borrell, 2012).

An additional level of proliferation regulation and fate determination is related to calcium. In the VZ, spontaneous calcium waves during cortical development regulate neuronal production. These calcium waves seem to be in charge of orchestrating the progenitors' proliferation in a coordinated manner, such that disruption of calcium waves reduces proliferation. This mechanism seems to depend on ATP receptors and IP3-mediated calcium release. Calcium diffuses through connexin hemichannels between cells (Weissman et al., 2004). Lately, another type of proliferation regulation via calcium has been reported. Along cortical development, apical progenitors decrease

their membrane resting potential concomitantly with the transition to generate late neurons and IPs. Hyperpolarization induces a shift to precocious late neuron production, changing the neurogenic potential of progenitors (Vitali et al., 2018). Radial communication within RGCs has been also suggested to take place by calcium bidirectional propagation. RGC fibers provides a link between proliferative and postmitotic zones allowing long distance communication. This mechanism for information transmission is induced by Notch signaling and growth factors (Rash et al., 2016).

3.5.1.2 Basal progenitor abundance

In addition to a larger VZ, gyrencephalic species also present a dramatically thickened SVZ. This is subdivided in inner and outer domains (ISVZ and OSVZ, respectively) and populated by an outstanding number of basal progenitors, particularly within the OSVZ. I previously mentioned that the SVZ has an essential role in the outstanding enlargement of the cerebral cortex, and in particular the OSVZ and its constituent basal progenitors are key in cortex folding. Contrary to the scarce amount of bRGCs in mice, in gyrated animals these are in much greater quantity and have a greater self-amplificative potential, and exert a profound impact on cortical development (Borrell and Reillo, 2012; De Juan Romero and Borrell, 2015; Martinez-Martinez et al., 2016; Nonaka-Kinoshita et al., 2013; Reillo et al., 2011; Sauerland et al., 2018; Smart et al., 2002; Taverna et al., 2014; Toda et al., 2016). Intriguingly, the massive production of basal progenitors in gyrencephalic cerebral cortices is remarkably higher in prospective gyri than sulci, producing a larger final number of cortical neurons. Studies using ferret as a model of gyrification demonstrate that bRGCs forming the OSVZ are generated at a specific critical time period during embryogenesis (E34-E36), in which aRGCs undergo self-consuming divisions to massively produce bRGCs. After this brief time window, progenitor cells in the OSVZ follow an independent lineage, and VZ aRGCs go back to their normal self-renewal regime (Martinez-Martinez et al., 2016).

3.5.1.3 Regulation of neuronal migration

One crucial and characteristic factor of cortical development is radial migration. Its disruption leads to an altered neuronal positioning and cortical layering, and several proteins that participate in this process have shown to have an impact in cortical folding. One particular example are the Leucine-rich repeat transmembrane proteins 1 and 3 (FLRT1/3). These cell-adhesion molecules have a role in radial migration of cortical neurons and their genetic ablation in mice induces the formation of cortical folds (Del Toro et al., 2017). Similarly, Cajal-Retzius cells secrete, among others, Reelin, a crucial factor for neuronal radial migration (Taverna et al., 2014). In humans, mutations in Reelin signaling severely impair cortical folding (Hong et al., 2000; Rice and Curran, 2001). Another key regulator of radial migration and cortical lamination that impairs gyrification is doublecortin (DCX). Human mutations on this gene, as well as *Dcx*-KO ferrets, display alterations of cortical folding (Gleeson et al., 1999; Kou et al., 2015; Pilz et al., 1998).

On the other hand, in gyrencephalic species, radially-migrating neurons disperse tangentially within the developing cerebral cortex, thus increasing cortical surface area and, ultimately, folding (Borrell and Reillo, 2012). It has been suggested that an evolutionary increase in branching of the leading process favors this tangential dispersion of radial migrating neurons, and thus cortical folding. Accordingly, loss-of-function for CDK5, a protein important for neuronal migration and leading process branching, severely impairs upper-layer neuron migration and cortical folding in ferrets (Martinez-Martinez et al., 2018; Shinmyo et al., 2017).

3.5.1.4 Extracellular matrix integrity

Whereas so far we have only considered factors intrinsic to cortical progenitor cells, these are not isolated but embedded in a complex extracellular matrix (ECM) that surrounds them within the tissue. This ECM largely defines tissue consistency and, it has been shown that specific ECM components directly regulate cortical expansion and folding. In particular, folding is induced in human fetal tissue cultures treated with HAPLN1, Collagen 1 and lumican (Long and Huttner, 2019; Long et al., 2018). Remarkably, recent studies reported an increase in ECM components expression in

gyrencephalic (humans) compared to lissencephalic species (mice), suggesting that changes in ECM exert a crucial influence on cortical expansion and folding (Fietz et al., 2012; Florio et al., 2015; Pollen et al., 2015).

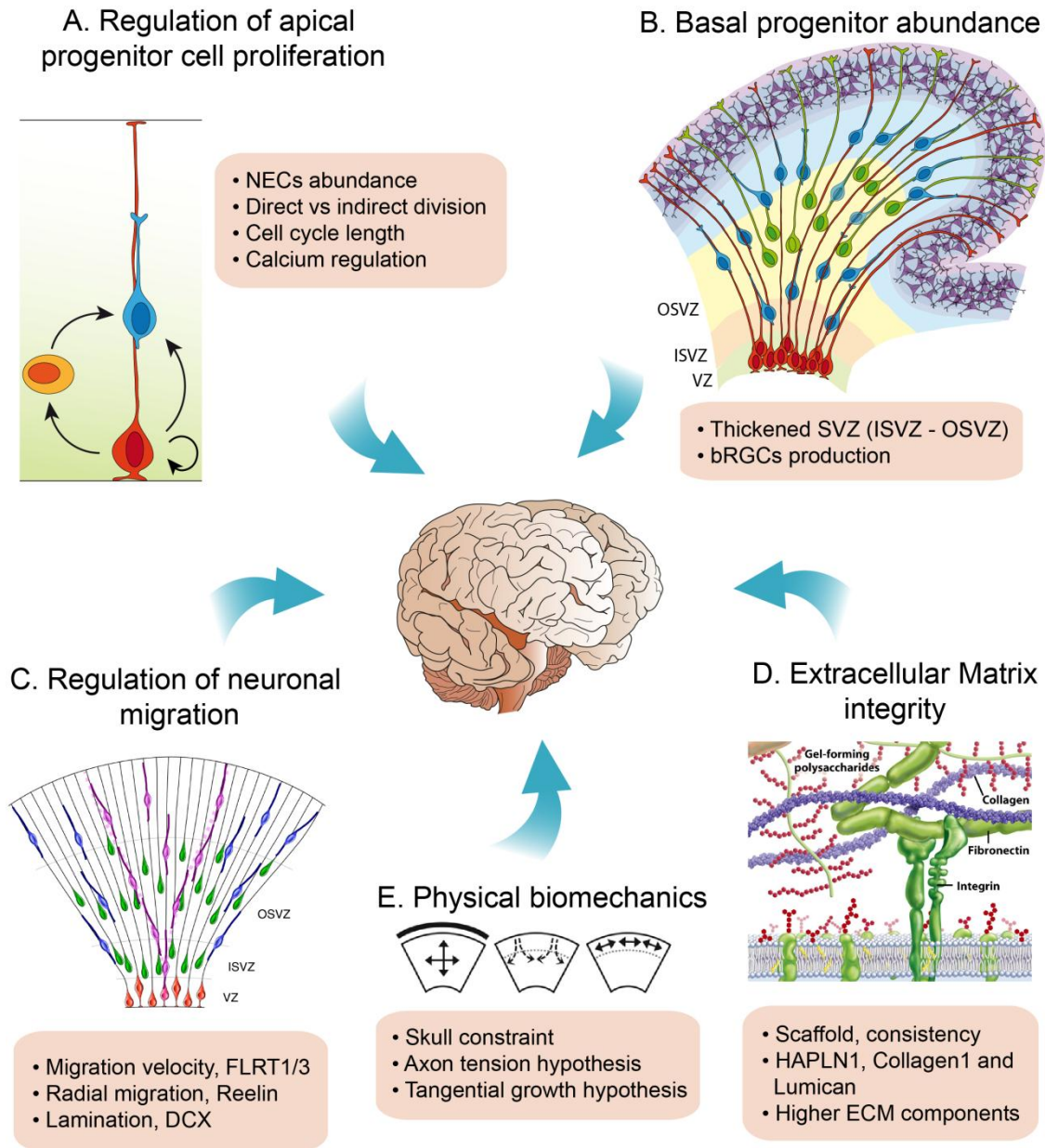


Figure 10. Primary factors underlying cortical folding. (A) Apical progenitors (red cell) abundance highly affects cortical folding, but their division decisions and their cell cycle length are crucial for the further output. aRGCs are also regulated by calcium. (B) Basal progenitor cells (orange cells) and SVZ (orange and yellow layers) size directly influence cortical folding. (C) The migration of the newly formed neurons affect folding by their migration velocity (specified by Flrt1/3 molecules), Reelin signaling and DCX expression. Adapted from Borrell and Gotz, 2014 (D) The high structural complexity of the ECM leads to its integrity and allowing cortical folding. Adapted from Freeman and Hamilton, 2005 (E) The different theories about physical biomechanics that induce cortical expansion and folding. Modified from Garcia et al., 2018.

3.5.1.5 Physical biomechanics

Beyond these biological factors, there is a clear biomechanical aspect to the cortical folding process. The specific role of physical constraints on cortical folding has been target of controversial arguments during decades. Many models have been proposed to explain and unravel gyrification. Classically, folding was presumed to be the direct consequence of the cerebral tissue growing within a limited cranial volume. However, folding of the cerebral cortex occurs before skull ossification and even in the absence of other non-cortical brain structures (Fernandez et al., 2016; Le Gros Clark, 1945). Later on, the "Axon tension hypothesis" speculated that cortex folding is a consequence of axonal connectivity between cortical areas (Van Essen, 1997). However, *ex vivo* experiments cutting axon tracts in ferret cortical slices refuted this hypothesis (Xu et al., 2010). Alternatively, the "tangential growth hypothesis" proposes that the different velocities in tangential growth between early and late cortical neuronal layers drive folding of the cortical mantle. This hypothesis is particularly interesting because it takes into account the biology of the tissue (Tallinen et al., 2014).

3.5.2 Secondary factors

Primary factors are influenced by other, secondary factors the alteration of which leads to cortical folding impairment. These secondary factors are listed below and mainly affect the tangential dispersion of migrating neurons and the generation of bRGCs.

3.5.2.1 RGCs

The importance and variability of cortical progenitor cell proliferation and lineage has already been mentioned above. However, other features of RGCs also affect cortical development and the ability to produce an expanded cortex. In addition to their proliferative role, RGCs serve as scaffold for the migration of newly generated neurons. In species with lissencephalic brains, the basal fibers of aRGCs are arranged radially in the developing cortex, perpendicular to the ventricular surface, and neurons migrate parallel to them. Accordingly, the final position of these neurons is directly in register with the position of their progenitor cells. In gyrencephalic species, in contrast, neuronal

migration has two essential components: radial and tangential. Given that neurons are produced in higher numbers, the presence of only parallel radial fibers would lead to a thicker cerebral cortex without folds. Concomitantly, radial fibers present a divergent conformation that allows the tangential dispersion of radially migrating neurons, thus increasing surface area and folding of the cerebral cortex (Borrell and Reillo, 2012; Nonaka-Kinoshita et al., 2013).

3.5.2.2 Neurons

Several studies have reported that neurons regulate cortical development both directly by their migration and indirectly by feedback signaling onto progenitor cells. For instance, migrating neurons have been shown to release neurotransmitters that activate or inhibit the proliferation of progenitor cells in the developing cerebral cortex by changes in intracellular calcium (Joo et al., 2007; LoTurco et al., 1995; Wang and Kriegstein, 2009). Another great example of the influence of neurons on the behavior of progenitor cells are Cajal-Retzius cells. As previously mentioned, these cells secrete Reelin, an essential factor for neuronal radial migration that also enhances Notch activation in aRGCs indirectly, regulating bIPs generation (Taverna et al., 2014).

Additionally, the axonal projections of neurons profoundly influence cortical development and folding in gyrencephalic species (like monkeys, ferret, dogs, raccoons...). Eye enucleation in fetal monkeys, before axonal connections are established, cause a reorientation of sulci and a reduction of cortical area size. These alterations take place around the primary visual cortex (influenced by eye removal), but also at distant areas including the contralateral hemisphere. Thalamic axons also regulate neurogenesis via direct signaling to cortical progenitor cells (Dehay et al., 1996; Dehay et al., 1989; Sun and Hevner, 2014). Thus, afferent innervation can modify cortical progenitor cells proliferation, possibly by the secretion of growth-promoting factors.

3.5.2.3 Extracellular matrix

Classically, the extracellular matrix was considered purely as a scaffold network of proteins. However, it has been lately shown that ECM directly signals to influence cell proliferation, differentiation and migration, among others (Long and Huttner, 2019). Thus, it is being increasingly suggested that extracellular matrix components shape brain development and cortex folding.

One of the main types of ECM molecules identified as being involved in cortex development are proteoglycans. Their glycosylated chains are typically related to structural support, but their disruption can induce cell detachment, overmigration, increase in G1 lengthening or regulation of the proliferation. How proteoglycans affect cellular dynamics is still under study, but hypothetically the network alters molecules moving and distribution within the tissue. Thereby this network generates a gradient of factors capable of reaching the progenitors' membrane receptors (Long and Huttner, 2019).

Another one of the main characters in this play are laminins and their counterpart, integrins. Each laminin contains one alpha, one beta and one gamma subunit, and until now, 15 different chains have been identified. Each integrin includes one alpha and one beta subunit (in mammals 18 and 8 different subunits, respectively). This variability confers a wide variety of options to specifically regulate different processes within the developmental cortex (Long and Huttner, 2019). Among all the reported studies, a few of them are underlined bellow:

- In cell cultures, laminin enhances survival, proliferation and differentiation of neural stem cells by modulating growth factors and directly binding integrins (Drago et al., 1991).

- Integrin $\alpha 5 \beta 3$ activation in mouse neocortex increased proliferation by inducing cell cycle re-entry and regulating proliferative divisions of bRGCs at ferret OSVZ (Fietz et al., 2010; Long and Huttner, 2019).

- Overexpression of integrin $\beta 1$ activates proliferation and the production of basal progenitor cells. Also, this glycoprotein activation promoted differentiation of non-expressing neighboring cells. Disruptions on integrin $\beta 1$ cause progenitor cell death after the detachment of the basal processes. Moreover, its loss produces microcephaly in

the mouse developing cortex. In addition, it is involved in the basal contact of aRGCs to maintain the bipolar morphology. Integrin $\beta 1$ regulate end-feet regeneration after mitosis independently of the division angle at early neurogenic states. Although the regeneration capability declines at late neurogenic stages and oblique divisions induce the translocation of the RGCs to basal positions (Fujita et al., 2020; Long and Huttner, 2019; Radakovits et al., 2009).

- Lacking laminin $\gamma 1$ alters INM inducing divisions of the aRGCs at basal positions in zebrafish neural tube (Tsuda et al., 2010).

- Another player of this ECM network is hyaluronic acid (HA). This non-sulfated glycosaminoglycan necessary for extracellular matrix structure is involved in neurite movement, neural migration and tissue consistency (Long and Huttner, 2019; Long et al., 2018).

The formation and maintenance of adherent junctions require a dynamic transport and recycling of adherent molecules and membrane. Thus, alterations in the dynamic remodeling could derive also in the modification of RGCs activity (Arai and Taverna, 2017; Taverna et al., 2016).

3.5.2.4 Cerebrospinal fluid

Progenitor cells of the cerebral cortex receive not just local cues but also signaling from remote locations, in particular from the choroid plexus. This vascularized secretory epithelium produces and regulates the composition of the cerebrospinal fluid (CSF), which fills the cavities of the ventricles. The molecular composition of CSF is very complex, quite conserved during evolution and dynamically regulated during development. The CSF in the developing brain contains several factors, ions, lipids, hormones, molecules and membrane-bound particles that may affect progenitor dynamics (Johansson et al., 2013). Thanks to the continuous attachment to the apical surface, NECs and aRGCs are regulated by CSF during development. The receptors for many of the CSF molecules are placed in the apical membrane and the primary cilium of aRGCs. By this mechanism, and taking advantage of the highly polarized structure of the cortex, progenitor cells are locally regulated during neocortex development. Moreover, when a progenitor cell delaminates from the VZ surface to basal positions, it

also stops sensing all these signals and may begin activating other regulatory pathways. CSF molecules and pathways regulating cortical progenitor proliferation include Otx2, Shh, IGFs, FGFs, BMPs and Wnt signaling (De Juan Romero and Borrell, 2015; Taverna et al., 2014).

3.5.2.5 Signaling from the meninges and basal lamina

In addition to the apical signals from the ventricle, some evidences show that signals from the meninges at the basal lamina also regulate neuronal migration and cortical progenitor dynamics. The meninges secrete molecules creating a gradient within the cortex, including factors like chemokines, necessary for the proper tangential migration of Cajal-Retzius cells to their final position (Borrell and Marin, 2006). The meninges are also the primary source of retinoic acid, which has been implicated in the reduction of glia self-renewal, bIP generation, neuronal differentiation and tangential expansion of the neocortex (Siegenthaler et al., 2009).

Immediately below the meninges, the basal lamina anchors the end-feet of RGCs and acts as a physical barrier for migrating neurons. A disruption in the RGCs contact to the basal lamina induces a displacement of Cajal-Retzius cells (Kwon et al., 2011). The migration speed of these cells also regulates the size of high order areas (Barber et al., 2015). All these features suggest that an active crosstalk exists between the basal lamina and RGCs, and that it affects cortical cell behavior. Laminins are the main glycoproteins at the basal lamina and, as mentioned above, have been related to proliferation, differentiation, migration and cell adhesion. Loss of function mutations in laminin $\beta 1$ (*LAMBI*) cause cobblestone lissencephaly, a type of human cortical malformation where neurons overmigrate past their termination zone and generate an irregular and bumped cortical surface (Radmanesh et al., 2013).

3.5.2.6 Genetic regulation of bRGC generation

The size and pattern of cortical folds are seemingly conserved between individuals and, to some extent, between species within individual clades. This strongly suggests that patterning of cortex folds is under strong genetic regulation (Borrell and Reillo, 2012).

However, the genetic mechanisms by which the production of bRGCs by aRGCs is controlled remains poorly understood. Some laboratories have focused on unveiling key genes for cortical expansion and folding that are specific to higher mammals, namely human and non-human primates. Transcriptomic analyses of progenitor cells have been especially important for these questions. In this context, several human-specific candidates for expansion regulation have been identified, such as *ARHGAP11B* and *NOTCH2NL*. Changes in the aRGCs expression of any of these genes promotes basal progenitor cells generation affecting their proliferation (Fietz et al., 2012; Florio et al., 2015; Florio et al., 2018; Johnson et al., 2015; Pollen et al., 2015). However, taking into account the highly regionalized brain of gyrencephalic species, both the expression of specific genes and differences in gene expression within the cerebral cortex could be in charge of defining cortical regions and folding patterns. Accordingly, De Juan Romero *et al.* identified differences in gene expression between sulci and gyri within germinal layers of the developing ferret cortex. Differently expressed genes along the OSVZ showed a remarkable correlation with the eventual pattern of cortex folding, a regionalization of gene expression not occurring in the lissencephalic mouse cortex (de Juan Romero et al., 2015).

Several studies have addressed the implication of genes expressed on aRGCs regulating basal progenitor cells production, like *Shh* (Wang et al., 2016); *Hopx* (Vaid et al., 2018); *EOMES* (de Juan Romero et al., 2015; Toda et al., 2016) and *Pax6* (Wong et al., 2015), among others. An extraordinary example of a gene able to modulate migration and proliferation is *Trnp1*. In mouse model, overexpression of *Trnp1* induce progenitor cell self-renewal and neuronal tangential expansion, while low levels of this gene on apical progenitors promote an increase in basal progenitor cells and cortex folding (Stahl et al., 2013).

In addition, tight genetic regulation at the critical period for bRGCs production is necessary to coordinate all the proliferative changes that would give rise to the unique germinal layer OSVZ. Previous studies from our laboratory analyzed the changes in expression of the aRGCs at the gyri VZ in charge of bRGCs generation. In fact, the study showed that a coordinated downregulation of *Trnp1* and *Cdh1* at this time window defined the OSVZ bRGCs production. Thus, overexpression of these two genes reduces bRGCs production preventing OSVZ setting (Fig. 11).

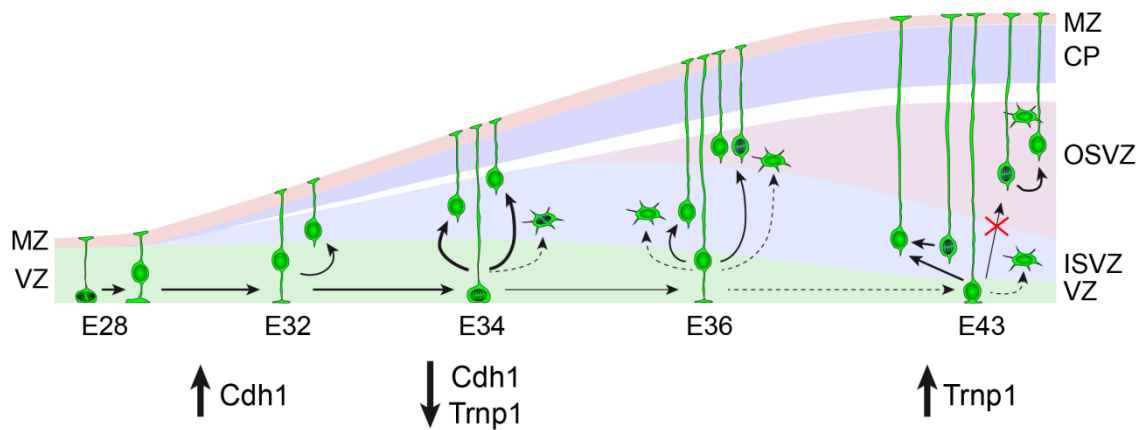


Figure 11. Model of developmental formation of OSVZ. At early ferret embryonic development aRGs self-renew coinciding with high levels of *Cdh1*. During the critical period for bRGs generation at E34-E26, *Cdh1* is downregulated and combined with low levels of *Trnp1*, driving aRGs to self-consuming divisions that massively produce bRGs. The formed bRGs become founders of the OSVZ. After birth (E42/P0), *Trnp1* is upregulated blocking the generation of bRGs to the OSVZ. At this point, the critical period finishes and the OSVZ follows an independent lineage sustained by bRG self-amplification. Modified from Martinez-Martinez et al., 2016.

Intriguingly, from this analysis of the expression dynamics at the aRGs on the VZ during the critical period for bRGs, only one gene expression appeared to mimic the aRGs dynamics, the Synaptic Vesicle Glycoprotein 2B (*Sv2b*) (Martinez-Martinez et al., 2016). This suggest that *Sv2b* could be an interesting candidate for regulate bRGs generation and hence, cortical expansion and cortical folding.

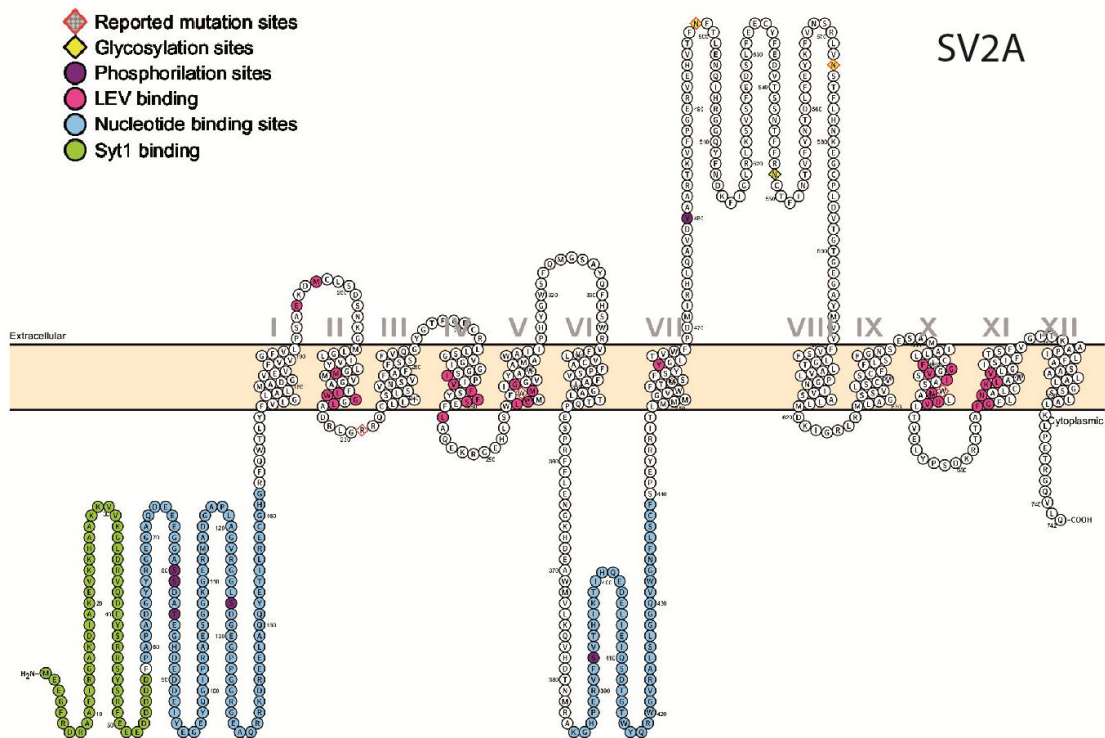
3.6 Synaptic Vesicle proteins 2 (SV2)

3.6.1 General features

Synaptic vesicle proteins 2 (SV2) were identified in the mid-'80s and have been widely used as synaptic vesicle and endocrine granules marker since then (Buckley and Kelly, 1985). Although they have been highly studied (especially in rodents or cell cultures), their exact function remains unknown. The SV2 family is composed of three members encoded by different genes: *Sv2a*, *Sv2b* and *Sv2c*, which share 65% identical amino acids and 80% structural homology (Bajjalieh et al., 1994; Bajjalieh et al., 1992; Janz

and Sudhof, 1999). SV2 paralogs maintain similar structure between different mammalian species as mouse/rat, ferret and human proteins. In particular, they present a 90% identity in protein alignment. Between ferret protein and mouse or human protein sequence, significant differences accumulate in the N-terminal and the extracellular loop (Fig 12 . Uniprot data).

No closed orthologs of SV2 proteins have been discovered in non-vertebrate species. On the contrary, these three isoforms are postulated to be related with SVOP (SVtwO-related Protein) and SVOP-like protein (SVOPL), two paralogous ancient and evolutionary well-conserved synaptic proteins already present in invertebrates like *Drosophila melanogaster* and *Caenorhabditis elegans*. Both present a sequence homology of 20-22% but a very similar structure (Janz et al., 1998). No clear function has been discovered for either SVOP/SVOPL proteins.



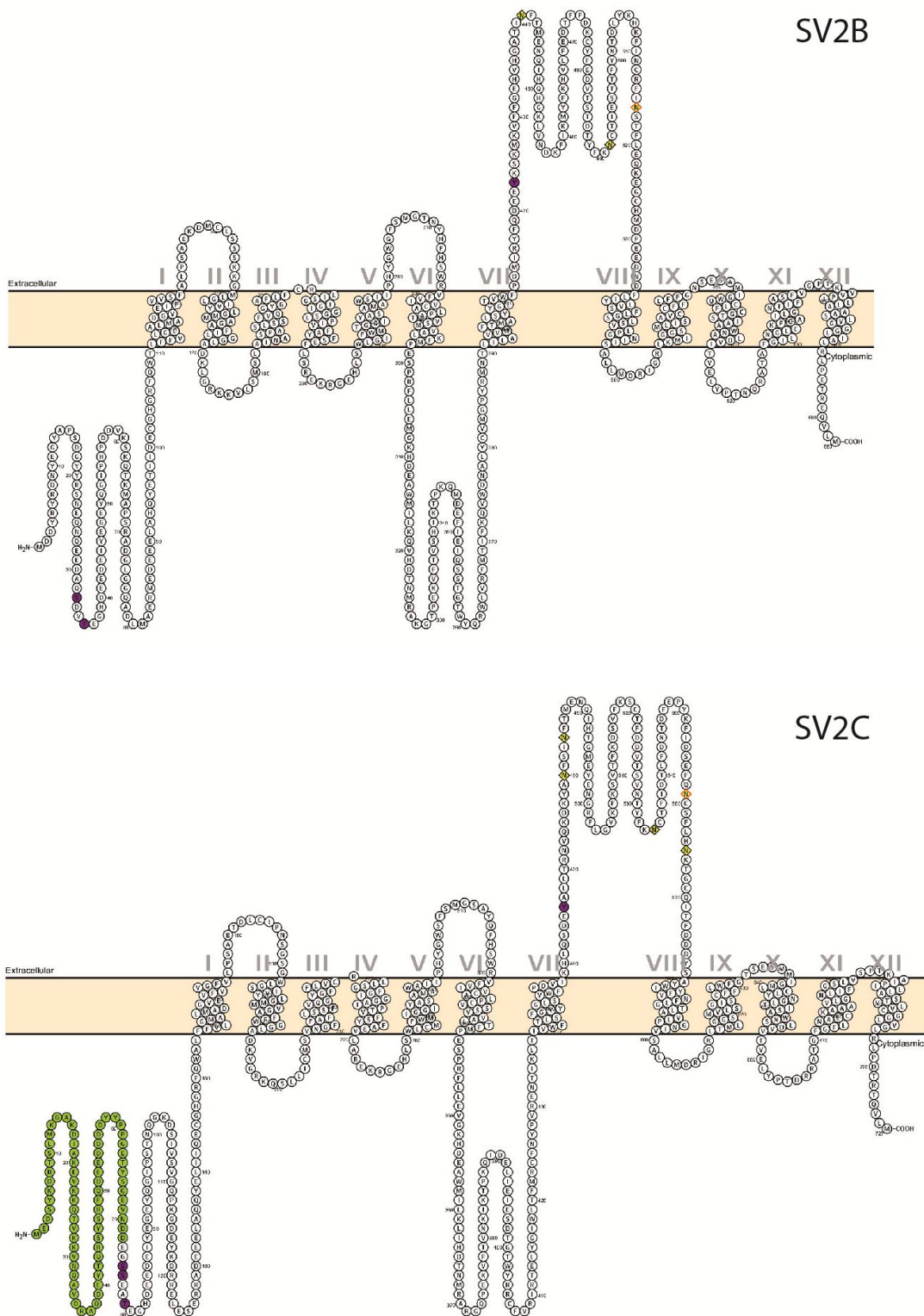


Figure 12. Mouse SV2A, SV2B and SV2C predicted structure. High homology between SV2 proteins can be observed. The N-termini is the most variable part. Each circle correspond to one amino-acid of the protein. In purple, the phosphorylated sites; in green, the synaptotagmin 1 (SYT1) binding sites; in yellow, the glycosylation sites, in blue, predicted nucleotide binding sites and in pink, Levetiracetam binding sites. Reported mutations on important sites are highlighted with a red edge. Images were created using Protter tool, <http://wlab.ethz.ch/protter/start/>).

3.6.2 SV2 structure

The three isoforms present 12 transmembrane regions (TMRs), two highly conserved large loops (one cytoplasmic and another luminal), a cytosolic N-terminal and a luminal C-terminal. In general, the loops connecting TMRs are short, except for the loop between 6^o and 7^o TMR in the cytoplasm and the other big loop in the luminal face between 7^o and 8^o TMRs. These large loops and the N-termini present less homology (Janz and Sudhof, 1999) (Fig. 12). In contrast, SVOP and SVOPL lack these large loops.

SV2 protein sequence and general structure present high homology to neurotransmitter transporters, and due to these features, they were classified into the major facilitator superfamily (MFS) (Feany et al., 1992). By protein tomography, two major conformations have been described for SV2A: one like a compact pore with a funnel structure, and a second one with an open cleft towards the lumen, further supporting its classification into the MFS (Löscher et al., 2016; Lynch et al., 2008) (Fig. 12 and 13).

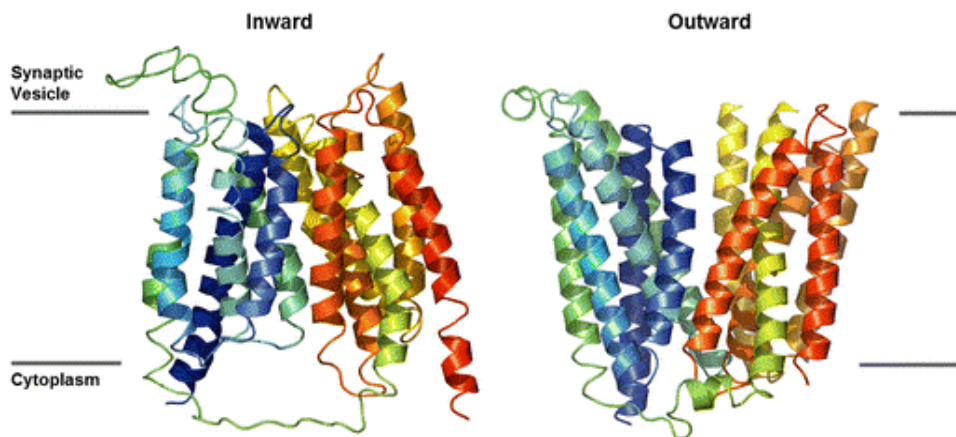


Figure 13. Schematic model of SV2A with 12 α -helix traversing the plasma membrane. In this image is represented the two possible pore conformations opened to the cytoplasm or the lumen. Adapted from Löscher et al., 2016.

Each member of the SV2 family also has several splicing variants and known single nucleotide polymorphisms. SV2B N-termini is substantially shorter (around 50 amino acid less). The N-termini of the SV2 family proteins shows high N-glycosylation, in contrast to SVOP/SVOPL which are not, though suggesting a more complex function of the SV2 proteins (Janz et al., 1998). In particular, SV2 proteins are glycosylated by

keratan sulfate (Scranton et al., 1993). SV2A and SV2B show three glycosylation sites into the large luminal loop, while SV2C stands up to five sites. Even if its exact role is not clear, N-glycosylation sites seem necessary for a proper function of the SV2 proteins as the amino acidic mutations are enough to induce a phenotype (Kwon and Chapman, 2012). They also present sensitive sites for phosphorylation. In fact, it has been shown that in SV2A and SV2C Thr84 site is phosphorylated by casein kinase family 1 protein (Fig. 12) (Zhang et al., 2015).

Mutations in glycosylation or into the TM regions of SV2A produce disruptions in the correct folding of the protein (Fig. 12 and 13). As a consequence, SV2 normal localization and trafficking is impaired forming cytoplasmic aggregations, therefore suggesting importance of the proper folding of SV2A to developed its usual function (Chang and Sudhof, 2009; Kwon and Chapman, 2012; Nowack et al., 2010; Yao et al., 2016; Yao et al., 2010).

3.6.3 SV2 expression patterns

Interestingly, besides their structural similarities, the three isoforms present different mRNA expression profiles in rodents. Both *Sv2a* and *Sv2b* start being expressed at early stages of development when the earliest neurons are first generated (E12 as the earliest time examined). While *Sv2a* expression is stabilized after birth and no variations on expression are furthered detected, the *Sv2b* distribution changes as development progresses. *Sv2b* is widely expressed in the immature brain where newly produced cells have not yet induced stable synaptic contacts. Indeed, at the cerebral cortex, its expression is limited to the superficial layers (E17) and it is also expressed in regions where it no longer appears in the adult brain as the globus pallidus and the dentate gyrus of the hippocampus (P5-16). *Sv2b* is also expressed at P15 in the proliferating external germinal layer of the cerebellum. This layer contains cells on their final round of cell division before migrating to their final destination in the granule cell layer and making their first synaptic contacts (Bajjalieh et al., 1994; Crevecoeur et al., 2013). The expression pattern of *Sv2c* during mouse development has not been described.

In adult murine central nervous system (CNS), the expression patterns of *Sv2a* and *Sv2b* exhibit a broader expression, but *Sv2c* is confined to phylogenetically old

brain areas. While *Sv2a* is ubiquitously expressed in the adult brain, *Sv2b* is more restricted than *Sv2a* and its expression is excluded from the dentate gyrus of the hippocampus, the globus pallidus, the cerebellum (but granule cells), the reticular nucleus of the thalamus and the reticular part of the substantia nigra. On the other hand, *Sv2c* mRNA is observed in the olfactory bulb, olfactory tubercle, nucleus accumbens, dorsal striatum, ventral pallidum and the ventral tegmental area. The protein is found, in addition, in the globus pallidus and the substantia nigra. *Sv2c* isoform remains utterly absent from cerebral cortex or hippocampus (Dardou et al., 2011; Janz and Sudhof, 1999).

According to immunolabeling of SV2 proteins, SV2A and SV2B remain almost absent from cellular layers, such as the pyramidal cell layer of the hippocampus, and is highly present in synapse-rich molecular layers as in the cerebellum. On the other hand, SV2C is expressed in the cell bodies of TH-positive midbrain dopamine neurons and striatal GABAergic medium spiny neurons. SV2A is expressed in all cortical cerebellar neurons, GABAergic and glutamatergic. However, SV2B is limited to glutamatergic granule cells of the cerebellum. SV2B expression is not linked to glutamate presence and is not expressed in other types of glutamatergic neurons (Bajjalieh et al., 1994; Crevecoeur et al., 2013). SV2 proteins are distributed with high precision through the individual's vesicles, containing an average of five copies of SV2 proteins per unit with low variability between vesicles (Mutch et al., 2011).

Thus, it has been shown that the expression patterns of SV2A and SV2B have a widespread overlap. Furthermore it has been reported that at some cases, both isoforms are expressed in the same cell at different relative levels (as in hippocampal CA2 neurons). By immunoprecipitation assays, previous studies show that both isoforms can coexist in the same vesicle overlapping with other synaptic vesicle proteins as synaptotagmin or synaptophysin, although one of the isoforms is usually predominant. The expression of SV2 proteins seems not to correlate with any other synaptic vesicle isoforms as Synaptotagmin, VAMP or Synaptophysin, rejecting a possible correlation in terms of function (Bajjalieh et al., 1994). Regarding SV2C protein, it is densely expressed in around 45% of cholinergic interneurons, in GABAergic striatal projection neurons and in most dopaminergic neurons (more than 70%) in the substantia nigra and the ventral tegmental area (Dardou et al., 2011). SV2A and SV2B are coexpressed not

only in several types of neurons but also in the very same vesicle. Colocalization of other SV2s and SV2C has not been assessed.

SV2 proteins are also expressed in the peripheral nervous system. SV2A appears to be present in peripheral sympathetic synapses. SV2B is the main isoform expressed in the retina. In all motoneurons, SV2B and SV2C have been detected, but SV2A is only present in slow motoneurons. Also, neuroendocrine cells express SV2 in the human gastrointestinal tract, adrenal medulla, pancreas, thyroid/parathyroid and pancreas. In this latest organ, SV2A and SV2C were explicitly found in insulin containing granules. SV2B is also highly expressed in the cortical layer of the embryonic kidney, not in adults (Bajjalieh et al., 1994). Finally, SV2A is expressed in platelets.

Surprisingly, Stockburger *et al.*, demonstrate that SV2A is not just restricted to vesicles but is also present in mitochondria (Stockburger et al., 2016).

3.6.4 *Sv2* Knockout mice

At the end of the 90s, knockout (KO) mice were generated to unravel the role of SV2 proteins (Janz et al., 1999). Mutant *Sv2a* mice present a reduction in body size and a small brain in proportion to their reduced body (Fig. 14). Apparently, *Sv2a* KO rodents developed normally until one or two postnatal weeks when they begin to suffer severe seizures and die. The epileptic phenotype increased in severity and frequency over time. Indeed, compared to other strains with resemblant responses, the observed seizures are more exhausting, stronger and longer lasting (Crowder et al., 1999; Janz and Sudhof, 1999). Moreover, behavioral analysis in conditional KO mice with ablated expression specifically in the hippocampal glutamatergic neurons, show an increase in anxiety-like features and spatial memory deficit compared to wild type mice (Serrano et al., 2019). On the contrary, *Sv2b* single KO mice is a viable strain that shows no apparent phenotype neither in development nor in adulthood. Indeed, *Sv2b* KO neurons form normal ultrastructural synapses on *in vitro* assays (Crowder et al., 1999; Janz and Sudhof, 1999).

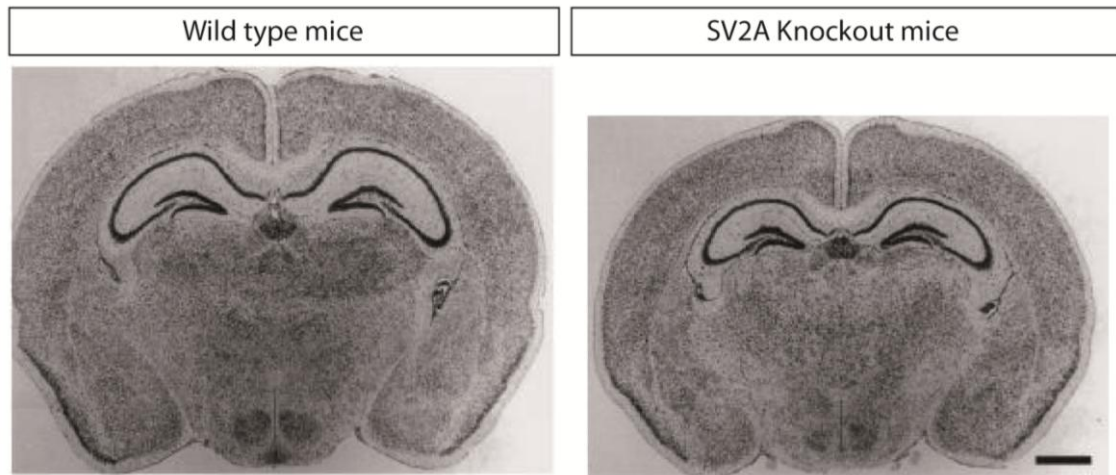


Figure 14. P14 coronal sections with Nissl staining from wild type and *Sv2a* knockout mice. It is easily observed the difference in size, although no noticeable structural changes are detected. Adapted from Crowder et al., 1999.

Sv2b KO and heterozygous *Sv2a* mice are fertile and show a standard mortality rate. Double *Sv2a/Sv2b* KO show similar phenotypes to those observed in *Sv2a* KO mice. Unlike other epileptic models that present anatomic malformations, each of these single or double mutants present typical Nissl stained brain structures. In addition, SV2A or SV2B lacking hippocampal neurons do not show appreciable ultrastructural differences to wild type on *in vitro* assays. In order to determine alterations in synaptic vesicles amount or composition, other synaptic proteins quantity has been checked in those mutants. However, no variation has been detected in other synaptic vesicle protein expressions like synaptotagmin or syntaxin. SV2B levels were increased in *Sv2a* KO mice, but not the total amount of SV2. These quantifications suggest that the synaptic vesicles components, morphology and abundance in neurons remain barely invariable. In the adrenal medulla, SV2C is 4 times more expressed in SV2A lacking mice than in wild type animals. Although this compensatory effect, the phenotype is not entirely rescued and a reduction in the number of vesicles fused to the membrane is still detected. So, a complete redundant function for the three isoforms is not probable (Crowder et al., 1999; Xu and Bajjalieh, 2001).

Experiments measuring the frequency and amplitude of Miniature Inhibitory Postsynaptic Currents (mIPSCs) in CA3 neurons show no differences in *Sv2a* KO animals compared to wild type, suggesting that SV2A is not required either for vesicle fusion or postsynaptic receptor action or expression. Nevertheless, after preventing

glutamatergic neurotransmission in CA3 pyramidal neurons, Spontaneous Inhibitory Postsynaptic Currents (sIPSCs) frequency and amplitude were reduced in *Sv2a* KO. An increase in inhibitory events and its amplitude suggests abnormal inhibitory neurotransmission in the hippocampus (Crowder et al., 1999). Furthermore, double knockout cells exhibit an increase in intracellular Ca^{2+} after consecutive action potentials. Calcium deregulation may be causing the abnormal release of neurotransmitter and, thus, epilepsy (Janz et al., 1999).

Although less studied, there is also an *Sv2c* knockout mouse. Interestingly, *Sv2c* KO mice do not present compensatory changes in the expression of SV2A or SV2B. It presents normal levels of dopamine synapses and synapse density. However, *Sv2c* genetic ablation induces a reduction in dopamine release at the dorsal striatum (Dardou et al., 2011; Dunn et al., 2017).

3.6.5 SV2 functions

SV2 proteins are found in almost every mammalian neurosecretory vesicle, suggesting its essential role in vesicular function. Some studies propose that the three isoforms may be performing the same function. In fact, the genetic deletion of *Sv2a* or *Sv2c* induces a compensatory upregulation of the other isoform maintaining the total SV2 levels. However, despite the upregulation of the other isoform, the neurotransmission remains disrupted and, for example, the SV2B loss in the retina does not alter SV2A levels, reducing the total SV2 expression by 50%. In *Sv2a* knockout mice, SV2B expression is increased, but they still present a severe phenotype (Crowder et al., 1999). If we also take into account the variability in the specific expression patterns of each SV2 previously explained, once again, a completely redundant role seem unlikely.

Through to the variability on previous studies in the field, it has been suggested that they would be related with several functions, such as transport of ions or neurotransmitters, priming of synaptic vesicles or Ca^{2+} regulation levels. However, its particular role remains mainly unidentified.

3.6.5.1 Vesicular transporter

Initially, as seen in the SV2 structure section, due to its sequence and structural similarities to previously known transporters, a similar function was assumed. Furthermore, SV2 proteins contain several conserved charged residues that bring to mind the possible transport of a positively charged molecule (Janz et al., 1999). In spite of it, no such activity has been directly demonstrated for any of these proteins in vertebrate models (Janz et al., 1999; Yao et al., 2013).

A role as a specific neurotransmitter transporter seems unlikely due to SV2A being expressed independently in GABA and glutamatergic neurons (Bajjalieh et al., 1994). In addition, vesicle size and number are similar in *Sv2a* KO mice compare to wild types (Xu and Bajjalieh, 2001), and the morphology of the synapse remain normal, supporting an improbable role in neurotransmitter transport into the vesicle.

Previous studies have underlined the importance of carbohydrates to the proper function of the nervous system. In this regard, it has been proposed a hexose transporter role for SV2 proteins. As a first sign, Iezzi *et al.*, determined that silencing *Sv2a* or *Sv2c* in INS-1E cells results in a reduction of insulin release (Iezzi et al., 2005). Later, by overexpressing the human isoform of SV2A in mutant *Saccharomyces cerevisiae* lacking all hexose transporters, a study has shown a growth increment in galactose supplemented media. This uptake is blocked by the addition of levetiracetam (Madeo et al., 2014). Even so, this has not been assessed in higher order organisms and studies addressing the uptake of substrates from the synaptic cleft into the neuron did not detect traditional vesicular transport.

However, several studies have demonstrated that botulinum and tetanus neurotoxins (BoNT and TeNT) use SV2 to enter into the cells and translocate to the cytoplasm where its particular targets are placed. The toxins interact with the luminal domain of SV2 proteins when they are exposed after the vesicle fusion to get into the neurons. The three isoforms can internalize BoNT/A into the cell taking advantage of the endosomal recycling pathway (Fig. 15). But, in detail, BoNT/A and E bind in a different way than BoNT/D. SV2A and B, but not SV2C, mediate the entrance of BoNT/E through the fourth luminal domain into cultured hippocampal neurons. In particular, it seems that N-glycosylation site N573Q is necessary to BoNT/E and

facilitates BoNT/A binding. The interaction of other molecules as gangliosides of the lipid membrane is also needed to SV2A and B mediated internalization of BoNT/E and D (Dong et al., 2008; Dong et al., 2006; Peng et al., 2011). On its side, TeNT can be introduced into the central neurons through two different pathways depending on SV2A/B (Yeh et al., 2010).

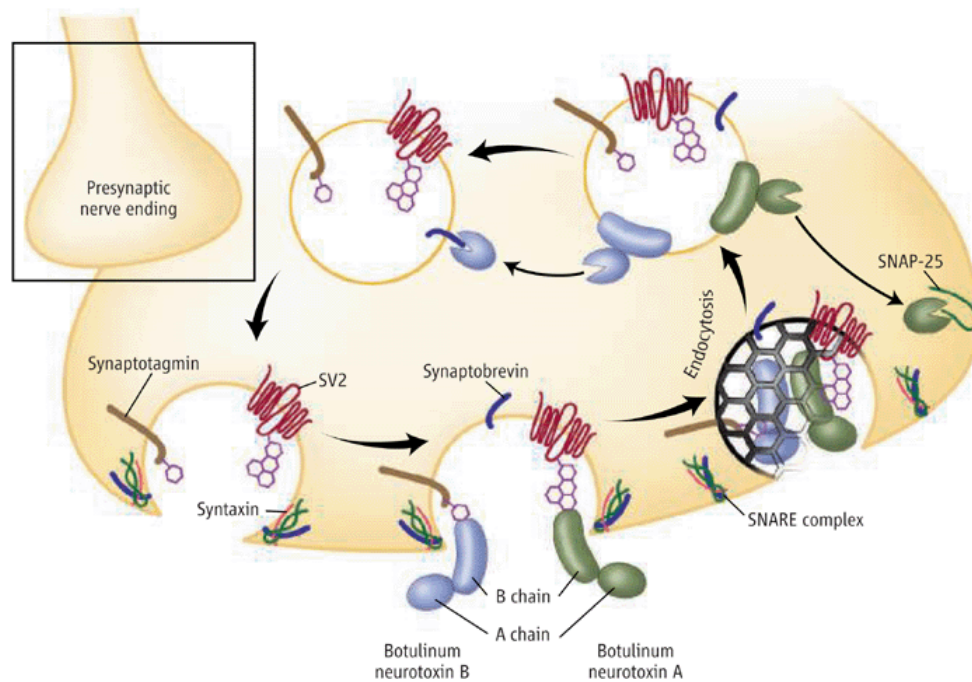


Figure 15. Botulinum neurotoxin A and B entry into the synapse. Botulinum neurotoxin A and B bind to SV2 and SYT1 respectively. Then, both are translocated from where the active part of the toxins cleavage their targets disrupting the proper synapse functioning. Adapted from Jahn, 2006.

3.6.5.2 Vesicular backbone

It has been hypothesized that the transmembrane domain of SV2 proteins could be acting as scaffold to maintain vesicle curvature and morphology (Janz et al., 1998). Although genetic ablation of SV2 proteins does not alter vesicle morphology or formations (Wan et al., 2010). In addition, the luminal part of the vesicle is formed by a complex matrix necessary to, for example, modulation of the neurotransmitter release after vesicular fusion or possibly for the proper orientation of other proteins to enable correct neurotransmission. SV2, Synaptobrevin and SYT1 are transmembrane proteins candidates to contribute to the stability of this luminal density. This structure opens a

world of possibilities regarding the anchor of other molecules. Indeed, an assembly of SV2 proteins to form a multimeric complex has already been identified in rat brain homogenates, where SV2s seem to interact with SYT1, Synaptophysin and/or RAB3A (Bennett et al., 1992). Moreover, as mentioned in a previous section, SV2s include a large luminal loop with several glycosylation sites. In acidic environments, as in the interior of the vesicle, proteoglycans become negatively charged and could stabilize positive neurotransmitters or other molecules. This balance of charges would also allow the package of higher concentrations of molecules (Fig. 16).

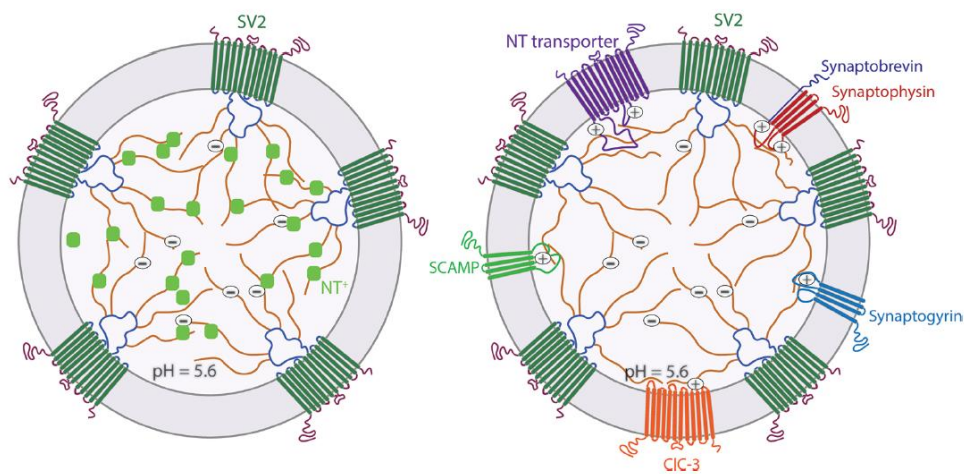


Figure 16. SV2B as a vesicular backbone protein. Vesicles typically show by average five copies of SV2. The intraluminal loops (dark blue) are highly glycosylated (brown). In acidic environment (left), proteoglycans become negatively charged and this allows the stabilization of positively charged or zwitterionic neurotransmitters (light green). By this strategy, the vesicles are able to carry neurotransmitter higher concentrations. Moreover, in this acidic environment, positive charged proteins likely interact with SV2 negative charges (right). This protein interaction with the vesicular backbone would allow the correct location of each protein to enable rapid neurotransmission. Adapted from Stout et al., 2019.

3.6.5.3 Calcium regulator

From experiments with *Sv2a/b* KO mice, several studies have shown a close link between impaired neurotransmission and SV2 modification. As neurotransmission can be calcium dependent, a possible SV2 role in calcium regulation as a calcium sensor, transporter or linker to calcium sensor proteins has been suggested. One fact that

supports this correlation is that *Sv2a* KO animals and mice lacking both isoforms present a reduction in calcium-induced neurotransmission in excitatory and inhibitory neurons. In contrast, *Sv2a/b* double knockout hippocampal neurons exhibit reduced synaptic release but an increase in calcium dependent synaptic transmission as a paired-pulse response and synaptic facilitation during stimulus trains (Chang and Sudhof, 2009; Custer et al., 2006; Janz et al., 1999; Vogl et al., 2015). For these studies, *Sv2b* knockout neurons were used as controls after showing not significant neurotransmission differences with wildtype neurons.

In SV2B deleted rod bipolar neurons calcium concentration raised two times in resting and stimulus-induced conditions. In parallel, readily releasable vesicle pool and calcium sensitivity during exocytosis were reduced. In addition, these cells needed more time to recover their membrane capacitance and show early facilitation during initial pulses of stimulation trains. This phenotype is calcium dependent since elevating calcium concentration in wildtype neurons mimic similar impairments in neurotransmission while, reducing calcium concentration in *Sv2b* KO animals rescue the normal neurotransmission (Vogl et al., 2015; Wan et al., 2010).

However, changes in synaptic calcium affinity or relative inhibitory postsynaptic current amplitudes at escalating calcium dose after *Sv2a/b* ablation was not detected, which challenges the possible calcium transporter role of SV2 proteins (Chang and Sudhof, 2009; Iezzi et al., 2005). Thus, direct evidence of calcium transport has still not been demonstrated.

As previously mentioned, SV2 is present in mitochondrias, well known cellular calcium sinks. Therefore, the observed calcium effects may be a consequence of disruption in mitochondria function rather than directly vesicular (Stockburger et al., 2016).

3.6.5.4 Vesicle dynamics

An appropriate vesicle trafficking function is also crucial to ensure neurotransmission. Several steps occur in this process like the vesicle transport to the active zone, anchoring, fusion and recycle. Some studies hypothesized that SV2 might be involved in any of these processes (Fig. 17).

Genetic ablation of *Sv2a* in neurosecretory adrenal chromaffin cells causes a reduction in the readily releasable pool size to its half (Xu and Bajjalieh, 2001). This dysregulation is tied to a decrease in SNARE complex molecular weight, a needed complex that acts prior to fusion. Thus, this suggests that SV2 could be related somehow with vesicle brought to the active zone or vesicle rendering. This initial decrease has been shown in several other cell types (Chang and Sudhof, 2009; Custer et al., 2006). For instance, the earlier explained delay in the readily releasable pool after stimulus-induced depletion induces to think about an SV2 role in vesicle dynamics too (Wan et al., 2010).

Currently, just one SV2 direct endogenous interactor is known at the vesicular level, SYT1, a vesicular protein involved in vesicle docking and fusion. SYT1 and SV2A are cotrafficked in the same vesicles. All three isoforms are able to bind SYT1, but SV2B presents a reduced affinity for it (Schivell et al., 1996; Schivell et al., 2005). The interaction is direct so that proteins immunoprecipitated together. SV2A and SV2C paralogs, but not SV2B, bind SYTs through a C2B domain in the cytoplasmic N-terminus (Schivell et al., 1996). This site is unique and necessary to the proper neurotransmission as evoked postsynaptic potentials remain disturbed when N-terminal peptides are expressed (Schivell et al., 2005). To regulate the interaction, SV2 recruits SYT1 by phosphorylated Thr84 (Schivell et al., 2005; Zhang et al., 2015).

Sv2a deletion or mutation reduces SYTs vesicular localization (Yao et al., 2010). Interestingly, less SYT is detected in *Sv2b* KO rod receptor cells, where this isoform is the only one expressed (Lazzell et al., 2004). This reduction suggests that SV2 regulates SYTs at two different levels: modulating its expression and its internalization from the plasma membrane. In fact, this latest feature of SV2 depends on a tyrosine-based endocytosis motif predicted to bind clathrin adaptor AP2, a central component of the recycling machinery (Yao et al., 2010).

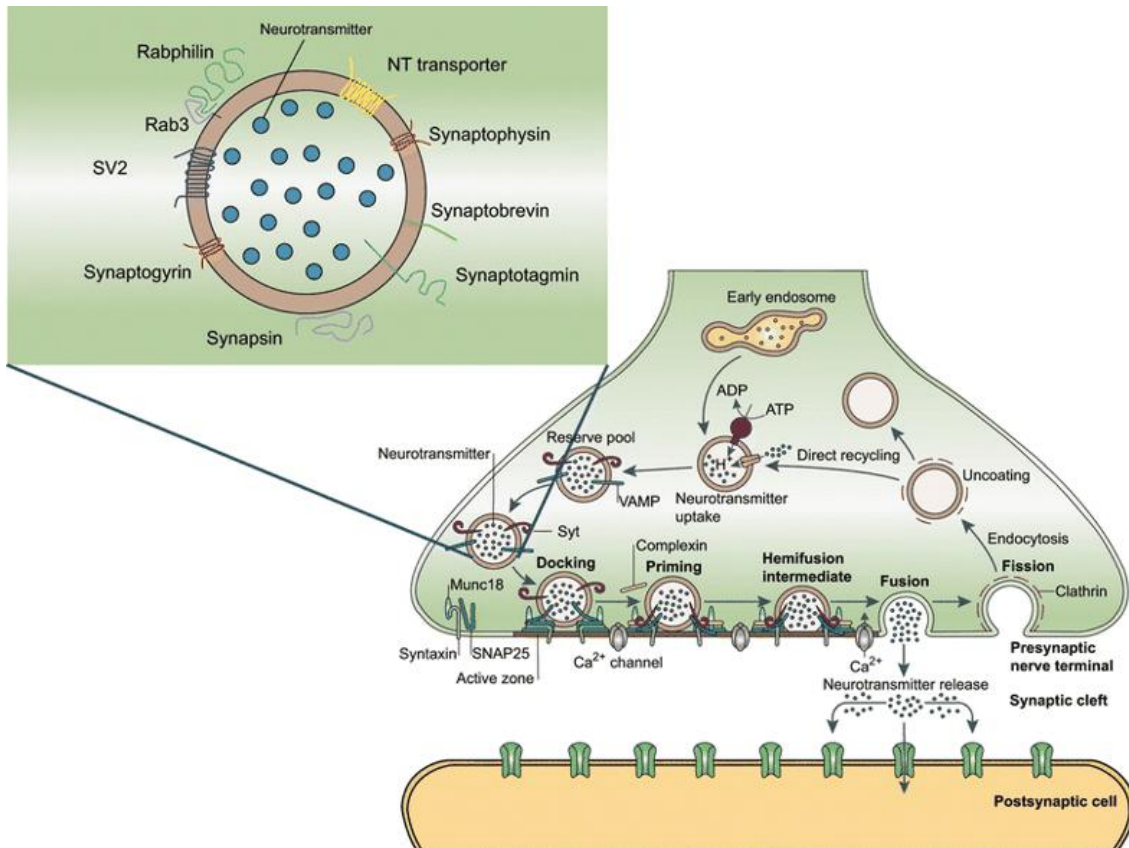


Figure 17. Schematic illustration of the vesicular dynamics in neurotransmitter release on a presynaptic terminal. At the presynaptic terminal neurotransmitter (blue dots) is accumulated in synaptic vesicles, membranous spheroids with a wide variety of transmembrane proteins. The high-magnification on the left shows some of the main proteins at synaptic vesicles (except for the proton pump) and their basic structure. Docking: Synaptic vesicles are positioned close to the plasma membrane and the SNARE complex (formed by syntaxin 1, SNAP25, VAMP and the effectors MUNCs). Priming: after a change in calcium concentration, proteins from the complex change their conformation and both membranes fuse. Fusion: the vesicle lumen is open to the extracellular space and later, the neurotransmitter is release being accessible to the postsynaptic receptors. Fission: the empty synaptic vesicle is coated by clathrin, and the membrane proteins are recycled. The recycled membrane and proteins can be charged with neurotransmitters again or derived to early endosomes what can lead to further degrading. It is still unknown if SV2 may be involved in any of these steps. From Loscher et al., 2016.

There is still some controversy about SYT need to SV2s proper function (Chang and Sudhof, 2009). As far as it is known, the neurotransmission phenotype of *Sv2* KO cells is not identical to neurons lacking SYT, so that probably SV2 may have additional functions to SYT regulation (Geppert et al., 1994; Nishiki and Augustine, 2004). On the

other hand, SYT1 acts as a calcium sensor and the interaction with SV2s is sensitive to calcium too, for what it could be that SV2 would be inducing the vesicles to a calcium-synaptotagmin sensitive state (Schivell et al., 1996). Its interaction is also regulated by phosphorylation (Zhang et al., 2015). Interactions involving SV2s and the other 14 SYTs has not been studied yet.

3.6.5.5 Attachment to the extracellular matrix

SV2 proteins could also be acting as an extracellular matrix component receptor. As previously mentioned, SV2 forms a large keratan sulfate proteoglycan in the luminal part of the vesicle (Scranton et al., 1993). After vesicle fusion to the plasma membrane, the interior of the vesicle becomes exposed to the synaptic cleft, also exposing the luminal part of the proteins. As a highly glycosylated protein, SV2 could be interacting with the extracellular matrix proteins, like forming part of the synaptomatrix to stabilize the synapse, modulating neurotransmitter availability or receiving extracellular signals.

Furthermore, it has been reported in electric organ synapses (homologous to neuromuscular junctions) that SV2 is complexed with $\alpha 5 \beta 1 \gamma 4$ laminin on synaptosomes but not in synaptic vesicles. It also binds to purified laminin1 (Son et al., 2000). In addition, Knight et al., 2003 showed that $\beta 2$ -laminin deficient terminals present fewer SV2 positive vesicles. Finally, *Sv2b* KO mice show defects in CD2AP, nephrin, NEPH1 and the maintaining of slit diaphragm by the SV2B-Neurexin complex (Fukusumi et al., 2015).

3.6.5.6 Nucleotide binding

Several photoaffinity labelling experiments have revealed that SVOP and SV2 bind nucleotides. Indeed, SVOP presents a single region in between membrane domain 9 and 12 (position 411-518 amino acid) with high affinity for NAD, while SV2A presents two different binding sites with high affinity for adenine nucleotides (ATP and NAD). These two nucleotide binding domains extend from 59 to 162 residues (located in the N-terminal) and from 385 to 439 amino acid (at the loop between 6 and 7 TM) (Fig.12 SV2 structure). SV2B also binds ATP and NAD with high affinity, and some

experiments suggest that SV2C is also able to, but particular sites have not been studied yet (Yao and Bajjalieh, 2008, 2009).

Given these features, the SV2 family could be acting as an ATP transporter or performing other function, related to transport or not, that is regulated by ATP binding. As a related example, the human Glucose Transporter 1 (GLUT1) that belongs to MF family too, binds ATP inversely to its activity, inhibiting Glut1 function in high energy conditions. Similarly, SV2 family could be acting as a link between cellular energy levels and vesicular secretion (Stout et al., 2019).

However, the binding sites in these MF family proteins are different among them. Some previous studies suggest that SV2, GLUT1 and SVOP nucleotide binding sites are not evolutionary conserved and thus, they arose separately. If that has been the case, SV2 ATP binding ability could be not related to the modulation of its function like Glut1 (Yao and Bajjalieh, 2008, 2009).

3.6.6 SV2 and pathology

Firstly, human mutations in SV2s have been rarely described. Nevertheless, it has been reported a homozygous mutation in *Sv2a* gene that results in severe symptoms early in development as untreatable epilepsy, involuntary movements, microcephaly and developmental and growth retardation. This particular case was due to a mutation R383Q, altering the second nucleotide binding site (Serajee and Huq, 2015).

On the other side, even previous to the SV2 finding, a novel antiepileptic drug was discovered in 1977, the Levetiracetam (LEV). However, it was not until 2004 that SV2A was identified as its molecular target (Lynch et al., 2004). LEV and its derivatives are the only anti-epileptic drugs that target synaptic vesicles. From that moment, SV2 proteins became a possible druggable target for epilepsy treatment and other neurodegenerative disorders (Stout et al., 2019).

SV2A protein expression is reduced in animal epilepsy models and epilepsy patients. Taking into account the phenotypic severe seizures that *Sv2a* KO mice suffer, it is suggested that a reduction in SV2A facilitates epileptogenesis. In fact, a direct correlation exists between the levels of SV2A expression and the ability to respond to

LEV doses in human glioma-associated tumors (de Groot et al., 2011). Even phenotypic alterations due to overexpression of SV2A are reversed by LEV (Nowack et al., 2011). Furthermore, it seems that there is a positive regulation of SV2A expression during seizures events. In this way, it has been demonstrated that SV2A expression is increased after low frequency stimulation of the hippocampus in pharmacoresistant rats with spontaneous epilepsy (Wang et al., 2014). The modification of this expression results in a reduction of seizure frequency. In the same context, SV2A expression increases at *status epilepticus* and during seizures in several other models (Contreras-Garcia et al., 2018; Ohno et al., 2009).

LEV seems to impair the readily releasable pool of vesicles (Garcia-Perez et al., 2015). However, how the interaction of SV2 and LEV reduces the seizure phenotype remains unknown. Besides, LEV has shown to be effective in the treatment of other neurologic alterations such as neuropathic pain, anxiety disorders, dyskinesias, posttraumatic stress disorder and for other particular clinical cases (Kaufman, 2011). Interestingly, LEV administration to nonepileptic animals and humans do not show hyperexcitability. Therefore, LEV could be a candidate for a prophylactic drug to prevent sensitivity to seizures and other neurological disorders (Stout et al., 2019).

Similarly, abnormal hyperexcitability in the hippocampus has been reported in Alzheimer's Disease cases and mouse models. Since seizures in the later stages of Alzheimer have been related with a significant decrease in cognitive function (Vessel et al., 2013), LEV has been used in Alzheimer treatments to reduce hippocampal hyperactivity, showing an improvement in cognitive deficits. This enhancement has also been reported in several Alzheimer's mouse models, in Alzheimer's non-epileptic mouse models and nondemented epilepsy patients. LEV meliorate memory performance in Alzheimer's Disease, but also neuritogenesis (Celikyurt et al., 2012; Chan et al., 2015; Cumbo and Ligor, 2010; Devi and Ohno, 2013; Löscher et al., 2016; Siwek et al., 2015; Sola et al., 2015; Stockburger et al., 2016; Wu et al., 2009; Ziyatdinova et al., 2016).

LEV presents a high specificity to SV2A binding, and although it slightly interacts with SV2B or SV2C, these isoforms show to be also related to Alzheimer pathogenesis. In this way, a particular *Sv2b* transcript is upregulated after Alzheimer's Disease associated cytotoxic A β 1-42 treatment in *in vivo* cells (Heese et al., 2001). The

results further support the observation that *Sv2b* knockout mice present protection against features produced by injected A β oligomers like oxidative stress, the cholinergic deficit in the hippocampus and cognitive impairments. So, these mice showed no impairments in recognition memory, working memory, spatial reference memory and long-term contextual memory (Detrait et al., 2014). Moreover, as previously mentioned, SV2 proteins are highly glycosylated, and it has been widely reported that β amyloid peptides heavily interact with proteoglycans to form the toxic plaque accumulations characteristic of Alzheimer disease, suggesting once again an involvement of SV2 proteins in neurodegenerative disorders (Yanagisawa, 2007).

Finally, *Sv2c* has been highly studied for its enriched expression at the basal ganglia in dopamine related diseases as Parkinson's disease, Huntington disease or psychiatric disorders. In *Sv2c* knockout mice, the motor function is compromised, and dopamine release reduced (Dunn et al., 2017). Moreover, SV2C expression was recently reported to be reduced in Parkinson's patients' tissue, and mutations in *SV2C* affects sensitivity to L-DOPA (Berezcki et al., 2018). It has been demonstrated that in dopaminergic cell lines, statins, a treatment for blood pressure that reduce Parkinson's disease risk, upregulates SV2C expression. All this data suggests that the proper vesicular function is essential for dopaminergic integrity and to prevent Parkinson's disease development, further supporting treatments through SV2C protein (Stout et al., 2019).

Curiously, in neuroblastoma cells and Huntington's disease mouse models, mutant huntingtin selectively reduces SV2C expression, probably leading to aberrant dopamine release (Stout et al., 2019).

SV2 expression also appeared to be altered in other disrupted secretion related disorders. In particular, SV2 and SYT1 expression are reduced in spinal muscular atrophy of different animal models altering neurotransmitter release (Dale et al., 2011; Hao le et al., 2011). On the other hand, less has been assessed in neuroendocrine disorders, but it has been reported that gut carcinomas express SV2 (Jakobsen et al., 2002).

All these results suggest that SV2 proteins are in charge of not just one function but an intricate role in neurotransmission.

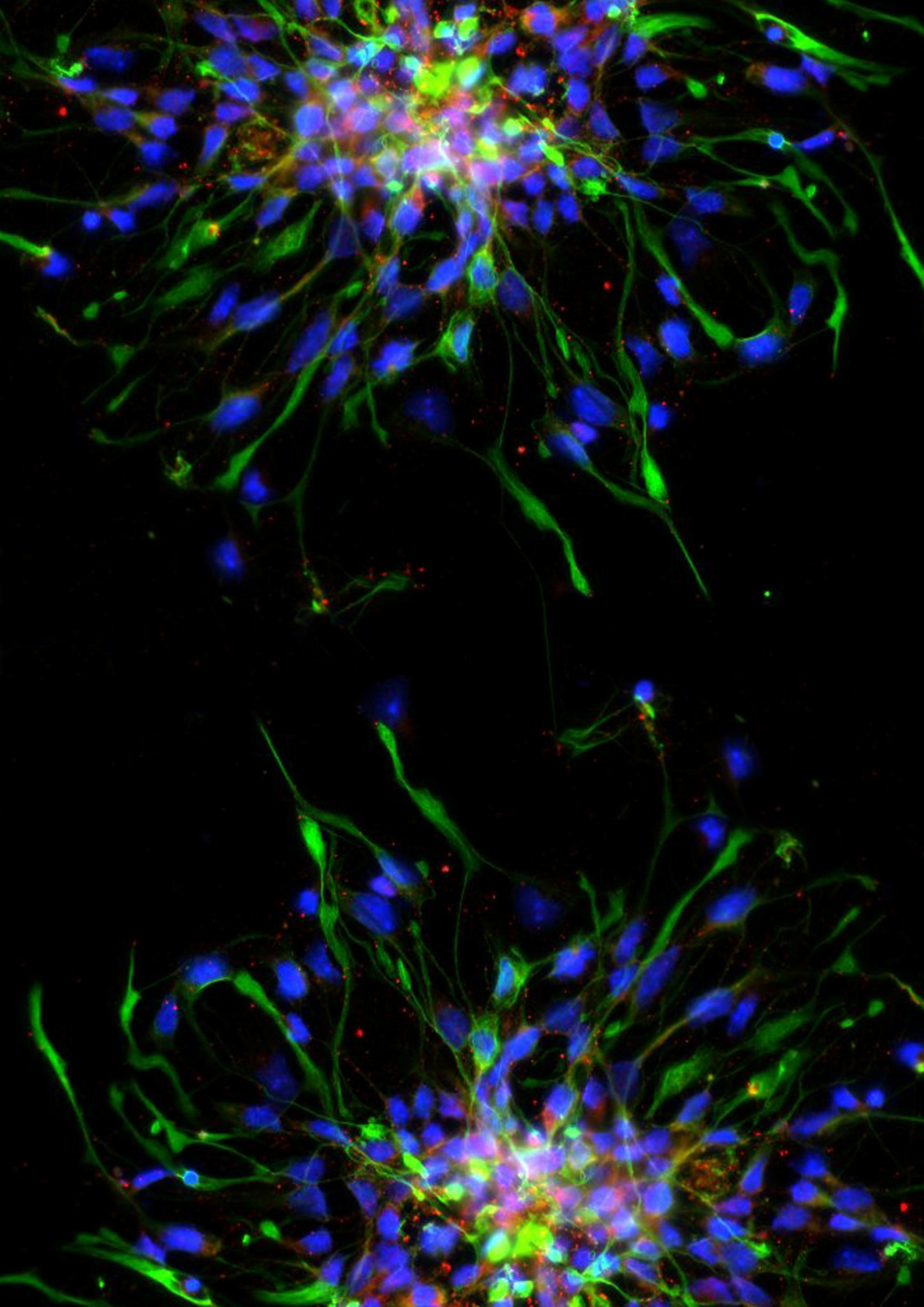
3.6.7 SV2 mutations

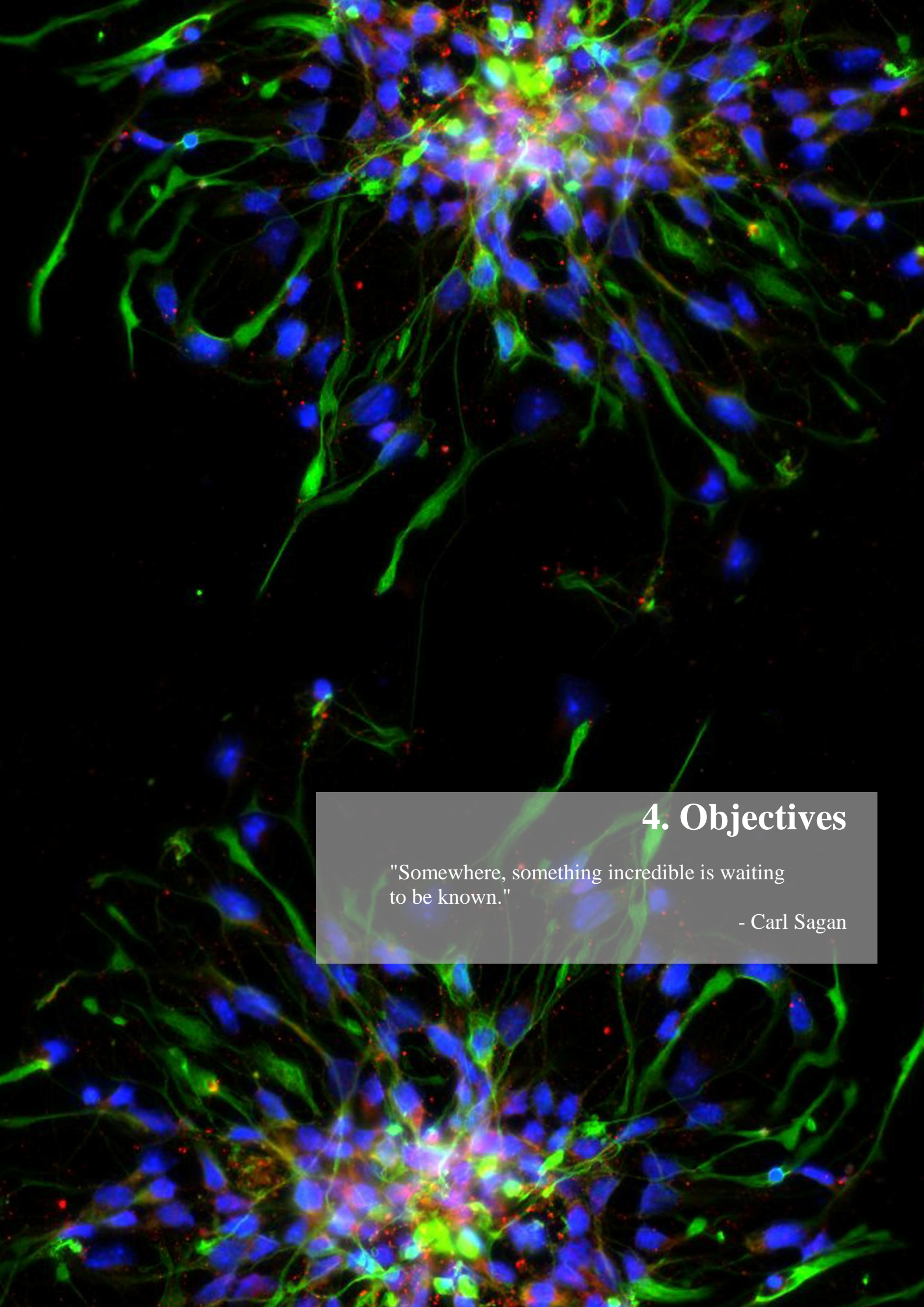
To further explore the different possible functions of SV2 proteins, several studies focused their attempts on single amino acid mutations. It has been reported that SV2A-R231Q affects normal levels of SYT expression and internalization. In contrast, SV2A tryptophans 300 and 666 are not able to restore normal synaptic depression in SV2A lacking cells (Fig. 12) (Nowack et al., 2010).

Sv2a mutants for the glycosylation sites N498Q/N573Q (single or double) present SV2A localized diffusely on the cytoplasm, in a similar way to when SV2A has a disrupted folding (Kwon and Chapman, 2012). A single mutation in SV2A N573Q does not show a phenotype. In contrast, modification in one glycosylation site for SV2B (N516A) or SV2C (N559A) is enough to induce a reduction of expression (Fig. 12) (Yao et al., 2016).

3.6.8 Regulation of *Sv2* expression

Little is known about *Sv2* gene regulation. Some bioinformatics tools suggest potential targets for transcription factors binding, like the transcriptional factor Heat Shock transcription Factor Y-linked 1 (HSFY1) that may interact as an SV2B regulator (HuRI mapping project). However, none of them has been functionally demonstrated. Similarly, bioinformatics screenings have identified some possible motifs for miRNA regulation. Cohen and colleagues identified a miRNA that targets *Sv2a*, miR-458. Indeed, miR-485 overexpression or *Sv2a* silencing produce similar phenotype in terms of reduction of spontaneous synaptic responses and a reduction in dendritic spine density (Cohen et al., 2011).





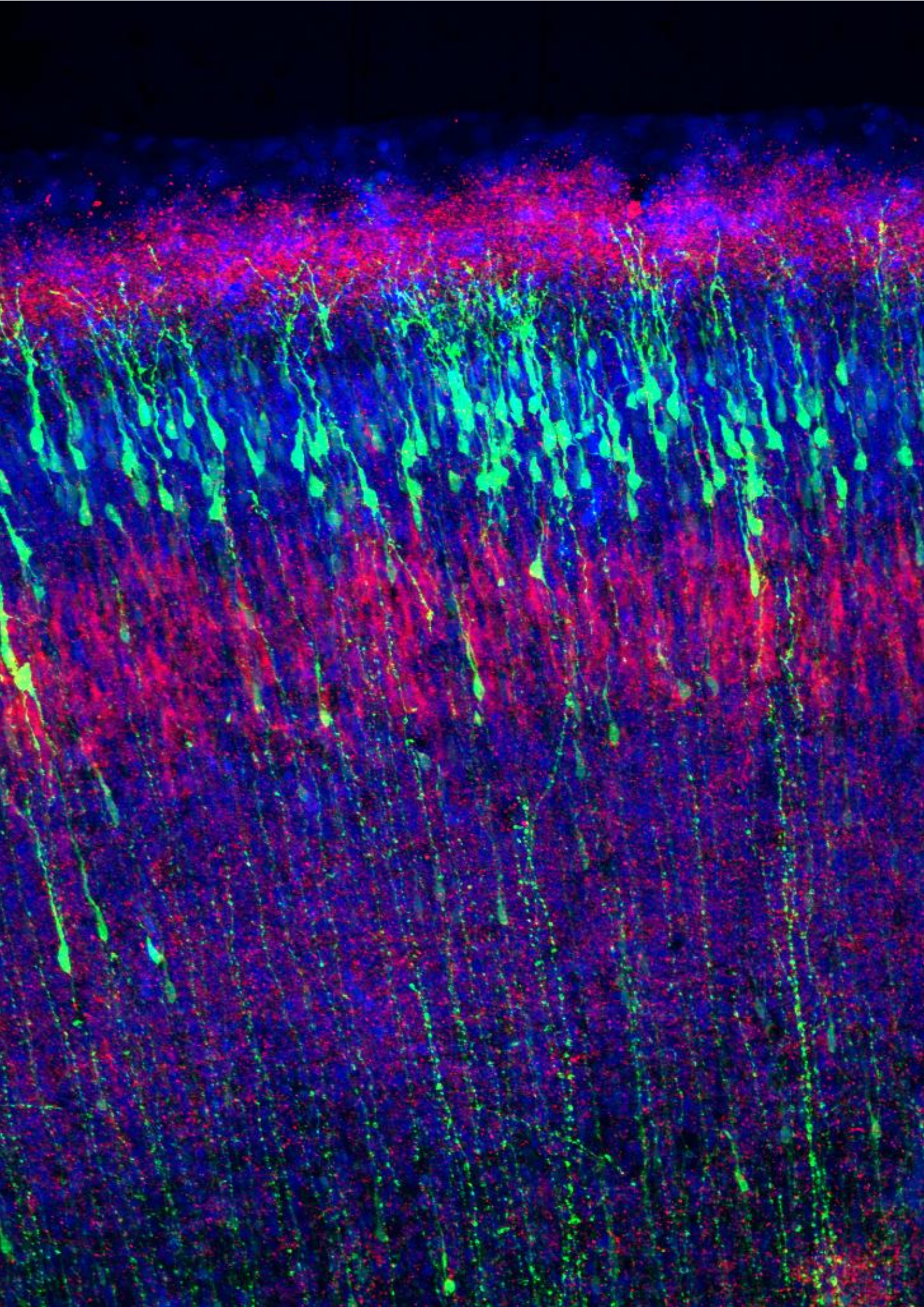
4. Objectives

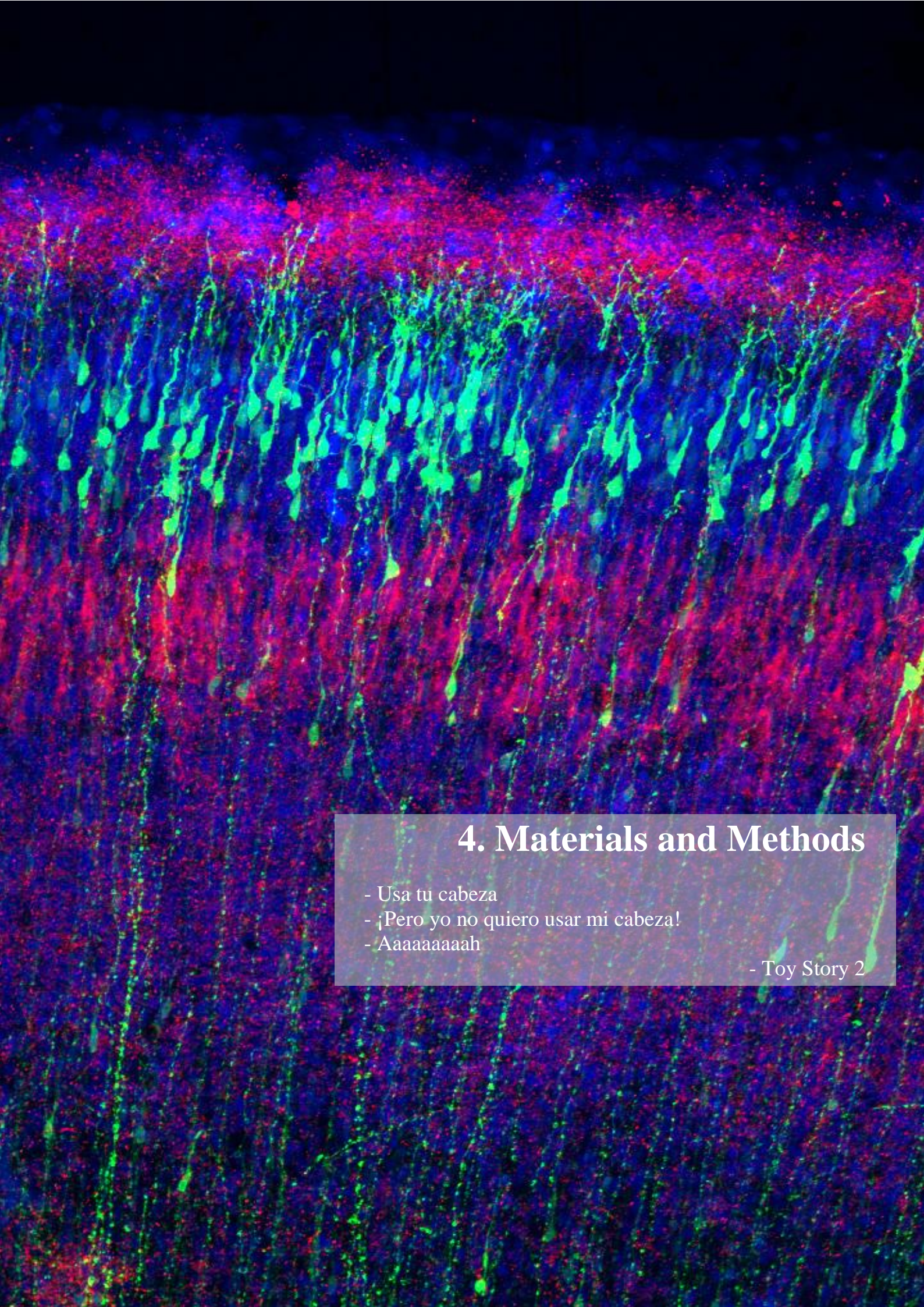
"Somewhere, something incredible is waiting
to be known."

- Carl Sagan

The main goal of this project was to unravel genetic mechanisms responsible for the expansion and folding of the cerebral cortex. Particularly, we were interested in determining the role of SV2B on the generation of bRGCs. To this end, and based on the knowledge available, we set to address the following specific aims:

1. To characterize the endogenous expression of *Sv2b* in mouse cerebral cortex during embryonic development.
2. To determine the impact of expressing SV2B in mouse cortical progenitor cells on their proliferation and delamination.
3. To characterize the endogenous expression of *Sv2b* in ferret cerebral cortex during embryonic development.
4. To study the potential role of SV2B in the generation of bRGCs during ferret cerebral cortex development.
5. To investigate the distribution of SV2B and its influence on cortical progenitor cell proliferation in human.





4. Materials and Methods

- Usa tu cabeza
- ¡Pero yo no quiero usar mi cabeza!
- Aaaaaaaaah

- Toy Story 2

Experimental models

All the animals used in this project were tested naive and no procedures were previously performed on them. The day of the vaginal plug (mice) or the day after mating (ferrets) was considered as embryonic day (E) 0.5. The developmental stage of the experimental model was determined by the requirements of each experiment. Animals were employed independently of their gender.

Animals were kept at the Animal Facilities of the Instituto de Neurociencias de Alicante and Universidad Miguel Hernández on a 16:8h light:dark cycle in accordance with Spanish (RD 53/2013) and EU regulations. Experimental protocols were approved by the Universidad Miguel Hernández Institutional Animal Care and Use Committee (IACUC).

Mice

Homozygous *Sv2b* knockout strain was obtained crossing *Sv2a^{het}/Sv2b^{het}*. Mice carrying loss-of-function alleles for *Sv2b* gene were maintained in homozygosity in an C57BL/6 background (obtained from J. Wesseling laboratory) (Jackson Laboratory, Cat# JAX:006383, RRID:IMSR_JAX:006383). *Sv2b* KO mice were generated by homologous recombination to replace the exon 1 of the gene (Crowder et al., 1999). Wild type mice in an ICR background were used for the electroporation experiments further detail below.

Ferrets

Sable wild type ferrets (*Mustela putorius furo*) were obtained from Euroferret (Copenhagen, Denmark).

Human organoids

Male human fibroblast (ATCC® CRL-2522™) were used to induce pluripotent stem cells (iPSCs) (obtained from S. Capello laboratory).

IPSCs and human organoids were cultured at incubators set at 37°C, 5% CO₂ and ambient oxygen level. Electroporations on the generated organoids were performed at 38 days after initial embryo body formation and fixed 4 or 10 days post electroporation.

Primary P0 ferret cultures

Ferret P0 brains were dissected in ice-cold ACSF freshly prepared (140mM NaCl, 5mM KCl, 10mM HEPES, 24mM D-glucose, 1mM CaCl₂, 1mM MgCl₂) to isolate the cortex. The tissue was passed to medium solution (MEM supplemented with 10% FBS, 1% Penicillin/Streptomycin, 1% Glutamax, 1% Na Pyruvate and 1% D-glucose) where DNase and trypsin was added. After a 10 minutes incubation at 37°C the enzymes were blocked by the addition of serum and the tissue was dissociated. The cells were shortly centrifuge at 800 rpm during 2 minutes and resuspended in media. Around 40000 cells were plated per well into 12mm cover-slips. Two hours later the media was changed to a maintenance media (Neurobasal supplemented with 1% Penicillin/Streptomycin, 1% Glutamax, 2% B27 and 1% D-glucose). Cell cultures were maintained at 37°C, 5% CO₂ and ambient oxygen level. The cells were fixed in Paraformaldehyde/Sucrose 4% (Paraformaldehyde, PFA; Sigma, Ref #441244-1KG) solution during 10 minutes and PBS washed.

Ferret cell line culture

Mustela putorius furo brain cells (Mpf cells; ATCC® CRL-1656™) were cultured in growth medium (Basal medium (Eagle) in Earle's BSS, 86%; lamb serum, 14%) at 37°C, 5% CO₂ and ambient oxygen level for western blot experiments. To maintain them, every 2-3 days cells were detached by trypsin-EDTA during 2 minutes, centrifuge at 800 rpm 2 minutes and subcultured in a 1:5 dilution.

hTERT RPE-1 cells

Homo sapiens sapiens retina pigmented epithelium cells (hTERT RPE-1, ATCC® CRL-4000™) were cultured on DMEM F12 supplemented with Glutamine, 1% Penicillin/Streptomycin and 10% FBS in a 24 well. Cell cultures were maintain at 37°C, 5% CO₂ and ambient oxygen level.

PCR genotyping

In order to genotype the different strains, the following primers were used:

Sv2b wt: 5'- TCATCCAGATGATGTCAAGTCTAAGC -3'

Sv2b common: 5'- GGCACTCAGCCACTAACTCTCAGTACA -3'

Sv2b mut: 5'- GAGCGCGCGCGGCGGAGTTGTTGAC -3'

To performed the PCR reactions for genotyping we have used KAPA2G Fast HotStart ReadyMix PCR Kit (Ref. #KK5609). Thermocycling conditions were set as: previous double-strand DNA denaturing at 95°C during 3min followed by 35 cycles of 15s at 95°C, 60s at 60°C and 60s at 72°C. The genotyping reactions contained Fast HotStart ReadyMix 1x, 0,5µM primers and approximately 200ng of DNA template. PCR products were analyzed by 2% agarose gel electrophoresis. The expected bands were:

Sv2b KO: 220bp for mutants and 305bp for wild type samples.

Constructs

For overexpression assays, we designed a construct encoding human *Sv2b* gene under a CAG promoter and followed by a *T2A-Gfp*, allowing the same amount of expression for both genes (bought from Vector Builder company). For the control samples, we used a GFP encoding constructs downstream a CAG promoter into a MMLV retroviral packaging vector (generous gift of F.H. Gage). For the retroviral delivery we clone the overexpression cassette from the overexpression plasmid into the same MMLV retroviral packaging vector. We include two new restriction sites at the edges of the cassette to the directional cloning (*AgeI* and *PmeI*). The designed primers used were:

AgeI Sv2b Fw: 5' - CTAGTAACCGGTATGGATGACTACAAG - 3'

Sv2b Rv PmeI: 5' - CCTAGTAGTTTAAACTTACTTGTACAGCTC - 3'

For the time-lapse experiments, we designed a plasmid encoding the human *SV2B* gene fused with *Gfp*, also under CAG promoter, but it presents a 3 tandem Simian Virus 40 polyadenylation signal (SV40) floxed cassette in between the promoter and *SV2B* gene (bought from Vector Builder company). By the usage of this design, SV2B:GFP would only being express in a co-electroporation with CRE (pCAG-Cre, generous gift of M. Götz) that will remove the SV40 tandem allowing the expression. All the vesicles carrying overexpressed SV2B will be labeled with GFP. Moreover, the SV2B:GFP cassette is immediately followed by a *T2A-mKate* cassette to label the entire electroporated cell. As a control, we used a construct encoding mKO that integrates into the plasma membrane under the same promoter and floxed SV40 in between (generous gift of M. Götz).

Regarding the ISH (*in situ* hybridization) probes, we subcloned them by PCR from mouse or ferret cDNA into pBS from pUC19ckD11 (generous gift of J. Galcerán). Specific primers for both species were designed:

Mouse Sv2a Fw: 5' - AACGTGGGGAGCATTGGA - 3'

Mouse Sv2a Rv: 5' - CCAGGAAGCACAGCCAGT - 3'

Mouse Sv2b Fw: 5' - CCACGTGCCATTTCTTTAC - 3'

Mouse Sv2b Rv: 5' - GAACTGGCCTGGCATCTAAG - 3'

Ferret Sv2a Fw: 5' - GTCTTTGTGGTGGGCTTTGT - 3'

Ferret Sv2a Rv: 5' - TCGATATTCGGGACCAAAC - 3'

Ferret Sv2b Fw: 5' - GCCCACCAGTACGAGAACAT - 3'

Ferret Sv2b Rv: 5' - ACCAGACCACAGCCAGAATC - 3'

CRISPR plasmids to downregulate the expression of *Sv2b* in ferret neural cells were generated by annealing the following oligomers into pSpCas9(BB)-2A-GFP plasmid (PX458, Addgene), after a BbsI digestion as described in Zhang Lab's protocol. The newly designed guides used were:

CRISPR ferret Sv2b 1.1: CACCGATATAGCTCGAGAGGCGAGC

CRISPR ferret Sv2b 1.2: AAACGCTCGCCTCTCGAGCTATATC

CRISPR ferret Sv2b 2.1: CACCGGCCGGCAGTCCCGGACCCAA

CRISPR ferret Sv2b 2.2: AAACCTTGGGTCCGGGACTGCCGGCC

iPSC culture

hiPSCs were cultured at 37°C, 5% CO₂ and ambient oxygen level on Geltrex coated plates in mTeSR1 medium (STEMCELL Technologies, Ref #05850) with daily medium change. For passaging, hiPSC colonies were incubated with StemPro Accutase Cell Dissociation Reagent diluted 1:4 in PBS for 4 minutes. Pieces of colonies were washed off with DMEM/F12, centrifuged for 5min at 300 x g and resuspended in mTeSR1 supplemented with 10µM Rock inhibitor Y-27632(2HCl) for the first day.

Generation of cerebral organoids

Cerebral organoids were generated as previously described (Lancaster and Knoblich, 2014). Briefly, iPSCs were dissociated into single cells using StemPro Accutase Cell Dissociation Reagent (Ref #A1110501, Life Technologies) and plated in the concentration of 9000 single iPSCs/well into low attachment 96-well tissue culture plates in hES medium (DMEM/F12GlutaMAX supplemented with 20% Knockout Serum Replacement, 3% ES grade FBS, 1% Non-essential amino acids, 0.1mM 2-mercaptoethanol, 4ng/ml bFGF and 50µM Rock inhibitor Y27632) for 6 days in order to form embryoid bodies (EBs). Rock inhibitor Y27632 and bFGF were removed on the 4th day. On day 6 EBs were transferred into low attachment 24-well plates in NIM medium (DMEM/F12GlutaMAX supplemented with 1:100 N2 supplement, 1% Non-essential amino acids and 5µg/ml Heparin) and cultured for additional 6 days. On day 12 EBs were embedded in Matrigel drops and then they were transferred in 10cm tissue culture plates in NDM without A medium (DMEM/F12GlutaMAX and Neurobasal in ratio 1:1 supplemented with 1:100 N2 supplement; 1:100 B27 without Vitamin A, 0.5% Non-essential amino acids, insulin 2.5µg/ml and 50µM 2-mercaptoethanol) in order to form organoids. 4 days after Matrigel embedding, cerebral organoids were transferred into an orbital shaker and cultured until electroporation in NDM with A medium (DMEM/F12GlutaMAX and Neurobasal in ratio 1:1 supplemented with 1:100 N2 supplement; 1:100 B27 with Vitamin A, 0.5% Non-essential amino acids, insulin

2.5µg/ml, 1:100 Antibiotic-Antimycotic and 50µM 2-mercaptoethanol). During the whole period of cerebral organoid generation, cells were kept at 37°C, 5% CO₂ and ambient oxygen level with medium changes every other day. After transferring the cerebral organoids onto the shaker, medium was changed twice per week.

Electroporation of cerebral organoids

Cerebral organoids were kept in antibiotics-free conditions prior to electroporation. Electroporations were performed in cerebral organoids at 38 days after the initial plating of the embryo bodies and fixed 4 days post electroporation. During the electroporation cerebral organoids were placed in an electroporation chamber (Harvard Apparatus, Holliston, MA, USA) under a stereoscope and using a glass microcapillary 1-2µl of plasmid DNAs was injected together with Fast Green (0.1%, Sigma) into different ventricles of the organoids. The plasmid DNAs injected were 1µg/µL of *Gfp* in controls or 1µg/µL of *SV2B-Gfp* in experimental condition. Cerebral organoids were subsequently electroporated with 10 pulses applied at 80V for 50ms each at intervals of 2000ms (Ref #ECM830, Harvard Apparatus). Following electroporation, cerebral organoids were kept for additional 24hr in antibiotics-free media, and then changed into the normal media until fixation. Cerebral organoids were fixed using 4% PFA-Sucrose for 20 minutes at 4°C, cryopreserved with 30% sucrose and stored at -20°C. For immunofluorescence, 16µm cryosections were prepared.

Western Blot and validation of CRISPR/Cas-mediated gene editing

For the endogenous SV2B protein quantification, ICR WT cortices were dissected at different stages and immediately freeze by liquid nitrogen. After collecting all the samples, the same day were defrosted and sonicate in pH 7,4 sterile cold lysis buffer (20mM HEPES, 150mM KCl, 1mM EGTA, 1mM EDTA, 0,1mM DTT, 40mM NaF, 1mM Na₃VO₄, 1% Triton-X and protease inhibitor).

For the validation of the CRISPR guides we transfected 7th passage Mpf cells by Lipofectamine 2000 (Thermo Fisher Scientific) with pSpCas9(BB)-2A-GFP plasmid containing guides and a condition with an empty one for controls. After 48 hours, cells were harvested, washed with cold PBS and lysate by sterile cold lysis buffer.

The amount of protein on each sample was quantified by western blot as follows. In brief, from the soluble fraction after 15 minutes 15000rpm centrifuge, the protein concentration was determined by Pierce BCA Protein Assay Kit (Thermo Fisher Scientific; Ref #23227). Samples were heat treated at 45°C during 15 minutes in Laemi Sample Buffer 1x (LSB). 30µg of total protein per well and condition was run into a 8% SDS-PAGE gel during 2 hours at 120mV in Running Buffer 1x (Tris-Glicine 1X, SDS 0,1%). The wet transfer to a 0.45µm nitrocellulose membrane (GE Healthcare Life Science, Ref #10600002) was done overnight at 4°C 30mV in already cold transfer buffer (Tris-Glycine 1x, Methanol 1%, SDS 0,01%). After washing and fixing with Ponceau S, the membrane was blocked in 5% milk TBS-T buffer while shaking during one hour at room temperature. Antibodies were diluted on blocking solution in a concentration of 1:1000 anti-SV2B rabbit IgG (Synaptic systems, Cat# 119 102, RRID:AB_887803) and 1:2000 Goat Peroxidase anti-rabbit IgG (Thermo Fisher Scientific, Cat# 31462, RRID:AB_228338). Primary antibody was incubated overnight at 4°C shaking and secondary antibody during 2 hours at room temperature. To detect the labeling, Chemiluminescent HRP substrate (Millipore, Ref #WBKLS0100) was applied and the membrane exposed in a Amersham Imager 680 Bioimager. The quantification was normalized to the tubulin amount using anti-Tub mouse primary antibody 1:1000 (Sigma, Cat# T5168, RRID:AB_477579) and 1:2000 Goat Peroxidase anti-mouse IgG (Thermo Fisher Scientific, Cat# 31444, RRID:AB_228321). Mean intensity was measured by ImageJ Fiji and statistically analyzed by unpaired t-student test.

Brain electroporations

Mouse and ferret embryos were electroporated *in utero* in the neocortex at needed embryonic day (E). Briefly, pregnant females were deeply anesthetized with 2% isoflurane and the uterine horns exposed. DNA solution (approximately 1µL) was injected into the lateral ventricle using pulled borosilicate glass micropipettes (Ref #WPI 1B150F-4), and square electric pulses (35-45V, 50ms on – 950ms off, 5 pulses for mice; 75V for ferrets) were applied with an electric stimulator (Cuy21EDIT Bex C., LTD) using round electrodes (CUY650P5, Nepa Gene or CUY650P7, Nepa Gene).

Postnatal ferrets were deeply anesthetized with 2% isoflurane and injected at the telencephalic ventricle following the stereotaxic coordinates set in previous studies of our laboratory (Martinez-Martinez et al., 2016): antero-posterior = -0.5mm, latero-medial = 2.0mm, dorso-ventral = 2.0mm with an inclination of 22.5°. Approximately 1µL of DNA solution was injected into the ventricle thanks to the same pulled borosilicate glass micropipettes. We used round paddles (CUY650P7, Nepa Gene) to pass the square electric pulses from the skull (75-80V, 50ms on - 950ms off, 5 pulses) with an electroporator (Cuy21EDIT Bex C., LTD).

Plasmid concentrations were as follows: *Gfp* = 0.75µg/µl; *hSV2B*, *hSV2B:GFP*, *cSv2b* guides-Cas9, *Cas9* = 1µg/µl. Combinations of these plasmids were done maintaining the same final individual concentrations.

RPE-1 cells transfection

For the overexpression of SV2B:GFP fusion protein on human cells, hTERT RPE-1 (ATCC® CRL-4000™) were transfected by Lipofectamine 2000 (Thermo Fisher Scientific) in DMEM F12 during 4 hours. The concentration used was 200ng of SV2B:GFP fusion protein plasmid and 200ng of *Cre* plasmid. Then, the medium was removed and changed to 50% new and 50% old medium. After 36 hours from transfection, cells were fixed by 4% PFA during 15 minutes, washed with PBS and proceed with the immunostaining.

Retroviral stocks preparation and concentration

High-titre Murine Moloney Leukemia Virus-based (MMLV-based) retrovirus encoding GFP or SV2B under the CAG promoter were prepared by transient transfection with Lipofectamine 2000 (Thermo Fisher Scientific) (together with CMV-vsrg and CMV-gp plasmids) of human embryonic kidney 293T (HEK293) cells as a package cell line, concentrated by ultracentrifugation and viral titre estimated by clonal infection (Borrell et al., 2012). Viral solutions were injected using pulled glass micropipettes into ferret embryos.

Bromodeoxyuridine labeling experiments

Bromodeoxyuridine (BrdU, Sigma, Ref #B5002-1G) was diluted at 10mg/ml in 0.9% NaCl and always administered at 50mg/kg body weight. For cell cycle exit calculation, 24h after *in utero* electroporation at E14.5 with *CAG-Gfp* or *CAG-SV2B*, we injected intraperitoneally one dose of BrdU to the pregnant females (E15.5) and we fixed the embryos 24h after injection (E16.5). Then, the percentage of GFP+ BrdU+ Ki67-labeled cells was quantified. For interkinetic nuclear migration analysis, pregnant mice females were *in utero* electroporated at E14.5 with *CAG-Gfp* or *CAG-SV2B* and intraperitoneally injected with BrdU at E15.5 (24h before fixing) or at E16.5 (30 min before fixing). Following, the distribution of BrdU+ cells along VZ/SVZ was analyzed in both conditions.

Immunohistochemistry and ISH

After the needed survival, mice pregnant females were sacrificed by cervical dislocation while ferret females were injected intraperitoneally with an overdose of sodium pentobarbital (Dolethal, Ref #570681.8). Animals were fixed with 4% PFA in phosphate buffer 0.1M (PB) pH 7.3 at 4°C. Mice embryos until E15.5 were fixed in 4% PFA ice-cold 30 to 60 minutes. Embryos older than E16.5, postnatal mice and ferrets were perfused intracardially and postfixed 30 to 120 minutes with 4% PFA before histological processing. Brains for *in situ* hybridization were postfixed overnight.

Brains were sequentially cryoprotected with 15% to 30% sucrose (Sigma, Ref #S7903-1KG), embedded in Cryo-medium Neg-50 (Thermo Scientific, Ref #6502), frozen and sectioned under a cryostat at 20µm; or cut under the cryotome at 50µm for ferret and postnatal mice tissue. For immunohistochemistry, sections were permeabilized in PB 0.1M containing 0.25% Triton X-100 (Sigma, Ref #T8787-250ML) and blocked in 10% of Normal Horse Serum (GIBCO, Ref #16050-122) and 2% Bovine Serum Albumin (BSA, Sigma, Ref #A9576-50ML) during 2 hours. Brain slices were incubated with primary antibodies overnight in blocking solution, followed by appropriate fluorophore-conjugated secondary antibodies and counterstained with DAPI (Sigma, Ref #D9542). Primary antibodies used were:

Primary antibody (anti-)	Host	Dilution	Source	Identifier
BrdU	Rat monoclonal	1:200	Abcam	Cat# ab6326, RRID:AB_2313786
Calbindin	Rabbit	1:5000	Swant	Cat# C9638, RRID:AB_2314070
Ctip2	Rat monoclonal	1:500	Abcam	Cat# ab18465, RRID:AB_2064130
Cux1	Rabbit polyclonal	1:500	Santa Cruz	Cat# sc-13024, RRID:AB_2261231
EEA1	Mouse monoclonal	1:1000	BD Biosciences	Cat# 610457, RRID:AB_397830
GFP	Chicken polyclonal	1:1000	Aves Lab	Cat# GFP-1020, RRID:AB_10000240
GFP	Human monoclonal	1:400	Recombinant Antibody Platform Institut Curie (A-R-H#11)	
GRASP65	Rabbit monoclonal	1:2000	Abcam	Cat# ab174834
Ki67	Rabbit polyclonal	1:200	Abcam	Cat# ab15580, RRID:AB_443209
Laminin	Rabbit	1:500	Merk Millipore	Cat# AB2034, RRID:AB_91209
Lamp1	Rabbit monoclonal	1:200	Cell Signaling Technology	Cat# 9091, RRID:AB_2687579
NeuroD2	Rabbit	1:400	Abcam	Cat# ab104430, RRID:AB_10975628
Par3	Rabbit polyclonal	1:500	Merck Millipore	Cat# 07-330, RRID:AB_2101325
Pax6	Rabbit polyclonal	1:500	Merck Millipore	Cat# AB2237, RRID:AB_1587367
Pax6	Mouse monoclonal	1:500	Hybridoma Bank	Cat# pax6, RRID:AB_528427

Phosphohistone 3	Rabbit polyclonal	1:500	Upstate	Cat# 06-570, RRID:AB_310177
Phosphovimentin	Mouse monoclonal	1:1000	Abcam	Cat# ab22651, RRID:AB_447222
Rab6	Rabbit Monoclonal	1:400	Recombinant Antibody Platform Institut Curie	
Rab7	Rabbit monoclonal	1:100	Cell Signaling Technology	Cat# 9367, RRID:AB_1904103
Sv2b	Rabbit polyclonal	1:200	Synaptic Systems	Cat# 119 102, RRID:AB_887803
Tuj1 (bIII-Tubulin)	Mouse monoclonal	1:1000	Covance	Cat# MMS-435P, RRID:AB_2313773
Vimentin	Mouse	1:400	Chemicon	Cat# MAB3400, RRID:AB_94843

Secondary antibodies were the followed in a 1:200 concentration.

Secondary antibody (anti-)	Host	Dilution	Source	Identifier
Rabbit IgG Alexa 555	Donkey	1:200	Jackson Immunoresearch	Cat# A-31572, RRID:AB_162543
Rabbit IgG Alexa 647	Goat	1:200	Jackson Immunoresearch	Cat# 111-605-144, RRID:AB_2338078
Mouse IgG Alexa 555	Donkey	1:200	Invitrogen	Cat# A-31570, RRID:AB_2536180
Mouse IgG Alexa 647 Fab fragment	Donkey	1:200	Jackson Immunoresearch	Cat# 715-605-150, RRID:AB_2340862
Rat IgG Cy3 Fab fragment	Donkey	1:200	Jackson Immunoresearch	Cat# 712-167-003, RRID:AB_2340670
Chicken IgY Alexa 488	Donkey	1:200	Jackson Immunoresearch	Cat# 703-545-155, RRID:AB_2340375

For ISH, sense and anti-sense cRNA probes were synthesized and labeled with digoxigenin (DIG; Roche Diagnostics, Ref #11175025910). Sections of 20 μ m-thick frozen mouse brain or 50 μ m ferret slices were pretreated during 2 hours at 62°C in hybridization buffer [50% Formamide (Ambion, Ref #AM9342), 10% Dextran sulfate (Sigma, ref: D8906-100G), 0.2% tRNA (Invitrogen, Ref #15401-011), 1x Denhardt's solution (from a 50x stock; Sigma, Ref #D2532), 1x salt solution (containing 0.2M NaCl (Sigma, Ref #S9888-2.5KG), 0.01M Tris-HCl (Sigma, Ref #T3254-1KG), 5mM NaH₂PO₄ (Sigma, Ref #71505-250G), 5mM Na₂HPO₄ (Sigma, Ref #S3264-500G), 5mM EDTA, pH 7.5)]. DIG-labeled cRNA probes were applied in hybridization solution to the tissue at 62°C for overnight hybridization. The sections were washed and then blocked during 2 hours at room temperature in MABT buffer solution 1x, 10% Sheep Serum, 10% Blocking reagent. Later, slides were incubated with alkaline phosphatase-coupled anti-digoxigenin Fab fragments (Roche, Ref #11093274916) in blocking solution overnight at 4°C. To reveal the hybridize probes, 3.4 μ l/ml of nitroblue tetrazolium (NBT, Sigma, Ref #N6639-1G) and 3.5 μ l/ml of 5-bromo-4-chloro-3-indolyl phosphate (BCIP, Roche, Ref #11585002001) in reaction buffer was applied until the labeling shows.

Time lapse recordings

For live imaging of individual SV2B⁺ vesicles in mouse progenitor cells, embryos were electroporated *in utero* at E14.5 with *CAG-SV2B:Gfp* encoding the fusion protein or *CAG-flox-EGfp* as a control (0.75 μ g/ μ L) and *pCAG-Cre* (0.1 μ g/ μ L). The low concentration of Cre plasmid allowed a sparse labeling of progenitor cells upon recombination of the floxed cassette (Pilz et al., 2013), essential to identify single separated cells. The day after the electroporation (E15.5), the brains were dissected out, embedded in 4% low melting agarose and cut. The tissue was slide in a vibratome at 250 μ m in ice-cold ACSF freshly prepared (140mM NaCl, 5mM KCl, 10mM HEPES, 24mM D-glucose, 1mM CaCl₂, 1mM MgCl₂). Then, slices were embedded in medium (N2 100x, B27 50x, EGF 200 μ g/mL, FGF 20 μ g/mL, FBS, NHS, Glucose, Sodium bicarbonate, Penicillin/Streptomycin, DMEM/F-12) at 37°C. Imaging was performed on an inverted spinning-disc microscope and Nikon 100x immersion. Stacks of frames separated 0.2 μ m were captured every approximately 1.2sec for 1-2min.

IMAGING, QUANTIFICATION AND STATISTICAL ANALYSES

Electroporation analysis

In mouse and ferret embryo experiments, to minimize the significant variability between animals and the possible methodological effects, counts in the electroporated hemisphere of each experimental animal were normalized with the electroporated controlled hemisphere at the same rostro-caudal and latero-medial level. All quantifications were made in at least 3 independent embryos.

Cultures analysis

In co-localization cell cultures experiments, individual cells from at least 3 different cover-slips were imaged using Olympus FV10 confocal microscope and analyze by JaCoP plugin from ImageJ Fiji.

Histological analysis

For co-localization studies, images from a single confocal plane were obtained and analyzed using Olympus FV10 confocal microscope or Zeiss Apotome microscope. Proper expression of SV2B protein by the overexpression plasmids was observed by immunohistochemistry against SV2B protein and GFP expressed by the T2A linker.

Western blot analysis

For western blot analysis, images were processed to 8 bits and the mean signal intensity in the area of interest was measured using ImageJ software (n=3 independent samples for each group).

Bromodeoxyuridine labeling experiments

To determine cell cycle exit, DAPI BrdU GFP positive Ki67 negative nuclei in VZ and SVZ were quantified. To include the nucleus as positive for BrdU staining, at least 25% of the nucleus should be labeled.

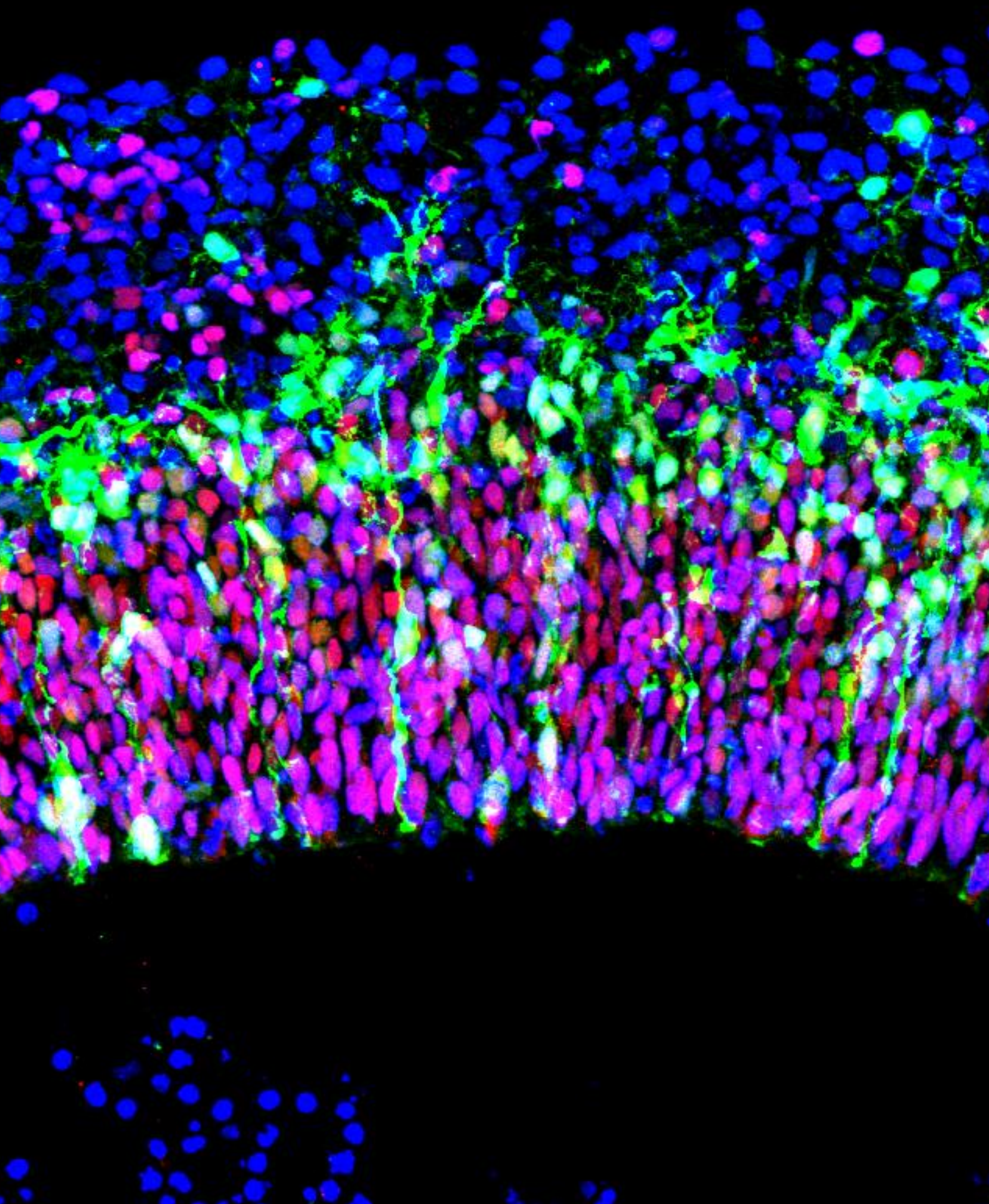
For BrdU distribution analysis, projection images were plotted in ImageJ Fiji to its mean intensity histogram. After, each intensity value per pixel was normalized to neighbouring pixels to soften the signal and show the trend. Each sample was also normalized to its maximum value and for each all the samples were averaged together.

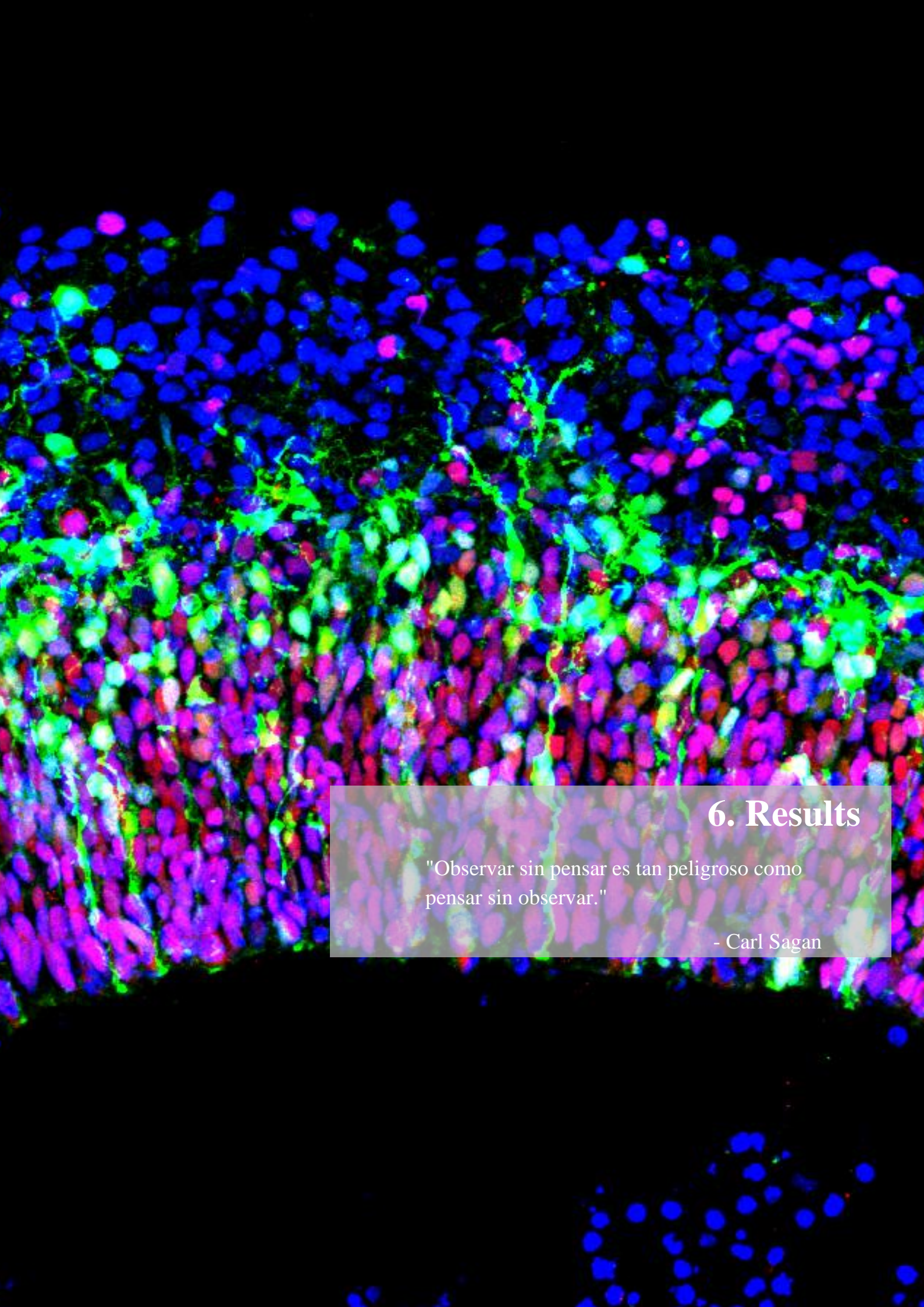
Time lapse analysis

Vesicles time-lapse image stacks were collapsed to maximum projection, contrast enhanced and analyzed with Imaris software's by Spots semiautomatic tracking. Each individual vesicle was followed until the end of the movie to determine its behavior. Vesicles were discarded if they were out of focus at some stack.

Statistical analysis

Statistical analysis was carried out with GraphPad Software. To assume statistical significance, p values were set below 0.05. All values represent mean \pm standard error of the mean (SEM). Pair-wise t-test or independent samples t-test were used to compare statistical differences between two experimental groups. χ^2 -test was used to determine the equality of proportion between different groups. To compare the statistical differences between at least three experimental groups, One way-ANOVA was used. Similar variance across experimental distributions was assumed. Samples were obtained independently and the observations were sampled randomly and independently. For each experiment, embryos for at least two different females were used. In each figure legend, it is detailed the experimental n, the statistical test used and the statistical significance.





6. Results

"Observar sin pensar es tan peligroso como pensar sin observar."

- Carl Sagan

Part 1. Overexpression of *SV2B* in embryonic mouse telencephalon leads to alterations in progenitor cell adhesion, cell cycle and proliferation

Characterization of *Sv2a* and *Sv2b* endogenous expression in mice

In order to understand the potential role of SV2B during embryonic development of the cerebral cortex, we firstly detected their endogenous expression on wild type mice. We designed and generated specific RNA probes against *Sv2a* and *Sv2b*. Figure 1 shows the *in situ* hybridization stains in coronal sections at different stages, demonstrating the evolution of their expression along development.

Contrary to previous assumptions (Crevecoeur et al., 2013), *Sv2b* is already expressed at E12.5 in multiple parts of the developing telencephalon, including the retinal pigmented epithelium (Fig. 1A''), early post-migratory cortical neurons just below the marginal zone (Fig. 1A'), the most latero-ventral aspect of the intermediate zone of the lateral ganglionic eminence, and in the hippocampus (Fig. 1A). At this early stage (E12.5) *Sv2a* is also expressed, mainly at the intermediate zone of the medial and lateral ganglionic eminences (Fig. 1B), in newly formed neurons of the cortex (Fig. 1B') and at the retinal pigmented epithelium (Fig. 1B''). At E14.5 *Sv2b* expression is more confined to particular areas (Fig. 1C), whereas *Sv2a* has a more widespread expression (Fig. 1D). *Sv2b* is expressed in the cortical plate and subplate (Fig. 1C'), insular cortex, piriform cortex, hippocampus and ganglion cells of the ventral retina (Fig. 1C''). *Sv2a* mRNA is found at the ganglion cell layer at the eye (Fig. 1D''), cortical plate (Fig. 1D') and intermediate zone of the ganglionic eminences (Fig. 1D). Later in development (E17.5; Fig. 1E), *Sv2b* expression continues restricted to the hippocampal formation (CA1, CA2, CA3 and dentate gyrus), cortical plate and (particularly) subplate (Fig. E'), amygdala and in some sparse cells of the thalamus. In contrast, *Sv2a* expression becomes almost ubiquitous to the entire brain (Fig. 1F), being highly expressed at the cortical plate (Fig. 1F'). In summary, the areas of expression of both isoforms increase during embryonic development, each one showing different and unique expression patterns. In agreement with previous reports, expression of *Sv2* family members was found confined to differentiated neurons. *Sv2b* expression was never detected in germinal layers of the embryonic mouse cortex.

To confirm that SV2B protein, and not only mRNA, is expressed in the early embryonic cerebral cortex, we performed a western blot analysis of dissected mouse cortices at different stages of embryonic development and newborn pups. We used an isoform-specific antibody to detect SV2B. SV2B protein was already detected by E11.5,

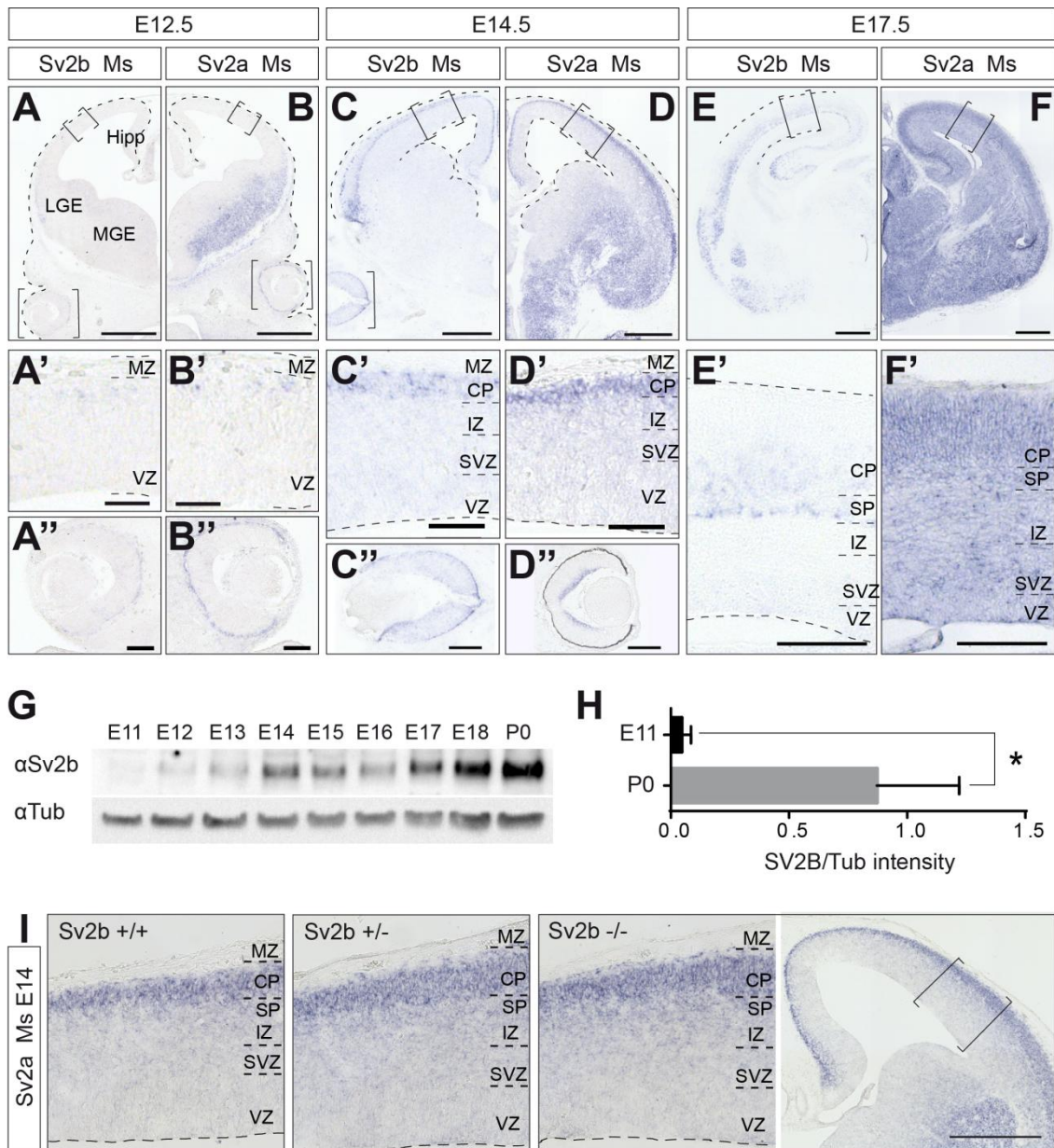


Figure 1. *Sv2a* and *Sv2b* endogenous expression in mice. (A-F) Coronal sections of WT animals at E12.5, E14.5 and E17.5 showing the endogenous expression of *Sv2a* and *Sv2b* by *in situ* hybridization. (A'-F') High magnifications of the areas inside the brackets at the cortex. (A''-D'') High magnifications of the eyes. Scale bars: 500 μ m (A-F panels); 50 μ m (A'/A''-F'/D'' panels). (G) Representative western blot of SV2B protein in mice cortices at different stages (E11-P0) and Tubulin protein. For the same amount of Tubulin, SV2B increases during development. (H) Quantification of SV2B ratio respect the Tubulin protein to normalize the data. Data are shown as mean \pm SEM, n=3, *p_value<0.05 Unpaired two-tailed t-test. (I) *In situ* hybridization on cortical coronal sections of *Sv2b* mutant mice at E14.5 (WT, HE and HO). Hipp: Hippocampus; LGE: Lateral Ganglionic Eminences; MGE: Medial Ganglionic Eminences.

and its expression increased during development, in parallel to the increase in number of newly generated neurons (Fig. 1G,H). This is in agreement with already published RNAseq data where *Sv2b* was found expressed at higher levels in the cortical plate (CP) compared to VZ and SVZ (Fietz et al., 2012).

It has been strongly suggested that due to the similarity between the three isoforms of the SV2 family members, they may perform redundant functions, compensating the role of the paralogous form in its absence. We tested this possibility by performing *in situ* hybridizations on *Sv2b* knockout mouse tissue at E14. We found that *Sv2a* expression was not altered in the absence of *Sv2b*, and the standard expression pattern at the cortical plate was detected. We could not observe changes in intensity nor distribution of *Sv2a* RNA in *Sv2b* KO or heterozygous (HE) mice compared to WT littermates (Fig. 1I). Nevertheless, the absence of changes in mRNA expression does not eliminate possible alterations in protein amount, which could be affected by other mechanisms including mRNA translation or protein stability.

SV2B overexpression causes delayed neuronal migration and disruption of the VZ

Trying to mimic the scenario in the developing ferret cortex, where *Sv2b* is expressed at the VZ at mid-neurogenesis (Martinez-Martinez et al., 2016), we planned to *in utero* electroporate the embryonic cortex of mice to overexpress *Sv2b*. To do so, we designed a cassette encoding human SV2B under a CAG promoter, directly followed by green fluorescent protein (GFP). *Gfp* was encoded following a T2A self-cleaving peptide, to ensure equimolarity of SV2B and GFP proteins. This plasmid was transduced into aRGCs lining the cortical VZ at E14.5 (Fig 2A).

Upon electroporation of SV2B at E14.5 and analysis at E17.5 we first noticed a significant delay in the radial migration of cortical neurons. GFP+ cells accumulated at the germinal layers compared to control embryos electroporated with *Gfp* alone. Accordingly, the proportion of GFP+ cells at the IZ and CP was reduced in SV2B-electroporated embryos compared to controls (Fig. 2B and 2C). We reasoned that this phenotype might result from: altered radial migration of newborn neurons, and/or altered proliferation of progenitor cells with a delay in neurogenesis and, hence, a delay in the initiation of neuron migration.

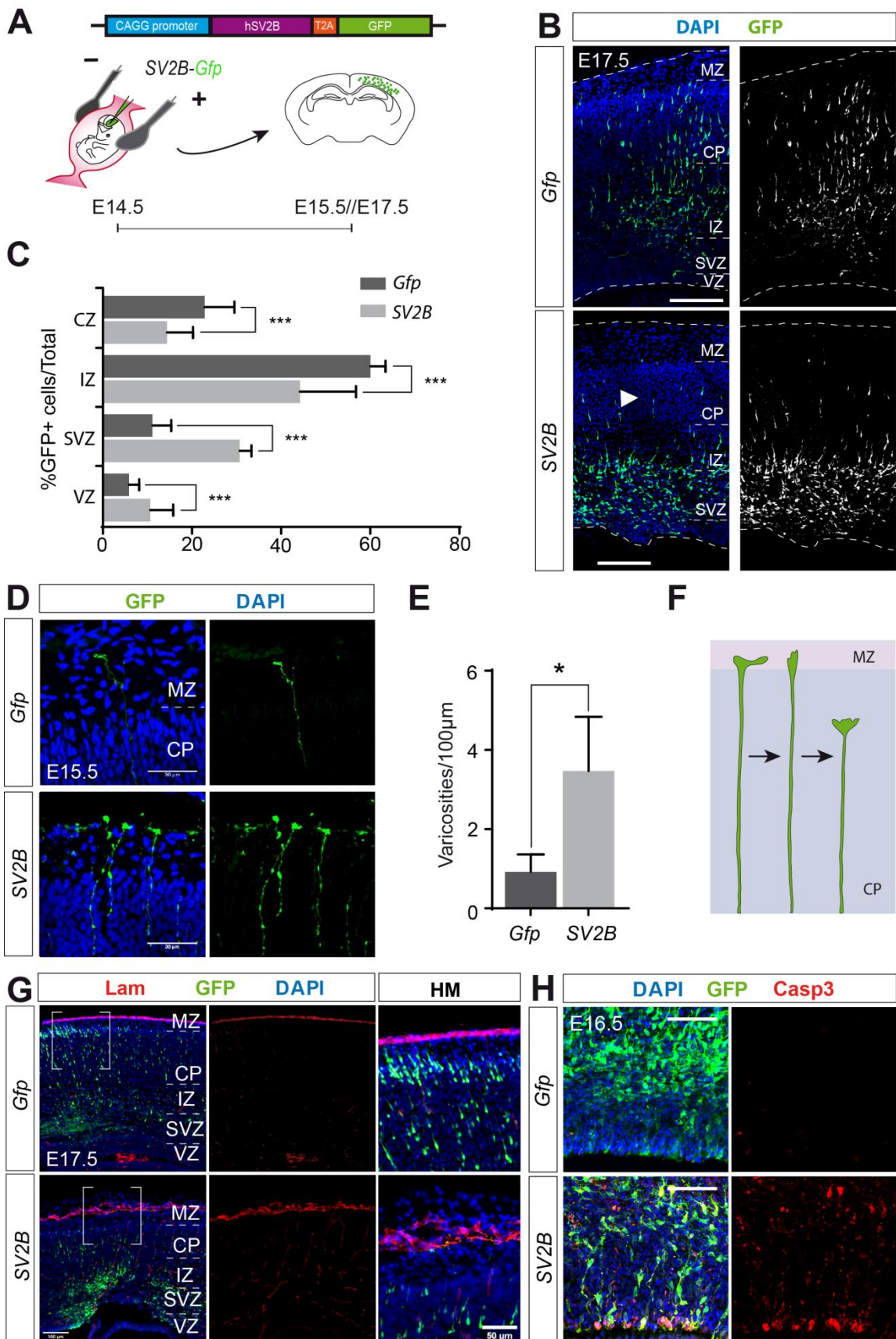


Figure 2. SV2B overexpression phenotype on the basal lamina. (A) Schema of the *Sv2b* overexpression plasmid and the experimental design. E14.5 embryos were *in utero* electroporated with the previous plasmid or one encoding *Gfp* as a control. Samples were collected at E15.5 (D), E16.5 (H) or E17.5 (C, G) depending on the experimental design. (B, D, G, H) Immunostainings of 20 μ m coronal cryosections of the electroporated dorsal telencephalon showing DAPI (blue) and GFP (green). (B) Differential distribution of the migrating cells (green and white). The long dashed lines limit the tissue, and the arrowhead show the reduction on migrating cells at the CP and IZ. Scale bar: 100 μ m. (C) Quantification of the percentage of electroporated GFP positive cells on each layer respect the total GFP positive cells. Data is shown as *Gfp* controls in dark grey and *SV2B* in light grey. Chi-square statistics; average \pm SEM; n=3; ***p value<0.001. (D) High magnification of the basal end-feet of electroporated aRGCs. Scale bar: 30 μ m. (E) The number of varicosities per 100 μ m of aRGC basal process. T-student statistics; average \pm SEM; n=3; *p value<0.05. (F) Scheme of how end-feet may aggregate at the CP. (G) Immunofluorescent staining showing the Laminin (red) of the basal lamina. Scale bar: 50 μ m. (H) Immunofluorescent staining showing Caspase3 (red) at the VZ and SVZ. Scale bar: 50 μ m.

Regarding the first option, the primary cells affected in an electroporation are aRGCs, which act as scaffold for the radial migration of the newborn cortical neurons. So, modifications that affect the basal processes of aRGCs could have an effect on neuronal migration. To assess the occurrence of alterations on aRGC basal processes, we overexpressed SV2B at E14.5, waited for 24h and examined the aRGCs' basal process and end-feet. Basal processes exhibited a very dramatic increase in the density of varicosities (Fig. 2D and 2E), and their morphology at the basal end-feet was abnormal (Fig. 2D). These end-feet were reminiscent of collapsed axonal growth cones, with a rounded tip that suggested instability of the aRGCs attachment to the basal lamina (Fig. 2D and 2F). The tips of the basal processes are in contact with the basal lamina, so we next investigated the structure of this basal lamina upon SV2B overexpression. To this end we immunostained electroporated samples against Laminin, the main component of the basal lamina. As shown in Figure 2G, the basal lamina was severely disrupted forming aggregates, in contrast to the compact arrangement in control embryos (Fig. 2G).

In addition to all these defects, at the center of the electroporation we observed that the VZ was considerably disrupted (Fig. 2B and 2G). This could be the result of abundant death of aRGCs. To test this possibility we electroporated mouse embryos at

E14.5 and analyzed them at E16.5 by immunostaining with the apoptosis marker activated Caspase 3. We observed a high amount of Casp3⁺ cells, both progenitors and neurons, in the cortex of embryos electroporated with *SV2B*, but not in *Gfp*-electroporated controls (Fig. 2H). Intriguingly, the increased Casp3⁺ cells were not only GFP⁺ (electroporated cells) but also GFP⁻, suggesting the occurrence of a non-cell autonomous effect.

SV2B overexpression disrupts the apical adherens junction belt and the position of aRGCs

Death of aRGCs may result from alterations in the apical adherens junction belt. Analysis of at E16.5 of brains electroporated at E14.5 revealed significant alterations in VZ structure and an apparently disrupted ventricular surface (Fig. 3A and 3B, DAPI). To directly assess the potential disruption of the apical adherens junctions belt, we immunostained electroporated brains with the apical lamina marker Par3. Consistent with our previous observations, Par3 labeling was severely disrupted at the center of the electroporated area, with many cells protruding into the tissue and interrupting the continuity of the apical adherens junction belt (Fig. 3A and 3B). This phenotype remained throughout development and even increased in severity one day later (E17.5; Fig. 3D and 3E). Intriguingly, we observed Par3 staining at basal positions within the cortical parenchyma, where it is absent in normal embryos (Fig. 3B' and 3E'). Par3 is only expressed by aRGCs as part of their attachment to the apical belt, so this aberrant expression of Par3 away from the ventricular surface suggested an alteration on aRGCs themselves (Fig 3C).

To assess this possibility, we examined PAX6 expression in E17.5 embryos electroporated at E14.5 (Fig. 3F and 3G). We found a dramatic increase in PAX6⁺ progenitor cells at basal positions compared to control embryos. Whereas in controls 90% of PAX6⁺ cells were lining the ventricle in a normal and compact VZ, and less than 10% were in SVZ; in *SV2B* embryos only 50% of PAX6⁺ cells were in found VZ, while nearly 40% were in SVZ and even 10% in IZ (Fig. 3H). In this analysis again, we observed that the mislocalized PAX6⁺ cells were both GFP positive and negative, consistent with a strong non-cell autonomous effect of *SV2B* overexpression.

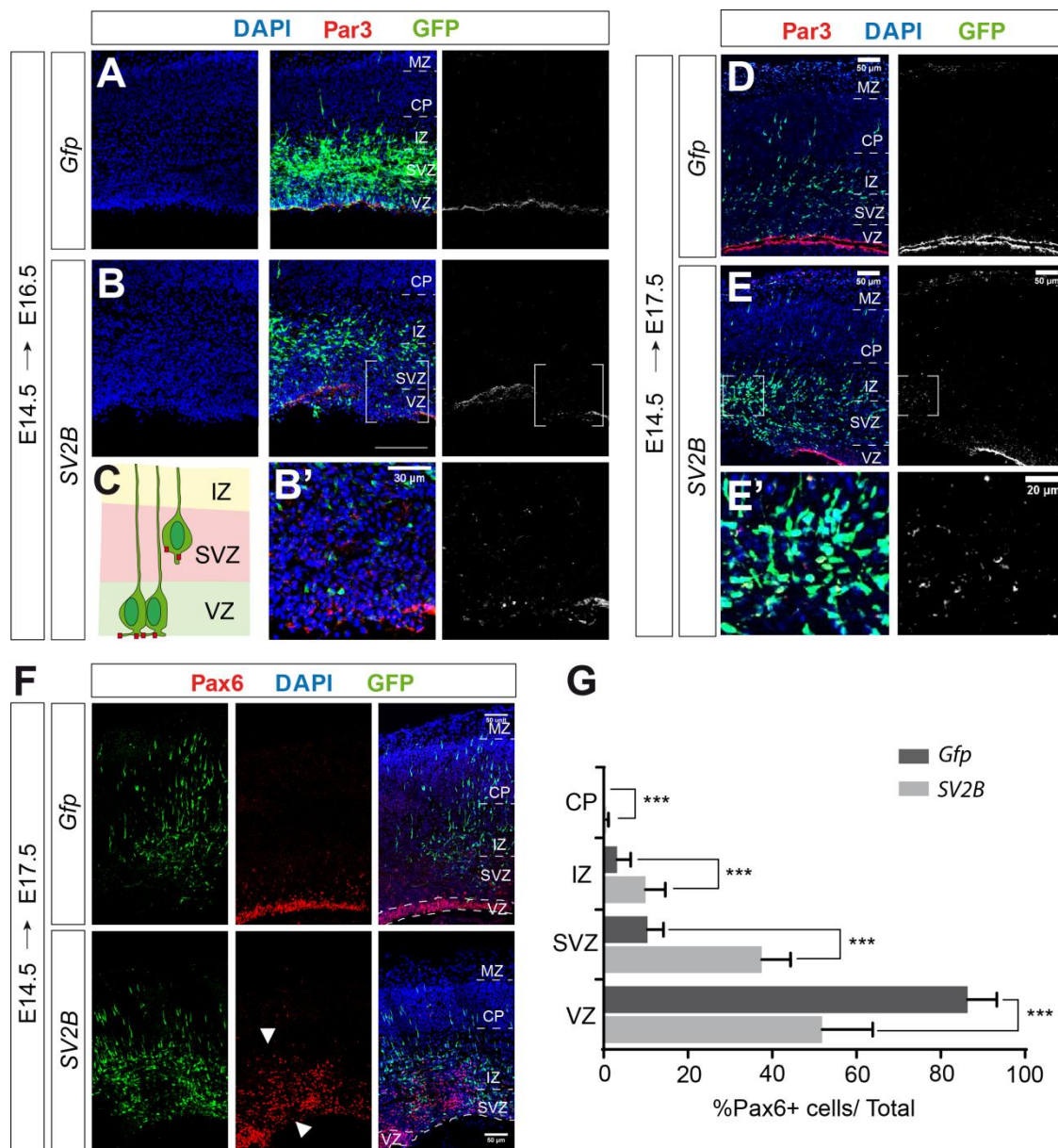


Figure 3. SV2B overexpression phenotype on the apical lamina. E14.5 embryos were *in utero* electroporated with the overexpression plasmid or one encoding *Gfp* as a control. Samples were collected at E16.5 (A-B) or E17.5 (D-G) depending on the experimental design. Immunostainings of 20 μ m coronal cryosections of the electroporated dorsal telencephalon show DAPI (blue) and GFP (green). (A) Immunofluorescent staining showing Par3 (red) of the apical lamina. Scale bar: 100 μ m. Scheme of the delaminated aRGCs maintaining Par3 molecules. Lower panels show high magnifications of the VZ between the brackets at the *SV2B* condition. Scale bar: 30 μ m. (B) Immunofluorescent labeling showing Par3 (red) of the apical lamina. Scale bar: 50 μ m. Lower panels show high magnifications of the VZ between the brackets at the *SV2B* condition. Scale bar: 20 μ m. (C) Differential distribution of the PAX6 positive progenitor cells (red). The long dashed lines limit the tissue, and the arrowheads show the misplaced progenitors. Scale bar: 50 μ m. (D) Quantification of the percentage of the PAX6 positive cells with respect to the total. Data is shown as *Gfp* controls in dark grey and *SV2B* in light grey. Chi-square statistics; average \pm SEM; n=3; ***p value<0.001.

SV2B overexpression alters cell cycle, interkinetic nuclear migration and cell division

Given that SV2B overexpression leads to the basal displacement of Pax6+ aRGCs, we wondered whether these cells were still proliferative. To this aim we electroporated mouse embryos at E14.5, injected BrdU 24hrs later (E15.5), and analyzed the following day (E16.5). BrdU is incorporated during DNA duplication, which occurs at the basal domain of the VZ, and as nuclear marker for cycling cells we used Ki67. We quantified the rate of progenitor cell cycle exit by measuring the number of cells positive for GFP and BrdU but negative for Ki67. Cells that were cycling 24hrs before fixing would incorporate BrdU, and if they are still cycling at E16.5, they will also retain Ki67 labeling (Fig. 4A). On the contrary, cells negative for Ki67 would have exited from the cell cycle. We found that the amount of GFP+/BrdU+/Ki67- cells was nearly half in SV2B-overexpressing embryos compared to controls (Fig 4B and 4C), indicating a very significant decrease in cell cycle exit upon SV2B expression. This result is compatible with a higher cell cycle reentry or with a cell cycle arrest (Borrell et al., 2012) after SV2B overexpression.

Interestingly, the distribution of BrdU+ nuclei was also affected by SV2B overexpression (Fig. 4B and 4D). At a first glance, in the brains injected with BrdU 24hrs before analysis, controls presented a uniform BrdU labeling across the thickness of the VZ, while SV2B-electroporated samples showed a BrdU+ cells absence in the central part of the VZ. After a precise analysis of BrdU+ nuclei dispersion we show that S phase nuclei from the central region accumulate at the apical third of the VZ upon SV2B overexpression (Fig. 4B and 4D). Commonly, such a phenotype might be related to alterations in the translocation of the nuclei during cell cycle: the interkinetic nuclear migration (INM). To determine if SV2B expression was associated with this phenomenon, we analyzed where aRGCs were undergoing S phase of the cell cycle. So we injected BrdU intraperitoneally 30 minutes before fixing at E16.5 (Fig. 4E). As expected, in control embryos BrdU+ nuclei clustered at the basal part of the VZ (Fig. 4F and 4G); in contrast, in SV2B embryos BrdU+ nuclei were distributed all along the VZ and the SVZ (Fig. 4G). This abundance of misplaced cells strongly suggested that INM is aberrant upon SV2B overexpression, altering the location where cells undergo the diverse phases of the cell cycle.

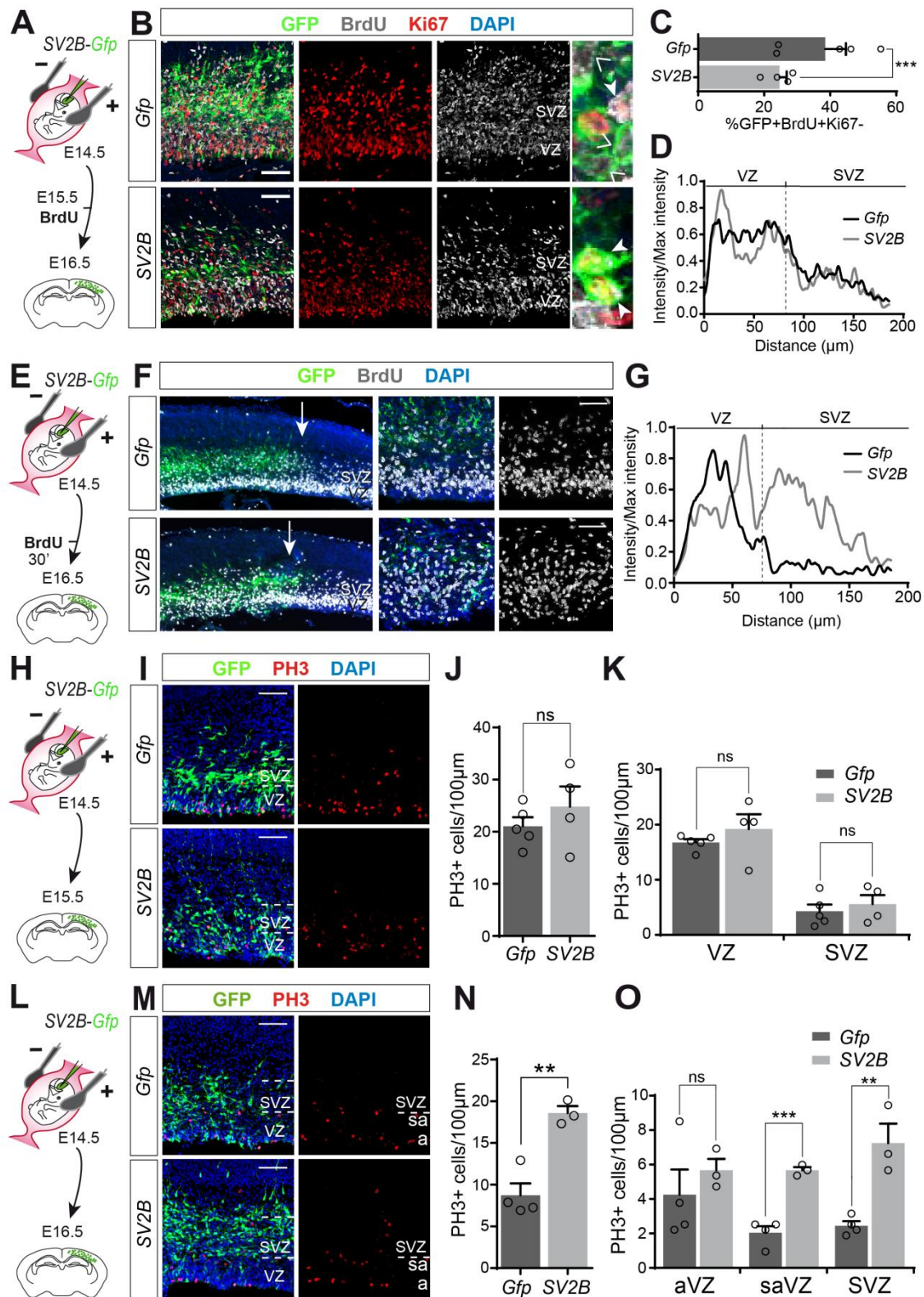


Figure 4. Alterations in proliferation after SV2B overexpression. (A) Cell cycle exit. Schema of the experimental design where E14.5 embryos were *in utero* electroporated with the overexpression plasmid or one encoding *Gfp* as a control. 24hrs later, females were intraperitoneally BrdU injected, and samples were fixed at E16.5. (B, F, I, M) Immunostainings of 20 μ m coronal cryosections of the electroporated dorsal telencephalon showing DAPI (blue) and GFP (green). (B)

Immunofluorescence showing Ki67 positive progenitors (red) and BrdU positive cells (white). Right panels show high magnification of GFP+BrdU+Ki67+ (filled arrowheads) and GFP+BrdU+Ki67- (empty arrowheads). (C) Cell cycle exit rate was quantified as the percentage of GFP+BrdU+Ki67- respect the total GFP+ cells. Data is shown as *Gfp* controls in dark grey and *SV2B* in light grey. Chi-square statistics; average \pm SEM; n=5; ***p value<0.001. (D) Graph showing the intensity ratio of the BrdU positive cells distribution. Distance from the ventricular surface was set as zero. (E) Schema of the experimental design where E14.5 embryos were *in utero* electroporated with the overexpression plasmid or one encoding *Gfp* as a control. Females were intraperitoneally BrdU injected 30 minutes before fixing the embryos at E16.5. (F) Immunofluorescence showing BrdU positive cells (white). Left panels show a low magnification of the electroporation site (white arrows sign the edges). (G) Graph showing the intensity ratio of the BrdU positive cells distribution. Distance from the ventricular surface was set as zero. (H, L) Schema of the experimental design where E14.5 embryos were *in utero* electroporated with the overexpression plasmid or one encoding *Gfp* as control and fixed at E15.5 or E16.5 respectively. (I, M) Immunofluorescence showing PH3 positive cells (red). (J, N) Quantification of total PH3 positive cells per 100 μ m of the ventricular surface. (K, O) Quantification of PH3 positive cells per 100 μ m of ventricular surface in each layer. Mitosis at the VZ was divided into apical (aVZ, nucleus lining the ventricle) or subapical (saVZ). Data is shown as *Gfp* controls in dark grey and *SV2B* in light grey. T-student statistics; average \pm SEM; n=5 *Gfp* n=4 *SV2B*; **p value<0.01, ***p value<0.001. Scale bar 50 μ m

If the above hypothesis was correct, we might expect also the mispositioning of cells at mitosis. In fact, taking also into account the decrease in cell cycle exit, dividing cells might be not just misplaced but also in higher amount. To test these possibilities we analyzed the abundance and location of mitotic cells after electroporation at E14.5 (Fig. 4H). Immunostainings against phosphohistone H3 (PH3) revealed a slight but not significant increment in the abundance of apical nor basal mitoses at E15.5 (Fig. 4I to 4K). However, in *SV2B*-electroporated embryos PH3+ mitoses occurred at more basal positions than in controls, in both VZ and SVZ, such that the neat string of apical mitoses was not visible in *SV2B* embryos (Fig. 4I to 4K). Given that the effects of *SV2B* expression seemed to always increase in severity over time, we decided to repeat this analysis at E16.5 after electroporation at E14.5 (Fig. 4L). The amount of progenitors dividing at E16.5 was lower compared to earlier stages, but the mitotic nuclei lining the ventricular surface was still obvious in controls (Fig. 4M). After two days of *SV2B* overexpression, PH3+ mitoses were not aligned apically anymore, and the density of total PH3+ nuclei was double than controls (Fig. 4N). Considering the

location of mitoses, SV2B did not affect the density of apical mitoses, but it increased very significantly subapical (in VZ) and basal (SVZ) mitoses (Fig. 4O). Thus, overexpression of SV2B induces a decrease in cell cycle exit accompanied by an increase in dividing cells, namely at basal positions, and an abnormal INM. These results are compatible again with a cell cycle arrest at M-phase or with a cell cycle reentry increasing the number of dividing cells.

SV2B+ vesicles are highly motile along the apical process

Once we identified several effects caused by SV2B overexpression, we next wanted to investigate what is the mechanism of action of this protein. Remarkably, nothing is known about the subcellular localization or dynamics of *Sv2b*, especially in progenitor cells. SV2B is a protein associated to vesicles and thought to participate in vesicular trafficking (exo- or endocytosis), thus in a wide variety of functions from attachment to communication. To gain insights into the mode of action of SV2B in cortical progenitors, we first aimed at defining the intracellular dynamics and behavior of SV2B+ vesicles. This should provide us a fundamental entry point to understand its biological function in aRGCs, and if/how SV2B+ vesicles dynamics may be critical for aRGCs function in cortex development. First, we designed and generated a plasmid encoding human SV2B plus GFP as fusion protein, expressed only upon Cre recombination, such that we would obtain labeling of aRGCs at a very low density. The hSV2B:GFP expression cassette was designed followed by a T2A linker and the far-red fluorescent reporter protein mKate, expressed in equimolarity with SV2B (Fig. 5A).

In order to monitor the trafficking of SV2B+ vesicles, we delivered our expression plasmids into the developing cortex of E15.5 wild type embryos by *in utero* electroporation. After 24hrs, GFP+ cells in brain slices were recorded under a Spinning disk microscopy. This enabled us to examine individual processes of electroporated aRGCs at high resolution and high speed while monitoring individual SV2B+ vesicles (Fig. 5B and 5C). We first observed that these vesicles mainly accumulated at the varicosities and end-feet of aRGC radial processes (Fig. 5D). Dynamically, we were able to identify abundant bidirectional traffic of SV2B:GFP vesicles through the cell body of aRGCs, their basal and apical processes (including their varicosities), and end-feet (Fig. 5D). SV2B:GFP+ vesicles showed wide variable

dynamics. Some vesicles were seen travelling along the processes, some did not move, and others moved circularly within the varicosities or the cell soma.

A detailed analysis of their dynamics revealed that in the apical process 51% of vesicles followed an apical direction (to the ventricular surface), 47% a basal direction (to the soma of the cell) and 2% of them stayed immobile during the short recording (Fig. 5E). On the other hand, at the basal process 55% of vesicles followed an apical direction (to the cell soma), 44% a basal direction (to the basal end-feet) and 1% were immobile. Thus, although vesicles travelled in both directions, there was a slight tendency to move towards the apical side of the cell: the cell soma and apical end-foot. We also observed that this traffic seemed to be more active in the apical than the basal process (Fig. 5F). Around 70% of SV2B+ vesicles at the basal process moved at less than 1 $\mu\text{m/s}$, while almost 80% of the vesicles at the apical process moved between 1 and 3 $\mu\text{m/s}$ (Fig. 5G). This impacted on the average speed of vesicles, which was significantly faster in the apical process (2 $\mu\text{m/s}$) than in the basal process (about 1 $\mu\text{m/s}$; Fig. 5F). Concomitantly, we found that the vast majority of vesicles in the basal process traveled shorter net distances (5 μm) than those in the apical process (about 10 μm ; Fig. 5H and I). Finally, we also determined the straightness of the displacement of vesicles (ratio between net displacement and length travelled). According to this ratio, the closer to 1 the more straight or direct is the displacement. In general, the movement of SV2B vesicles was quite vibrational, and nearly 60-70% of the apical and basal vesicles respectively showed a straightness of equal or less than 0.2. This means that the majority of vesicles diverted and jittered long ways before arriving to their final location. Nevertheless, vesicles in the apical process presented a higher average straightness than those in the basal process, with 35% of apical vesicles exhibiting a ratio between 0.2 and 0.6, in contrast to the 20% present at the basal processes (Fig. 5J and 5K). Finally, we determined that neither the speed nor straightness varied depending on the direction of vesicles (apically- or basally-directed), but on the cell process where they were located.

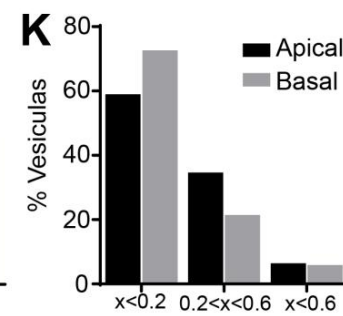
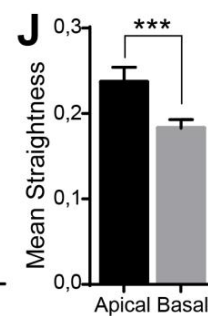
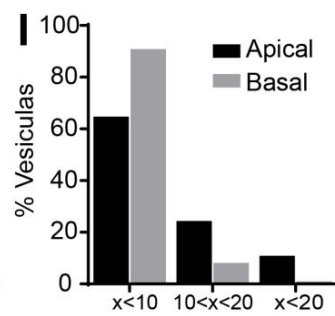
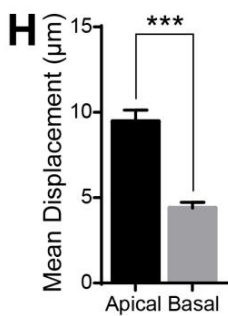
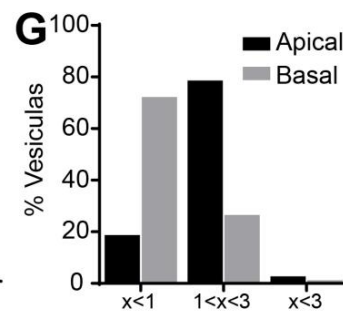
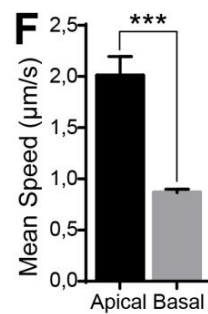
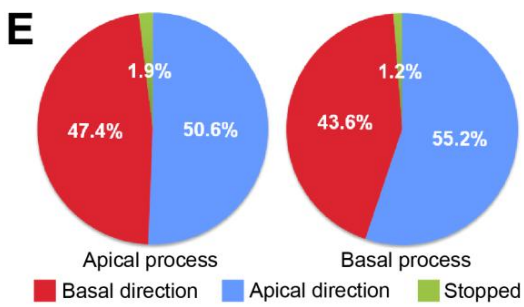
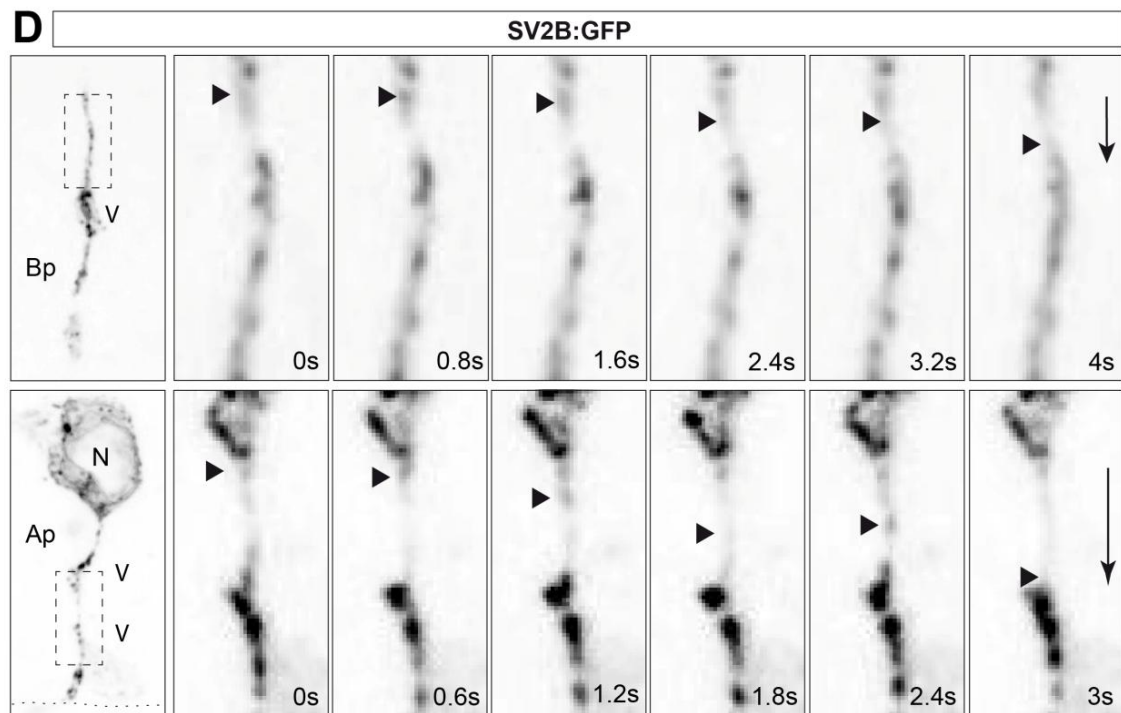
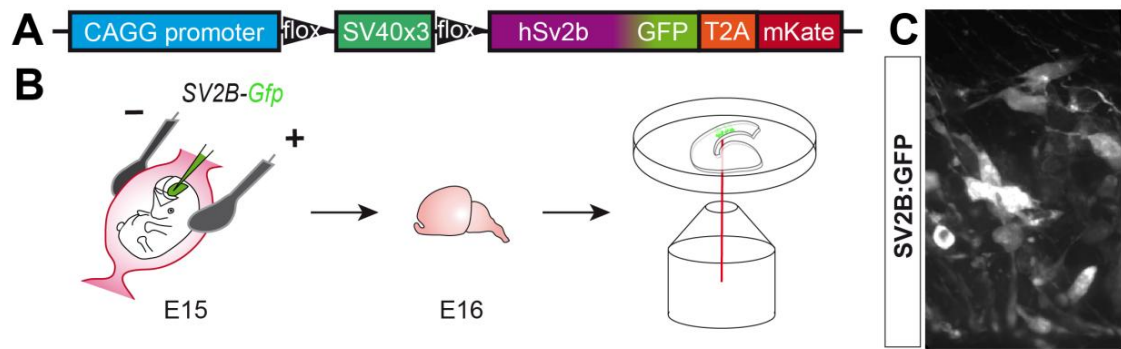


Figure 5. SV2B subcellular dynamics in mice aRGCs. (A) Scheme of SV2B:GFP fusion protein expression plasmid. After the CAG promoter, three SV40 on tandem are flanked by flox sequences. An equimolar expression of the fluorescent protein mKate is allowed by a T2A sequence. (B) E15 embryos were *in utero* electroporated with the fusion protein plasmid. After 24hrs, the brains were sliced and single processes recorded in an inverted spinning disc microscope 100x objective. (C) Representative electroporated slice showing SV2B:GFP in white. (D) Basal and apical process stack. Time-lapse of the area inside the dashed lines. Arrowheads point a single vesicle through time. The arrows show the complete displacement. Ap: apical process, Bp: basal process, V: varicosity, N: nucleus. (E) Graphs showing the proportion of the vesicles stopped or following an apical or basal direction. (F) Quantification of the vesicles average speed along the apical or basal process. (G) Quantification of the vesicles average displacement along the apical or basal process. (H) Quantification of the vesicles average straightness along the apical or basal process. Data is shown as apical processes in black and basal processes in light grey. Chi-square statistics; average \pm SEM; vesicles n=156 apical n=407 basal; animals n=5 n=7 basal; ***p value<0.001.

SV2B overexpression leads to a bulge formation

Previous studies show that increased proliferation can lead to the production of folds in lissencephalic brains (Florio et al., 2015; Stahl et al., 2013). Subsequent to the observed alterations in SV2B expressing progenitor cells, we wondered whether the gross organization of the cerebral cortex would be affected upon long-term SV2B overexpression. To test this notion we *in utero* electroporated the overexpression plasmid in mouse embryos at E14.5 and waited until postnatal day 5 (P5) (Fig. 6A). Electroporated neurons arrived to their final position at the CP in controls and experimental samples. However, in SV2B overexpressing embryos we observed the existence of a fold-like bulge (n=5/5 pups), while no distinguishable alterations were detected in *Gfp* controls (n=4 pups). The cortical “fold” showed the marginal zone (MZ) folded onto itself (Fig. 6B).

At E14.5 neurons for layer 2/3 are being generated. These neurons become positive for CUX1, as shown in the control animals. Green cells in SV2B-electroporated animals were also positive for CUX1 (Fig. 6B), suggesting that the alterations in cell cycle and positioning of progenitor cells did not affect the fate of the neuronal progeny. Interestingly, the cortical fold was also composed of CUX1+ layer 2/3 neurons. In fact, this included not just electroporated cells, but neighboring cells were also dragged into it, again implying a non-cell autonomous effect of SV2B expression on cortex folding.

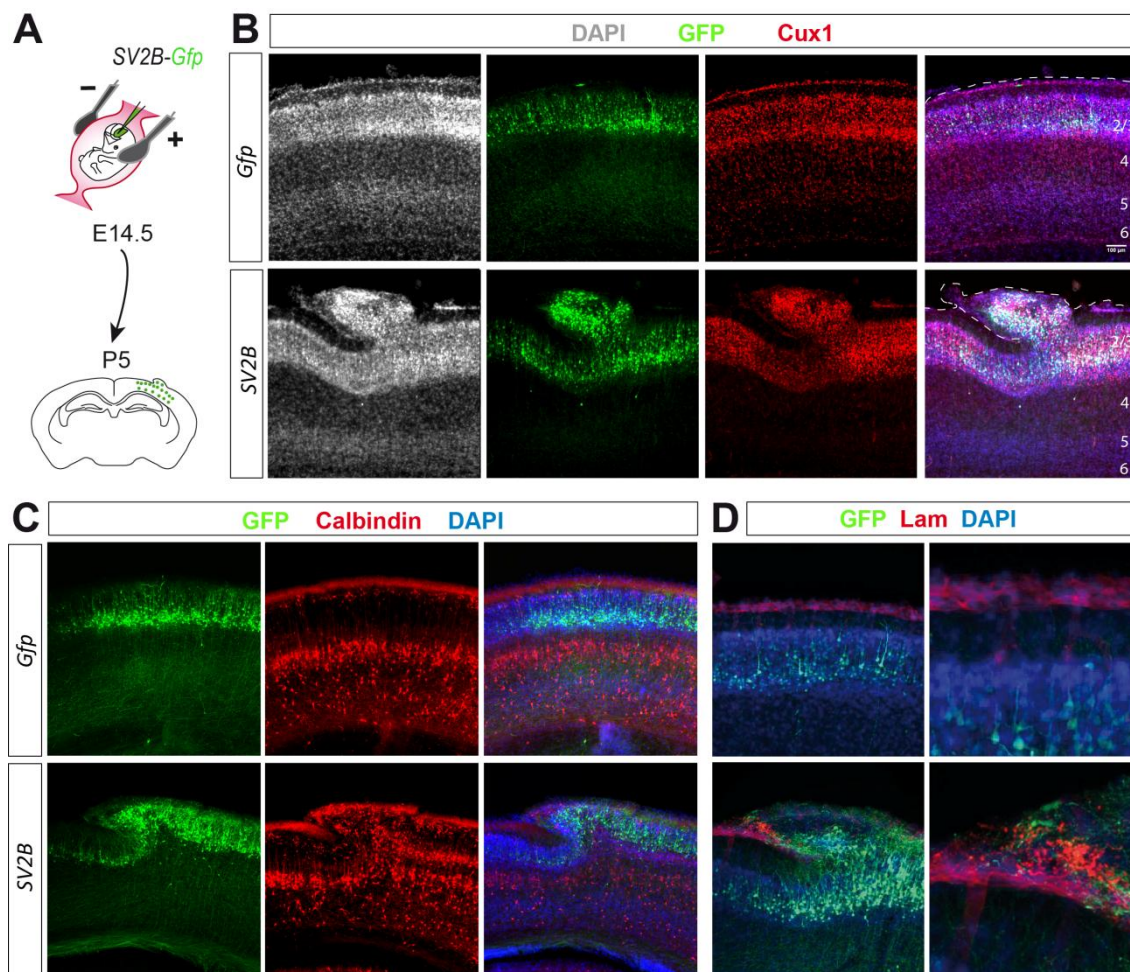


Figure 6. SV2B overexpression induces a bulge formation. E14.5 embryos were *in utero* electroporated with the overexpression plasmid or one encoding Gfp as a control. Samples were collected at P5. (A, B, C) Immunostainings of 50µm coronal cryosections of the electroporated dorsal telencephalon showing DAPI (blue), GFP (green) and Cux1 (A), Calbindin (B) or Laminin (D) in red. Scale bar: 100µm. The dashed line shows the apical limit of the tissue.

To further delve into the scope of this phenotype, we performed immunostainings against Calbindin as a marker of cortical inhibitory interneurons. Even though these cells are generated far away from the electroporation site, in the ganglionic eminences, they were also dragged into the fold (Fig. 6C). Because SV2B expression leads to the disruption of the basal lamina at E17.5, we next examined this structure at P5 by anti-laminin labeling. This central component of the basal lamina was homogeneously lining the MZ in control embryos, as expected, but in SV2B electroporated embryos it was highly disrupted around the cortical fold. Laminin was found forming aggregates or nearly absent from the basal lamina (Fig. 6D). Hence, formation of this cortical fold

seems to be a consequence of neuronal overmigration, apparently due to the severe perturbation of the basal lamina upon overexpression of SV2B by aRGCs.

Part 2. *Sv2b* is expressed in ferret germinal layers and its genetic modification in ferret leads to alterations in progenitor cell proliferation

***Sv2a* and *Sv2b* are highly expressed in germinal layers of the developing ferret cortex**

Previous studies showed that changes in gene expression of aRGCs at the VZ regulate their dynamics of proliferation and generation of basal progenitor cells (Martinez-Martinez et al., 2016). In ferret, there is a critical period for massive bRGCs production between E34 and E36, when aRGCs at the VZ undergo self-consuming divisions to give rise to bRGCs massively (Fig 7A). One gene whose expression levels in the ferret VZ followed the same dynamics as aRGC production is *Sv2b*. In particular, *Sv2b* is highly expressed at early stages (E30) and it is downregulated 3.65-fold by E34. Later on, *Sv2b* is upregulated again 2-fold at birth (Fig. 7B). Interestingly, during the critical period, the expression of *Sv2b* is higher at the SVZ, where the bRGCs are placed, compared to the VZ by more than 3.5-fold (Fig. 7C).

In order to elucidate the endogenous function of SV2B in the developing ferret cerebral cortex, we initially confirmed the expression of *Sv2b* in the germinal layers of the ferret cerebral cortex. As a first approach, we designed and produced specific RNA probes against ferret *Sv2b* and *Sv2a* and performed *in situ* hybridizations in ferret tissue. *Sv2b* mRNA was detectable in cortical germinal layers at all stages examined (Fig. 7D). At E30, *Sv2b* was expressed at high density in the VZ and in a salt and pepper pattern in the rest of the cortex. Expression was higher in the gyrus than the sulcus. At later stages of development, *Sv2b* was expressed in new layers as these gradually emerged. At E34, *Sv2b* mRNA was detected at the CP but not in the intermediate zone (IZ; Fig. 7D). *Sv2b* was also expressed in VZ and ISVZ, and to a lesser extent in the nascent OSVZ. In the splenial gyrus, expression at the VZ was lower than at the SVZ, confirming published data (Fig. 7C). At this stage, there were also obvious differences between gyrus and sulcus. At birth, levels of *Sv2b* expression were similar between VZ, ISVZ and OSVZ. By P2, VZ and ISVZ increased *Sv2b* expression compared to the OSVZ, and in agreement with published RNAseq data (De Juan Romero et al., 2015), expression at the OSVZ was significantly higher in the splenial gyrus than the lateral sulcus (Fig. 7D and 7E).

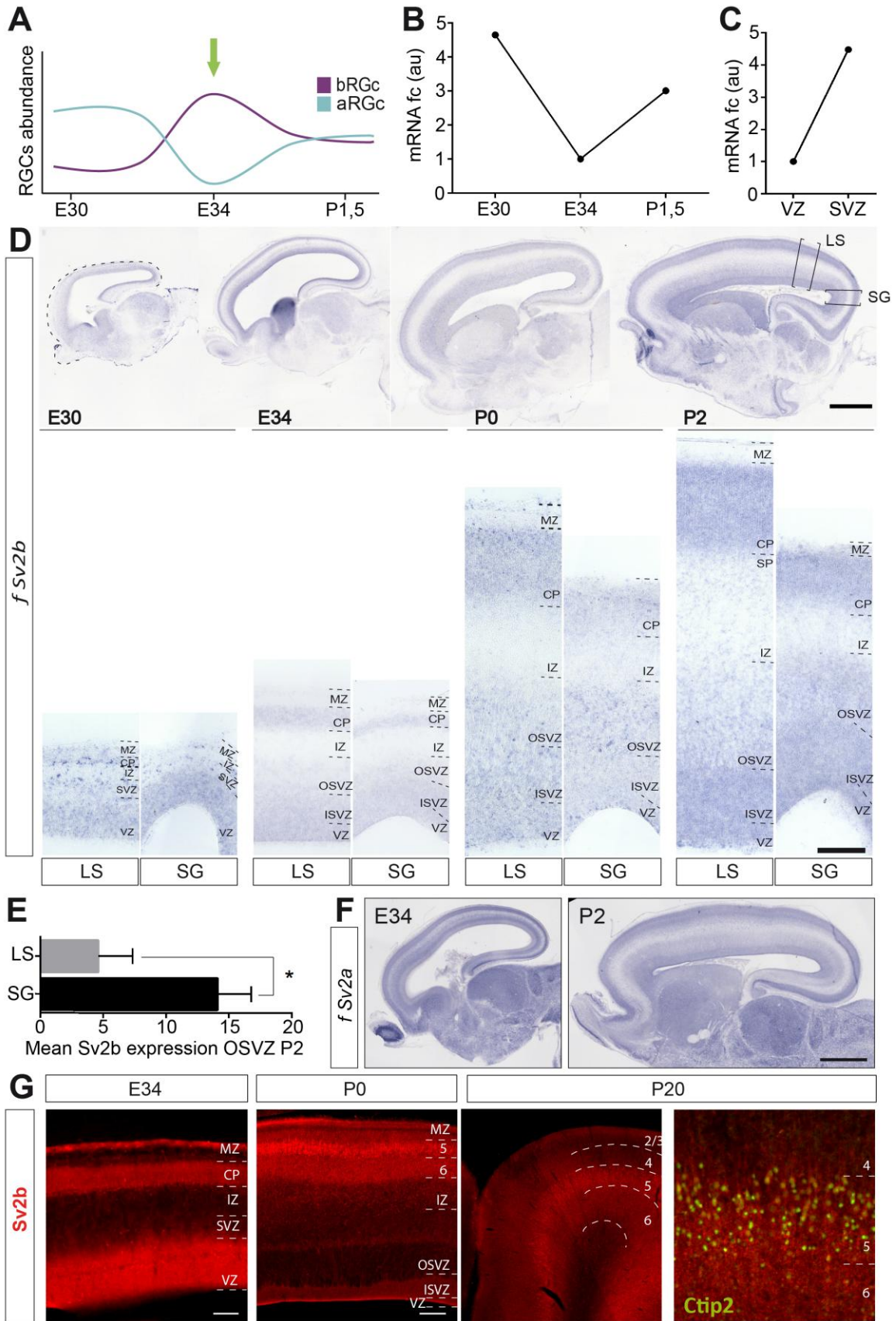


Figure 7. *Sv2b* endogenous expression characterization in ferret. (A) Schema of the bRGCs generation and aRGCs dynamics at the critical period in ferret embryonic development. (B) Microarray data from Martínez-Martínez *et al.*, 2016. *Sv2b* fold change at different stages. (C) Microarray data at E34 of *Sv2b* expression in VZ and SVZ. (D) *In situ* hybridization of *Sv2b* ferret gene on sagittal sections of ferret tissue at E30, E34, P0 and P2. Lower panels show high magnifications of sulci and gyri for each stage. (E) RNAseq analysis for *Sv2b* from OSVZ at P2. T-student statistics; average \pm SEM; n=3; * p value < 0.05. (F) *In situ* hybridization of *Sv2a* ferret gene on sagittal sections of ferret WT tissue at E34 and P2. (G) Immunostainings against SV2B on WT ferret tissue at different stages (E34, P0 and P20). Right panel shows a high magnification of layer V neurons co-labelled with CTIP2. Scale bars: 1000 μ m (D upper panels and F); 100 μ m (D lower panels).

Analysis of *Sv2a* mRNA expression revealed that in ferret, similar to mouse, this is more ubiquitously expressed than *Sv2b*. *Sv2a* was found highly expressed throughout the brain at embryonic and postnatal stages. Similar to ferret *Sv2b*, and in contrast to mouse, ferret *Sv2a* was expressed in all germinal layers (Fig. 7F). In agreement with published transcriptomic data (Martínez-Martínez *et al.*, 2016), expression levels at the VZ were not significantly different during development (data not shown).

Taking into account the similarities observed in levels and areas of expression, it seemed possible that *Sv2a* and *Sv2b* might serve redundant functions in the developing ferret cortex. Nevertheless, *Sv2b* has shown a unique expression regulation at the VZ in the developing ferret cortex. Consequently, a complete redundant function on this area and time period seems improbable. Moreover, analysis of Uniprot data showed us that ferret SV2A and SV2B proteins have a 59% of sequence alignment, similar to human (64%) and rodents results (65%). On the other hand, SV2B is highly conserved between species, with 90 or 95% of protein sequence similarity between human and ferret or mouse, respectively (Uniprot data). Thus, SV2 proteins remain similar between species but have diverge between isoforms and a divergence also in function seems likely.

Next, we wanted to determine the pattern of SV2B protein expression. To this aim we performed immunofluorescence using a specific anti-SV2B antibody at different ferret stages. Overall, the patterns of protein immunostain at E34 and P0 were similar to those for mRNA, with high expression levels at the VZ and CP. In the mature cortex (P20), SV2B was highly expressed by layer V neurons, which co-expressed CTIP2, a marker of deep layer neurons (Fig. 7G).

Subcellular characterization of SV2B in ferret

Once we have addressed the general features of *Sv2b* expression in the developing ferret telencephalon, and found that it is highly and variably expressed in germinal zones, we next investigated the subcellular distribution of this vesicle-associated protein. To directly observe SV2B distribution in ferret cells, we first performed primary cell cultures from newborn (P0) ferret cerebral cortex (Fig. 8A), an age when *Sv2b* expression is again high after the critical period of bRGC generation. Dots resembling vesicles positive for SV2B were nicely identified along the entire extent of cultured cells. Interestingly, the pattern of subcellular distribution was different between postmitotic neurons (labeled with the neuronal marker Tuj1, negative for Vimentin) and progenitor cells (negative for Tuj1, positive for Vimentin). In neurons, SV2B accumulated significantly at the tips of growing processes, and much less in the cell body (Fig. 8B-B'), while in progenitor cells the highest concentration of SV2B+ dots was perinuclear (Fig. 8C-C'). The precise subcellular localization of SV2B+ vesicles may be an essential feature of this protein's function. To gain further insight into this aspect, we quantified the amount of SV2B protein overlapping with the Golgi apparatus within the soma, identified with the marker GRASP65. The degree of co-localization of SV2B with Golgi apparatus was significantly different between neurons and progenitor cells. In progenitor cells only about 30% of SV2B overlapped with the Golgi apparatus, and hence most of this protein was elsewhere in the cell. In neurons, the proportion of SV2B found in the Golgi apparatus was much higher, almost 50%. In summary, our observations indicated that in neuronal cells much of SV2B associates with the Golgi apparatus, but most of the rest of it targeted to the tips of growing processes (axon or dendrites). In progenitor cells, SV2B seems to be more somatic, but less associated to Golgi apparatus. Thus, an interpretation of these findings could be that much of SV2B protein in neurons localizes at the vesicle production machinery, whereas in progenitor cells it is quickly carried out of the Golgi apparatus to exert some, yet undefined, cellular function nearby the nucleus (Fig. 8D-E).

Whereas the analysis of dissociated cells enables a high level of subcellular resolution, we wondered to what extent our observations really recapitulated the situation *in vivo*. So we next set to determine the pattern of endogenous SV2B protein subcellular localization in aRGCs of the developing ferret cortex. To identify individual aRGCs and their processes, we electroporated GFP-encoding plasmids into the VZ of

newborn ferrets, and then stained the transduced tissue with anti-SV2B antibodies. We observed that ferret aRGCs contain a high abundance of SV2B+ punta resembling vesicles, and that these were preferentially accumulated at the cell soma, at the varicosities and at the end-feet of the apical and basal processes (Fig. 8F). This distribution was highly reminiscent of that in mouse aRGCs upon overexpression of SV2B, where SV2B+ vesicles were at high density in varicosities, end-feet and around the nucleus (Fig. 5), and also where SV2B overexpression altered the density of varicosities at the basal process (Fig. 2).

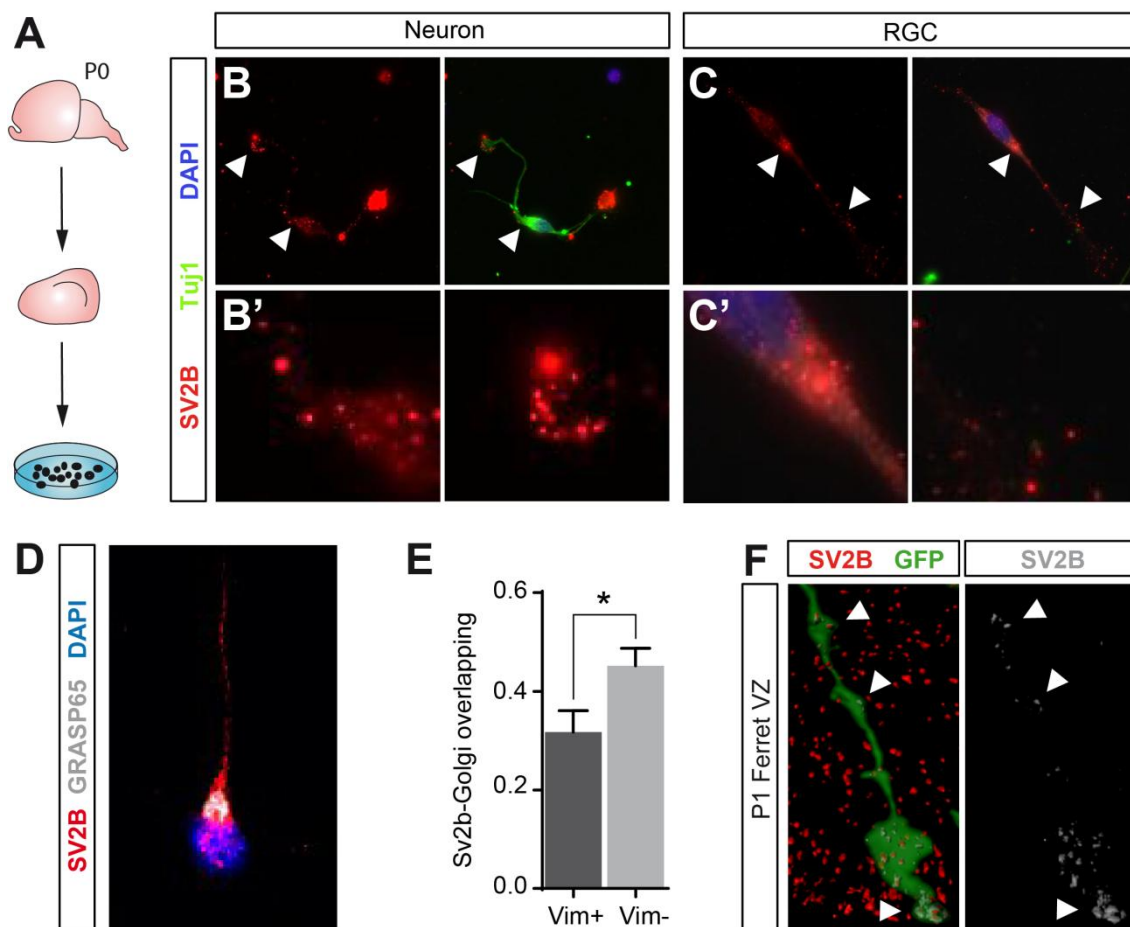


Figure 8. Subcellular characterization of SV2B in ferret. (A) Schema of the experimental design. P0 ferret brains were dissected and plated for 36hrs. (B-C) Immunofluorescence show DAPI (blue), Tuj1 (green) and SV2B (red). Left panels show high magnifications of the nucleus and end-feet. (D) Immunofluorescence on dissociated cells shows DAPI (blue), GRASP65 (white) and SV2B (red). (E) Quantification of the SV2B-GRASP65 (Golgi marker) overlapping. T-student. Average \pm SEM, n=20 per condition, *p value<0.05. (F) Immunofluorescence on P1 fixed tissue shows an aRGC positive for GFP (green) and SV2B (red). SV2B inside GFP positive cell is labelled in white. Arrowheads point the vesicle accumulations.

In conclusion, we found that endogenous *Sv2b* expression in gyrencephalic species like ferret is abundant at germinal layers but also dynamically regulated, in contrast to lissencephalic species like mouse. Furthermore, overexpression of SV2B in mouse aRGCs mimics the subcellular distribution in these cells in ferret.

SV2B overexpression in ferret reduces neural production and regular migration

Once we understood the endogenous patterns of SV2B expression, our next aim focused on experimentally modulate its expression levels and investigate potential effects on progenitor proliferation or fate. We injected a *SV2B*-encoding retrovirus into the telencephalic ventricle of E34 ferrets and analyzed them at E36 (Fig. 9A). With this strategy, we aimed to directly see the early output of the overexpressing progenitors at the precise moment where the endogenous expression shows to be downregulated. In *SV2B*-overexpressing animals, GFP positive cells were mainly found in the VZ, while more than half of GFP+ cells in control animals moved away to basal positions in the SVZ (Fig. 9B and 9C). More importantly, the fate of this cellular progeny was also altered by SV2B. Whereas in controls nearly 50% of GFP+ cells were NeuroD2+, (a early neuronal marker, revealing a differentiated fate), most *SV2B*-overexpressing cells were PAX6+ and merely a 4% of the GFP+ cells were NeuroD2 + (Fig. 9D and 9E).

In order to determine the long-term effects of SV2B overexpression at the population level, we electroporated ferret embryos at E32, prior to the endogenous downregulation of *Sv2b* expression at the critical period (Fig. 7B). This allowed us to bypass the downregulation of *Sv2b* at the critical period and induce a sustained expression throughout development. Embryos were analyzed at E41, one day before birth, to allow the migration of the electroporated progeny (Fig. 9F). Sustained expression of *SV2B* induced a delay in radial migration, with an abnormal higher proportion of GFP+ positive cells remaining in the lower cortical layers, especially the ISVZ and IZ (Fig. 9G and 9H). These delayed cells showed a polarized migratory morphology with a leading process following aRGCs scaffold (Fig. 9G, high magnification). This kind of alteration in migration was similar to the observed in mice upon SV2B overexpression (Fig. 2B and 2C). However, contrary to what we found in mice, the ventricular surface of ferret embryos was not disrupted, and no aRGCs appeared to be displaced into cortical parenchyma (Fig 2C and 9G).

A change in the laminar position of cortical neurons might be due to a disruption on the migratory process itself, or a consequence of alterations in progenitor cell proliferation and neurogenesis. Taking into account the alterations we previously observed in mouse cortical progenitors, we decided to analyze if the location and distribution of progenitor cells were affected by the SV2B overexpression. Interestingly, the percentage of GFP⁺ and PAX6⁺ cells increased significantly in ferret embryos upon SV2B overexpression compared to controls (Fig. 9I). Concomitantly, the proportion of neurons generated after electroporation was reduced by 10% (Fig. 9J). Thus, the alteration on GFP⁺ cells by SV2B overexpression in ferret embryos was caused by an increased progenitor cell production coupled to a reduced neurogenesis. Normally, at E34 aRGCs undergo self-consuming divisions to massively produce bRGCs for the OSVZ, at the time when *Sv2b* is downregulated. With this experiment we bypassed this critical period of *Sv2b* downregulation, which induced progenitor cells to give rise to PAX6⁺ aRGCs in VZ or ISVZ, as hypothesized. These outcomes imply that SV2B expression drives progenitors into a state where they reduce neuron production favoring progenitor self-renewal. Although this hypothesis would be the most probable explanation, we cannot discard that the reduction on neuron generation was due to a cell cycle arrest upon SV2B overexpression.

We have previously demonstrated that *Sv2b* is upregulated at postnatal stages, parallel to the reduction in bRGCs production by aRGCs in the VZ. When we upregulated *Sv2b* expression at even higher levels, by means of electroporation at P1, at P6, we found a significant reduction in the proportion of cells arriving at basal positions (Fig. 9K,L). More importantly, increased SV2B specifically reduced the amount of progenitor cells in the OSVZ (Fig. 9M). Concomitantly, GFP⁺ and GFP⁺PAX6⁺ cells increased at the VZ, with no changes in ISVZ (Fig. 9L and 9M), as predicted by our original hypothesis.

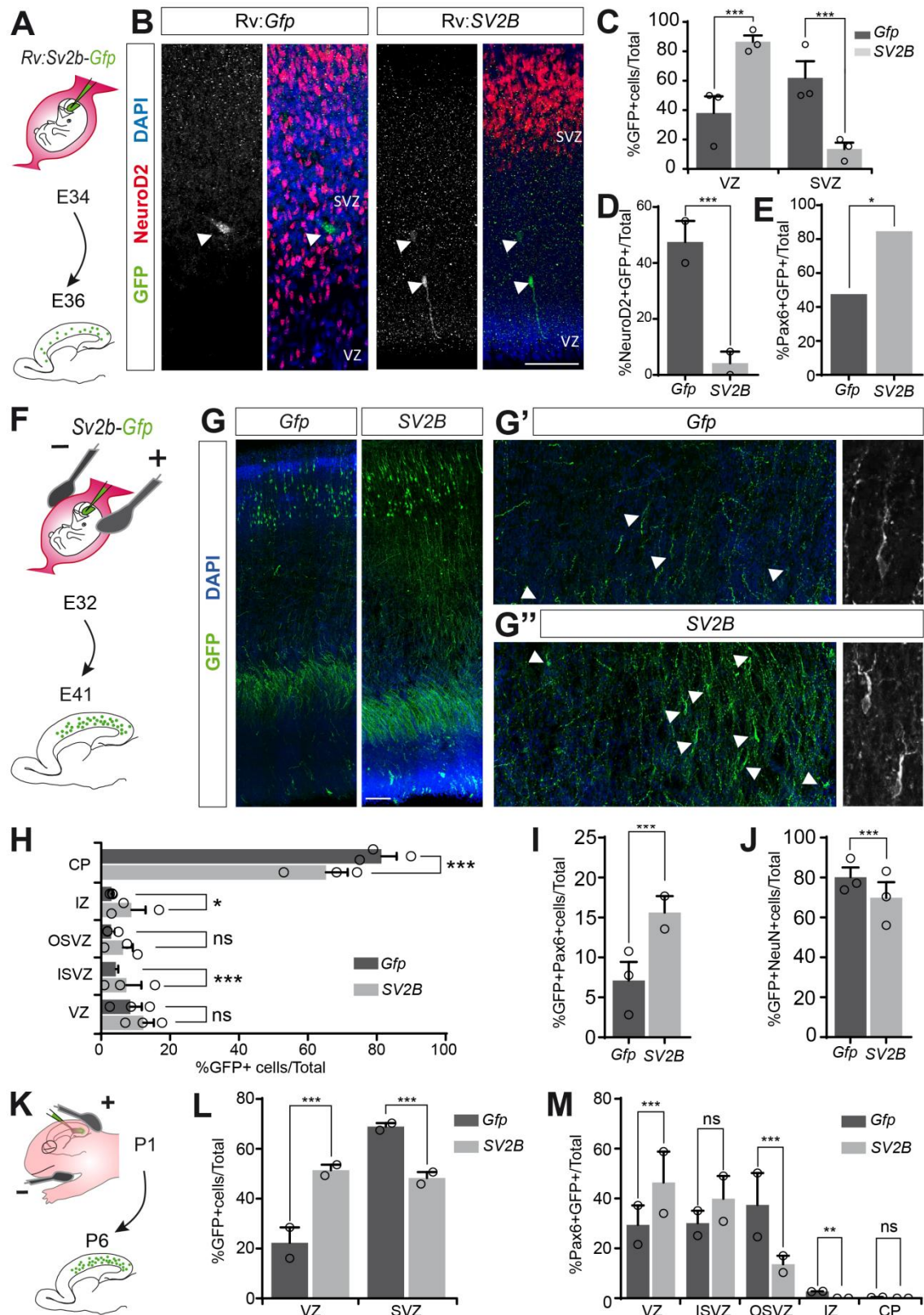


Figure 9. SV2B overexpression in ferret. (A) Scheme showing a retroviral injection in a ferret embryo at E34 with a retroviral overexpression plasmid and fixed two days later at E36. (B) Immunofluorescence showing DAPI (blue), GFP (green or white) and NeuroD2 (red). White arrowheads show the clonal cells. Scale bar: 50 μ m. (C) Quantification of the GFP positive cells among the total. (D) Quantification of the

proportion of GFP and NeuroD2 positive cells respect the total GFP cells. (E) Quantification of the percentage of GFP and PAX6 positive cells respect the total electroporated cells. (F) Scheme showing electroporation of a ferret embryo at E32 with the overexpression plasmid and fixed at E41. (G) Immunofluorescence showing DAPI (blue) and GFP (green). High magnification of the migrating neurons upon *Gfp* control condition (G') or *SV2B* overexpression (G''). Right panel shows an example of migrating neuron morphology. White arrowheads show the migrating neurons at the IZ. Scale bar: 100 μ m. (H) Quantification of the proportion of electroporated cells along the cortex. (I) Quantification of the percentage of GFP and PAX6 double positive cells respect the total electroporated cells. (J) Quantification of the percentage of GFP and NeuN double positive cells respect the total electroporated cells. (K) Scheme showing electroporation of a postnatal P1 ferret with the overexpression plasmid and fixed at P6. (L) Quantification of the proportion of electroporated cells at germinal layers. (M) Quantification of the percentage of GFP and PAX6 positive cells respect the total electroporated cells. Data is shown as *Gfp* controls in dark grey and *SV2B* in light grey. Chi-square statistics. Average \pm SEM; n=3 (C, D, E, H), n=2 (I, L, M), n=1 (J) each condition; ***p value<0.001, ns=not significant.

SV2B ablation in ferrets induces an increase in basal mitosis

To better understand the role of SV2B in ferret progenitor cells, we next ablated its expression from the aRGCs using specific CRISPR guides against the first exon of the ferret *Sv2b* locus. We used two different guides that were close to each other but in opposite DNA chains, to favor the genetic disruption. Both guides were cloned into a plasmid encoding for all the CRISPR machinery, including the gRNA scaffold, Cas9 and GFP as a reporter of transduced cells (Fig. 10A and 10B). To validate if we were ablating specifically *Sv2b* from ferret cells we transfected this plasmid into Mpf cells and collect total protein samples after 48h of expression. We performed a western blot against SV2B protein, normalized by the amount of Tubulin protein. The total endogenous SV2B protein was reduced one third compared to the control (Fig. 10C). Once the CRISPR guides were validated, the same plasmid was electroporated into the telencephalic ventricle of E36 ferret embryos to target aRGCs to avoid endogenous *Sv2b* expression upregulation after the critical period at E34. Embryos were analyzed two days later (Fig. 10D). We quantified the distribution of PAX6+ cells to determine if the generation of bRGCs had changed. Upon *Sv2b* loss-of-function, the proportion of GFP cells in germinal layers positive for PAX6 increased significantly compared to

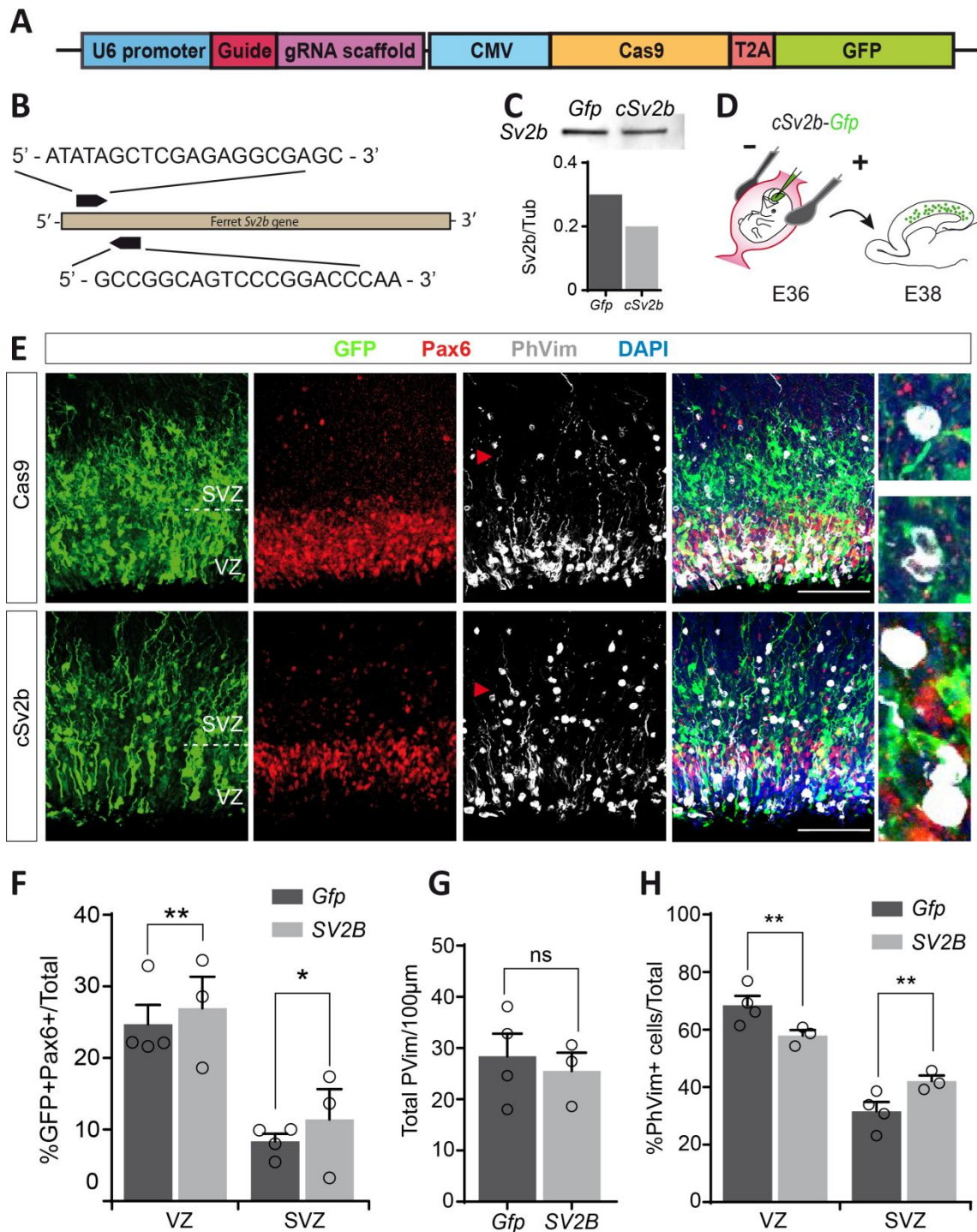


Figure 10. CRISPR for *Sv2b* on ferret phenotype characterization. (A) Scheme of the CRISPR guides Cas9 expression plasmid. This plasmid encodes the guides followed by gRNA scaffold. It also encodes for Cas9 and GFP as a fluorescence protein. (B) *Sv2b* CRISPR guides sequences against ferret *Sv2b* first exon. The scheme shows where these sequences would anneal in *Sv2b* gene. (C) Western Blot against SV2B of Mpf cells overexpressing CRISPR guides. It is plotted the amount of SV2B endogenous protein normalized by the amount of Tubulin protein. (D) CRISPR guides and Cas9 were in

utero electroporated into ferret embryos at E36 and fixed at E38. **(E)** Immunofluorescence showing DAPI (blue), GFP (green), PAX6 (red) and PhVim (white). Right panels show high magnification of the electroporation site (red arrowheads show the misplaced mitotic cells). Scale bar 100 μ m. **(F)** Quantifications of the proportion of GFP and PAX6 positive cells from the total GFP positive cells. **(G)** Quantification of the total number of phospho-Vimentin positive cells per 100 μ m **(H)** Quantification of the percentage of phospho-Vimentin positive cells at the VZ or SVZ respect the total phospho-Vimentin cells. Data is shown as *Gfp* controls in dark grey and *SV2B* in light grey. Chi-square statistics. Average \pm SEM; *Gfp* n=4 *SV2B* n=3 each condition; *p_value<0.05, **p_value<0.01.

controls (Fig. 10E and 10F). Hence, the absence of SV2B after the critical period increases the production of RGC progenitors. Importantly, the total number of mitosis was unchanged (Fig. 10E and 10G), but the distribution of the phospho-Vimentin positive cells was altered after *Sv2b* ablation, with basal mitoses (in SVZ) significantly increased compared to control embryos, in detriment of apical mitoses (in VZ; Fig. 10E and 10H).

Thus, genetic loss of function of *Sv2b* leads to an increase in phospho-Vimentin+ basal progenitor cell proliferation, in agreement with a net extension of the critical period for bRGC formation. Further analyses with longer survival periods should be performed to determine the consequences of these effects on the final fate of these increased basal progenitors, on the formation of the OSVZ, and on the eventual expansion and folding of the cerebral cortex.

Part 3. SV2B expression in human cells and its role in embryonic development

SV2B is distributed along the exocytic and endocytic pathways in human RPE-1 cells

To investigate the potential role of SV2B in development of the human cortex, we first studied its subcellular distribution, by transfecting RPE-1 cells with the SV2B:GFP fusion protein plasmid, as before. Following 36hrs after transfection, we analyzed the co-localization of SV2B:GFP with markers of subcellular compartments by means of immunohistochemistry. We used RAB6 as a marker of Golgi apparatus, EEA1 for early endosomes, LAMP1 for late endosomes and RAB7 for lysosomes. SV2B was present in all compartments, but a careful quantitative analysis revealed that Manders' coefficient was not high enough to assume co-localization (less than 0.7-0.8). Even though SV2B is present all along the secretory pathway, we found that it is not restricted to one cellular compartment (Fig 11A). Instead of being part of the specific machinery of a subcellular compartment, SV2B might be a cargo performing its function at the cytoplasmic membrane, or it may be necessary to transport other cargo to its final position.

SV2B overexpression in human cerebral organoids does not induce changes in apical lamina, ventricular surface integrity or cell delamination

Our previous results showed that electroporation of SV2B in mice altered the apical lamina. To characterize the potential function of SV2B in human cortex development we next studied if overexpression of SV2B also disrupts the apical adherent junctions in human cerebral organoids. We electroporated the ventricles of human cerebral organoids at 38 days in culture and analyzed the effect at 42 days (Fig. 11B). To analyze the integrity and composition of the apical lamina, we stained our organoids with anti-Arl13b antibodies (a marker of apical primary cilia) and anti-Par3 antibodies (component of the apical adherens junction complex). We observed no relevant differences between SV2B-overexpressing and control ventricles. The vast majority of primary cilia were nicely aligned along the ventricle in both conditions, and the apical adherens junction belt was seemingly undisturbed (Fig. 11C). In conclusion, overexpression of SV2B in human cerebral organoids neither perturbed the ventricular surface nor caused the delamination of apical progenitors, similarly to our previous findings in ferret and in contrast to the effects we previously observed in mouse embryos.

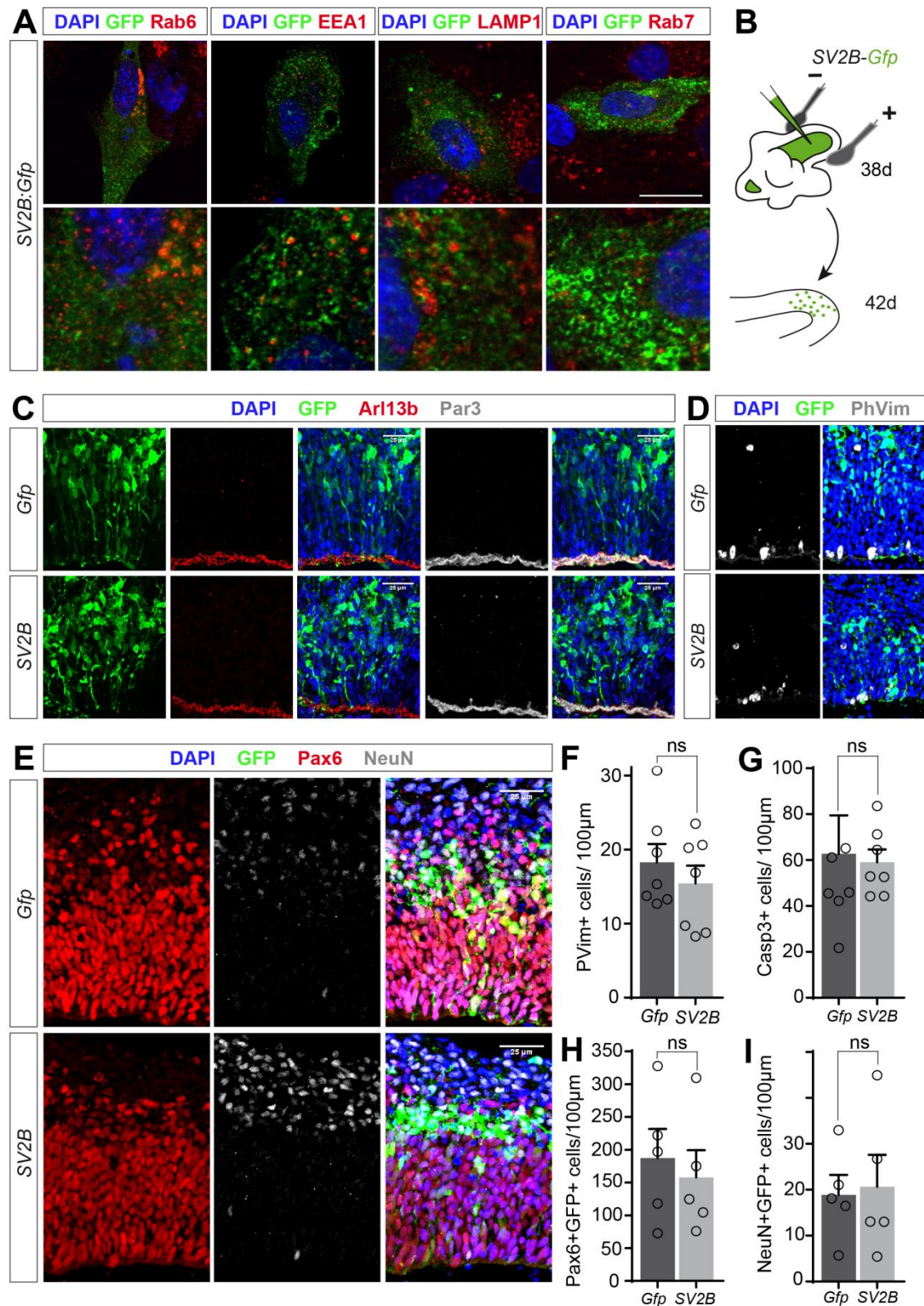
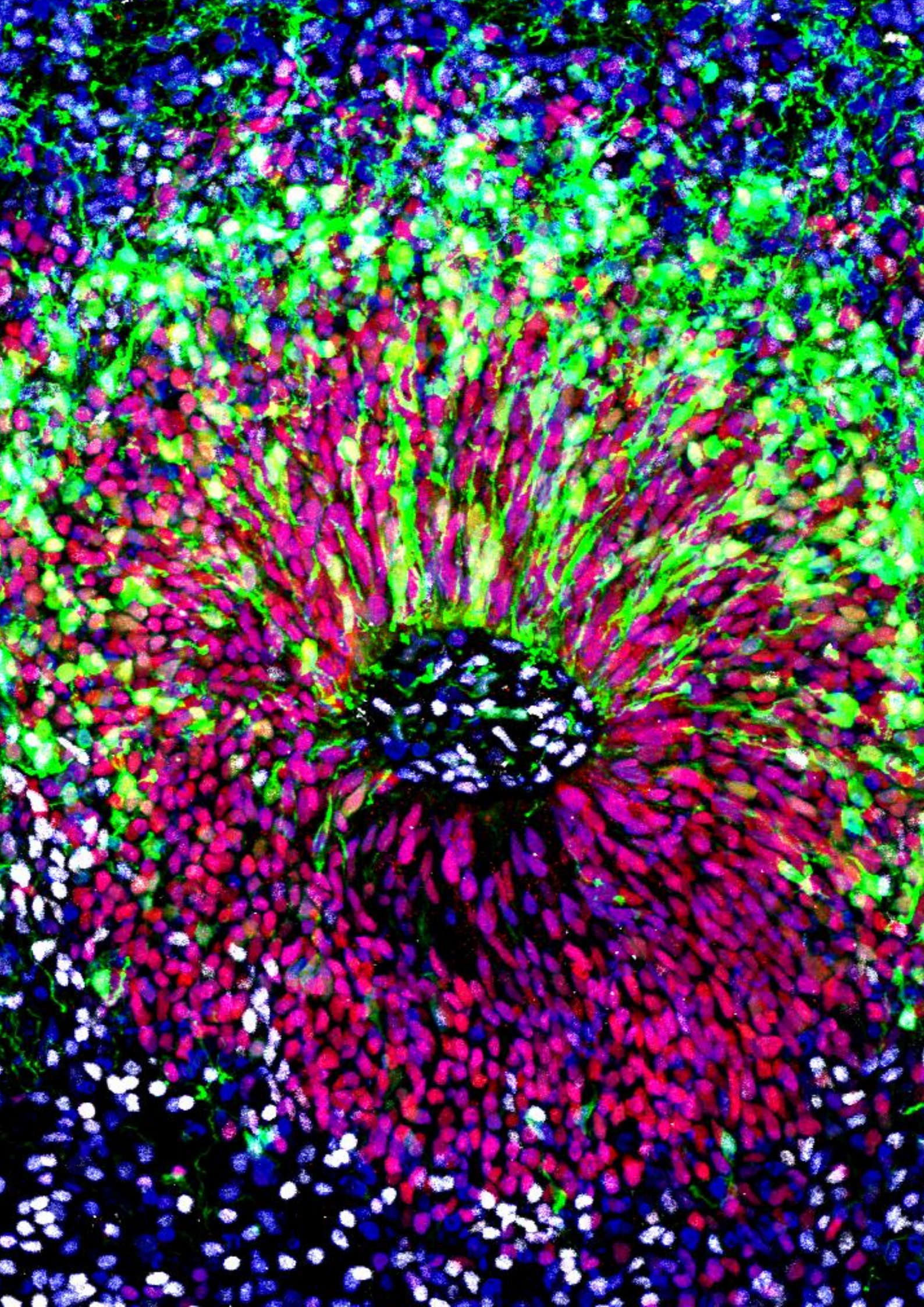


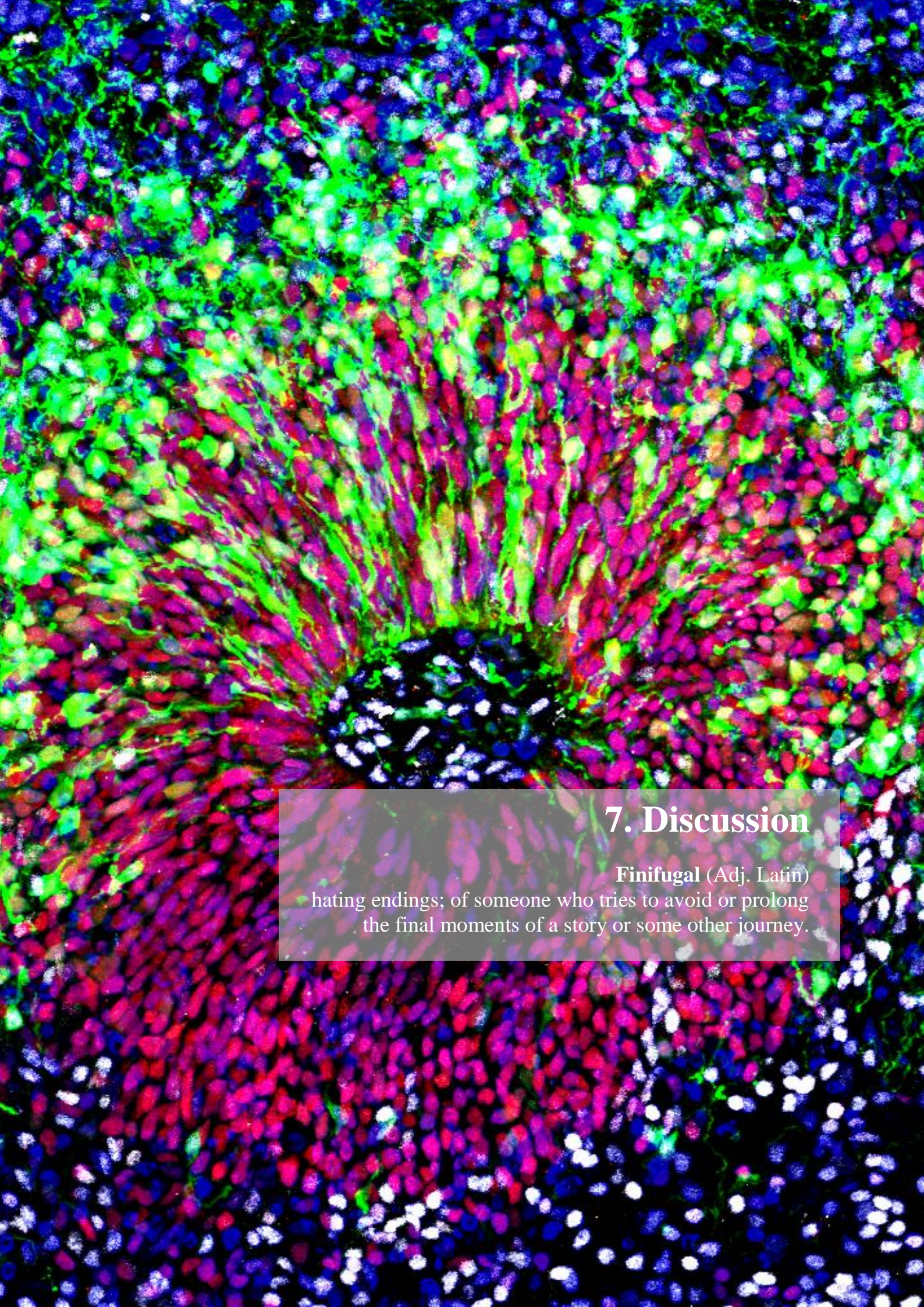
Figure 11. SV2B subcellular dynamics in RPE-1 cells and SV2B overexpression in human cerebral organoids. (A) RPE-1 cells were transfected with SV2B:GFP fusion protein and immunostained against different subcellular compartments (Rab6: Golgi apparatus; EEA1: early endosomes; LAMP1: late endosomes and Rab7: Lysosomes). Scale bar: 25µm. (B) Human cerebral organoids of 38 days were electroporated with SV2B overexpression plasmid or *Gfp* plasmid in the controls. After 4 days, organoids

were fixed and cryoslided. Immunostainings of 16 μ m cryosections of the electroporated organoids showing DAPI (blue) and GFP (green). (C) Immunofluorescence showing apical cilia with the marker Arl13b (red) and apical junction marker Par3 (white). Scale bar: 25 μ m. (D) Immunofluorescence showing apical cilia with the mitosis marker Phospho Vimentin (PVim) (white). Scale bar: 25 μ m. (E) Immunofluorescence showing progenitor cells marker PAX6 (red) and the neuronal marker NeuN (white). Scale bar: 25 μ m. Quantification of the phospho-Vimentin (F) or Caspase3 (G) positive cells per 100 μ m of ventricular surface. Quantification of the GFP and PAX6 (H) or GFP and NeuN (I) double positive cells per 100 μ m of ventricular surface. Data is shown as *Gfp* controls in black and *SV2B* in light grey. T-student statistics; average \pm SEM; ventricles n=5.

SV2B overexpression in human cerebral organoids tends to decrease mitotic activity and apical progenitors

Even though we observed normal apical adherens junctions upon overexpression of SV2B in human cerebral organoids, we reasoned that the proliferation and/or fate of progenitor cells might still be altered, as we observed in ferret. Analysis of mitotic activity revealed a tendency for decreased proliferation upon *SV2B* expression (Fig. 11D and 11F), which was not due to augmented cell death, as revealed by activated Caspase 3 quantifications (Fig. 11G). We also observed a tendency for GFP⁺ cells in VZ to be less frequently PAX6⁺ in *SV2B*-overexpressing organoids (Fig. 11H), which was not accompanied by differences in neuronal production (Fig. 11I). Organoids were highly variable and we could find no significant differences. Overall, our conclusion was that SV2B overexpression in human cerebral organoids tends to decrease the abundance of progenitor cells at the VZ and their proliferation. As human cell cycles are longer than in rodents, further experiments with more extended periods of survival are needed to unravel a potential phenotype in human samples.





7. Discussion

Finifugal (Adj. Latin)
hating endings; of someone who tries to avoid or prolong
the final moments of a story or some other journey.

The mammalian cerebral cortex experienced a dramatic expansion in surface area during evolution, along with an increase in complexity and cognitive capacities. Cortical expansion was accompanied by folding, which allowed including a large cortical surface within a limited cranial volume. This evolutionary process is recapitulated during embryonic development and its alterations during the formation further leads to severe problems as seizures, other developmental impairments, intellectual disabilities...

aRGCs are the main type of progenitor cells in the cerebral cortex, forming the VZ. aRGCs give rise to IPCs and bRGCs, that populate the SVZ. In gyrencephalic species, like ferret, macaque or human, the SVZ is dramatically enlarged and subdivided into inner and outer domains (ISVZ and OSVZ), densely populated by bRGCs and playing critical roles in cortex expansion and folding. To regulate the output of aRGCs, multiple cell and molecular mechanisms must act at a precise moment and location. The genetic regulators directly and specifically involved in cerebral cortex folding during development remain largely unknown. By using ferret as animal model, previous studies in our laboratory identified a brief period during embryonic development that is critical for cerebral cortex expansion. During this interval, aRGCs switch from amplificative divisions to self-consuming divisions, producing massive amounts of bRGCs, that then go on to establish the OSVZ. Blockade of bRGC production during this critical period profoundly impairs the formation of the OSVZ and disrupts the formation of folds and fissures (Martinez-Martinez et al., 2016; Poluch and Juliano, 2015). Genes expressed at different levels before, during and after this critical period are potential candidates to regulate changes in aRGCs lineage during this process, and hence to play a key role in cortex folding. Transcriptomic analyses performed by Martínez-Martínez et al., identified only one gene whose temporal dynamics of expression levels parallel the changes in aRGCs lineage divisions: *Sv2b* (Martinez-Martinez *et al.*, 2016). This gene encodes for the Synaptic Vesicle Glycoprotein 2B, with no known function in progenitor cells or cerebral cortex development.

Mutations in human *SV2B* have not been described, but a homozygous mutation in *SV2A* has been reported that results in severe developmental symptoms as epilepsy, involuntary movements, developmental and growth retardation, and more important, microcephaly (Serajee and Huq, 2015).

Characterization of *Sv2a* and *Sv2b* expression

First of all, to understand the role of SV2B in cortical development we need to perform a comprehensive study of the endogenous expression of this gene. We used wild type mice tissue to detect mRNA expression of the *Sv2* paralogs at different embryonic stages (E12.5, E14.5 and E17.5). *Sv2* increased its areas of expression in the brain as neurons rise up. *Sv2a* is widely expressed as development progresses, being almost ubiquitously expressed at E17.5. *Sv2b* expression in the cortex was confined to the SP and CP since early stages and along development. *Sv2b* was not expressed in germinal cortical layers at all. In fact, the only proliferative rodent tissue where *Sv2b* is expressed is on the proliferating external germinal layer of the cerebellum at P15. This layer contains cells on their final round of division before migrating to their final destination in the granule cell layer and making their first synaptic contacts (Bajjalieh et al., 1994; Crevecoeur et al., 2013). So *Sv2b* seems to be more related with early differentiation of neurons in mouse rather than progenitor cells. It was postulated (but not shown) that *Sv2b* would start to be expressed by E12 with the first neurons generated (Crevecoeur et al., 2013). Nevertheless, we have found that *Sv2b* is already present at E11 and that at E12 it is present at the CP, the hippocampus, the retinal pigmented epithelium and the most latero-ventral intermediate zone of the lateral ganglionic eminences.

Some studies address the possibility of functional redundancy for SV2 proteins (Crowder et al., 1999; Xu and Bajjalieh, 2001), but this is highly controversial. The vast majority of studies were done in adult rodents, and a developmental compensatory effect of SV2A on *Sv2b* KO animals has not been addressed. Moreover, *Sv2a* KO mice are lethal at early postnatal stages but not *Sv2b* KO mice. As *Sv2a* expression is more widespread than *Sv2b*, it may be able to compensate *Sv2b* loss but not the other way around. We have directly addressed this issue and we have determined that *Sv2a* expression seems not modified in the absence of *Sv2b*, as seen by *in situ* hybridization of *Sv2b* KO mice. Taking into account such a different expression pattern and the unaltered expression of *Sv2a* on *Sv2b* KO animals, it seems unlikely that they have completely redundant functions during development, although partial redundancy remains possible. In addition, changes in protein translation or stability while conserving mRNA levels, may be important mechanisms to compensate a loss of expression.

In lissencephalic species like mouse, *Sv2b* is confined to the SP and CP and completely absent from progenitor cells areas, apparently restricted to neurons that begin to differentiate. In contrast, *Sv2b* mRNA expression in ferret is considerably different. We have demonstrated for the first time that SV2B is expressed in germinal layers during embryonic development of the ferret. At first glance, *in situ* hybridizations, reveal clear mRNA labeling in germinal layers. *Sv2b* is downregulated at the VZ from E30 to E34, and upregulated afterwards. Thus, *Sv2b* expression changes at the critical period for bRGCs production during ferret embryonic development. Moreover, expression of *Sv2b* is significantly higher at SVZ compared to the VZ at E34 when bRGCs are being massively produced by aRGCs. Before cortical folds begin forming, genetic changes along germinal layers give rise to essential differences that will define the prospective gyri and sulci (de Juan Romero et al., 2015). Interestingly, *Sv2b* is among the genes distinctly expressed at the OSVZ of the developing gyrus compared to the future sulcus in ferret. In this gyrencephalic model, *Sv2a* is also wider expressed through the nervous system than *Sv2b*, but the cortical pattern is quite similar. For these reasons, even if *Sv2a* does not show significant differences in expression during embryonic development, some redundancy in function cannot be excluded.

The regulation of *Sv2* expression remains elusive. Bioinformatic predictions (StarBase® database), suggest several candidate microRNAs to target *Sv2b*. Curiously, one of the possible candidates, miR421, appears also to be differently expressed during the critical period for bRGCs formation (Martinez-Martinez et al., 2016). In particular, this miRNA shows a 2-fold change decrease from E34 to P1, when *Sv2b* increases. Moreover, miR421 has been related with cell proliferation and apoptosis resistance in human carcinomas (Chen et al., 2013).

Differences on gene expression between lissencephalic and gyrencephalic brains highlight the importance of using different animal models to assess evolutionary mechanisms and suggest the emergence of a new function for SV2B essential for the development of enlarged cortices. Indeed, several reports have demonstrated unique genetic features involved on gyrencephalic expansion. That is the case of expression boundaries presented on ferret germinal layers that are not shown in mouse (de Juan Romero et al., 2015). Another example of genetic regulation for the emergence of folded brains is found in species-specific genes as *ARHGAP11B* or *NOTCH2NL* in humans (Fietz et al., 2012; Florio et al., 2015; Florio et al., 2018; Johnson et al., 2015;

Pollen et al., 2015). In fact, no SV2 homologs have been identified in invertebrate species, so SV2s are an evolutionary late acquisition and probably encode specific features for vertebrates.

Gyrencephaly is a mammalian-specific trait extended in almost all mammalian orders. For that reason and together with statistic phylogenetic analyses, the most parsimonious hypothesis proposes that Lissencephaly appeared as a secondary loss of Gyrencephaly (Kelava et al., 2013). Taking into account this phenomenon, *Sv2b* expression on germinal layers could be a consequence of a new emergence or a evolutionary loss of gene regulatory elements.

A synaptic protein involved in proliferation

Several hypotheses have been postulated around the role of SV2 since it was identified. However, the vast majority of these results were related to differentiated cells and rodent animal models. Given the observed expression patterns, the most likely role of *Sv2b* in rodents is as an important protein for communication in the early establishment of synapses. Even so, its endogenous expression in ferrets reveal a more complex context. Thus, a wide scenario of possible roles and involved pathways stand up. Interestingly, it has been reported that KO mice for another synaptic vesicle protein, Synapsin III, show alterations in adult neurogenesis. These mice present an increased cell survival and a reduction in proliferation on adult hippocampus (Kao et al., 2008). Thus, changes in vesicle proteins seem to not just affect neuronal activity, but also progenitor cell behavior.

Moreover, little is known about intracellular vesicles present in neural progenitors. Martínez-Martínez *et al.*, showed significant expression changes at the VZ of SV2B and other synaptic proteins like synaptotagmin 6, 7 and 9, suggesting a possible role for vesicular proteins in RGCs. In this project, we have characterized for the first time the presence and distribution of vesicles in progenitor cells of the cerebral cortex. Moreover, we have demonstrated also for the very first time the presence of SV2B positive vesicles in aRGCs and their vesicle dynamics by subcellular videomicroscopy. These evidences suggest that not only progenitor cells present vesicles, but that they are tightly regulated during development.

To determine the possible role of SV2B in progenitor cells, we genetically modified its levels. As we have widely exposed, genetic modulations of *Sv2b* expression alter neuronal migration, progenitor cell positioning and proliferation. The promoted alterations affected electroporated cells and neighboring cells, probably meaning a non-cell autonomous effect. In the mouse cerebral cortex, VZ integrity was disrupted, apical and basal lamina were altered, cell death was increased and progenitor cells delaminated upon *Sv2b* expression. SV2B overexpression induced a delay in neuronal migration in both species, ferret and mouse. Indeed, a cortical bulge formed after long term SV2B overexpression. These features involve cellular contacts, suggesting a role for SV2B on attachment. Cortical disruption was not observed upon SV2B overexpression in ferret embryos and human cerebral organoids. Thus, the effect SV2B is causing on progenitor cells seems to be better accepted by progenitor cells of gyrencephalic species than mouse.

In murine cortex, *Sv2b* gain of function derived on delaminated progenitor cells, higher basal mitosis and altered INM, probably due to the previous disruption of the tissue or to the unbalanced attachment of RGCs. However, INM disruption is not sufficient to alter cell cycle progression (Taverna and Huttner, 2010), so SV2B is probably also affecting cell cycle progression. Our results in mice showing a reduction in cell cycle exit and a higher amount of basal divisions are compatible with cell cycle arrest or cell cycle reentry. Changes in cellular division type from neurogenic to amplificative will also induce a reduction in cell cycle exit, thus increasing RGCs number. On the other hand, most common factors to cell cycle arrest or cell cycle elongation are derived from check-point arrest after detecting DNA damage and inappropriate replication. Nevertheless, it has not been reported any activity of SV2B on DNA damage or repairing. Interestingly, G2 phase nuclear movements are straighter in mice than in ferret (Miyata et al., 2015; Okamoto et al., 2014) and cell cycle length is also longer in gyrencephalic species (Borrell and Calegari, 2014; Fernandez et al., 2016; Reillo and Borrell, 2012). SV2B overexpression in mouse, mimicking ferret aRGCs, could be affecting G2 nuclear translocation and/or directly increasing cell cycle length. This phenotype would explain the higher amount of G2/M phase apical nuclei, the reduction on cell cycle exit and alterations on INM. It is interesting to underlie that the delamination of aRGCs to more basal positions would prevent the contact between these cells and needed factors from the CSL probably changing important signaling.

Also, the disruption of the ventricular zone would induce the exposure of basal cells to these factors altering basal cells signaling and thus behavior.

In gyrencephalic species, *Sv2b* is downregulated during the critical period for bRGCs generation (around E34). SV2B overexpression at the critical period leads to higher proportion of apical progenitors with a decrease in NeuroD2+ cells. Additionally, bypassing the critical period by overexpressing SV2B from E32 to E41, we not only produce a delay in neuronal migration but also bypass bRGCs production to the SVZ, increasing the generation of VZ and ISVZ RGCs. By overexpressing SV2B from P1 to P6 we are able to reduce bRGCs quantity at the OSVZ. Thus, SV2B overexpression is sufficient to change cell fate and reduce bRGCs production to the OSVZ, a key germinal layer for cortical folding (Fig. 1) (Toda et al., 2016).

Interestingly, *Sv2b* loss of function on ferret embryo between E36-E38 (after the critical period) significantly increased the number of progenitor cells at both germinal layers (VZ and SVZ) but inducing higher basal mitosis at the expense of apical mitosis, hence increasing bRGCs or their production after the critical period. As we have observed an increase in progenitor cells amount at both germinal layers, but a reduction on apical mitosis, a delamination of the progenitor cells do not fully explain the phenotype. It is known that cell cycle length may vary depending on the daughter cell fate (Betizeau et al., 2013; Borrell and Calegari, 2014; Pilz et al., 2013; Taverna et al., 2014; Turrero Garcia et al., 2016), but differences in the time needed for apical or basal RGC generation have not been determined yet. When an aRGC undergoes a non-self amplifying division, other transcriptional programs need to be activated or repressed to induce daughter cell fate. This process requires more time than copying the same transcriptional program of the cell for a symmetric proliferative division, and cell cycle length increases over the production of more differentiated cells. In fact, neuronal generation shows longer cell cycles than the production of progenitors (Betizeau et al., 2013; Borrell and Calegari, 2014; Pilz et al., 2013; Taverna et al., 2014; Turrero Garcia et al., 2016). Similarly, bRGCs generation may need longer cell cycles compared to aRGCs self-amplification. Attending to this hypothesis, upon *Sv2b* ablation a higher amount of basal progenitors are being produced, and as a consequence of a longer cell cycle, less mitosis would be detected at the VZ. At the SVZ the timing for divisions would be the same in the control than for the experimental condition so, due to the higher number of bRGCs, a direct increase in mitosis would be observed. This

hypothesis perfectly matches *Sv2b* ablated phenotype. Thus, levels of SV2B regulate bRGCs production during ferret embryogenesis. In this scenario, several mechanisms by which SV2B could be acting are considered below.

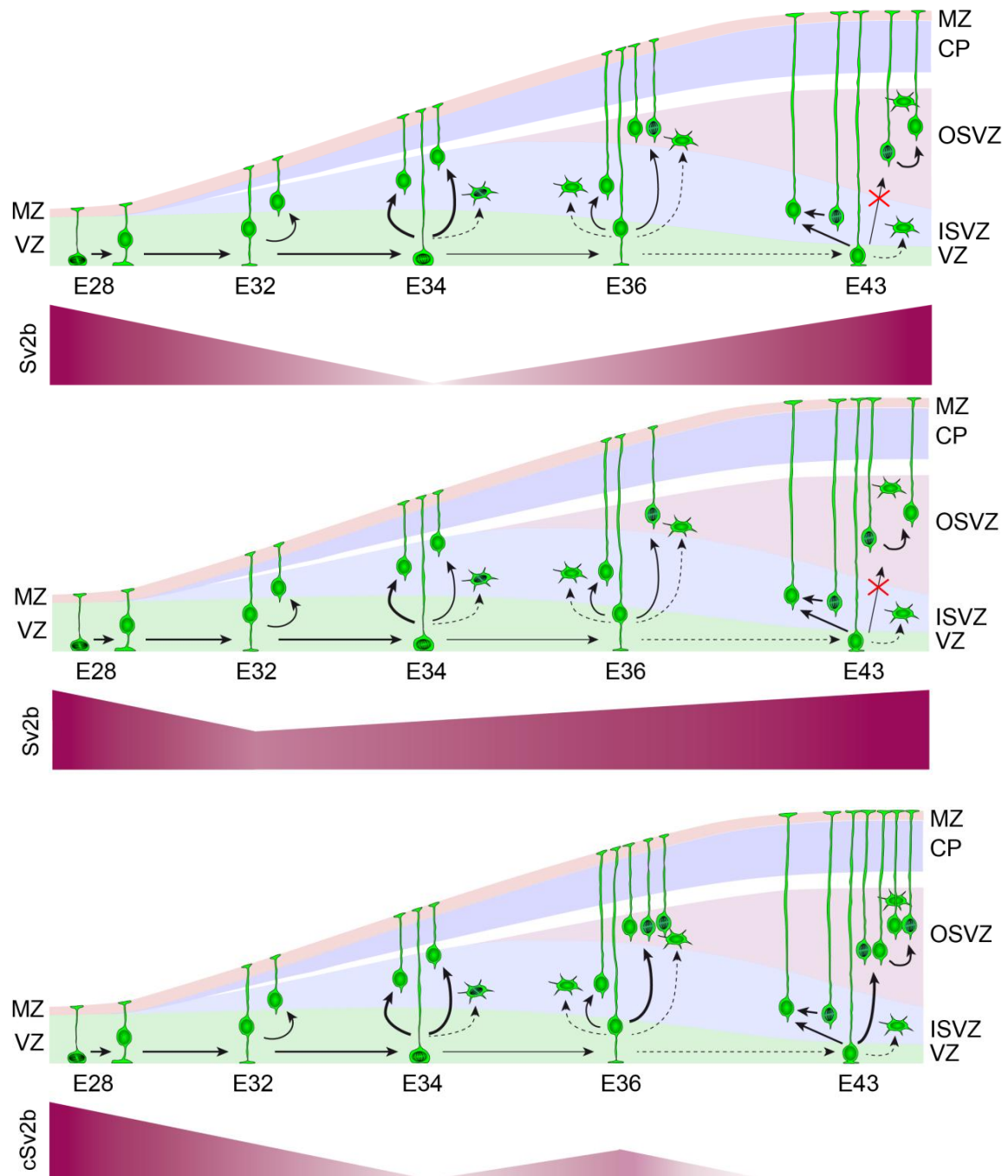


Figure 1. *Sv2b* expression modulates bRGCs generation. (A) bRGCs production upon endogenous *Sv2b* expression. (B) bRGCs production upon overexpression of *Sv2b*. (C) bRGCs production upon *Sv2b* ablation. OSVZ bRGCs are highly reduced when *Sv2b* is upregulated, while the amount of bRGCs for the OSVZ increase after *Sv2b* downregulation.

SV2B may be modulating proliferation through calcium regulation

Classically, SV2B has been related with calcium regulation. However, direct evidences for calcium transport or calcium binding has not been demonstrated. On the other hand, while several previous reports show Ca^{2+} influences on proliferation (Rash et al., 2016; Vitali et al., 2018; Weissman et al., 2004), the molecular players remain unidentified. Spontaneous calcium waves and hyperpolarization of progenitor cells have been shown to be necessary for the proper induction of progenitor cell proliferation. Thus, a specific regulation of intracellular calcium is necessary to allow these processes. Additionally, it has been shown that neurotransmitter signals (GABA and Glutamate) from young neurons induce an increase in intracellular Ca^{2+} concentration and inhibition of S-phase synthesis (LoTurco et al., 1995). Calcium waves rely on intracellular calcium storage (Weissman et al., 2004). Interestingly, SV2B is also present in mitochondria (Stockburger et al., 2016), a major calcium storage site for cells. SV2 absence leads to intracellular calcium increments in neurons (Janz et al., 1999). Accordingly, SV2B in progenitors may be acting as a calcium binding protein, such that a downregulation of this gene may lead to an increase on intracellular calcium and, thus, proliferation. Moreover, at the critical period for bRGCs production there is a high proliferation requirement coinciding with *Sv2b* downregulation.

Curiously, when extracellular calcium is quenched by EGTA administered into the telencephalic ventricle, apical adherent junctions are disturbed, the VZ is disrupted and apical mitosis translocate to basal positions (Nagashima et al., 2014). These results coincide with SV2B overexpression effects on mouse aRGCs, where the VZ integrity is altered and RGCs divisions take place basally. Thus, an overexpression of SV2B may alter the balance of calcium between intra- and extracellular space, blocking adherent junctions, and inducing delamination and changes in cell cycle. In this way, SV2 family could be the unknown players for calcium regulation on proliferative events.

The other way around, SV2B activity could be under calcium regulation. Intracellular calcium variations have been shown to modify neurogenesis of aRGCs. Rash *et al.*, showed that calcium activity is bidirectional and distributed all along the RGCs, including the processes and end-feet. Radial propagation of calcium was induced by FGF and Notch signaling, thus calcium communication transmits extracellular information through the entire cell (Rash et al., 2016). If SV2B is regulated by calcium,

it could be the effector of these morphogenic cues. Coincidentally, we have shown that SV2B positive vesicles are dynamically distributed also along the processes, suggesting a role in communication between progenitors and/or neurons migrating through the radial fibers and the aRGCs.

Nevertheless, we have not specially focused on this possible function in this project, but for future experiments addressing the pathways of SV2B action, variations on calcium spontaneous waves could be measured in SV2B overexpressing embryos.

SV2B may be acting as a transporter to modulate proliferation

In germinal layers, several extracellular molecular cues are the origin of important signaling that regulates progenitors behavior. Recent studies have shown how internalization of secreted molecules into early endosomes is sufficient to activate growth-cone turning programs (Ferent et al., 2019). Furthermore, it has been largely shown that progenitor cells produce exosomes (small extracellular vesicles) filled with proteins and genetic material essential for cell to cell communication (Stronati et al., 2019). On the other hand, a transporter-like role has also been suggested for SV2 due to its sequence and structure (Janz et al., 1999; Löscher et al., 2016). Once again, no direct transport has been detected for any of the isoforms, except for the translocation of botulinum and tetanus neurotoxins inside the cell through SV2 direct binding (Dong et al., 2008; Yeh et al., 2010). Thus, in a similar manner, SV2B could be binding and/or helping on the internalization of morphogenic extracellular signals or exosomes that regulate progenitor cells proliferation. Depending on the available molecules and the type of signals that SV2 would bind, different proliferation pathways will be affected. SV2B effects present a non-cell autonomous phenotype that would go accordingly to the internalization of extracellular cues unbalancing the signaling for the overexpressing cells and the neighboring ones.

SV2B may modulate proliferation through interaction with nucleotides

One particular interesting feature of this protein is the ability to bind nucleotides. This characteristic suggests that SV2B could be acting as an ATP transporter to incorporate

the necessary energy for proliferating mechanisms (Yao and Bajjalieh, 2008, 2009), or that SV2B activity is regulated by ATP binding, like human glucose transporter 1 (Glut1), or regulating ATP availability linking its role with the energetic levels of the cell (Stout et al., 2019). Regarding this later option, the majority of the intracellular processes require some kind of energy, even calcium regulation of proliferation (Weissman et al., 2004), relating this characteristic with the previous section. Hence, alterations in ATP balance would affect several pathways at a time. Indeed, the cell cycle needs high amounts of energy to be completed. M phase is when the cells need a peak of energy to finally divide into two separated cells. An overexpression of a molecule that recruits ATP in progenitor cells could lead to the alteration of the cell cycle and even cell death, as the severe phenotype observed in mice overexpressing SV2B. As we have observed a higher number of dividing cells, it is possible that these cells are blocked in mitotic phase due to alteration on energy levels. This modification of the energetic molecules available would also affect other processes that require high energy for movement, like INM and neuronal migration, causing misplaced S-phase nuclei and delayed migrating neurons. Previous studies showed that blockade of intracellular ATP selectively impairs basal progenitor migration to the SVZ (Liu et al., 2008). In ferret, tight regulation of the endogenous levels of ATP by SV2B would allow fewer basal translocations before the critical period with high SV2B quenching much ATP, and high migration of basal progenitors during the critical period when *Sv2b* is downregulated, quenching less ATP.

SV2B may regulate vesicle dynamics or conformation at progenitor cells

Little is known about intracellular vesicles and their dynamics in progenitor cells. We have shown that ferret aRGCs present SV2B positive vesicles distributed all along the cells. In particular, these vesicles tend to accumulate near the nucleus, at the end-feet and on the varicosities of their radial processes. This endogenous distribution of SV2B in ferret is recapitulated in aRGCs of mice overexpressing SV2B.

Overexpression of SV2B:GFP fusion protein in human RPE cells reveal that, rather than being part of the specific machinery of a subcellular compartment, SV2B could be a cargo that would have its function at the plasmatic membrane, or that it is necessary to transport other cargo to its final position. Alternatively, SV2B may be part

of the scaffold proteins to maintain vesicle conformation or to help vesicles to arrive to the active zone.

To better understand the behavior of SV2B positive vesicles, we performed time-lapse imaging of aRGCs expressing SV2B:GFP in brain slices. Previous studies have defined that the velocity in vesicles can differ *in vitro* compared to *in vivo* assays. If we check the data on intact murine brains (Knabbe et al., 2018), the average speed of neuronal dense core vesicles in axons is around 1 μ m/s, similar to our results for SV2B in basal processes. On the contrary, at apical processes the observed mean speed is twice the basal, similarly to anterograde synaptic vesicles *in vivo* in *C. elegans* (Maeder et al., 2014). In both studies the mean speed in axons is also different in anterograde or retrograde transport, but we do not see significant differences based on direction. Taking into account the high activity at apical processes compared to the basal ones, is possible that SV2B needs to be faster replaced and actively supported to the apical subpart.

Additionally, as SV2B positive vesicles showed different dynamics, it is possible that it is part of different types of vesicles as a stabilizer of vesicle containing molecules, buffering the charged transported molecules at the glycosylated sites (Stout et al., 2019). On the other hand, it has been shown that after *Sv2* ablation, the releasing of vesicles is reduced due to a reduction in ready to fuse vesicles, suggesting a role on the regulation of vesicle priming (Vogl et al., 2015; Wan et al., 2010). The content of these vesicles would influence cells in an autonomous and non-autonomous manner, as observed after overexpression of SV2B.

SV2B may modulate the localization of vesicular components

One of the most characteristic features of aRGCs is their highly polarized morphology. Their bipolar shape also represents a strict polarized subcellular compartment distribution (Arai and Taverna, 2017; Taverna et al., 2016). In this way, there must be a regulated and active transporter of the polarized molecules needed for the proper function of aRGCs. For example, altering newly generated proteins transport to the adherent junctions would probably induce similar effects to directly affect those proteins. In this context, if SV2B conforms part of this transporter machinery, a

disruption on the apical adhesion proteins turnover would lead to the *Sv2b* genetic modification observed phenotype: delamination of the progenitors to basal positions, changes in the INM affecting the cell cycle progression and delays in migration.

SV2B may modulate proliferation through extracellular matrix interactions

The essential role of the extracellular matrix in cortical development, especially in gyrencephalic species, is gaining strength. Contrary to what was classically established, this complex network of molecules is not just acting passively as a scaffold, but actively modulating signaling and cellular behavior. Many of the molecules directly involved in these processes are proteoglycans that modulate attachment and signaling diffusion. Disruption of proteoglycans network would alter the spreading of molecules and their concentration, thus leading to overmigration and changes in proliferation depending on extracellular cues (Long and Huttner, 2019). SV2B could be one of these molecules as it is highly glycosylated and transported to the plasma membrane (Scranton et al., 1993). SV2B overexpression would induce a disrupted signaling affecting cellular processes as proliferation or cell migration. Indeed, SV2B overexpression caused aberrant neuronal migration, a bulge formation and changes in proliferation, such as a reduction in cell cycle exit and an increase on mitotic cells at basal positions. This hypothesis would also explain the non-cell autonomous effect because the sequestering of molecules would affect neighboring cells, inducing also their delamination from the apical side.

Other important components of the ECM are Laminins and their receptors, Integrins (Drago et al., 1991; Long and Huttner, 2019). Interestingly, SV2B has been reported to be downregulated in β 2-laminin deficient terminals, and directly bind α 5 β 1 γ 4 laminin (Knight et al., 2003; Son et al., 2000). Laminins mainly participate in cellular attachment but they also play a role in the regulation of INM. Mutations in laminin γ 1 induce a disrupted INM and mitosis at basal positions (Tsuda et al., 2010). Furthermore, blockade of integrin β 1 results in the detachment of the apical process (Fietz et al., 2010; Fujita et al., 2020; Long and Huttner, 2019; Radakovits et al., 2009; Stenzel et al., 2014). The ablation of the same integrin or laminins α 2 or 4 detached basal end-feet and induced apoptosis (Loulrier et al., 2009). In mouse cortices, the activation of Integrin α 5 β 3 leads to an increase in proliferation by inducing cell cycle

re-entry. This integrin also regulates proliferative divisions of bRGCs at ferret OSVZ (Fietz et al., 2010; Long and Huttner, 2019). Finally, alterations on basal attachment by integrin $\beta 1$ or laminin disruption leads to microcephaly (Radakovits et al., 2009), like in human SV2A mutation (Serajee and Huq, 2015).

These phenotypes on both species resemble the effects of modifying *Sv2b* expression. In our results, modifications of SV2B levels induced basal lamina disruption and laminin aggregation. If SV2B is directly binding cortical laminin it may be sequestering the protein, depriving the attachment of other cells and leading to the misplacement of progenitor cells and mitosis. Thus, the complete structure would be affected, probably leading to the severe disruption of the VZ integrity and the fold-like structure formation at P5. SV2B overexpression could be directly or indirectly altering the attachment of the aRGCs to the apical junction belt facilitating their translocation to basal positions. In that case, PAX6 positive cells would be presented in basal positions away from the VZ while still conserving Par3 expression, as we observed in mice. After *Sv2b* gain of function, we also detect an increase in cell death and collapsed basal end-feet morphology.

Among aRGC functions, they act as scaffold for migrating cells at the cortex. Thus, alterations in these established highways may cause indirect disruptions on electroporated cells movements. Moreover, adhesion molecules are also essential to determine migration speed, what has shown to be crucial to induce cortical folding (Del Toro et al., 2017). In the same way, we have observed a delay in migration of neurons upon SV2B overexpression in both mice and ferrets. Moreover, the overmigration of the neurons induces a fold-like structure formation in mice upon SV2B overexpression. If SV2B is involved in cell attachment, its overexpression could be inducing higher interactions with the environment and slower migration.

Fietz *et al.*, reported the detection of integrins on the varicosities of the basal processes of bRGCs at the ferret OSVZ (Fietz et al., 2010). Interestingly, SV2B vesicles were also accumulated in the varicosities like these laminin receptors. Varicosities increase in number when approached mitosis (Weissman et al., 2003), what fits with the SV2B phenotype, in which overexpression leads to an increase in varicosities followed by higher amount of divisions (PH3 positive cells). The role of varicosities in the radial process of RGCs is not known, but some researchers defend that they may be working

as small Golgi apparatus subpart, for attachment, or a place for communication with the environment. Thus, alterations of these varicosities could potentially directly affect those pathways.

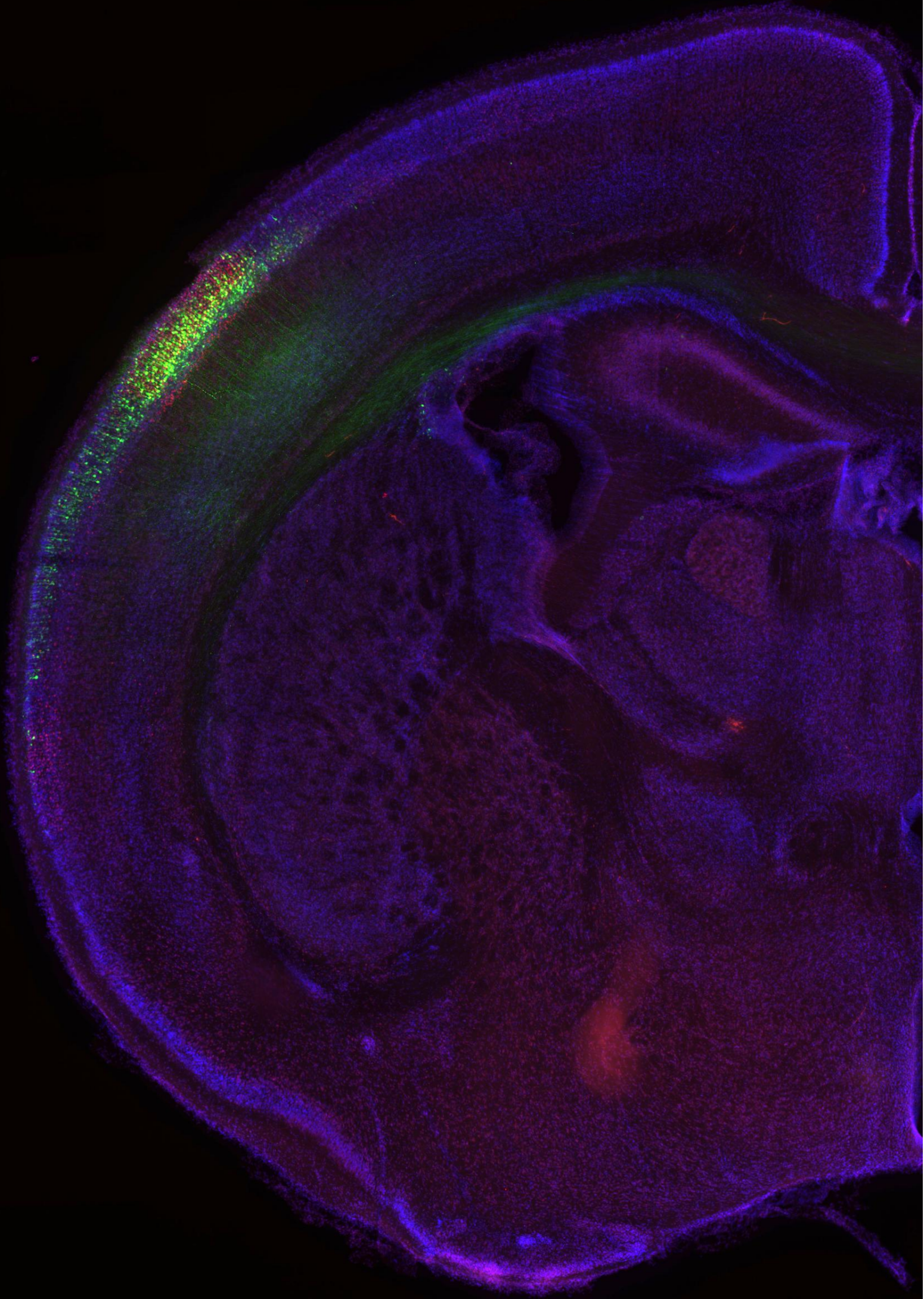
In summary, it seems that gyrencephalic species have a tighter regulation of extracellular matrix components than lissencephalic species (Fietz et al., 2012; Florio et al., 2015; Pollen et al., 2015). In accordance, inducing a downregulation of *Sv2b* at E34, when bRGCs for the OSVZ are mainly produced, would help the delamination of basal progenitors, while an increased expression out of the critical period would attach aRGCs apically. Intriguingly, an overexpression of SV2B seems to lead to a similar phenotype as in its absence: the delamination of apical cells (reported by mouse overexpression or by ferret loss of function, respectively). In one case, the electroporated cells would unbalance the attachment by recruiting to many adhesion molecules, and in the ablation context no attachment would be possible. By this mechanism, the effects would be affecting both electroporated cells and neighboring cells, as seen in our experiments. Importantly, the ventricular surface after genetic modifications is not disrupted in ferret like in mice. This could mean that extracellular matrix in gyrencephalic species is more complex and compensated that in lissencephalic ones, making it more difficult to unbalance. Progenitor cells modifying the environment to modulate delamination or migration during development, and thus control nervous system formation, is not a new idea. In fact, during neural crest development, the generation of neural crest cells and their migration is regulated by the production of hyaluronic acid and its receptors (Long and Huttner, 2019).

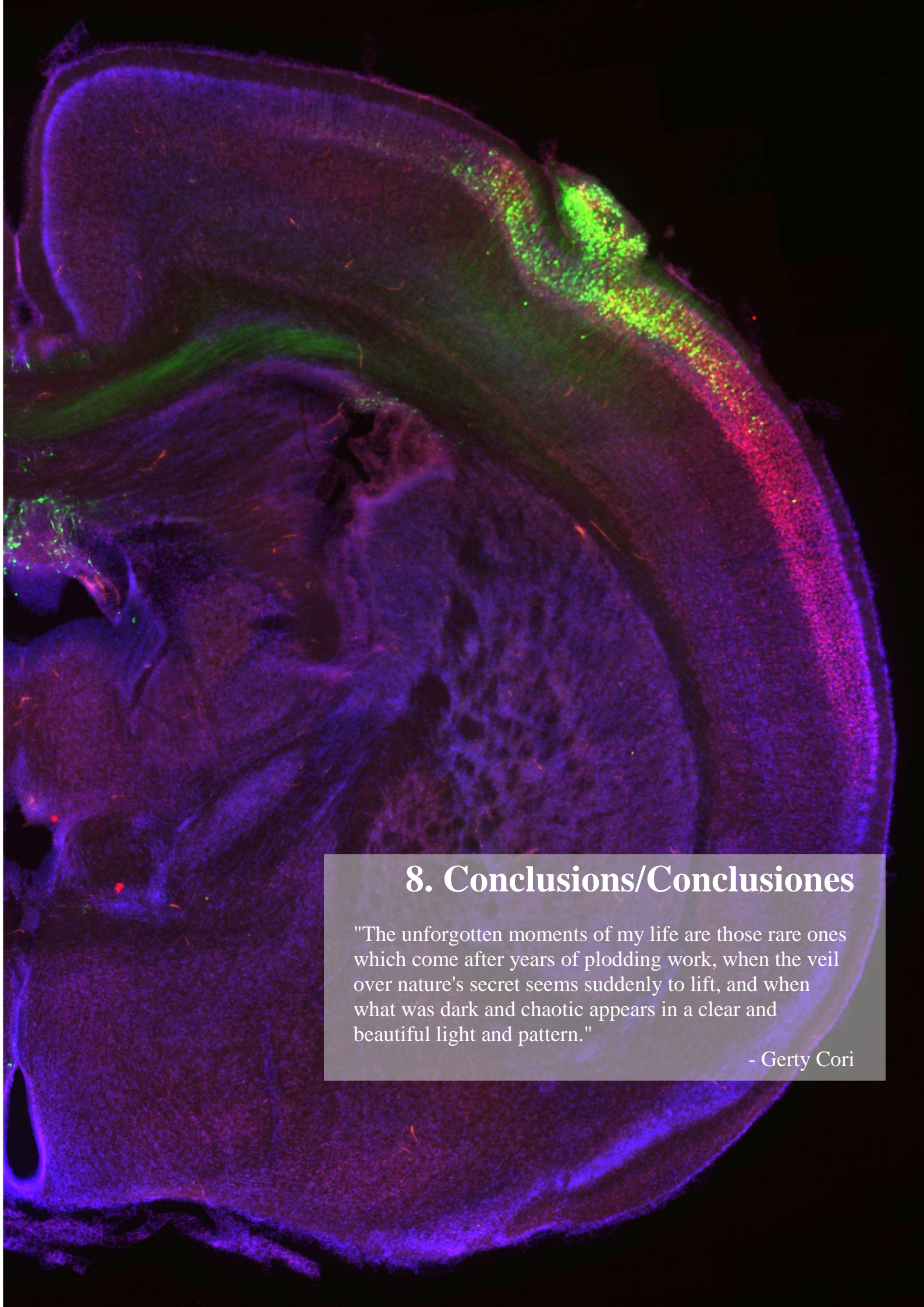
In conclusion, the observed phenotype on the genetic modification of *Sv2b* during embryonic development shows high similarities with the ones observed after alterations on ECM. SV2B has also been demonstrated to have features linked to adhesion molecules. In these cases, brains with wider cortices would need a more complex system due to the long basal processes compared to smooth cortices. Certainly, it has been reported that in humans and higher mammals the amount of extracellular matrix components went through an evolutionary increase (Fietz et al., 2012; Florio et al., 2015; Pollen et al., 2015). Consistently, it is reasonable to hypothesize the emergence of new regulators, mechanisms or receptors to actively and continuously coordinate the different cells that conform the complex gyrencephalic tissue. SV2 proteins may have emerged to directly help with cell attachment, as a linker to transmit or process

molecular information, or to drive receptors to a particular subcellular compartment. It is still barely known how aRGCs communicate each other, interact and sense the extracellular environment to act consequently with it (Reillo et al., 2017), and SV2B could have emerged as a crucial player in this process.

To further examine this hypothesis, future experiments addressing the possible ECM targets of SV2B in gyrencephalic animals are needed. Firstly, co-labeling of already known ECM components with SV2B will offer specific candidates for SV2B binding. Also, the identification of SV2B binding protein at the ECM by immunoprecipitation and mass-spectrometry would lead to potential candidates to unravel the SV2B pathway. Finally, time-lapse recordings of SV2B overexpressing slices will help to determine adhesion disruptions, migration problems through the germinal tissue and cell cycle alterations.

Studies like de Juan Romero, et al., 2015 show that the differently expressed genes at the germinal layers of the gyrencephalic cerebral cortices are mainly involved in biological processes as regulation of transcription, cell adhesion, extracellular matrix, cytoskeleton and cell cycle. Most of them were altered upon *Sv2b* genetic modification, and understanding the complete process would also help to unravel the evolutionary process to regulate the cerebral cortical formation on lissencephalic and gyrencephalic species. Along this project we have characterize *Sv2b* expression on mouse, ferret and human and how its genetic modification promotes changes in proliferation during embryogenesis. We have demonstrated for the very first time SV2B presence in RGCs on gyrencephalic species, contrary to lissencephalic models, describing also vesicle presence and distribution on apical progenitors. Moreover, in ferret *Sv2b* gain of function blocks bRGC generation, while its loss of function allows basal progenitor production for the SVZ and their proliferation. Indeed, SV2B potentially links communication among RGCs and progenitor expansion. Although the mechanism of action remains unclear and further experiments need to be done, SV2B levels are certainly influencing RGCs positioning and proliferation.





8. Conclusions/Conclusiones

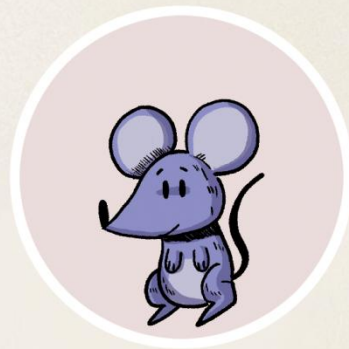
"The unforgotten moments of my life are those rare ones which come after years of plodding work, when the veil over nature's secret seems suddenly to lift, and when what was dark and chaotic appears in a clear and beautiful light and pattern."

- Gerty Cori

1. In the embryonic cerebral cortex of mouse, *Sv2b* expression is limited to the cortical plate and subplate.
2. SV2B overexpression in aRGCs of mouse embryos induces disruption of the INM, reduction in cell cycle exit, disruption of the basal and apical lamina, basal translocation of aRGCs and delay in neuronal migration.
3. At long term, SV2B overexpression induces folding of the cortical surface similar to human cobblestone.
4. SV2B positive vesicles are highly dynamic within the basal and apical process of aRGCs, moving bidirectionally and accumulating at the varicosities and end-feet.
5. In the gyrencephalic ferret cerebral cortex, *Sv2b* is expressed at the cortical plate and the germinal layers, with significant differences in expression levels before, during and after the critical period for bRGCs formation.
6. SV2B overexpression in ferret aRGCs at the critical period reduces neurogenesis and promotes the production of apical progenitor cells in ferrets, without disruption of the apical lamina.
7. *Sv2b* ablation before the critical period promotes the proliferation of aRGCs and increase of basal mitoses.
8. SV2B overexpression in human cerebral organoids tends to increase progenitor cell proliferation.

1. En la corteza cerebral embrionaria de ratón, la expresión de *Sv2b* se limita a la placa cortical y la subplaca.
2. La sobreexpresión de SV2B en embriones de ratón induce retraso en la migración neuronal, la disrupción de las láminas apicales y basales, la translocación de las aRGCs, una reducción en la salida de ciclo celular y disrupción del INM.
3. A largo plazo, la sobreexpresión de SV2B induce el plegamiento de la superficie cortical de forma similar al fenotipo *cobblestone* en humanos.
4. Las vesículas positivas para SV2B son muy dinámicas a lo largo del proceso basal y apical de las aRGCs, moviéndose bidireccionalmente y acumulándose en los pies de los procesos.
5. En la corteza cerebral girencefálica de hurón, *Sv2b* se expresa en la placa cortical y en las capas germinales, con diferencias significativas en los niveles de expresión antes, durante y después del periodo crítico para la formación de bRGCs.
6. La sobreexpresión de SV2B en el periodo crítico reduce la neurogenesis y promueve la producción de células progenitoras apicales en hurones, sin disrupción de la lámina apical.
7. La ablación en hurón de *Sv2b* antes del periodo crítico promueve la proliferación de aRGCs y el aumento de las mitosis basales.
8. La sobreexpresión de SV2B en organoides cerebrales humanos aumenta ligeramente la proliferación de células progenitoras.





9. Annex. Author's published scientific contributions

" Lo importante es no tener arrugas en el cerebro."

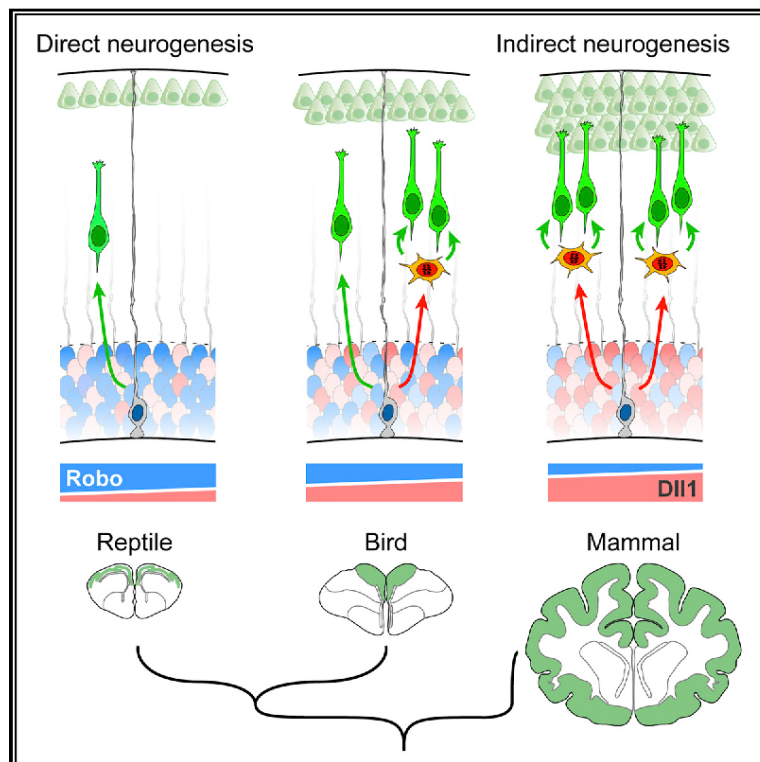
- Margarita Salas

**Annex 1 . Evolution of Cortical Neurogenesis in Amniotes
Controlled by Robo Signaling Levels.**

doi: [10.1016/j.cell.2018.06.007](https://doi.org/10.1016/j.cell.2018.06.007)

Evolution of Cortical Neurogenesis in Amniotes Controlled by Robo Signaling Levels

Graphical Abstract



Authors

Adrián Cárdenas, Ana Villalba, Camino de Juan Romero, ..., Micha Drukker, Silvia Cappello, Víctor Borrell

Correspondence

vborrell@umh.es

In Brief

Levels of Robo and Notch signaling across amniotes determines their predominant mode of neurogenesis, with consequences on final cerebral cortex size and complexity

Highlights

- Neurogenesis in mammalian neocortex is largely indirect, direct in reptiles and birds
- Low Robo and high Dll1 signaling is necessary for indirect neurogenesis
- Blocking Robo and increased Dll1 in non-mammals induces indirect neurogenesis and SVZ
- High Robo–low Dll1 blocks indirect neurogenesis in human cerebral organoids



Evolution of Cortical Neurogenesis in Amniotes Controlled by Robo Signaling Levels

Adrián Cárdenas,¹ Ana Villalba,¹ Camino de Juan Romero,¹ Esther Picó,¹ Christina Kyrousi,² Athanasia C. Tzika,^{3,4} Marc Tessier-Lavigne,⁵ Le Ma,⁶ Micha Drukker,⁷ Silvia Cappello,² and Víctor Borrell^{1,8,*}

¹Instituto de Neurociencias, Consejo Superior de Investigaciones Científicas & Universidad Miguel Hernández, Sant Joan d'Alacant, 03550 Alacant, Spain

²Developmental Neurobiology, Max Planck Institute of Psychiatry, 80804 Munich, Germany

³Department Genetics and Evolution, University of Geneva, 1205 Geneva, Switzerland

⁴SIB Swiss Institute of Bioinformatics, 1211 Geneva, Switzerland

⁵Department of Biology, Stanford University, Stanford, CA 94305, USA

⁶Department of Neuroscience, Jefferson Synaptic Biology Center, Vickie and Jack Farber Institute for Neuroscience, Sidney Kimmel Medical College, Thomas Jefferson University, Philadelphia, PA 19107, USA

⁷Institute of Stem Cell Research and the Induced Pluripotent Stem Cell Core Facility, Helmholtz Center Munich, 85764 Neuherberg, Germany

⁸Lead Contact

*Correspondence: vborell@umh.es

<https://doi.org/10.1016/j.cell.2018.06.007>

SUMMARY

Cerebral cortex size differs dramatically between reptiles, birds, and mammals, owing to developmental differences in neuron production. In mammals, signaling pathways regulating neurogenesis have been identified, but genetic differences behind their evolution across amniotes remain unknown. We show that direct neurogenesis from radial glia cells, with limited neuron production, dominates the avian, reptilian, and mammalian paleocortex, whereas in the evolutionarily recent mammalian neocortex, most neurogenesis is indirect via basal progenitors. Gain- and loss-of-function experiments in mouse, chick, and snake embryos and in human cerebral organoids demonstrate that high *Slit/Robo* and low *Dll1* signaling, via *Jag1* and *Jag2*, are necessary and sufficient to drive direct neurogenesis. Attenuating *Robo* signaling and enhancing *Dll1* in snakes and birds recapitulates the formation of basal progenitors and promotes indirect neurogenesis. Our study identifies modulation in activity levels of conserved signaling pathways as a primary mechanism driving the expansion and increased complexity of the mammalian neocortex during amniote evolution.

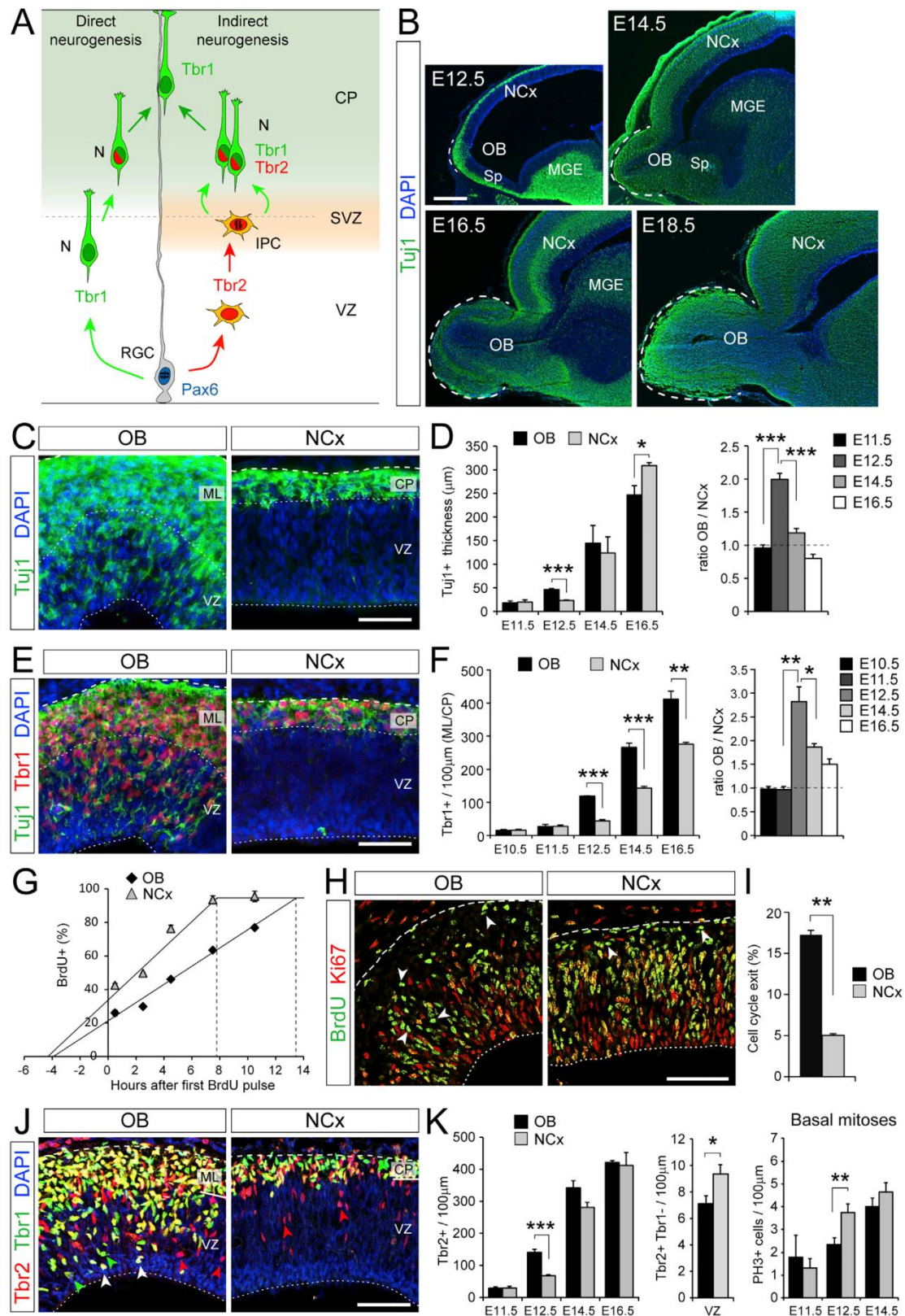
INTRODUCTION

Brain size differs dramatically among amniotes (i.e., reptiles, birds, and mammals), largely due to differences in size of the cerebral cortex. This is thought to reflect the evolutionary expansion of the cerebral cortex, which culminated in the mammalian neocortex (NCx) (Finlay and Darlington, 1995; Northcutt, 2002). Cortical expansion during amniote evolution involved a signifi-

cant increase in neuron number and the generation of new neuron types that formed new layers, extending the three-layered reptilian paleocortex into the six-layered mammalian NCx (Dugas-Ford and Ragsdale, 2015). The developmental mechanisms that regulated this evolutionary expansion and complexification of the cerebral cortex remain unknown.

Differences in cerebral cortex size and composition are thought to result from variations in the lineage of neural progenitor cells during development (De Juan Romero and Borrell, 2015; Fish et al., 2008; Kriegstein et al., 2006). Radial glia cells (RGCs) are the primary type of progenitors in the embryonic cortex; they cluster to form the ventricular zone (VZ) and undergo mitosis on the VZ apical side. Prior to cell division, each RGC must make a binary decision to leave the cell cycle or to stay. In the former, the RGC produces daughter cells that differentiate as neurons, a process known as “direct neurogenesis” (Figure 1A). In the latter case, daughter cells re-enter the cell cycle and remain as progenitors (Malatesta et al., 2000; Noctor et al., 2001; Noctor et al., 2004). When re-entering the cell cycle, RGCs may produce other RGCs or intermediate progenitor cells (IPCs). IPCs migrate basally to form the subventricular zone (SVZ), where they divide to ultimately produce neurons, a process known as “indirect neurogenesis” (Figure 1A) (Haubensak et al., 2004; Miyata et al., 2004; Noctor et al., 2004). Direct neurogenesis produces neurons fast, but RGCs can only produce one or two neuron(s) per cell cycle; thus, the number finally produced is small. With indirect neurogenesis, neuron production is slower because it involves intermediate steps of IPC generation and SVZ formation, but final neuron production is greater (Kriegstein et al., 2006). Reptile and bird embryos do not form an SVZ in the dorsal telencephalon (Cheung et al., 2007), so development of their small cortex homolog (Dugas-Ford and Ragsdale, 2015) depends on direct neurogenesis. In contrast, mouse embryos display a distinct SVZ with abundant IPCs, and indirect neurogenesis substantially contributes to the formation of their larger cortex (Attardo et al., 2008; Kowalczyk et al., 2009; Vasistha et al., 2015). In humans and other primates with a very large





(legend on next page)

cerebral cortex, their abundant neurogenesis involves the massive generation of IPCs and other basal progenitors, forming an exceptionally sized SVZ (Hansen et al., 2010; Smart et al., 2002).

The balance between progenitor cell self-renewal and neurogenesis is subject to complex molecular regulation (Taverna et al., 2014). Genetic screens and functional analyses have identified key signaling pathways regulating progenitor cell lineage and NCx development in mammals (Florio et al., 2015; Taverna et al., 2014). However, the genetic mechanisms underlying cerebral cortex evolution in amniotes, including the emergence of IPCs, increased number and types of neurons, and especially the regulation of direct versus indirect neurogenesis, remain largely unknown (Florio et al., 2017; Nomura et al., 2016). To identify developmental mechanisms responsible for the evolutionary expansion of the amniote cortex and emergence of the mammalian NCx, we first focus on mouse, comparing the early embryonic NCx (“evolutionarily new cortex”) and olfactory bulb (OB), a component of the paleocortex (“evolutionarily old cortex”). We find that direct neurogenesis is abundant in OB but scarce in NCx and that this difference is established by regulation of Slit/Robo signaling levels. Our gain- and loss-of-function experiments show that high Robo1 and Robo2 signaling leads to low levels of Dll1 and increased Jag1 and Jag2 expression. We show that this is necessary and sufficient to elicit direct neurogenesis in NCx and impair the formation of superficial layer neurons in favor of deep layers. We show that the same signaling mechanism operates in the cortex of birds and reptiles, where endogenous high Robo and low Dll1 expression sustain the predominance of direct neurogenesis. Strikingly, attenuation of Robo1 and Robo2 and increased Dll1 is sufficient to drive IPC formation in snake cortex, otherwise devoid of indirect neurogenesis. Finally, we show that gain of Robo1 and Robo2 plus loss of Dll1 impairs basal progenitor formation and drives direct neurogenesis also in human cerebral organoids. Our results suggest that attenuation of Robo signaling during amniote evolution was a primary mechanism driving the expansion and increased complexity of the mammalian cerebral cortex.

RESULTS

Faster Neuron Accumulation in the Early Mouse Embryonic OB than NCx

To identify genetic mechanisms involved in the evolutionary expansion of the amniote cerebral cortex, we first investigated developmental mechanisms that recapitulate this expansion. Focused on mouse, we compared the embryonic development

of the evolutionarily young NCx with the evolutionarily older OB (Dugas-Ford and Ragsdale, 2015). The latter is much less expanded than the NCx and part of the paleocortex (the most primitive form of cortex), while both structures develop from regions of the dorsal telencephalic primordium that are virtually indistinguishable at the onset of neurogenesis.

Between embryonic day (E) 12.5 and E14.5, the prospective OB grows much faster than the adjacent NCx, prompting its evagination (Figure 1B), so we investigated the cellular mechanisms underlying these different expansion rates. Differences between OB and adjacent NCx were first evident at E12.5, when the thickness of the neuronal layer in OB doubled that of NCx (Figures 1B–1D). The larger number of neurons in OB was not due to decreased developmental apoptosis nor to a massive immigration of GABAergic interneurons (major constituents of the mature OB), as these were absent at E12.5 and a small minority at E14.5 (Figures S1A–S1C). Instead, the initial distinction between OB and NCx emerged from the precocious accumulation of excitatory neurons in the OB, as identified by expression of Tbr1 and β III-tubulin (Tuj1; Figures 1E and 1F) (Englund et al., 2005). This suggested that the differential growth between OB and NCx starting at E12.5 is due to an accelerated neurogenesis from progenitor cells within the OB primordium, producing excitatory neurons more rapidly than in the NCx. Accordingly, Tbr1+ excitatory neurons populating the OB are born mostly during a very brief period between E11.5 and E12.5 (Figures S1D–S1G), corresponding to mitral cells (Blanchart et al., 2011). This was confirmed by lineage tracing of progenitor cells in the OB primordium (Figures S1H and S1I).

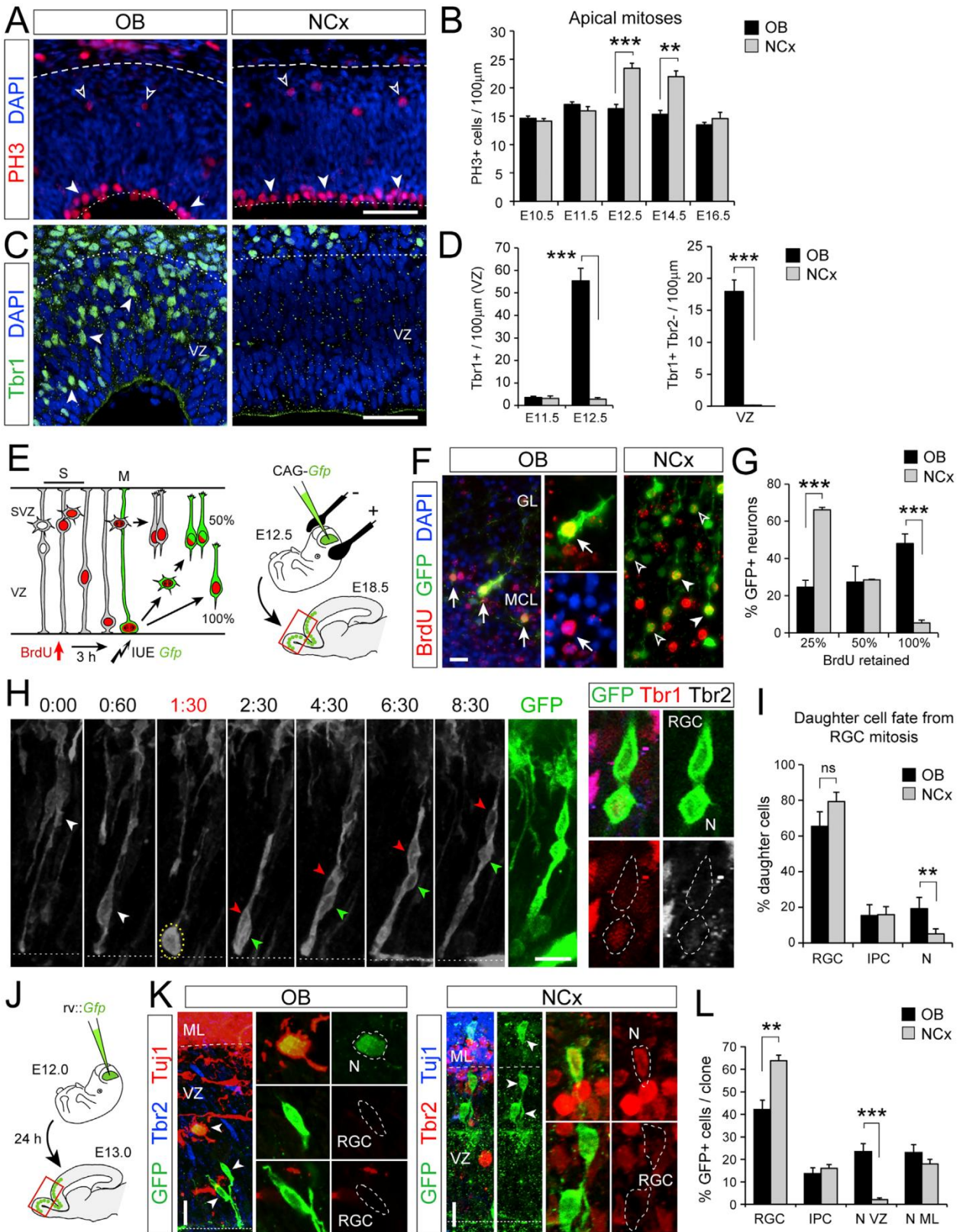
Extensive Direct Neurogenesis in OB but Limited in NCx

To determine the mechanism for fast neurogenesis in the OB compared to the adjacent NCx, we studied the behavior of progenitor cells. We found that the cell cycle is 5 hr (40%) longer in OB progenitors than in NCx (Figures 1G, S1J, and S1K). A longer cell cycle in the embryonic telencephalon is a hallmark of progenitor cells committed to exiting cell cycle and producing neurons (Arai et al., 2011). Measures of cell-cycle exit rate showed that this is 3-fold higher in OB than NCx at E12.5 (Figures 1H and 1I), indicating increased neurogenesis in OB at this stage.

Given that most excitatory neurons in NCx are born from IPCs (Kowalczyk et al., 2009; Vasistha et al., 2015), we next compared their abundance. Using Tbr2 as marker, we found that there were twice as many Tbr2+ cells in OB than NCx at E12.5 (Figures 1J and 1K). Because newborn neurons co-express Tbr2 and Tbr1 for some time (Englund et al., 2005), we only considered

Figure 1. Early Neurogenesis Is More Abundant in OB than Adjacent NCx in Mouse Embryo

(A) Schematic of progenitor cell lineages in direct and indirect neurogenesis. N, neuron; CP, cortical plate.
 (B) Parasagittal sections of developing mouse telencephalon. Dashed lines indicate extent of the OB. MGE, medial ganglionic eminence; Sp, septum.
 (C–F) Distribution and abundance of neurons (Tuj1+ and Tbr1+ cells) in OB and NCx at E12.5, and quantifications as indicated (n = 3–9 embryos per group; t test). ML, mantle layer.
 (G) Cumulative BrdU labeling at E12.5 to measure cell cycle length (n = 3 embryos per time-point).
 (H and I) Analysis of cell cycle exit at E12.5 (BrdU+Ki67–, arrowheads; n = 3 embryos per group; χ^2 -test).
 (J and K) Distribution of IPCs (Tbr2+Tbr1–, red arrowheads) and neurons (Tbr1+, green arrowheads; or Tbr2+Tbr1+, white arrowheads) at E12.5, and quantifications of Tbr2+ cells, IPCs (E12.5) and basal mitoses at the indicated ages (n = 3–11 embryos per group; t tests for density, χ^2 -tests for co-localization). Values are mean + SEM; *p < 0.05; **p < 0.01; ***p < 0.001. Scale bars: 300 μ m (B), 50 μ m (C–J). See also Figure S1.



(legend on next page)

Tbr2+ and br1 – cells as genuine IPCs. This marker combination revealed that, in fact, IPCs were 25% less abundant in OB than NCx at E12.5 (Figures 1J and 1K). To confirm this result, we measured the occurrence of basal mitoses, characteristic of IPCs, by PH3 stains (marker of mitosis). We found a significant lower density of basal mitoses in OB than NCx at E12.5 (Figure 1K). These results demonstrated that neurogenesis is greater in the early OB than NCx, but that IPCs are less abundant, consistent with a lower rate of indirect neurogenesis in OB.

Greater total neurogenesis with fewer IPCs in OB suggested higher direct neurogenesis than in NCx (Figure 1A). We found that the density of apical mitoses, characteristic of RGCs, is ~30% lower in OB than NCx at E12.5 and E14.5 (Figures 2A and 2B). This was consistent with RGCs in OB having a longer cell cycle—as measured above (Figure 1G)—typical of neurogenic divisions, supporting that much neurogenesis in OB might be direct from RGCs without involvement of IPCs. This would be a key difference with the NCx, where indirect neurogenesis seems to predominate (Attardo et al., 2008; Haubensak et al., 2004; Kowalczyk et al., 2009). We tested this hypothesis in several ways. First, we studied whether differences in apical mitoses between OB and NCx relate to Pax6+ RGCs or to Tbr2+ IPCs because the latter occasionally divide also at the apical surface (Kowalczyk et al., 2009). We found very few Tbr2+ apical mitoses, whereas Pax6+ apical mitoses were very abundant in NCx and reduced by ~30% in OB (Figures S2A and S2B). Second, Tbr1+ neurons were abundant within the VZ of E12.5 OB—as expected transiently if these are born from the apical divisions of RGCs—but were virtually absent in the NCx (Figures 2C and 2D). Third, IPC-born neurons may occasionally migrate down to the VZ (Noctor et al., 2004) while still retaining Tbr2 protein, whereas RGC-born neurons would be Tbr2-negative in the VZ. We found a high abundance of Tbr1+ and Tbr2– neurons in the OB VZ, virtually absent in the NCx (Figure 2D). Conversely, we observed Tuj1+ neurons retaining Pax6 protein in the OB VZ, but never in NCx (Figure S2C), consistent with direct neurogenesis in OB. Fifth, we performed short-survival BrdU labeling combined with Tbr1 stains to identify newborn neurons close to their birth site (Figures S2D and S2E). Tbr1+ and BrdU+ cells were seen near the apical surface in OB, but not in NCx, consistent with these OB neurons being recently born from apical mitoses. Sixth, we combined single-pulse BrdU incorporation with targeted labeling of apical progenitors by GFP in utero electroporation to identify neurons becoming post-mitotic upon apical division (Figure 2E). We found this to be the case for 48.1% of GFP+ neurons in OB but only 5.3% in NCx (Figures 2F, 2G, S2F, and S2G).

To directly visualize direct neurogenesis, we performed clonal analysis of RGCs. Sparse RGCs were labeled in utero by electroporation (Pilz et al., 2013), and their individual cellular lineage was monitored by videomicroscopy followed by marker analysis (Figure 2H). In OB, 19.2% of RGC mitoses produced neurons directly, while only 5.0% of RGC mitoses produced neurons directly in NCx (Figures 2I and S3; Videos S1, S2, S3, S4, and S5). To have an estimate at the population level *in vivo*, we analyzed the clonal lineage of individual RGCs in utero using low-titer *Gfp*-encoding retroviruses (Figures 2J–2L). In OB clones, 24.4% of GFP+ cells were neurons located in the VZ at the expense of one third of RGCs compared to the NCx, where GFP+ neurons in the VZ were 10-fold less frequent. Together, our results demonstrate that the different development of OB and NCx relies on the fate choice of RGCs, favoring direct neurogenesis in OB and indirect neurogenesis in NCx. This allows producing neurons quickly in OB at the expense of consuming RGCs and, thus, a faster but also more limited growth compared to the NCx.

Robo Receptors Promote Direct Neurogenesis in Mouse

In the parietal cerebral cortex of mouse embryos, Robo signaling modulates the balance between RGC self-renewal and IPC production (Borrell et al., 2012). We hypothesized that Robo signaling may also be important in determining whether RGCs undergo direct or indirect neurogenesis. Figures 3A and S4A show that the abundance of *Robo1* and *Robo2* mRNA in the VZ is 4-fold higher in OB than NCx starting at E12.5. *Robo1* and *Robo2* mRNA and protein were frequently expressed by Pax6+ RGCs and, to a lesser extent, by Tbr2+ cells in the VZ (Figures 3A, S4C, and S4D). While single mutant embryos deficient for *Robo1* or *Robo2* seemed unaffected, double mutants (*Robo1/2*^{-/-}) displayed prominent OB defects, with reduced evagination starting at E14.5 (Figures 3B and S5A–S5D) (Nguyen-Ba-Charvet et al., 2008), indicating a key role of *Robo1* and *Robo2* in early OB growth and development. In *Robo1/2*^{-/-} mutant embryos, the typical greater accumulation of neurons in OB compared to NCx at E12.5 was significantly diminished (Figures 3C and 3D). This was not due to increased cell death because control and mutant embryos displayed similarly scarce levels of apoptosis (data not shown). Instead, in *Robo1/2*^{-/-} mutants, most parameters that related to cell proliferation were remarkably similar between OB and NCx as opposed to control littermate embryos: abundance of apical and basal mitoses, abundance of Pax6+ and Tbr2+ mitoses, rate of cell-cycle exit, and cell-cycle length (Figures 3D–3G). Importantly, deficit in neurogenesis in the mutant OB was not

Figure 2. Higher Frequency of Direct Neurogenesis in OB than NCx

(A–D) Distribution of apical (solid arrowheads) and basal (open arrowheads) mitoses (A) and neurons (C) at E12.5, and quantifications as indicated (n = 3–11 embryos per group; t tests).

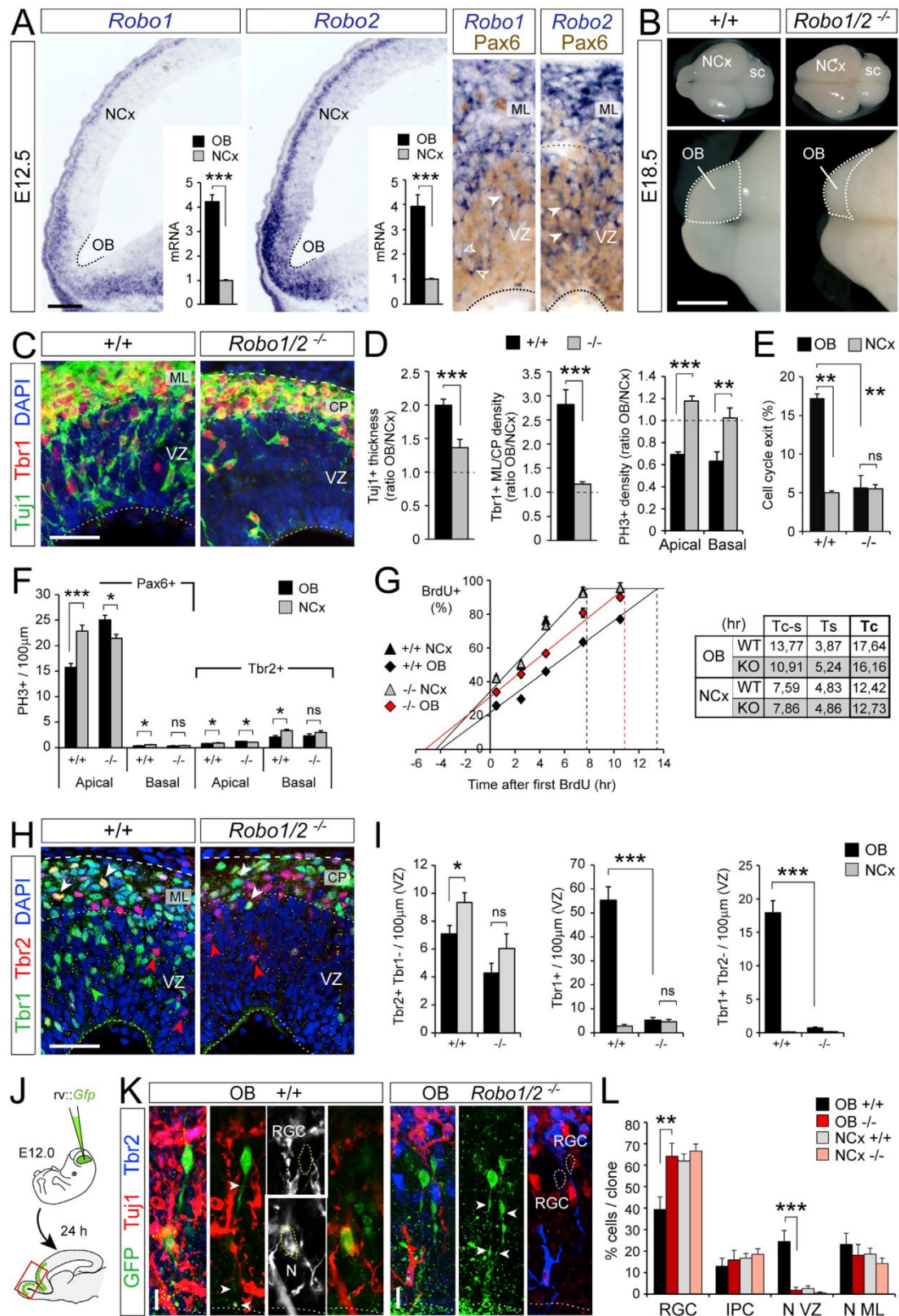
(E–G) Experimental design to identify neurons born by direct or indirect neurogenesis based on GFP labeling and BrdU retention, representative examples (OB, mitral cells with 100% BrdU [arrows]; NCx, projection neurons with 25% and 50% BrdU) and quantifications (n = 4 embryos per group; t tests).

(H and I) Time-lapse imaging frames from an RGC dividing in the OB (t = 1:30), and analysis of daughter cells (n = 44 divisions in NCx, 25 divisions in OB; 3 and 5 embryos, respectively; χ^2 -test).

(J–L) Experimental design for clonal analysis, representative examples and quantification (n = 116 clones NCx, 47 clones OB, 7 embryos; χ^2 -test). Arrowheads indicate soma of cells in clone. GL, glomerular layer; MCL, mitral cell layer.

Values are mean + SEM; *p < 0.05, **p < 0.01, ***p < 0.001. Scale bars: 50 μ m (A and C), 10 μ m (F, H, and K).

See also Figures S2 and S3.



(legend on next page)

related to deficit in IPCs, with similar abundance in OB and NCx of mutant embryos as opposed to controls (Figures 3H and 3I). Instead, mutant OBs contained much fewer Tuj1+ and Tbr1+ neurons in the VZ, very few of which were Tbr2– (non-IPC derived; Figures 3C, 3H, and 3I).

Altogether, these results are consistent with a dramatic reduction of direct neurogenesis in the OB of *Robo1/2* mutants. This was confirmed by short-term clonal analysis of apical progenitors *in vivo* using *Gfp* retroviruses. In OB clones from control littermates, 24% of cells were neurons in the VZ, and only 39% were RGCs, in sharp contrast to *Robo1/2*^{–/–} OB clones where only 2% of cells were neurons in the VZ and 64% were RGCs, the latter composition being highly similar to that of NCx clones in both controls and mutants (Figures 3J–3L).

The canonical ligands for Robo receptors are Slit1, 2, and 3. We found that *Slit1* and *Slit2* mRNAs are expressed in the VZ of NCx, septum, and basal ganglia, whereas *Slit2* and *Slit3* are highly expressed in the choroid plexus epithelium (Figures S4A and S4B). Although none were expressed in the OB primordium, Slit proteins are present in the cerebro-spinal fluid of E12.5 mouse embryos (Borrell et al., 2012), thus being readily available as ligands for Robo receptors expressed by OB RGCs. Analysis of the OB in *Slit1/2*^{–/–} embryos showed that they are phenocopies of *Robo1/2*^{–/–} mutants: scarcity of neurons in ML/CP and VZ and high density of apical mitoses, similar to the NCx (Figures S5E–S5H). This supported that Slit/Robo signaling promotes direct neurogenesis in the OB.

Accelerated early growth of the OB has been proposed to be triggered by pioneer axons from the olfactory epithelium onto OB progenitor cells (Gong and Shipley, 1995). Olfactory sensory neurons express and require Robo receptors to target the OB (Marillat et al., 2002; Nguyen-Ba-Charvet et al., 2008), so the deficient direct neurogenesis in OB of *Robo1* and *Robo2* mutants could be an indirect phenotype of RGCs from axon guidance defects. To test this, we used *in utero* electroporation to manipulate Robo signaling selectively in VZ progenitor cells of the OB in wild-type (WT) embryos, where pioneer olfactory axons are intact. We blocked *Robo1* and *Robo2* by overexpressing dominant-negative variants (*dnR1* and *dnR2*) (Stein and Tessier-Lavigne, 2001) as shown by axon growth cone collapse assays (Figure S6A). Overexpression of *dnR1/2* in OB RGCs reduced by 50% the abundance of GFP+ neurons in the VZ (Figures 4A to 4C). Conversely, we activated Robo signaling by electroporation of constitutively active Robo receptors

(*mR1* and *mR2*) (Bai et al., 2011; Stein and Tessier-Lavigne, 2001) as shown by axon branching assays (Figure S6B). Overexpression of *mR1/2* increased the already high abundance of neurons in the VZ of OB. This demonstrated that Robo receptors drive RGCs into direct neurogenesis independently from olfactory axons. Remarkably, in these experiments, we also observed significant variations of neuron numbers in the VZ among GFP-negative cells (Figures 4B and 4C), suggesting that Robo signaling influences direct neurogenesis both cell-autonomously and non-autonomously.

Robo-Dll1 Cooperation in Direct Neurogenesis

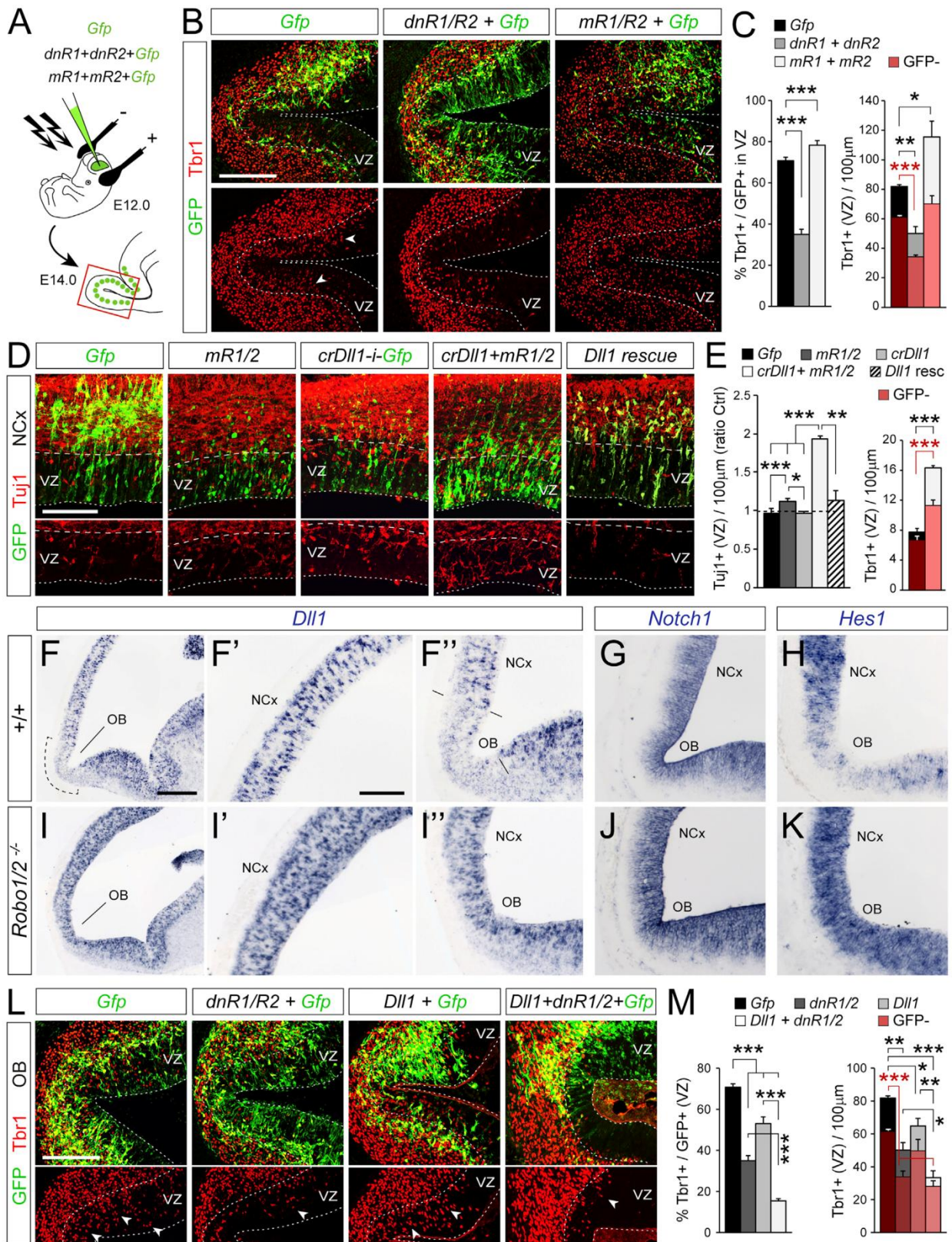
To test whether Robo signaling is a general mechanism promoting direct neurogenesis across the telencephalon, we overactivated *Robo1/2* signaling in the NCx, where endogenous expression is low and direct neurogenesis is scarce (Figure 3A). Unexpectedly, overexpression of *mR1/2* alone was insufficient to elicit a prominent increase of direct neurogenesis in NCx (Figures 4D and 4E). This suggested the possibility that other signals may cooperate with Robo to promote direct neurogenesis in OB, which may be absent in NCx.

The Notch signaling pathway is critical in regulating cortical neurogenesis, and it interacts with Slit/Robo signaling to regulate IPC production from RGCs (Borrell et al., 2012; Nelson et al., 2013). We analyzed the modulation of direct neurogenesis in this context. We found *Delta-like 1* (*Dll1*), a canonical ligand of Notch1, expressed at markedly lower levels in OB than NCx, while *Notch1* expression was similar (Figures 4F and 4G). Figures 4I and 4J shows that the local reduction of *Dll1* levels in OB is absent in *Robo1/2*^{–/–} mutants and thus is Robo-dependent. This suggested that reduced Dll1 expression might be downstream of Robo in regulating direct neurogenesis. However, CRISPR/Cas9-mediated impairment of *Dll1* expression (crDll1) alone had no effect on direct neurogenesis in NCx (Figures 4D and 4E and S6C–S6F). Instead, the combination of crDll1 and mRobo1/2 was sufficient to increase direct neurogenesis prominently, doubling the abundance of neurons in the VZ of NCx (Figures 4D and 4E). This effect was blocked by additionally expressing chick Dll1, resistant to our CRISPR RNA guides against mouse Dll1, demonstrating their specificity and the key involvement of Dll1 in this process (Figure 4E).

Next, we tested if Dll1 is also involved in regulating direct neurogenesis in OB. *In utero* overexpression of *Dll1* in OB decreased direct neurogenesis but less effectively than *dnR1/2*

Figure 3. Robo1 and Robo2 Promote Direct Neurogenesis in OB

(A) ISH and qRT-PCR for *Robo1* and 2 at E12.5 (n = 3 embryos; t tests). Arrowheads indicate Pax6+ cells expressing Robo mRNA.
 (B) Control and *Robo1* and *Robo2* mutant brains at E18.5; sc, superior colliculus.
 (C and D) Distribution and abundance of neurons and mitoses at E12.5 (n = 3–11 embryos per group; t tests). Images in (C) are from OB.
 (E) Cell-cycle exit at E12.5 (n = 3 embryos per condition; χ^2 -tests).
 (F) Linear density of apical and basal mitoses positive for Pax6 or Tbr2 at E12.5 (n = 4 embryos per group, 2–3 confocal planes per embryo).
 (G) Cumulative BrdU labeling at E12.5 to measure length of cell cycle phases (n = 3 embryos per group and time-point) and summary table of results. Tc, total cycle; Tc-s, cycle minus S-phase; Ts, S-phase.
 (H and I) Distribution and abundance of IPCs (Tbr2+Tbr1–, red arrowheads) and neurons (Tbr1+, green arrowheads; and Tbr2+Tbr1+, white arrowheads) and quantifications at E12.5 (n = 3 embryos per group; t test for density, χ^2 -test for colocalization).
 (J–L) Experimental design for progenitor cell clonal analysis, representative examples and quantification (WT: n = 116 clones NCx; 47 clones OB–KO; n = 125 clones NCx; 40 clones OB–7 embryos per group). One-way ANOVA and χ^2 -test.
 Values are mean + SEM; ns = not significant; *p < 0.05, **p < 0.01, ***p < 0.001. Scale bars: 100 μ m (A), 1 mm (B), 50 μ m (C and H), 10 μ m (K).
 See also Figures S4, S5, and S6.



(Figures 4L and 4M). Importantly, the two manipulations combined had the greatest effect, indicating that direct neurogenesis in OB is also induced by the coincident occurrence of high Robo and low Dll1 levels. Thus, high Robo signaling, with the necessary co-operation of low Dll1, is a conserved mechanism driving direct neurogenesis in both OB and NCx.

Robo-Dll1 Promotes Direct Neurogenesis via Jagged

Dll1 binding and activating Notch1 drives *Hes1* transcription and then maintenance of the stem cell fate (Ishibashi et al., 1995). Accordingly, alongside low *Dll1*, we found extremely low levels of *Hes1* mRNA in OB compared to NCx. In the OB of *Robo1/2* mutants, *Hes1* levels were much higher than in WT littermates, similar to NCx (Figures 4H and 4K). This difference was not due to *Hes1* being downregulated in NCx of *Robo1/2*^{-/-} mutants, shown previously (Borrell et al., 2012), as that effect is extremely modest compared to the dramatic difference observed here in OB. This suggested that Notch activity might be lower in OB and might be a requisite to promote direct neurogenesis. Our above manipulations caused changes in direct neurogenesis that included a cell-non-autonomous component (GFP⁻ cells), consistent with changes in Notch-Dll lateral inhibition. To confirm differences in Notch activity between OB and NCx, we analyzed levels of *Hes5* mRNA expression, a canonical downstream effector and faithful readout of Notch activation. We found identical levels of *Hes5* in OB and NCx (Figures 5A and 5B), indicating that levels of Notch activity are not significantly different between these regions, and thus, this does not determine the choice between direct and indirect neurogenesis.

Given the scarcity of *Dll1* in OB, we searched for other ligands activating Notch. We found *Jagged* (*Jag*) 1 and *Jag2* expressed in OB at modest levels but nearly double to NCx, with minimal expression, while they were nearly absent from OB in *Robo1/2*^{-/-} mutants (Figures 5C–5G). These expression patterns were complementary to *Dll1* and similar to *Robo1* and *Robo2*, such that high *Jag* expression correlated with abundant direct neurogenesis. Consistent with this, the combined gain of Robo and loss of Dll1 in NCx (in utero electroporation of mR1/2+crDll1), which drives direct neurogenesis, elicited the ectopic expression of *Jag1* and *Jag2* (Figure 5H). This suggested that upregulation of *Jag* may be downstream of Robo-Dll1 to mediate direct neurogenesis. Remarkably, overexpression of *Jag1* alone was sufficient to significantly increase direct neurogenesis in NCx (Figure 5I).

The above results showed that Robo, Dll1, and Jag are active players in defining direct versus indirect neurogenesis in mouse. Our analyses of *Robo1/2*^{-/-} mutants demonstrated that high

Robo reduces *Dll1* and increases *Jag1* and *Jag2* expression, and experimental gain of Robo and loss of Dll1 increases *Jag1*. Under both these conditions, direct neurogenesis predominates. To determine if Dll1 or Jag1 regulate Robo expression reciprocally, we electroporated crDll1 or *Jag1* in the NCx of WT embryos. Levels of Robo protein increased slightly (though significantly) upon electroporation of crDll1 but were not affected by *Jag1* overexpression, which also did not alter levels of Dll1 at our resolution of detection (Figures S6G–S6K). Our results demonstrated that under conditions of high Robo and low Dll1, *Jag1* expression is enhanced, driving direct neurogenesis.

Direct Neurogenesis Produces Deep Layer Corticofugal Neurons

While the OB is archaic in origin and common to amniotes, the NCx is an evolutionary innovation of mammals (Puelles et al., 2000; Rowe et al., 2011). Our above results supported the notion that the evolutionary expansion of the amniote cerebral cortex into the mammalian NCx resulted from a reduction in direct neurogenesis, favoring the more productive indirect mode. A prominent feature linked to expansion of the amniote cortex is the generation of new neuron types, forming the superficial layers 2/3, exclusive to mammals (Dugas-Ford and Ragsdale, 2015). If indirect neurogenesis contributed to this innovation, forced direct neurogenesis in mouse NCx should lead to a loss of superficial layer neurons and gain in deep layers, constituent of the reptile and avian cortex homolog. We studied the fate of mouse cortical neurons produced by direct neurogenesis upon mR1/2+crDll1 overexpression. We labeled neurons born directly from RGCs by combining a single BrdU pulse with in utero electroporation of GFP at E12.5 and analyzed their fate at maturity (Figure 5J). Overexpressing mR1/2+crDll1 caused a specific loss of GFP+ cells from layer 2/3 and increase in deep layers (Figures 5K and 5L). Layer-specific marker analysis showed that this change in position was not due to defective neuron migration but to the specific increase in bona fide deep layer neurons (Ctip2+) at the expense of superficial layers (Cux1+; Figures S7A–S7C). Focused on GFP+ cells retaining 100% of BrdU (Figure 5M), we found that induced direct neurogenesis led to 3–5 times more layer 5 and 6 neurons expressing Tbr1 and Ctip2 (Figures 5L and S7D) than controls. We confirmed the identity of directly generated neurons in layer 5 by tracing their cortico-spinal axonal projections with CTB (Figure S7E). In mR1/2+crDll1 mice, we found a higher abundance of CTB+ electroporated neurons and a much greater proportion of CTB+GFP+ neurons formed by direct neurogenesis (100% BrdU; Figures S7F and S7G), confirming their subcerebral projection identity.

Figure 4. Robo Receptors Cooperate with Dll1 to Regulate Direct Neurogenesis in OB and NCx

(A–C) Experimental design to manipulate Robo function in OB primordium, representative examples (arrowheads indicate Tbr1+ cells), and quantifications. (D and E) WT NCx electroporated with the indicated plasmid combinations, and ratio of density of Tuj1+ cells (red) in the VZ between electroporated and non-electroporated hemispheres. Dll1 rescue refers to electroporation with mR1/2+crDll1+chicken Dll1. (F–K) ISH for Notch pathway genes in control and *Robo1/2*^{-/-} embryos at E12.5. Dashed line in (F) indicates area with low Dll1 mRNA, corresponding to OB primordium. Panels shown in (F) and (I) are tiled images. (L and M) WT OB electroporated with the indicated plasmid combinations, and abundance of Tbr1+ cells in the VZ. Red shadowing and asterisks in (C, E, and M) indicates values in each experimental group corresponding to GFP⁻ cells. Values are mean + SEM; n = 3–5 embryos per condition; *p < 0.05; **p < 0.01; ***p < 0.001; one-way ANOVA followed by χ^2 -test for co-localization, or t test for density. Scale bars: 100 μ m (B, D, L), 300 μ m (F, I), 100 μ m (F'–H and I'–K). See also Figure S6.

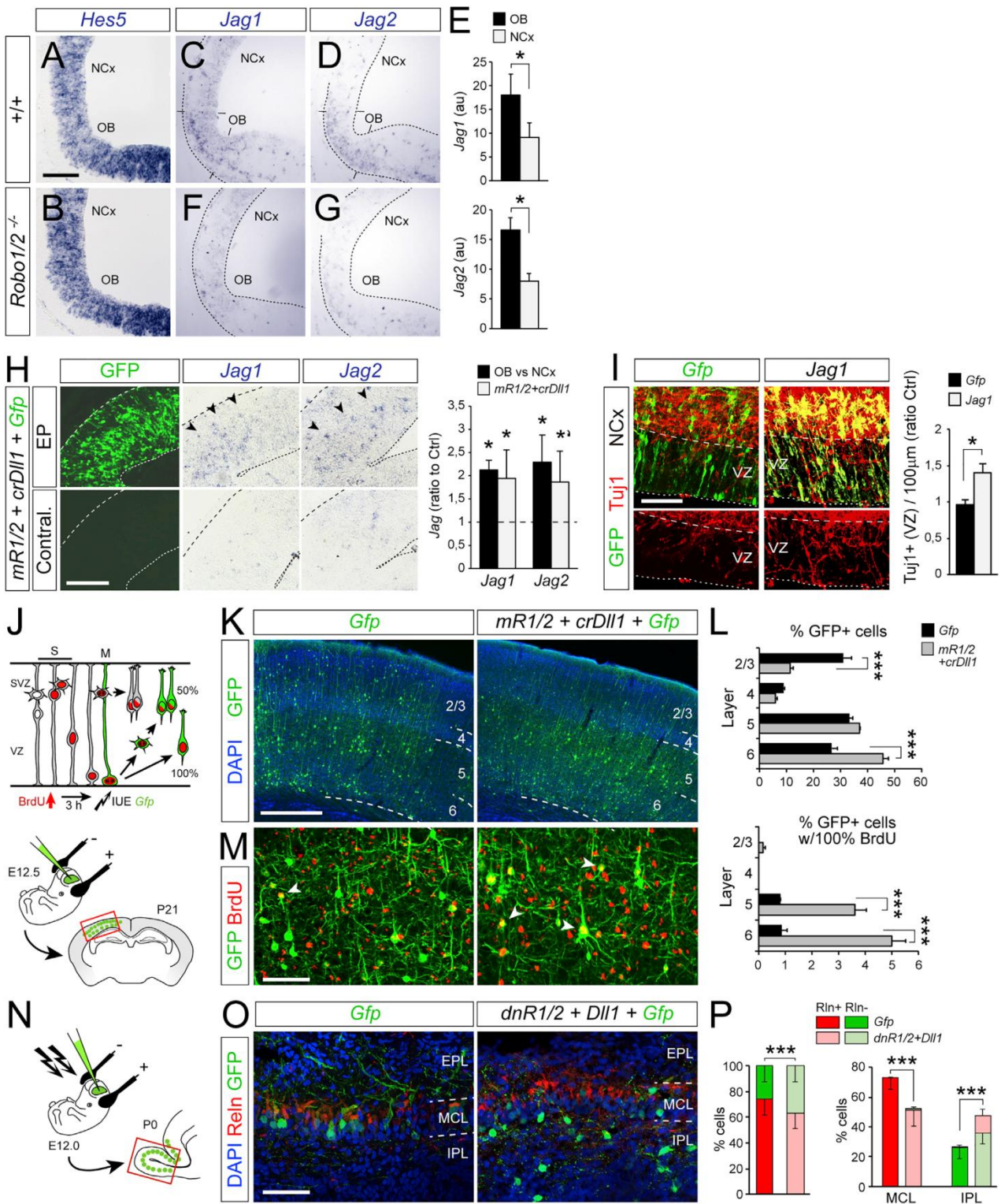


Figure 5. Robo/Dll1/Jag Signaling Drives Direct Genesis of Deep-Layer Corticofugal Neurons

(A-G) ISH stains for Notch pathway genes in control and *Robo1/2*^{-/-} embryos at E12.5, and intensity quantification (paired t test).

(H) ISH stains for *Jag1* and *2* in NCx upon electroporation of the indicated plasmid combination (EP), and quantification of intensity (ratio to contralateral non-electroporated hemisphere; paired t test).

(legend continued on next page)

We also investigated the fate of OB neurons generated upon blocking direct neurogenesis with *dnR1/2+Dil1*. Compared to controls, reduced direct neurogenesis led to a loss of ReIn+ and 42% gain of ReIn− cells, combined with the displacement of a significant number of ReIn+ cells from the mitral cell layer to the inner plexiform layer (Figures 5N–5P), as also observed in *Robo1/2*^{−/−} mutants (Figure S5D). Together, our results reinforced the notion that reduction of direct neurogenesis during embryonic development was a key event in the evolution of the amniote cerebral cortex, expanding neuron production and cortical size, as well as driving the generation of superficial layer neurons in NCx. At the molecular level in the mouse, this is achieved by attenuation of Robo expression levels.

Robo Function in Cortical Neurogenesis Is Conserved in Birds and Snakes

We next examined the occurrence of direct neurogenesis in other parts of the mammalian brain that are evolutionarily old like the OB, such as the hippocampus (part of archicortex, or “old cortex”) and spinal cord (SC) (Puelles et al., 2000; Rowe et al., 2011). Neurogenesis in SC occurs directly from RGC divisions (Das and Storey, 2014), evidenced by the lack of basal mitoses and abundance of Tuj1+ neurons in the VZ (Figure S7H). The hippocampal primordium also contains numerous Tuj1+ and Tbr1+ neurons in the VZ, similar to SC and OB and contrary to the NCx, indicative of ongoing direct neurogenesis (Figure S7J). At the molecular level, *Robo1* and *Robo2* expression in the VZ is relatively higher in hippocampus than NCx (Figure S7I). *Robo1/2*^{−/−} embryos displayed a dramatic reduction of neurons in the hippocampal VZ, down to levels similar to the NCx (Figures S7J and S7K). This finding supported that direct neurogenesis controlled by Robo receptors may be an evolutionarily conserved mechanism of telencephalic development.

To determine if Robo driving direct neurogenesis in the cerebral cortex is a mechanism conserved across amniote phylogeny, we analyzed the homolog of the embryonic cerebral cortex in two sauropsids: a bird (chicken) and a squamate reptile (African house snake). In chick embryos, two domains of the dorsal pallium (DP) were clearly distinguishable: a medial domain (mDP), containing virtually no basal mitoses and many Tuj1+ cells in the VZ, indicative of direct neurogenesis; and a lateral domain (lDP), with many basal mitoses and few Tuj1+ cells in the VZ, indicative of indirect neurogenesis (Figures 6A–6D). Concomitantly, the VZ of mDP exhibited high mRNA levels of *Robo1* and low *Dil1*, whereas the lDP displayed low *Robo1* and high *Dil1* levels (Figures 6E–6H). These differences between chick mDP and lDP were remarkably similar to those between the mouse OB and NCx. Importantly, levels of *Robo1* in the VZ were higher in chick than in mouse, outlining a progressive and significant reduction of Robo expression from

chick mDP to chick lDP, mouse OB, and mouse NCx (Figure 6I). We tested the functional significance of these regional differences by *in ovo* electroporation of chick embryos. Overexpression of *dnR1/2+Dil1* in the mDP led to a significant decrease in Tbr1+ VZ neurons and a 3-fold increase in basal mitoses, promoting indirect neurogenesis (Figures 6J–6L). Similar to the mouse NCx, only modification of Robo and Dil together, but not alone, affected significantly the balance direct versus indirect neurogenesis (Figure 6M). Identical results were obtained in lDP (Figures 6N and 6O). The changes that were most dramatic evidenced the existence of a cell non-autonomous component (changes in GFP− cells; Figures 6L and 6O), similar to our findings in mouse and consistent with a conserved signaling mechanism. Conversely, overexpression of *mR1/2* in lDP led to a dramatic increase in Tbr1+ VZ neurons and loss of basal mitoses, promoting direct neurogenesis (Figures 6N and 6O). Importantly, the basal mitoses that emerged most abundantly upon *dnR1/2+Dil1* were Tbr2+ (Figures 6P and 6Q), excluding that this was simply the result of delamination of RGCs and demonstrating a dramatic increase in IPCs. Finally, we examined the long-term consequences of promoting indirect neurogenesis in the chick DP by clonal analysis of single progenitor cell lineages (Figure 6R). Our results showed that promoting indirect neurogenesis by overexpressing *dnR1/2+Dil1* nearly doubled the neurons produced per VZ progenitor with a much greater number of clones containing more than 4 neurons (up to 9 per clone; Figures 6S–6U). These results demonstrated that the balance between direct and indirect neurogenesis in the DP of birds, including amplification of IPCs, is regulated by the levels of Robo-Dil1 signaling, as in the mammalian OB and NCx.

To extend our analyses to a wider range of amniotes, we studied the dorsal cortex (DC) of the African house snake (Figure 7A). In the DC of snake embryos, we found only apical mitoses accompanied by frequent neurons in the VZ (Figures 7B and 7C), but no basal mitoses, indicating that direct neurogenesis is the only mode of embryonic cortical neurogenesis in this reptile. As in mouse OB and chick mDP, *Robo* levels in the VZ of the snake DP were high (for *Robo2*, as *Robo1* was not expressed; data not shown) and *Dil1* levels were low (Figures 7D and 7E), again consistent with this combination promoting direct neurogenesis. To test whether this signaling axis regulates the mode of cortical neurogenesis also in squamate reptiles, we overexpressed *dnR1/2+Dil1* in snake embryos by *in ovo* electroporation (Figure 7F). Figures 7G and 7H show that this manipulation in the DP of snake embryos led to fewer neurons in the VZ and thus reduced direct neurogenesis. This manipulation also led to the emergence of abundant basal mitoses (Figure 7H, red circles), as we had observed in chick. The majority of basal mitoses were GFP− (73%, n = 33; Figure 7G'), consistent with

(I) WT NCx electroporated with the indicated plasmid combinations, and ratio of density of Tuj1+ cells (red) in the VZ between electroporated and non-electroporated hemispheres (t test).

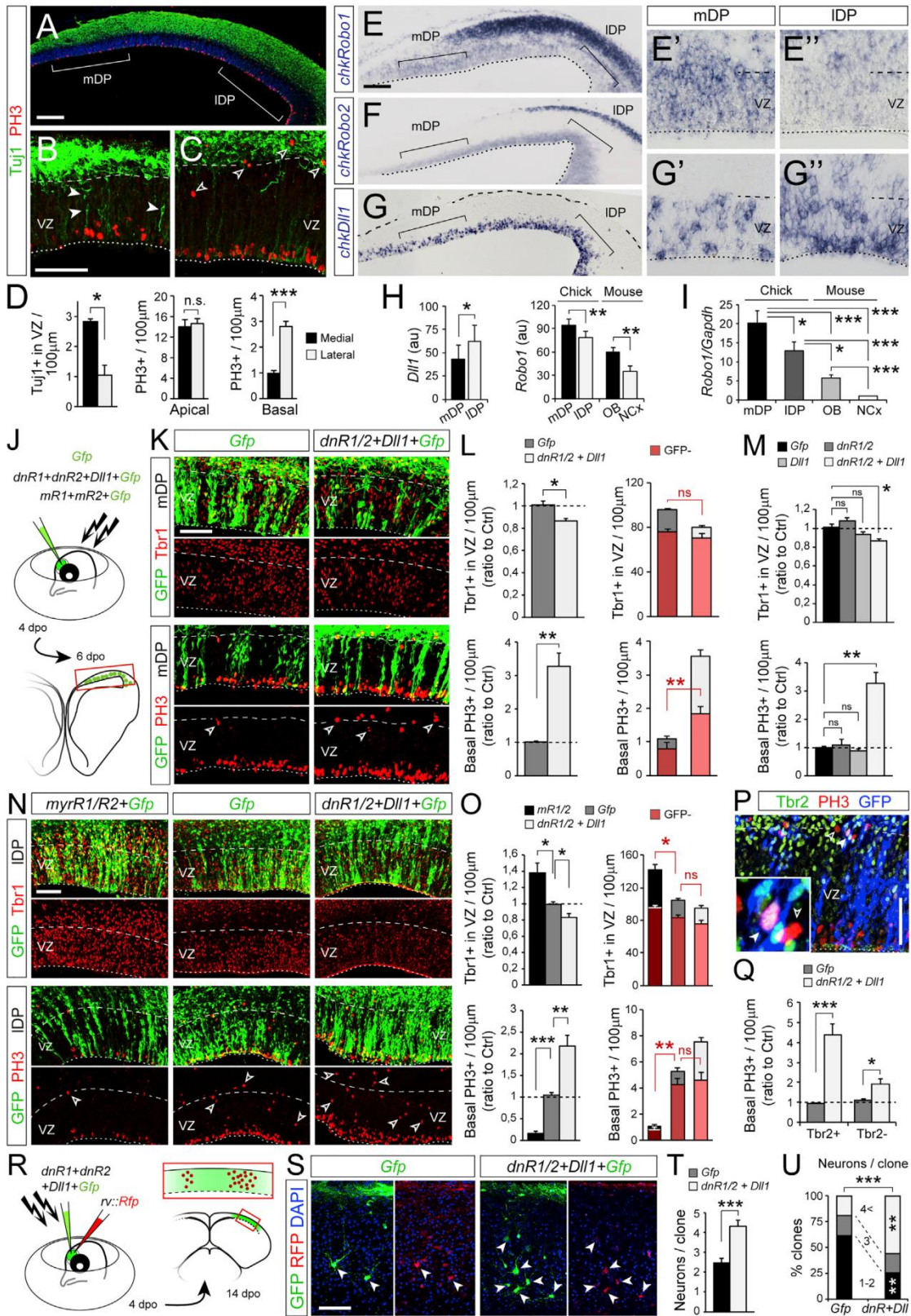
(J) Experimental design to identify the fate of neocortical neurons born by direct neurogenesis.

(K–M) WT NCx electroporated with the indicated plasmid combinations, and laminar distribution of all GFP+ cells (L, top) and with 100% BrdU label (born by direct mode, arrowheads; [L], bottom; one-way ANOVA followed by χ^2 -test).

(N–P) Identification of neuron types in WT OB electroporated with the indicated plasmid combinations, and quantification (χ^2 -test). Left plot is cell types in any layer; right plot is cell types sorted by layers.

Values are mean + SEM, n = 3–5 embryos per group; *p = 0.050; *p < 0.05; **p < 0.01; ***p < 0.001. Scale bars: 50 μ m (A–I, M, and O), 400 μ m (K).

See also Figures S6 and S7.



(legend on next page)

a significant contribution of cell non-autonomous mechanisms, as in mouse and chick. Remarkably, these basal mitoses systematically aligned at the basal border of the VZ, seemingly forming an SVZ like in the mammalian NCx. This is a most outstanding outcome because the presence of IPCs and basal mitoses in the developing cerebral cortex, forming a secondary germinal layer, are gold-standard milestones of neocortex mammalian evolution that are not existent in reptiles (Cheung et al., 2007).

The above findings demonstrated that high Robo signaling in the cortex of birds and reptiles promotes direct neurogenesis and blocks basal progenitor formation, limiting cortex size. In contrast, endogenous attenuation of Robo signaling in the rodent NCx reduces direct neurogenesis and promotes IPC generation, increasing neuron production and cortical size. Given that the human neocortex is one of the largest among mammals, we investigated if this same signaling mechanism operates in the early human embryo. We generated cerebral organoids from human iPS cells and, after 39 days in culture, electroporated *mRobo1/2+crDil1* (Figures 7I and S6D) (Lancaster and Knoblich, 2014). The overall morphology and appearance of organoids were not different between controls and those receiving *mR1/2+crDil1*. They were mainly comprised of a VZ, containing GFP+ cells with the elongated morphology typical of RGCs, plus a thin mantle zone (MZ) filled with NeuN+ and multipolar GFP+ cells, neuronal features (Figure 7J). NeuN+ neurons were rarely seen within the VZ. PH3+ mitotic nuclei were found abundant at the apical surface of VZ and in fewer numbers at its basal side, bordering the MZ. Organoid regions electroporated with *mR1/2+crDil1* displayed 3 times more NeuN+ neurons in the VZ and only 20% of basal PH3+ mitoses of adjacent non-electroporated regions within the same organoid ventricles or of organoids receiving control plasmids (Figures 7J and 7K). As in our previous experimental models, increased direct neurogenesis included a significant increase in GFP- neurons, indicating the involvement of cell-non-autonomous mechanisms. These results demonstrated that Robo signaling is also endogenously attenuated in VZ cells of human cerebral organoids, where it limits direct neurogenesis and promotes IPC generation and SVZ formation, as in mouse NCx.

DISCUSSION

The evolutionary emergence of mammals was critically marked by the formation of the NCx. Compared to the small and rela-

tively simple dorsal cortex of other amniotes, the mammalian NCx is much larger and complex, containing greater numbers and types of neurons. At the cellular level, this is associated with a binary decision of RGCs to generate or not generate neurons directly. In reptiles and birds, most cortical neurons are produced directly by RGCs, whereas in the mammalian NCx, most are produced indirectly via IPCs, greatly amplifying the neurogenic output (De Juan Romero and Borrell, 2015). Here, we identify for the first time a molecular signal that determines the mode of cortical neurogenesis across amniotes. Our results in snake, chicken, mouse, and human demonstrate that during amniote evolution, attenuation of *Robo1* and *Robo2* and increase of *Dil1* expression in RGCs changed the balance from direct to indirect neurogenesis. Our findings strongly suggest that this genetic evolution was key for cortical expansion in amniotes and the emergence of landmark features of the mammalian neocortex: formation of IPCs, SVZ, and layer 2/3 neurons (Cheung et al., 2010).

The evolution of development is thought to be significantly driven by gene cooption, promoting new uses for an existing genetic toolkit (True and Carroll, 2002). Previous studies demonstrate that the emergence of novel genes was likely central in the evolutionary expansion of the human cerebral cortex (Florio et al., 2015; Florio et al., 2017). Our results demonstrate for the first time the existence of a new and orthogonal mechanism driving cortical expansion in evolution: regulation of the activity levels of a highly conserved signaling pathway (Brose et al., 1999). High Robo signaling drives direct neurogenesis, limiting neuron number and size of telencephalic structures, as in OB and nonmammalian cortex, while low Robo allows indirect neurogenesis, producing basal progenitors and more neurons as in the mammalian NCx. However, complete absence of Robo, as in knockout mice, is severely deleterious to basal progenitors, impairing further expansion of NCx (Borrell et al., 2012). In the OB of these mutants, this deleterious effect combines with the suppressed direct neurogenesis, resulting in much-reduced neuron production and OB size. RGCs in direct neurogenesis mode have a longer cell cycle than in indirect mode, so loss of Robo also alters frequency of their apical mitoses. The magnitude of this effect varies between cortical regions (Borrell et al., 2012 and this study), likely owing to axial gradients in cortical development.

Our results show that the mode of neurogenesis is determined by the interaction between Robo and Notch signaling. High

Figure 6. Robo/Dil1 Signaling Regulates the Balance between Direct Neurogenesis and IPC Abundance in Chick Dorsal Pallium

(A–D) Analysis of chick dorsal pallium at 6 days post-oviposition (dpo), showing many neurons in the VZ (solid arrowheads) in the medial part (mDP; B) and basal mitoses (open arrowheads) in the lateral (lDP; C; n = 3 embryos; t tests).

(E–H) ISH in chick DP at 6 dpo, and quantifications of intensity (au, arbitrary units). High magnifications show *chkRobo1* (E' and E'') and *chkDil1* (G' and G'') in the indicated regions. Panel shown in (G) is a tiled image.

(I) qPCR analysis in the VZ of the regions and species indicated. Values are ratio *Robo1* to *Gapdh* (n = 12–15 replicates; paired or independent samples t tests).

(J–O) Experimental design to manipulate in ovo Robo and Dil1 in mDP and lDP, representative examples and quantifications of neurons in the VZ (*Tbr1+*) and basal mitoses (PH3, open arrowheads; n = 3–5 embryos per group; t tests in L and Q; one-way ANOVA followed by t tests in M and O). Red shadowing and asterisks in (L) and (O) indicate values within group corresponding to GFP- cells.

(P and Q) Expression of *Tbr2* in basal PH3+ mitoses (solid arrowhead, *Tbr2+*; open arrowhead, *Tbr2-*) upon electroporation of *dnR1/2+Dil1* in mDP (as in J and K), and quantification (n = 4–5 embryos; t tests).

(R–U) Analysis of neuronal clones (GFP+RFP+*Tuj1+*) upon overexpression of *dnR1/2+Dil1+Gfp*, representative examples and quantification (n = 52 clones Gfp, 59 clones *dnR1/2+Dil1+Gfp*, 3–7 embryos; t test or χ^2 -test).

Values are mean + SEM; *p < 0.05; **p < 0.01; ***p < 0.001. Scale bars: 100 μ m (A, E, F, and G), 50 μ m (B, C, K, N, P, and S).

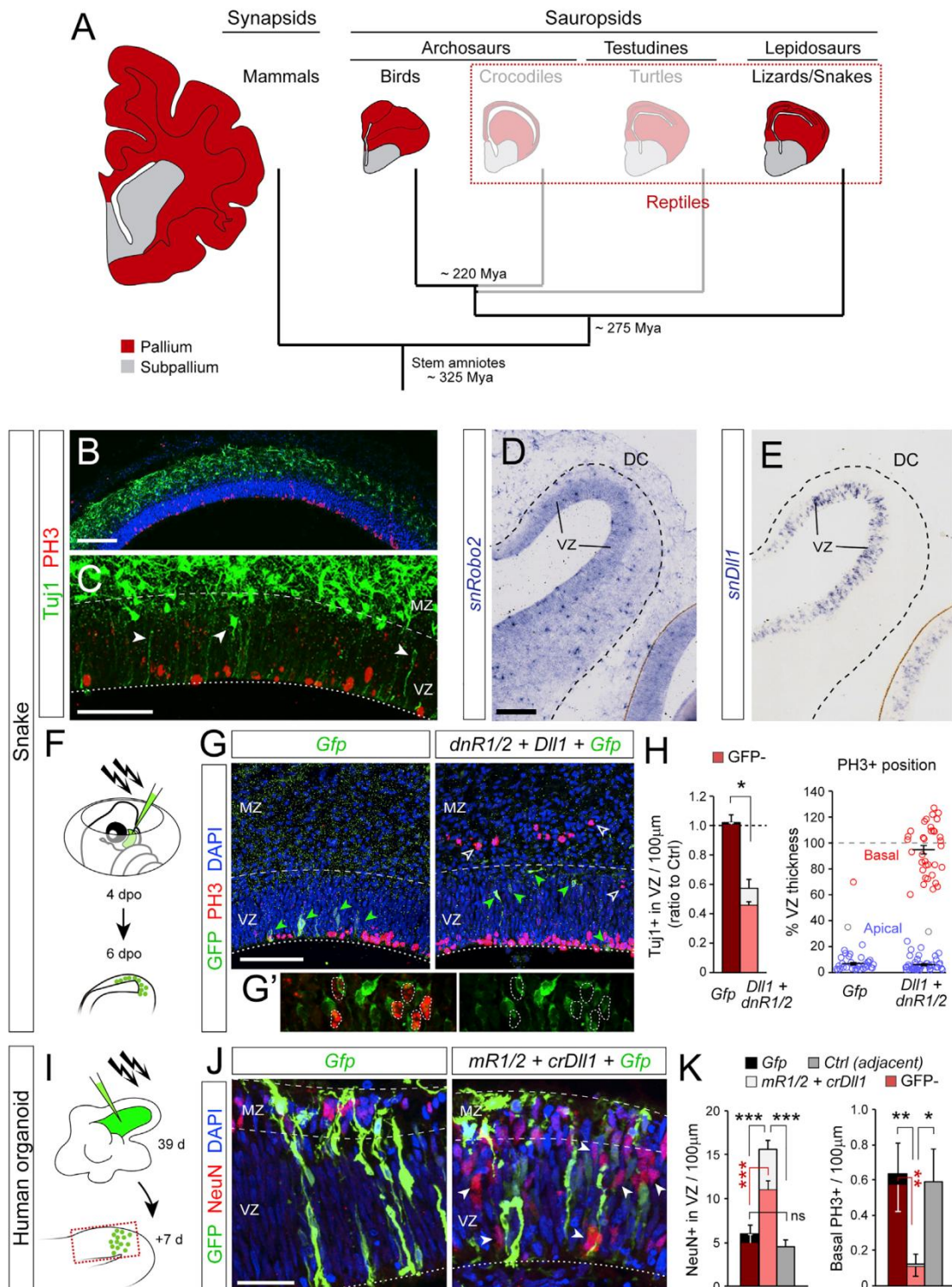


Figure 7. Conserved Function of Robo/Dll1 in Snake and Human Cortex to Regulate the Balance between Direct Neurogenesis and Basal Progenitor Formation

(A) Simplified phylogenetic tree of amniotes with approximate reference to relative brain size and layout. (B and C) Dorsal cortex of snake embryo at 6 dpo with neurons in the VZ (arrowheads) and apical but not basal mitoses (red). (D and E) ISH against snake Robo2 and Dll1 in snake dorsal cortex (DC) at 6 dpo. These panels are tiled images.

(legend continued on next page)

levels of Robo block expression of *Dll1*, and this combination promotes expression of *Jag1* and *Jag2*, driving direct neurogenesis, as observed in OB and contrary to the NCx. The classical Dll-Notch lateral inhibition pathway establishes that the levels of Dll1 determine the level of Notch activity on signal-receiving cells and thereon the fate of daughter cells (Kawaguchi et al., 2008). Here, we find that a shift in Notch ligand composition, without a significant variation in total Notch activity, defines the fate of daughter cells (neurons or IPCs) and thus the mode of neurogenesis. A similar mechanism determines the mode of tumor angiogenesis, depending on whether the Notch ligand is Jag or Dll (Kangsamaksin et al., 2015). Different Dll ligands activate Notch with different temporal dynamics, with consequences on downstream signaling including *Hes1* expression and fate of daughter cells in the chick neural crest (Nandagopal et al., 2018). Accordingly, our current and previous results from OB and NCx in Robo mutants (Borrell et al., 2012) congruently suggest that the presence or absence of *Jag1* and *Jag2* in the context of high or low levels of Robo expression, as in OB and NCx respectively, modifies how Robo influences *Hes1* expression in the telencephalon.

Previous studies of Dll1 manipulation have shown premature neurogenesis upon massive (but not sparse) loss of Dll1 (Kawaguchi et al., 2008). This may explain why our sparse electroporation of crDll1 alone is not sufficient to drive direct neurogenesis in NCx but requires the cooperation of Robo signaling to sufficiently block Dll1. We find that this increased direct neurogenesis in high Robo and loss of Dll1 may be mediated by upregulation of *Jag1* and *Jag2* and is coherent with the inverse effect of sparse overexpression of Dll1, promoting indirect neurogenesis (Kawaguchi et al., 2008). Future investigations should detail the molecular links between Robo, Dll, and Jag to regulate modes of neurogenesis.

The influence of Robo signaling on cortical expansion extends much beyond driving direct neurogenesis. Our results show that endogenous high Robo signaling prevents the formation of basal progenitors in the snake dorsal cortex, where they are virtually absent. Particularly remarkable is our finding in the dorsal cortex of snake embryos: experimental loss of Robo and gain of Dll1 is sufficient to induce *de novo* formation of abundant basal progenitors. These align basal to the VZ forming a proto-SVZ, recapitulating in a snake a process otherwise restricted to the mammalian NCx. Altogether, our experiments potentially uncover the key events that occurred during evolution of the mammalian brain: attenuation of Robo receptor signaling intensity was responsible for the evolutionary emergence of cortical basal progenitors and the SVZ; and the blockade of direct neurogenesis, which combined allowed the subsequent phenomenal expansion and complexification of the mammalian cerebral cortex.

STAR★METHODS

Detailed methods are provided in the online version of this paper and include the following:

- KEY RESOURCES TABLE
- CONTACT FOR REAGENT AND RESOURCE SHARING
- EXPERIMENTAL MODEL AND SUBJECT DETAILS
 - Mice
 - Chicken
 - Snake
 - Human organoids
 - Retinal explant cultures
- METHODS DETAILS
 - Immunohistochemistry and ISH
 - Bromodeoxyuridine labeling experiments
 - Constructs
 - Validation of Crispr/Cas-mediated gene editing
 - Embryonic brain electroporation
 - Retinal electroporation
 - Imaging experiments
 - Retroviral stocks preparation and concentration
 - Single progenitor clonal analysis
 - Tissue microdissection and quantitative real-time PCR
 - Reprogramming of human fibroblasts to induced pluripotent stem cells
 - iPSC culture
 - Cerebral organoids generation
 - Electroporation of cerebral organoids
 - Retinal growth cones collapse assay
 - MyrRobo1/2 construct validation
 - Neuron tracing experiments
- QUANTIFICATION AND STATISTICAL ANALYSIS
 - Histological analysis
 - Bromodeoxyuridine labeling experiments
 - Electroporation analysis
 - Imaging experiments
 - Single progenitor clonal analysis
 - Quantitative real-time PCR
 - Robo construct validation

SUPPLEMENTAL INFORMATION

Supplemental Information includes seven figures, one table, and five videos and can be found with this article online at <https://doi.org/10.1016/j.cell.2018.06.007>.

ACKNOWLEDGMENTS

We thank E. Llorens, S. Amin, and G. Exposito for excellent technical and imaging assistance, J. Galcerán, E. Herrera, B. Rico, A. Fairén, O. Marín,

(F–H) Experimental design for in ovo genetic manipulation of snake DC, representative examples and quantifications (n = 3–4 embryos per group; t tests). White arrowheads indicate basal mitoses, green arrowheads indicate GFP+ cells, typically sparse. Details in (G') are examples of basal mitoses in GFP– cells. Right plot in (H) shows the location of PH3+ nuclei (circles) relative to the apical-basal extent of the VZ.

(I–K) Experimental design for genetic manipulation of human cerebral organoids, examples, and quantifications (n = 3–4 organoids per group; t tests). Arrowheads indicate NeuN+ neurons in the VZ. Red shadowing in (H) and (K) indicates values within group corresponding to GFP– cells. Values are mean + SEM; *p < 0.05; **p < 0.01; ***p < 0.001; ns, not significant. MZ, mantle zone. Scale bars: 150 μm (B, D, and E), 75 μm (C and G), 50 μm (J). See also Figure S6.

and E. Stein for plasmids, O. Marín for GAD67-GFP mice, and M. Götz and E. Herrera for tips on videomicroscopy and collapse assays. We thank A. Nieto, M. Domínguez, D. Lyon, A. Bigas, I. Fariñas, and M. Milinkovitch for insightful discussions and critical reading of manuscript. A.C. was the recipient of an FPI fellowship from the Spanish Ministry of Economy, Industry, and Competitiveness (MINEICO) (BES-2010-030842), and C.d.J.R. was the recipient of an Eduardo Gallego Fellowship from Fundación Francisco Cobos. Work was supported by grants to A.C.T. from the Swiss National Science Foundation (FNSNF, grants 31003A_140785 and SINERGIA CRS113_132430) and a SystemsX.ch initiative (project EpiPhysX); to L.M. from NIH (NIH-NS062047); and to V.B. from MINEICO (BFU2012-03763, SAF2015-69168-R) and the European Research Council (309633). V.B. acknowledges financial support from the Spanish State Research Agency through the “Severo Ochoa” Programme for Centers of Excellence in R&D (ref. SEV-2013-0317).

AUTHOR CONTRIBUTIONS

Conceptualization, A.C. and V.B.; Methodology, A.C.; Investigation, A.C., A.V., C.d.J.R., E.P., C.K., A.C.T., L.M., and M.D.; Resources, M.T.-L., L.M., S.C., and V.B.; Writing – Original Draft, V.B.; Writing – Review & Editing, V.B.; Visualization, V.B.; Supervision, V.B.; Funding Acquisition, C.d.J.R., A.C.T., L.M., and V.B.

DECLARATION OF INTERESTS

The authors declare no competing interests.

Received: October 11, 2017

Revised: February 24, 2018

Accepted: June 1, 2018

Published: June 28, 2018

REFERENCES

- Arai, Y., Pulvers, J.N., Haffner, C., Schilling, B., Nüsslein, I., Calegari, F., and Huttner, W.B. (2011). Neural stem and progenitor cells shorten S-phase on commitment to neuron production. *Nat. Commun.* **2**, 154.
- Attardo, A., Calegari, F., Haubensak, W., Wilsch-Bräuninger, M., and Huttner, W.B. (2008). Live imaging at the onset of cortical neurogenesis reveals differential appearance of the neuronal phenotype in apical versus basal progenitor progeny. *PLoS ONE* **3**, e2388.
- Bai, G., Chivatakarn, O., Bonanomi, D., Lettieri, K., Franco, L., Xia, C., Stein, E., Ma, L., Lewcock, J.W., and Pfaff, S.L. (2011). Presenilin-dependent receptor processing is required for axon guidance. *Cell* **144**, 106–118.
- Blanchart, A., Martín-López, E., De Carlos, J.A., and López-Mascaraque, L. (2011). Peripheral contributions to olfactory bulb cell populations (migrations towards the olfactory bulb). *Glia* **59**, 278–292.
- Borrell, V., and Marín, O. (2006). Meninges control tangential migration of hem-derived Cajal-Retzius cells via CXCL12/CXCR4 signaling. *Nat. Neurosci.* **9**, 1284–1293.
- Borrell, V., Cárdenas, A., Ciceri, G., Galcerán, J., Flames, N., Pla, R., Nóbrega-Pereira, S., García-Frigola, C., Peregrín, S., Zhao, Z., et al. (2012). Slit/Robo signaling modulates the proliferation of central nervous system progenitors. *Neuron* **76**, 338–352.
- Brose, K., Bland, K.S., Wang, K.H., Amott, D., Henzel, W., Goodman, C.S., Tessier-Lavigne, M., and Kidd, T. (1999). Slit proteins bind Robo receptors and have an evolutionarily conserved role in repulsive axon guidance. *Cell* **96**, 795–806.
- Cheung, A.F., Pollen, A.A., Tavares, A., DeProto, J., and Molnár, Z. (2007). Comparative aspects of cortical neurogenesis in vertebrates. *J. Anat.* **211**, 164–176.
- Cheung, A.F., Kondo, S., Abdel-Mannan, O., Chodroff, R.A., Sirey, T.M., Bluy, L.E., Webber, N., DeProto, J., Karlen, S.J., Krubitzer, L., et al. (2010). The subventricular zone is the developmental milestone of a 6-layered neocortex: comparisons in metatherian and eutherian mammals. *Cereb. Cortex* **20**, 1071–1081.
- Das, R.M., and Storey, K.G. (2014). Apical abscission alters cell polarity and dismantles the primary cilium during neurogenesis. *Science* **343**, 200–204.
- De Juan Romero, C., and Borrell, V. (2015). Coevolution of radial glial cells and the cerebral cortex. *Glia* **63**, 1303–1319.
- Dugas-Ford, J., and Ragsdale, C.W. (2015). Levels of homology and the problem of neocortex. *Annu. Rev. Neurosci.* **38**, 351–368.
- Englund, C., Fink, A., Lau, C., Pham, D., Daza, R.A., Bulfone, A., Kowalczyk, T., and Hevner, R.F. (2005). Pax6, Tbr2, and Tbr1 are expressed sequentially by radial glia, intermediate progenitor cells, and postmitotic neurons in developing neocortex. *J. Neurosci.* **25**, 247–251.
- Escalante, A., Murillo, B., Morenilla-Palao, C., Klar, A., and Herrera, E. (2013). Zic2-dependent axon midline avoidance controls the formation of major ipsilateral tracts in the CNS. *Neuron* **80**, 1392–1406.
- Finlay, B.L., and Darlington, R.B. (1995). Linked regularities in the development and evolution of mammalian brains. *Science* **268**, 1578–1584.
- Fish, J.L., Dehay, C., Kennedy, H., and Huttner, W.B. (2008). Making bigger brains—the evolution of neural-progenitor-cell division. *J. Cell Sci.* **121**, 2783–2793.
- Florio, M., Albert, M., Taverna, E., Namba, T., Brandl, H., Lewitus, E., Haffner, C., Sykes, A., Wong, F.K., Peters, J., et al. (2015). Human-specific gene ARHGAP11B promotes basal progenitor amplification and neocortex expansion. *Science* **347**, 1465–1470.
- Florio, M., Borrell, V., and Huttner, W.B. (2017). Human-specific genomic signatures of neocortical expansion. *Curr. Opin. Neurobiol.* **42**, 33–44.
- Gong, Q., and Shipley, M.T. (1995). Evidence that pioneer olfactory axons regulate telencephalon cell cycle kinetics to induce the formation of the olfactory bulb. *Neuron* **14**, 91–101.
- Hansen, D.V., Lui, J.H., Parker, P.R., and Kriegstein, A.R. (2010). Neurogenic radial glia in the outer subventricular zone of human neocortex. *Nature* **464**, 554–561.
- Haubensak, W., Attardo, A., Denk, W., and Huttner, W.B. (2004). Neurons arise in the basal neuroepithelium of the early mammalian telencephalon: a major site of neurogenesis. *Proc. Natl. Acad. Sci. USA* **101**, 3196–3201.
- Ishibashi, M., Ang, S.L., Shiota, K., Nakanishi, S., Kageyama, R., and Guillemot, F. (1995). Targeted disruption of mammalian hairy and Enhancer of split homolog-1 (HES-1) leads to up-regulation of neural helix-loop-helix factors, premature neurogenesis, and severe neural tube defects. *Genes Dev.* **9**, 3136–3148.
- Kangsamaksin, T., Murtomaki, A., Kofler, N.M., Cuervo, H., Chaudhri, R.A., Tattersall, I.W., Rosenstiel, P.E., Shawber, C.J., and Kitajewski, J. (2015). NOTCH decoys that selectively block DLL/NOTCH or JAG/NOTCH disrupt angiogenesis by unique mechanisms to inhibit tumor growth. *Cancer Discov.* **5**, 182–197.
- Kawaguchi, D., Yoshimatsu, T., Hozumi, K., and Gotoh, Y. (2008). Selection of differentiating cells by different levels of delta-like 1 among neural precursor cells in the developing mouse telencephalon. *Development* **135**, 3849–3858.
- Koutelou, E., Sato, S., Tomomori-Sato, C., Florens, L., Swanson, S.K., Washburn, M.P., Kokkinaki, M., Conaway, R.C., Conaway, J.W., and Moschonas, N.K. (2008). Neuralized-like 1 (Neur1) targeted to the plasma membrane by N-myristoylation regulates the Notch ligand Jagged1. *J. Biol. Chem.* **283**, 3846–3853.
- Kowalczyk, T., Pontious, A., Englund, C., Daza, R.A., Bedogni, F., Hodge, R., Attardo, A., Bell, C., Huttner, W.B., and Hevner, R.F. (2009). Intermediate neuronal progenitors (basal progenitors) produce pyramidal-projection neurons for all layers of cerebral cortex. *Cereb. Cortex* **19**, 2439–2450.
- Kriegstein, A., Noctor, S., and Martínez-Cerdeño, V. (2006). Patterns of neural stem and progenitor cell division may underlie evolutionary cortical expansion. *Nat. Rev. Neurosci.* **7**, 883–890.
- Lancaster, M.A., and Knoblich, J.A. (2014). Generation of cerebral organoids from human pluripotent stem cells. *Nat. Protoc.* **9**, 2329–2340.

- López-Bendito, G., Sturgess, K., Erdelyi, F., Szabo, G., Molnar, Z., and Paulsen, O. (2004). Preferential origin and layer destination of GAD65-GFP cortical interneurons. *Cereb. Cortex* *14*, 1122–1133.
- Malatesta, P., Hartfuss, E., and Götz, M. (2000). Isolation of radial glial cells by fluorescent-activated cell sorting reveals a neuronal lineage. *Development* *127*, 5253–5263.
- Marillat, V., Cases, O., Nguyen-Ba-Charvet, K.T., Tessier-Lavigne, M., Sotelo, C., and Chédotal, A. (2002). Spatiotemporal expression patterns of slit and robo genes in the rat brain. *J. Comp. Neurol.* *442*, 130–155.
- Martínez-Martínez, M.A., De Juan Romero, C., Fernández, V., Cárdenas, A., Götz, M., and Borrell, V. (2016). A restricted period for formation of outer subventricular zone defined by *Cdh1* and *Trnp1* levels. *Nat. Commun.* *7*, 11812.
- Miyata, T., Kawaguchi, A., Saito, K., Kawano, M., Muto, T., and Ogawa, M. (2004). Asymmetric production of surface-dividing and non-surface-dividing cortical progenitor cells. *Development* *131*, 3133–3145.
- Nandagopal, N., Santat, L.A., LeBon, L., Sprinzak, D., Bronner, M.E., and Elowitz, M.B. (2018). Dynamic Ligand Discrimination in the Notch Signaling Pathway. *Cell* *172*, 869–880 e819.
- Nelson, B.R., Hodge, R.D., Bedogni, F., and Hevner, R.F. (2013). Dynamic interactions between intermediate neurogenic progenitors and radial glia in embryonic mouse neocortex: potential role in *Dll1*-Notch signaling. *J. Neurosci.* *33*, 9122–9139.
- Nguyen-Ba-Charvet, K.T., Di Meglio, T., Fouquet, C., and Chédotal, A. (2008). Robos and slits control the pathfinding and targeting of mouse olfactory sensory axons. *J. Neurosci.* *28*, 4244–4249.
- Noctor, S.C., Flint, A.C., Weissman, T.A., Dammerman, R.S., and Kriegstein, A.R. (2001). Neurons derived from radial glial cells establish radial units in neocortex. *Nature* *409*, 714–720.
- Noctor, S.C., Martínez-Cerdeño, V., Ivic, L., and Kriegstein, A.R. (2004). Cortical neurons arise in symmetric and asymmetric division zones and migrate through specific phases. *Nat. Neurosci.* *7*, 136–144.
- Nomura, T., Ohtaka-Maruyama, C., Yamashita, W., Wakamatsu, Y., Murakami, Y., Calegari, F., Suzuki, K., Gotoh, H., and Ono, K. (2016). The evolution of basal progenitors in the developing non-mammalian brain. *Development* *143*, 66–74.
- Northcutt, R.G. (2002). Understanding vertebrate brain evolution. *Integr. Comp. Biol.* *42*, 743–756.
- Pilz, G.A., Shitamukai, A., Reillo, I., Pacary, E., Schwausch, J., Stahl, R., Ninkovic, J., Snippert, H.J., Clevers, H., Godinho, L., et al. (2013). Amplification of progenitors in the mammalian telencephalon includes a new radial glial cell type. *Nat. Commun.* *4*, 2125.
- Puelles, L., Kuwana, E., Puelles, E., Bulfone, A., Shimamura, K., Keleher, J., Smiga, S., and Rubenstein, J.L. (2000). Pallial and subpallial derivatives in the embryonic chick and mouse telencephalon, traced by the expression of the genes *Dlx-2*, *Emx-1*, *Nkx-2.1*, *Pax-6*, and *Tbr-1*. *J. Comp. Neurol.* *424*, 409–438.
- Ran, F.A., Hsu, P.D., Wright, J., Agarwala, V., Scott, D.A., and Zhang, F. (2013). Genome engineering using the CRISPR-Cas9 system. *Nat. Protoc.* *8*, 2281–2308.
- Rowe, T.B., Macrini, T.E., and Luo, Z.X. (2011). Fossil evidence on origin of the mammalian brain. *Science* *332*, 955–957.
- Smart, I.H., Dehay, C., Giroud, P., Berland, M., and Kennedy, H. (2002). Unique morphological features of the proliferative zones and postmitotic compartments of the neural epithelium giving rise to striate and extrastriate cortex in the monkey. *Cereb. Cortex* *12*, 37–53.
- Stein, E., and Tessier-Lavigne, M. (2001). Hierarchical organization of guidance receptors: silencing of netrin attraction by slit through a Robo/DCC receptor complex. *Science* *291*, 1928–1938.
- Tashiro, A., Zhao, C., and Gage, F.H. (2006). Retrovirus-mediated single-cell gene knockout technique in adult newborn neurons in vivo. *Nat. Protoc.* *1*, 3049–3055.
- Taverna, E., Götz, M., and Huttner, W.B. (2014). The cell biology of neurogenesis: toward an understanding of the development and evolution of the neocortex. *Annu. Rev. Cell Dev. Biol.* *30*, 465–502.
- True, J.R., and Carroll, S.B. (2002). Gene co-option in physiological and morphological evolution. *Annu. Rev. Cell Dev. Biol.* *18*, 53–80.
- Vasistha, N.A., García-Moreno, F., Arora, S., Cheung, A.F., Arnold, S.J., Robertson, E.J., and Molnár, Z. (2015). Cortical and Clonal Contribution of *Tbr2* Expressing Progenitors in the Developing Mouse Brain. *Cereb. Cortex* *25*, 3290–3302.

STAR★METHODS

KEY RESOURCES TABLE

REAGENT or RESOURCE	SOURCE	IDENTIFIER
Antibodies		
Rat monoclonal anti-BrdU	Abcam	Cat# ab6326, RRID:AB_2313786
Rabbit polyclonal anti-cleaved Caspase 3	Cell signaling	Cat# 9661, RRID:AB_2341188
Chicken polyclonal anti-GFP	Aves Lab	Cat# GFP-1020, RRID:AB_10000240
Rabbit polyclonal anti-Ki67	Abcam	Cat# ab15580, RRID:AB_443209
Rabbit polyclonal anti-phosphohistone H3	Upstate	Cat# 06-570, RRID:AB_310177
Rabbit polyclonal anti-Tbr1	Abcam	Cat# ab31940, RRID:AB_2200219
Rabbit polyclonal anti-Tbr2	Abcam	Cat# ab23345, RRID:AB_778267
Mouse monoclonal anti-βIII tubulin	Covance	Cat# MMS-435P, RRID:AB_2313773
Rabbit polyclonal anti-Pax6	Merck Millipore	Cat# AB2237, RRID:AB_1587367
Rabbit polyclonal anti-GABA	Sigma	Cat# A2052, RRID:AB_477652
Rabbit polyclonal anti-Reelin	MBL	Cat# D223-3, RRID:AB_843523
Rabbit polyclonal anti-Cux1	Santa Cruz	Cat# sc-13024, RRID:AB_2261231
Rat monoclonal anti-Ctip2	Abcam	Cat# ab18465, RRID:AB_2064130
Mouse monoclonal anti-NeuN	Merck Millipore	Cat# MAB377, RRID:AB_2298772
Sheep polyclonal anti-Dll1	R&D Systems	Cat# AF3970, RRID:AB_2092836
Goat polyclonal anti-Robo1	R&D Systems	Cat# AF1749, RRID:AB_354969
Goat polyclonal anti-Robo2	R&D Systems	Cat# AF3147, RRID:AB_2181857
Rabbit polyclonal anti-DsRed	Clontech Laboratories	Cat# 632496, RRID:AB_10013483
Mouse monoclonal anti-c-Myc (9E10)	Santa Cruz	Cat# sc-40, RRID:AB_627268
Donkey Alexa488 anti-mouse IgG	Invitrogen	Cat# A-21202, RRID:AB_141607
Donkey Alexa555 anti-mouse IgG	Invitrogen	Cat# A-31570, RRID:AB_2536180
Donkey Alexa488 anti-rabbit IgG	Invitrogen	Cat# A-21206, RRID:AB_141708
Donkey Alexa555 anti-rabbit IgG	Invitrogen	Cat# A-31572, RRID:AB_162543
Donkey Alexa488 anti-chicken IgY	Jackson ImmunoResearch	Cat# 703-545-155, RRID:AB_2340375
Cy2-streptavidin	Jackson ImmunoResearch	Cat# 016-220-084, RRID:AB_2337246
Cy5-streptavidin	Jackson ImmunoResearch	Cat# 016-170-084, RRID:AB_2337245
Goat Biotinylated anti-Rabbit IgG	Vector Laboratories	Cat# BA-1000, RRID:AB_2313606
Goat Biotinylated anti-Rat IgG	Vector Laboratories	Cat# BA-9400, RRID:AB_2336202
Donkey Cy3 Fab fragment anti-Rat IgG	Jackson ImmunoResearch	Cat# 712-167-003, RRID:AB_2340670
Donkey Cy3 Fab fragment anti-Rabbit IgG	Jackson ImmunoResearch	Cat# 711-167-003, RRID:AB_2340606
Donkey Cy3 anti-Mouse IgG	Jackson ImmunoResearch	Cat# 715-165-150, RRID:AB_2340813
Alkaline phosphatase-coupled anti-digoxigenin Fab	Sigma	Cat# 11093274910, RRID:AB_514497
Donkey Alexa555 anti-Goat IgG	Thermo Fisher Scientific	Cat# A-21432, RRID:AB_2535853
Donkey Alexa 555 anti-Sheep IgG	Thermo Fisher Scientific	Cat# A-21436, RRID:AB_2535857
Bacterial and Virus Strains		
MMLV-based RV CAG-GFP	Tashiro et al., 2006	N/A
MMLV-based RV CAG-RFP	Tashiro et al., 2006	N/A
Chemicals, Peptides, and Recombinant Proteins		
Cholera toxin subunit B (CTB)	Thermo Fisher Scientific	Cat# C22842
Nucleofector Kits for Rat Neurons	Lonza	Cat# V4XP-3012
Recombinant Mouse Slit2 Protein, CF	R&D Systems	Cat# Q9R1B9
5-Bromo-2'-deoxyuridine	Sigma	Cat# B5002

(Continued on next page)

Continued

REAGENT or RESOURCE	SOURCE	IDENTIFIER
DIG RNA labeling mix	Roche	Cat# 11277073910
T3 polymerase	Roche	Cat# RPOLT3-RO
T7 polymerase	Roche	Cat# 10881767001
Sheep serum	Sigma	Cat# S2263
BCIP	Roche	Cat# 10881767001
NBT	Roche	Cat# 11087479001
Blocking reagent	Roche	Cat# 11096176001
Methylcellulose	Sigma	Cat# M0262
DMEM/F12	Thermo Fisher Scientific	Cat# 11320033
Insulin-transferrin-sodium selenite media supplement	Sigma	Cat# I1884
Corning® BioCoat Poly-L-Lysine 12 mm #1 German Glass Coverslip, 40/Pack, 80/Case	Thermo Fisher Scientific	Cat# 354085
HyClone Fetal Bovine Serum	GE Healthcare	Cat# SV30160.03HI
Pluriton Reprogramming Medium	Stemgent	Cat# 00-0070
carrier-free B18R Recombinant Protein	Stemgent	Cat# 03-0017
Lipofectamine RNAiMAX Transfection Reagent	Thermo Fisher Scientific	Cat# 31985062
STEMPRO hESC SFM	Thermo Fisher Scientific	Cat# A1000701
Collagenase Type IV	Thermo Fisher Scientific	Cat# 17104019
mTeSR1	StemCell Technologies	Cat# 05850
LDEV-Free Geltrex	Thermo Fisher Scientific	Cat# A1413302
Geltrex	Thermo Fisher Scientific	Cat# A1413302
StemPro Accutase Cell Dissociation Reagent	Life Technologies	Cat# A1110501
Rock inhibitor Y-27632(2HCl)	StemCell Technologies	Cat# 72304
Matrigel	Corning	Cat# 354234
Critical Commercial Assays		
SURVEYOR® Mutation Detection Kit - S100	IDT	Cat# 706020
pGEM®-T Easy Vector Systems	Promega	Cat# A1360
Maxima First Strand cDNA Synthesis Kit for RT-qPCR	Thermo Fisher Scientific	Cat# K1641
E.Z.N.A Plasmid DNA Mini Kit I	Omega	D6943-02
GFX PCR DNA and Gel Band Purification Kit	GE Healthcare	28-9034-70
RNeasy® Mini Kit	QIAGEN	Ref.74104
DNA, RNA and Protein Purification	Macherey-nagel	Ref.740410.50
Fast SYBR Green Master Mix	Life Technologies	Cat# 4385612
KAPA HiFi HotStart ReadyMix	Kapa Biosystems	Cat# KK2602
Experimental Models: Cell Lines		
Human embryonic kidney 293T	ATCC	Cat# CRL-3216, RRID:CVCL_0063
Human induced pluripotent stem cells (hiPSCs)	ATCC	Cat# CRL-2522, RRID:CVCL_3653
NuFF3-RQ IRR Human newborn foreskin feeder fibroblast	GlobalStem	GSC-3404
Experimental Models: Organisms/Strains		
<i>Gallus gallus</i> , fertilized chicken eggs	Granja Santa Isabel, Córdoba	www.granjasantaisabel.com ; Cat#800008
<i>Lamprophis fuliginosus</i> , fertilized snake eggs	Michel C. Milinkovitch's lab	https://www.lanevol.org/
ICR wild type	Jackson Laboratory	N/A
C57BL/6J mice	Jackson Laboratory	Cat#000664; RRID:SCR_004633; http://www.jax.org/
Slit1/2 knock out [CD-1/129Sv/C57BL/6]	Borrell et al., 2012 ; Thomas Jefferson University	N/A

(Continued on next page)

Continued		
REAGENT or RESOURCE	SOURCE	IDENTIFIER
Robo1/Robo2 knock out	Instituto de Neurociencias de Alicante; Borrell et al., 2012	N/A
GAD65-GFP p(C57/b6) transgenic mice	López-Bendito et al., 2004	N/A
Oligonucleotides		
See Table S1 for Crispr guides, qRT-RNA primers, ISH probes and Crispr validation primers	This paper	N/A
Recombinant DNA		
Expression plasmid: MMLV Retroviral CAG-GFP	F.H. Gage gift	N/A
Expression plasmid: MMLV Retroviral CAG-RFP	F.H. Gage gift	N/A
Expression plasmid: CMV-GP	F.H. Gage gift	N/A
Expression plasmid: CMV-VSVG	F.H. Gage gift	N/A
Expression plasmid: pCIG-DII1 plasmid	J. Galcerán gift	N/A
Expression plasmid: pCAG-Floxp-EGFP-farnesylated	M. Gotz (Pilz et al., 2013)	N/A
Expression plasmid: pCAG-Cre	M. Gotz (Pilz et al., 2013)	N/A
Expression plasmid: pCAG-Dn-Robo1	E. Stein gift (Stein and Tessier-Lavigne, 2001)	N/A
Expression plasmid: pCAG-Dn-Robo2	E. Stein gift (Stein and Tessier-Lavigne, 2001)	N/A
Expression plasmid: pCAG-myrRobo1	Borrell et al., 2012	N/A
Expression plasmid: pCAG-myrRobo2	Borrell et al., 2012	N/A
Expression plasmid: pSpCas9(BB)-2A-GFP (PX458)	Ran et al., 2013	Addgene Plasmid #48138
Expression plasmid: Jag1-HA pIRES	Koutelou et al., 2008	Addgene Plasmid #17336
Expression plasmid: pUC19ckDII1	J. Galcerán gift	N/A
Expression plasmid: pCMV-Myc-NICD-FL	J. Galcerán gift	N/A
Plasmid ISH probe: MsRobo1	O. Marín gift; Borrell et al., 2012	N/A
Plasmid ISH probe: MsRobo2	O. Marín gift; Borrell et al., 2012	N/A
Plasmid ISH probe: MsSlit1	O. Marín gift; Borrell et al., 2012	N/A
Plasmid ISH probe: MsSlit2	O. Marín gift; Borrell et al., 2012	N/A
Plasmid ISH probe: MsSlit3	O. Marín gift; Borrell et al., 2012	N/A
Plasmid ISH probe: MsHes5	R. Kageyama gift; Borrell et al., 2012	N/A
Plasmid ISH probe: MsDII1	J. L. R. Rubenstein; Borrell et al., 2012	N/A
Plasmid ISH probe: MsNotch1	J. L. R. Rubenstein; Borrell et al., 2012	N/A
Plasmid ISH probe: MsReelin	Borrell and Marín, 2006	N/A
Plasmid ISH probe: MsGrm1	A. Fairén gift	N/A
Plasmid ISH probe: MsBhlhe22	A. Fairén gift	N/A
Plasmid ISH probe: MsTbr2	B. Rico gift	N/A
Plasmid ISH probe: MsJag 1	Francois Guillemot gift	N/A
Plasmid ISH probe: MsJag 2	Francois Guillemot gift	N/A
Plasmid ISH probe: ChRobo1	Escalante et al., 2013	N/A
Plasmid ISH probe: ChRobo2	Escalante et al., 2013	N/A
Plasmid ISH probe: ChDII1	This paper	N/A
Plasmid ISH probe: SnRobo1	This paper	N/A
Plasmid ISH probe: SnRobo2	This paper	N/A
Plasmid ISH probe: SnDII1	This paper	N/A
Software and Algorithms		
Imaris 8	Bitplane	http://www.bitplane.com/Imaris ; RRID:SCR_007370

(Continued on next page)

Continued

REAGENT or RESOURCE	SOURCE	IDENTIFIER
ImageJ (Fiji), version 2.0.0	National Institutes of Health	https://imagej.net/Fiji ; RRID:SCR_003070
NeuroLucida Neuron Tracing Software	MBF Bioscience	http://www.mbfioscience.com/neuroLucida ; RRID:SCR_001775
SPSS 19	IBM	https://ibm-spss-statistics-64bits.softonic.com/?ex=BB-39.6 ; RRID:SCR_002865
Snapgene	Biotech LLC	http://www.snapgene.com/ ; RRID:SCR_015053
DNASTAR Lasergene Software	DNASTAR	https://www.dnastar.com/ ; RRID:SCR_000291
Blue ZEN 2.3 pro	Zeiss	https://www.zeiss.com/microscopy/int/products/microscope-software/zen.html ; RRID:SCR_013672
FV10-ASW 4.2 Software	Olympus	http://www.olympus-lifescience.com/en/ ; RRID:SCR_014215
LAS software	Leica Microsystems, Germany	https://www.leica-microsystems.com/products/microscope-software/ ; RRID:SCR_013673
StepOne Real-Time PCR Software v2.2	Applied Biosystems by Life technologies	https://www.thermofisher.com/mx/en/home/technical-resources/software-downloads/StepOne-and-StepOnePlus-Real-Time-PCR-System.html ; RRID:SCR_014281

CONTACT FOR REAGENT AND RESOURCE SHARING

Further information and request for resources and reagents should be directed to and will be fulfilled by the Lead Contact, Victor Borrell (vborell@umh.es).

EXPERIMENTAL MODEL AND SUBJECT DETAILS

None of the animals used in our experiments had been previously used for other procedures. All subjects were test- and drug-naive. The animals presented a healthy status and were employed independently of their gender. The developmental stage of experimental models was chosen depending on the requirements of each experiment, as further detailed below.

Mice

To generate mice carrying loss-of-function alleles for Robo1, the third intron of the Robo1 gene was targeted with a cassette containing a splice acceptor consensus sequence including a transmembrane domain, β -galactosidase/neomycin fusion protein, an internal ribosome entry site (IRES), placental alkaline phosphatase, and a polyA tail. To generate the Robo2 mutant allele, 135 bp of Robo2 DNA, including the 3' end of the putative first exon, and the 5' end of the adjacent intron, was replaced with an IRES-tauLacZ expression cassette and a self-excising floxed sperm-specific cre recombinase/neomycin-resistance expression cassette. Homozygous Robo mutant mice were obtained crossing heterozygous sires and dams. For the GAD65 strain, the *Gfp* open reading frame without its own translation start site was fused in frame to the first exon of the *GAD65* gene. WTs and mice carrying loss-of-function alleles for Robo1 and Robo2 were maintained in heterozygosity in an ICR background (Borrell et al., 2012) and WT mice and homozygous GAD65-GFP transgenics were in C57BL/6 background. Mice were kept on a 16:8h light:dark cycle at the Instituto de Neurociencias de Alicante in accordance with Spanish (RD 53/2013) and EU regulations, and experimental protocols were approved by the Universidad Miguel Hernández Institutional Animal Care and Use Committee (IACUC). *Slit1/2* mutants were generated in a mixed CD-1/129Sv/C57BL/6 background as described in (Borrell et al., 2012) and maintained in a mixed CD-1/129Sv background at Thomas Jefferson University. Homozygous mutants were generated by timed mating of heterozygous sires and dams. A portion of the coding region for the second leucine rich repeat, located in the 5'-region of the *Slit1* gene was replaced with an IRES, a tauGFP fusion protein, and a neomycin resistance gene flanked by a PGK-1 promoter and polyA tail, and by two loxP sites. To avoid translated partial peptides a stop codon and the endoplasmic retention sequence, KDEL, was placed in frame in the *Slit1* gene. Similar targeting strategy was used for *Slit2* employing the same cassette without the KDEL element. The cassette replaced the likely signal sequence and part of the first leucine rich repeat (LRR1). These animal procedures follow the Guidelines for the Care and Use of Laboratory Animals of the National Institutes of Health with the approved IACUC protocols from the Thomas Jefferson University. The day of vaginal plug was considered as embryonic day (E) 0.5.

ICR WT and Robo1 and Robo2 loss-of-function mice were used for ISH tissue collection and marker analysis at E10.5, E11.5, E12.5, E14.5, E16.5 and E18.5. Electroporations for imaging experiments and clonal analysis were performed at E12.0. Cortical

electroporations were done at E12.5 and olfactory bulb electroporations at E12.0. BrdU experiments were performed at E12.5 to determine cell cycle parameters and neuronal birthdating in the cortex. Mitral cell birthdating experiments in the OB were performed at E10.5, E11.5, E12.5 and E13.5. qPCR tissues were collected at E12.5. GAD65-GFP embryos were collected at E12.5 and E14.5 for interneuron migration analysis. For growth cone collapse experiments, E13.5 C57BL/6 WT embryos were used. Slit1/2 mutant and WT siblings embryos were used at E12.5 for marker analysis.

Chicken

Fertilized chicken (*Gallus gallus*) eggs were obtained from a poultry farm (Granja Santa Isabel, Córdoba) and incubated at 38°C. The day of lay was considered day 0 post-ovoposition (dpo). 6 dpo chickens were used for ISH and marker analysis. Electroporations for progenitor manipulation experiments or clonal analysis were performed at 4 dpo.

Snake

Fertilized eggs from snake (*Lamprophis fuliginosus*) were from a breeding colony at the University of Geneva and incubated at 28°C. Maintenance of, and experiments on, snakes were approved by the Geneva Canton ethical regulation authority (authorizations GE/82/14 and GE/73/16) and performed according to Swiss law. The day of lay was considered day 0 post-ovoposition (dpo). 6 dpo snakes were used for ISH and marker analysis. Electroporations were performed at 4 dpo for progenitor manipulation experiments.

Human organoids

Male human fibroblasts (CRL-2522, ATCC) were used to induce pluripotent stem cells (iPSCs). The use of iPSC cells to generate cerebral organoids was approved by the Ethics Commission of LMU (Ludwig-Maximilians-Universität München), with the associated number 115-16. iPSCs and human organoids were cultured at 37°C, 5% CO₂ and ambient oxygen level. During the whole period of cerebral organoid generation the medium was changed every day. Electroporations were performed in cerebral organoids at 39 days after the initial plating of the cells and fixed 7 days post-electroporation.

Retinal explant cultures

Retinal explants for growth cone collapse assays were cultured during 24 hr at 37°C, 5% CO₂ and ambient oxygen level. C57BL/6 embryos were employed independently of their gender.

METHODS DETAILS

Immunohistochemistry and ISH

Animals were fixed with 4% paraformaldehyde (PFA) in phosphate buffer (PB) pH7.3 at 4°C. Embryos older than E16, postnatal mice and 14 dpo chicken were perfused transcardially and postfixed 30-60 min with 4% PFA. Smaller embryos were fixed by immersion during 30-60 min. Brains were cryoprotected with 30% sucrose, embedded in Cryo-medium Neg-50 (Thermo Scientific), frozen and sectioned under a cryostat at 20µm, 40µm for clonal analysis tissue. P21 mice brains were also cryoprotected, frozen and cryotome cut at 50µm. For immunohistochemistry, sections were permeabilized in PBS containing 0.25% Triton X-100 and blocked in 10% of Horse Serum and 2% Bovine Serum Albumin (BSA) during 2 hr. Brain slices were incubated with primary antibodies overnight in blocking solution, followed by appropriate fluorophore-conjugated secondary antibodies and counterstained with DAPI. For non-fluorescent stains, sections were further processed for the ABC histochemical method (Vector). Primary antibodies used were: anti-BrdU (1:200, rat monoclonal, Abcam); anti-cleaved Caspase 3 (1:150, rabbit polyclonal, Cell signaling); anti-GFP (1:1000, chicken polyclonal, Aves Lab.); anti-Ki67 (1:200, rabbit polyclonal, Abcam); anti-phosphohistone H3 (1:500, rabbit polyclonal, Upstate); anti-Tbr1 (1:500, rabbit polyclonal, Abcam); anti-Tbr2 (1:250, rabbit polyclonal, Abcam); anti-βIII tubulin (1:1000, mouse monoclonal, Covance); anti-Pax6 (1:1000, rabbit polyclonal, Merck Millipore); anti-GABA (1:1000, rabbit polyclonal, Sigma); anti-Reelin (1:500, mouse monoclonal, MBL); anti-Cux1 (1:500, rabbit polyclonal, Santa Cruz); anti-Ctip2 (1:500, rat monoclonal, Abcam); anti-NeuN (1:500, mouse monoclonal, Merck Millipore), anti-Dll (1:200, sheep polyclonal, R&D Systems); anti-Robo1 (1:250, goat polyclonal, R&D Systems); anti-Robo2 (1:250, goat polyclonal, R&D Systems); anti-DsRed (1:1000, rabbit polyclonal, Clontech), anti-c-Myc (1:2000, Santa Cruz). Secondary antibodies used were: biotinylated anti-Rabbit and anti-Rat IgG (Vector); Alexa488 and Alexa555 anti-mouse and anti-rabbit IgG (Invitrogen); Alexa488 anti-chicken IgY; Cy2- and Cy5-streptavidin (Jackson ImmunoResearch); Cy3 Fab fragment anti-Rat and anti-Rabbit (Jackson ImmunoResearch); Cy3 anti-Mouse (Jackson ImmunoResearch); Alexa 555 anti-Goat and anti-Sheep (Thermo Fisher Scientific) and Alkaline phosphatase-coupled anti-digoxigenin Fab (Sigma); all diluted 1:200.

For ISH, sense and anti-sense cRNA probes were synthesized and labeled with digoxigenin (DIG; Roche Diagnostics) according to the manufacturer's instructions. Briefly, 20 µm-thick frozen brain sections were prehybridized during 2 hr at 62°C in hybridization solution [50% formamide (Ambion), 10% dextran sulfate, 0.2% tRNA (Invitrogen), 1 × Denhardt's solution (from a 50 × stock; SIGMA), 1 × salt solution (containing 0.2M NaCl, 0.01M Tris, 5mM NaH₂PO₄, 5mM Na₂HPO₄, 5mM EDTA, pH 7.5)] and hybridized with DIG-labeled cRNA probes overnight at 62°C diluted in hybridization solution. After sections were washed, blocking solution (MABT buffer solution 1X, 10% Sheep Serum, 10% Blocking reagent) during 2 hr at room temperature and alkaline phosphatase-coupled anti-digoxigenin Fab fragments in blocking solution were applied overnight at 4°C. For visualization of the labeled cRNAs, sections were incubated in nitroblue tetrazolium (NBT)/5-bromo-4-chloro-3-indolyl phosphate (BCIP) solution [3.4 µl/ml from NBT stock and

3.5 μ l/ml from BCIP stock in reaction buffer (100mg/ml NBT stock in 70% dimethylformamide; 50mg/ml BCIP stock in 100% dimethylformamide; Roche)].

Bromodeoxyuridine labeling experiments

Bromodeoxyuridine (BrdU, SIGMA) was diluted at 10mg/ml in 0.9% NaCl and always administered at 50mg/kg body weight. For cell cycle length determination, multiple doses of BrdU were intraperitoneally injected in pregnant females at E12.5, spaced every 2hr for a total maximum of 10h and fixed 30 min after injection for each pulse. For cell cycle exit calculation, a single intraperitoneal BrdU injection was administered at E12.5, embryos were fixed 24hr later and the percentage of BrdU+ cells labeled with Ki67 was calculated. For birthdating analysis, a single dose of BrdU was injected in timed-pregnant mice at E10.5, E11.5, E12.5 or E13.5, and the brains of labeled animals were analyzed at postnatal stage (P) P0 or P21. For BrdU dilution experiments, pregnant mice were injected at E12.5 with a single pulse of BrdU, 3hr later embryos were electroporated in the OB or the adjacent NCx with CAG-GFP plasmids, and analyzed at E18.5 or P21.

Constructs

For retroviral delivery we used GFP-encoding and RFP-encoding constructs subcloned into an MMLV retroviral packaging vector downstream of the CAG promoter (generous gift of F.H. Gage). For Dll1 overexpression we used a pCIG-Dll1 plasmid (generous gift of J. Galcerán). pCAG-Floxp-EGFP-farnesylated and pCAG-Cre, generous gift of M. Gotz (Pilz et al., 2013), were used for time-lapse imaging of single progenitor lineages. Plasmids encoding dominant-negative Robo1 and Robo2 (dn-Robo1, dn-Robo2) and constitutively active Robo1 and Robo2 (myrRobo1, myrRobo2) cloned in a pCAG vector were as described in (Borrell et al., 2012). Dn-Robo1 and dn-Robo2 were a generous gift of E. Stein (Stein and Tessier-Lavigne, 2001). Jag1 and Jag2 ISH probes were a generous gift of F. Guillemot and the plasmid encoding constitutively acting form of Jag1-HA pIRES was acquired from Addgene. Crispr plasmids were generated using pSpCas9(BB)-2A-GFP (PX458) from Addgene, following Zhang Lab's protocol. Guides against Dll1 were generated by annealing the following oligomers:

Crispr-mouse Dll1-1: CACCGTAACCGCGGGTGCACGCCGG

Crispr-mouse Dll1-2: AAACCCGGCGTGCACCCGCGGTAC

Crispr-human Dll1-1: CACCATATAAAGAACCGCGGCCTT

Crispr-human Dll1-2: AAACAAGGCCGCGTTCTTTATATC

For *in situ* hybridization (ISH) probe synthesis, the following plasmids were used: mouse Robo1, Robo2, Dll1, Notch1, Hes5, Slit1, Slit2, Slit3 (Borrell et al., 2012), reelin (Borrell and Marín, 2006), Gm1, Bhlhe22 (generous gift of A. Fairén) and Tbr2 (generous gift of B. Rico); chicken (*Gallus gallus*) Robo1, Robo2 (Escalante et al., 2013) and was subcloned into pBS from pUC19ckDll1 (generous gift of J. Galcerán); snake (*Lamprophis fuliginosus*) ISH probes were cloned by RT-PCR using the following primers:

snRobo1-Fw: TCATCTCATTGATTTTGTTC

snRobo1-Rv CAAGATATGAAATCCGTGATG

snRobo2-Fw: TGGCACTCCTGAAACCTAC

snRobo2-Rv CAGTTCATGGATGCTGTTGG

snDll1-Fw: TACCGCTTTGTGTGATG

snDll1-Rv GCACCAAATTGTAATCCACTG

Validation of Crispr/Cas-mediated gene editing

The cerebral cortex of ICR mouse embryos aged E12.5 was electroporated in utero with plasmids encoding the mDll1-specific guide and Cas9; for human-specific guides, d40 cerebral organoids were electroporated with plasmids encoding hDll1 guide and Cas9. Editing of the Dll1 genomic locus was analyzed 24-48hr later using the Surveyor Nuclease (Integrated DNA technologies) digestion protocol, following the manufacturer's instructions (mouse), or by sequencing (human). Briefly, the genomic DNA of electroporated tissue or transfected cells was isolated and PCR amplified with Xpert High Fidelity DNA polymerase (Mirage Biochemicals) and the following primers: Mouse: Fw: GATATAGCCCCGATGAATGC; Rv: AGAGAGCCCAGATGTTTCAGC, which produced 1,025 bp amplicons. Human: Fw: TGGGAGGAAGGAGGAAAACG; Rv: AGCAGCCCCTTCTTGTGAC, which produced 689 bp amplicons. PCR products were either cloned and sequenced (human), or digested with Surveyor Nuclease S at 42°C for 35min and digestion products analyzed by 2% agarose gel electrophoresis (mouse).

Embryonic brain electroporation

Mouse embryos were electroporated in utero in the NCx at E12.5, or in the OB at E12.0. Briefly, pregnant females were deeply anesthetized with isoflurane and the uterine horns exposed; DNA solution (1 μ l) was injected into the lateral ventricle using pulled glass micropipettes, and square electric pulses (28-35V, 50ms on – 950ms off, 5 pulses) were applied with an electric stimulator (Cuy21EDIT Bex C., LTD) using round electrodes (CUY650P5, Nepa Gene).

For chicken and snake *in ovo* electroporations, fertilized eggs were incubated as mentioned above until 4 dpo. The day before electroporation, a small portion of yolk was removed through a needle hole with a syringe. Previously to the electroporation, a small window was open in the egg shell to allow further manipulations. At 4 dpo, DNA solution was injected in the lateral telencephalic ventricle of embryos, and square pulses (30V, 5ms, 5 pulses each 500ms) were applied with an electric stimulator (TSS20 Ovodyne

Electroporator, MCI) using round electrodes (CUY650P3, Nepa Gene). Manipulated embryos were allowed to continue developing under the same temperature (38.5°C for chicken and 28°C for snake) and in humidity conditions for snake. Embryos were fixed in ice-cold 4% PFA, and their brains processed for IHC or ISH.

Plasmid concentrations were as follows: GFP = 0.75µg/µl; myr-Robo1, myr-Robo2, dnRobo1, dn-Robo2, Dll1, crDll1, Jag1 = 1µg/µl. Combinations of these plasmids were done maintaining the same final individual concentrations.

Retinal electroporation

For retinal electroporation, C57 WT embryos were electroporated in utero at E13.5 with a combination of plasmids including GFP = 0.75µg/µl; dnRobo1, dn-Robo2 = 1µg/µl. DNA solution (0.5µl) was injected subretinally using pulled glass micropipettes, and square electric pulses (35V, 50ms on – 950ms off, 5 pulses) were applied with an electric stimulator (Cuy21EDIT Bex C., LTD) using round electrodes (CUY650P3, Nepa Gene).

Imaging experiments

For live imaging of individual mouse progenitor cells, embryos were electroporated in utero at E12.0 with a combination of plasmids including pCAG-Flox-farnesylated-EGFP (0.4µg/µl) and pCAG-Cre (10ng/µl). The low concentration of Cre plasmid allowed sparse labeling of individual progenitor cells upon recombination of the floxed stop cassette (Piliz et al., 2013). 12hr after electroporation, the brains were dissected out and vibratome sliced at 250 µm in ice-cold DMEM-F12 (Sigma) bubbled with carbogen (5% carbon dioxide + 95% oxygen). Slices were embedded in collagen matrix (Nitta gelatin) on a filter membrane (Millipore) and cultured in DMEM-F12 (Sigma), 5% fetal bovine serum, 5% horse serum, N2 (1:100; Invitrogen), B27 (1:50; Invitrogen), PenStrep (100U/ml), glucose (0.7g/l) and sodium bicarbonate (0.3g/l) (Piliz et al., 2013). Imaging was performed on an inverted microscope under two-photon optics (LEICA SP2), 40x immersion and a 5% CO₂/37°C atmosphere (Martínez-Martínez et al., 2016). Stacks of frames separated 5 µm were captured every 30 min for 12–24 hr. Immediately after recording the time-point, slices were fixed in 2% PFA for 30 min, and then further processed for IHC.

Retroviral stocks preparation and concentration

High-titre Murine Moloney Leukemia Virus-based (MMLV-based) retrovirus encoding GFP or RFP under the CAG promoter were prepared by transient transfection (together with CMV-vsVg and CMV-gp plasmids) of human embryonic kidney 293T (HEK293) cells as a package cell line, concentrated by ultracentrifugation and viral titre estimated by clonal infection (Borrell et al., 2012). Viral solutions were injected using pulled glass micropipettes.

Single progenitor clonal analysis

ICR control and *Robo1*^{+/−} pregnant females carrying E12.0 embryos were deeply anesthetized with isoflurane and individual embryos were injected with 1µl of *Gfp*-encoding retroviruses (5x10⁶cfu/ml) into the telencephalic ventricles. After 24hr of survival embryos were sacrificed, their heads fixed in 4% PFA, cryostat-sectioned at 40µm and processed for immunohistochemistry as described above.

For chicken clonal analysis, *Rfp*-encoding retroviruses were injected immediately after electroporation of *Gfp* or *dnR1/2+Dll1+Gfp* encoding plasmids in the same telencephalic ventricle. Manipulations were performed as described previously at 4 dpo and chicken embryos were incubated until 14 dpo.

Tissue microdissection and quantitative real-time PCR

For RNA extraction E12.5 mouse brains were dissected in cold RNase free medium and tissue blocks were vibratome cut at 250µm. Living cortical slices were further microdissected with microscalpels in ice-cold RNase free medium to isolate pieces from OB and the adjacent NCx. Tissue pieces were immediately frozen in liquid nitrogen for RNA extraction. Total RNA from each region was extracted using RNeasy Mini Kit (Quiagen) followed by treatment with RNase-Free DNase Set (Quiagen). Template cDNA was generated using Maxima First Strand cDNA Synthesis Kit for quantitative real-time PCR (qRT-PCR; Thermo Fisher). Primers used were:

msRobo1-Fw: CCTTCAGACCTGATCGTCTCC
 msRobo1-Rv: TGAGCGCGGGTCATCTTTG
 msRobo2-Fw: CTTTGAACGACCCACATTTCTCA
 msRobo2-Rv: TCTCAGCGTGTAGTCATCTTTGA
 ms18S-Fw: CGGCTACCACATCCAAGGAA
 ms18S-Rv: GCTGGAATTACCGCGGCT

For comparison between species RNA was extracted from 6dpo chicken brains, dissected in cold RNase free medium and tissue blocks were vibratome cut at 250µm. Primers used in the mouse and chicken comparison are listed below:

ckROBO1-Fw AGAAGATTTCCACCTCG
 ckROBO1-Rv CTTGCCACGCAGACATAG
 ckGAPDH –Fw GTGGTGCTAAGCGTGTATCATC
 ckGAPDH –Rv GGCAGCACCTCTGCCATC
 msGAPDH_Fw CTCTTGCTCAGTGTCTTGTCTG
 msGAPDH_Rv ATGAATACGGCTACAGCAACAGG

Reprogramming of human fibroblasts to induced pluripotent stem cells

iPSCs were reprogrammed from human newborn foreskin fibroblasts (CRL-2522, ATCC). 2.5×10^5 NuFF3-RQ IRR human newborn foreskin feeder fibroblasts (GSC-3404, GlobalStem) were seeded per well of a 6-well tissue culture dish with advanced MEM (12491015, Thermo Fisher Scientific) supplemented with 5% HyClone Fetal Bovine Serum, 1% MEM NEAA and GlutaMAX (11140050; 35050061 Thermo Fisher Scientific). On day 1, 70%–80% confluent CRL-2522 fibroblasts were dissociated using 0.25% Trypsin-EDTA (25200056, Life Technologies), counted and seeded on the NuFF3-RQ cells at two different densities: 2×10^4 cells/well and 4×10^4 cells/well. On day 2, the medium was changed to Pluriton Reprogramming Medium supplemented with 500ng/ml carrier-free B18R Recombinant Protein. On days 3–18, a cocktail of modified mRNAs (mmRNAs) containing OCT4, SOX2, LIN28, C-MYC, and KLF mmRNAs at a 3:1:1:1:1 stoichiometric ratio was transfected daily. For that purpose, the mmRNAs were mixed in a total volume of 105 μ l and were combined with a mix of 92 μ l Opti-MEM I Reduced Serum Medium and 13 μ l Lipofectamine RNAiMAX Transfection Reagent after separate incubation at RT for 15 min. Cells were transfected for 4hrs, washed and fresh reprogramming medium supplemented with B18R was added to the cultures. The mmRNAs with the following modifications: 5-Methyl CTP, a 150nt poly-A tail, ARCA cap and Pseudo-UTP were obtained from the RNA CORE unit of the Houston Methodist Hospital. 5 days after the first transfection, the first morphological changes were noticed, while the first induced pluripotent stem cell (iPSC) colonies appeared by day 12–15. On day 16, the medium was changed to STEMPRO hESC SFM for five days. Harvesting of the iPSC colonies was performed after 40min incubation at 37°C with 2mg/ml Collagenase Type IV solution in DMEM/F12 (31331093, Thermo Fisher Scientific). The iPSCs were plated on γ -irradiated mouse embryonic fibroblasts (MEFs) and grown in STEMPRO hESC SFM for 10 additional passages. After that the iPSCs were further cultured in a feeder-free culture system, using mTeSR1 on plates coated with LDEV-Free Geltrex. iPSCs were authenticated after reprogramming by karyotyping.

iPSC culture

iPSCs were cultured at 37°C, 5% CO₂ and ambient oxygen level on Geltrex coated plates in mTeSR1 medium (STEMCELL Technologies, 05850) with daily medium change. For passaging, iPSC colonies were incubated with StemPro Accutase Cell Dissociation Reagent diluted 1:4 in PBS for 4 min. Pieces of colonies were washed off with DMEM/F12, centrifuged for 5min at 300 x g and resuspended in mTeSR1 supplemented with 10 μ M Rock inhibitor Y-27632(2HCl) for the first day.

Cerebral organoids generation

Cerebral organoids generation. Cerebral organoids were generated as previously described (Lancaster and Knoblich, 2014). Briefly, iPSCs were dissociated into single cells using StemPro Accutase Cell Dissociation Reagent (A1110501, Life Technologies) and plated in the concentration of 9000 single iPSCs/well into low attachment 96-well tissue culture plates in hES medium (DMEM/F12GlutaMAX supplemented with 20% Knockout Serum Replacement, 3% ES grade FBS, 1% Non-essential amino acids, 0.1mM 2-mercaptoethanol, 4ng/ml bFGF and 50 μ M Rock inhibitor Y27632) for 6 days in order to form embryoid bodies (EBs). Rock inhibitor Y27632 and bFGF were removed on the 4th day. On day 6 EBs were transferred into low attachment 24-well plates in NIM medium (DMEM/F12GlutaMAX supplemented with 1:100 N2 supplement, 1% Non-essential amino acids and 5 μ g/ml Heparin) and cultured for additional 6 days. On day 12 EBs were embedded in Matrigel drops and then they were transferred in 10cm tissue culture plates in NDM minus A medium (DMEM/F12GlutaMAX and Neurobasal in ratio 1:1 supplemented with 1:100 N2 supplement 1:100 B27 without Vitamin A, 0.5% Non-essential amino acids, insulin 2.5 μ g/ml, 1:100 Antibiotic-Antimycotic and 50 μ M 2-mercaptoethanol) in order to form organoids. 4 days after Matrigel embedding cerebral organoids were transferred into an orbital shaker and cultured until electroporation in NDM plus A medium (DMEM/F12GlutaMAX and Neurobasal in ratio 1:1 supplemented with 1:100 N2 supplement 1:100 B27 with Vitamin A, 0.5% Non-essential amino acids, insulin 2.5 μ g/ml, 1:100 Antibiotic-Antimycotic and 50 μ M 2-mercaptoethanol). During the whole period of cerebral organoid generation, cells were kept at 37°C, 5% CO₂ and ambient oxygen level with medium changes every other day. After transferring the cerebral organoids onto the shaker medium was changed twice per week.

Electroporation of cerebral organoids

Cerebral organoids were kept in antibiotics-free conditions prior to electroporation. Electroporations were performed in cerebral organoids at 39 days stages after the initial plating of the cells and fixed 7 days post electroporation. During the electroporation cerebral organoids were placed in an electroporation chamber (Harvard Apparatus, Holliston, MA, USA) under a stereoscope and using a glass microcapillary 1–2 μ L of plasmid DNAs was injected together with Fast Green (0.1%, Sigma) into different ventricles of the organoids. The plasmid DNAs injected were a mix of 0.75 mg/ml GFP with or without 1mg/ml myr-Robo1, 1mg/ml myr-Robo2, 1mg/ml Dil1 gRNA (+Cas9). Cerebral organoids were subsequently electroporated with 5 pulses applied at 80V for 50ms each at intervals of 500ms (ECM830, Harvard Apparatus). Following electroporation, cerebral organoids were kept for additional 24hr in antibiotics-free media, and then changed into the normal media until fixation. Cerebral organoids were fixed using 4% PFA for 1hr at 4°C, cryopreserved with 30% sucrose and stored at –20°C. For immunofluorescence, 16 μ m cryosections were prepared.

Retinal growth cones collapse assay

24hr after the electroporation, retinas were isolated and maintained in sterile DMEM/F12 culture medium. Electroporated retinas were selected and cut in small (200 μ m) pieces and explants plated on Corning BioCoat Poly-L-lisine coverslips after 1h of laminin

(20 μ g/ μ l) treatment. Retinal explants were cultured during 24 hr in culture medium [DMEM/F12 supplemented with 0.4% Methylcellulose (Sigma), 1% BSA (Sigma), 1% Insulin-transferrin-sodium selenite media supplement (Sigma) and 0.2% penicillin/streptomycin] in a humidified incubator at 37°C and 5% CO₂. After 24h of incubation, recombinant mouse Slit protein (R&D Systems) was added to the medium (250ng/ μ l) and the explants were fixed 1h later with PFA 2% during 15 min.

MyrRobo1/2 construct validation

To express EGFP and myrR1/2cyto, 4x10⁵ dissociated DRG neurons from E14 rat embryos were electroporated with 2-3 μ g of plasmid DNA using the nucleofection reagent for rat DRG neurons (Lonza). Cells were then incubated in 400 mL of growth medium at 37°C for 10 min, spun down, plated at 5x10⁴/20 μ l in collagen gels, and cultured in an F12 medium (Invitrogen) with the N3 supplement, 40 mM glucose, 0.5% fetal calf serum, plus NGF (25 ng/ml, 7 s, Sigma). After two-day in culture, neurons were fixed with 4% PFA, pH 7.4, for 1 h, and permeabilized, and blocked with PBS containing 0.1% Triton X-100 and 1% Goat Serum. The transfected cells were stained with a mouse anti-myc primary antibody (9E10, Santa Cruz) followed by a Cy3-conjugated secondary antibody (Jackson ImmunoResearch) to detect the myc tagged myrR1/2cyto. EGFP was imaged directly.

Neuron tracing experiments

Cholera toxin subunit B conjugated with Alexa 594 (CTB, Molecular probes) was prepared at 1 μ g/ μ l in PBS. CTB solution was injected in the pyramidal decussation of P15 juvenile ICR WT mice. Mice were deeply anesthetized with isoflurane, the pyramidal decussation was exposed and CTB solution (2 μ l) was stereotaxically injected into the tissue with pulled glass pipettes. Animals were fixed at P21 with 4% PFA and processed as previously described.

QUANTIFICATION AND STATISTICAL ANALYSIS

Data were statistically analyzed using SPSS software. Pairwise t test or independent samples t test were used to compare statistical differences between two experimental groups. χ^2 -test was used to determine the equality of proportion between different groups. To compare the statistical differences between at least three experimental groups, One way-ANOVA was used. Similarity of variance across experimental distributions was tested. Samples were obtained independently and observations were sampled randomly and independently. All values represent mean \pm standard error of the mean (SEM). The experimental *n*, the statistical test used and the statistical significance are indicated in figure legends. For each experiment, embryos from at least two different females were used. Significance was set at *p* = 0.05. More information about experimental analysis and quantifications can be found below.

Histological analysis

For immunohistological comparisons between OB and adjacent NCx, cells were counted in an equivalent ventricular surface separated by a transitional gap of 200 μ m. For each section, the total cell count was normalized per length of VZ apical surface. All quantifications were made in the same latero-medial level in at least 3 independent embryos. For co-localization studies, images from a single confocal plane were obtained and analyzed using a Leica TCS SL confocal microscope and Olympus FV10 confocal microscope.

For validation of *crD11* by ICC, and for ISH analyses, images were inverted, processed to 8 bits, and the mean signal intensity in the area of interest was measured using ImageJ software (*n* = 3-5 independent samples for each group). See [Figures 5 and 6](#) and [S6](#).

Bromodeoxyuridine labeling experiments

To determine cell cycle length, DAPI+ BrdU+ nuclei in the VZ and SVZ were quantified. Nuclei were considered as positive for BrdU only when at least 25% of the nucleus was labeled. To study G2+M length, we quantified phospho-histone3 and BrdU positive cells. *n* = 3 embryos per time point. See [Figures 1 and 3](#) and [S3](#). To analyze cell cycle exit, BrdU positive Ki67 negative nuclei were counted in the VZ and SVZ. *n* = 3 embryos per area and genotype. See [Figures 1 and 3](#). For mitral cell birthdating analysis, Tbr1-BrdU positive cells were quantified differentiating between 25%, 50% and 100% of total nucleus label. *n* = 3 embryos per developmental stage. See [Figure S1](#). For cortical neuron birthdating analysis, GFP+ 100% BrdU+ cells were quantified in each layer (*n* = 3 *Gfp* electroporated controls; *n* = 5 *MyrRobo+crD11* electroporated embryos). See [Figures 5 and S7](#).

Electroporation analysis

In mouse, chicken, and snake embryo experiments, to minimize the variability between animals, counts in the electroporated hemisphere of each animal were normalized with the non-electroporated contralateral hemisphere of the same animal at the same rostro-caudal and latero-medial level. All quantifications were made in at least 3 independent embryos. Cerebral organoid electroporations were normalized using a non-electroporated adjacent region. Several independent ventricles per organoid and condition were analyzed from 4-6 different organoids.

Imaging experiments

Digital images were acquired, contrast-enhanced and analyzed with Imaris software (Bitplane). Each individual apical mitosis was followed until the end of the movie to determine cell types derived from it, to then define the cell lineage tree (*n* = 25 divisions from 25 clones in the OB of 5 embryos; *n* = 44 divisions from 39 clones in NCx of 3 embryos). See [Figures 2 and S3](#).

Single progenitor clonal analysis

For the unequivocal assignment of GFP+ cells as belonging to a particular individual clone, the three-dimensional arrangement of labeled cells within the embryonic tissue was assessed by scanning the entire thickness of brain sections under confocal microscopy. In mouse clonal analysis, once all cells within a single clone were identified, they were counted and classified according to their expression of Tuj1, Tbr1, Tbr2 and morphology, namely being multipolar or containing an apical process extended to the ventricular surface. Quantifications were performed in 7 embryos per group (WT: n = 116 clones in NCx; 47 clones in OB - KO: n = 125 clones in NCx; 40 clones in OB). See [Figures 2 and 3](#).

For chicken clonal analysis, 3-7 embryos were used per condition (n = 52 clones, 128 cells *Gfp*; 59 clones, 254 cells *dnR1/2+Dl1+Gfp*). Only cells labeled with GFP (derived from electroporated, dorsal pallial progenitors), RFP (derived from individual progenitors) and contained within the neuronal layer, as defined by Tuj1 stain, were considered. The majority of these cells were as either singles or forming small clusters, and very sparsely distributed along the cortex (1-2 cells or cell clusters per section of whole cerebral hemisphere, 5000 μ m long). The diameter of these cell clusters, defined as the maximum separation between their constituent cells, was 65-80 microns on average ($63 \pm 5\mu$ m in *Gfp* clones; $79 \pm 3\mu$ m in *dnR1/2+Dl1+Gfp* clones). Cells were considered to be clonally related only if they were separated from the nearest neighbor cell less than the average cluster diameter, and from clones at least 150 μ m. In most cases, the separation between clusters or isolated cells was much greater. Pairs of cell clusters that, although distinctly separate, were found at a closer distance, were not included in the analysis.

Quantitative real-time PCR

Quantitative RT-PCR was performed using the Step One Plus sequence detection system and the SYBR Green method (Applied Biosystems) with each point examined in triplicate. Transcript levels were calculated using the comparative Ct method normalized using 18S. Each independent sample was processed in triplicate.

Robo construct validation

Growth cone collapse was measured as the degree of filopodia retraction in electroporated cells. Quantifications were performed in 3 embryos per group (n = 58 growth cones in *Gfp*; 52 growth cones in *Gfp+Slit*; 44 growth cones in *dnRobo1/2*; 48 growth cones in *dnRobo1/2+Slit*). Axon branching experiment was used to validate the MyrRobo constructs by measuring the branching degree in growing axons from single neurons of embryonic rat dorsal root ganglion (n = 5-10 neurons per group).

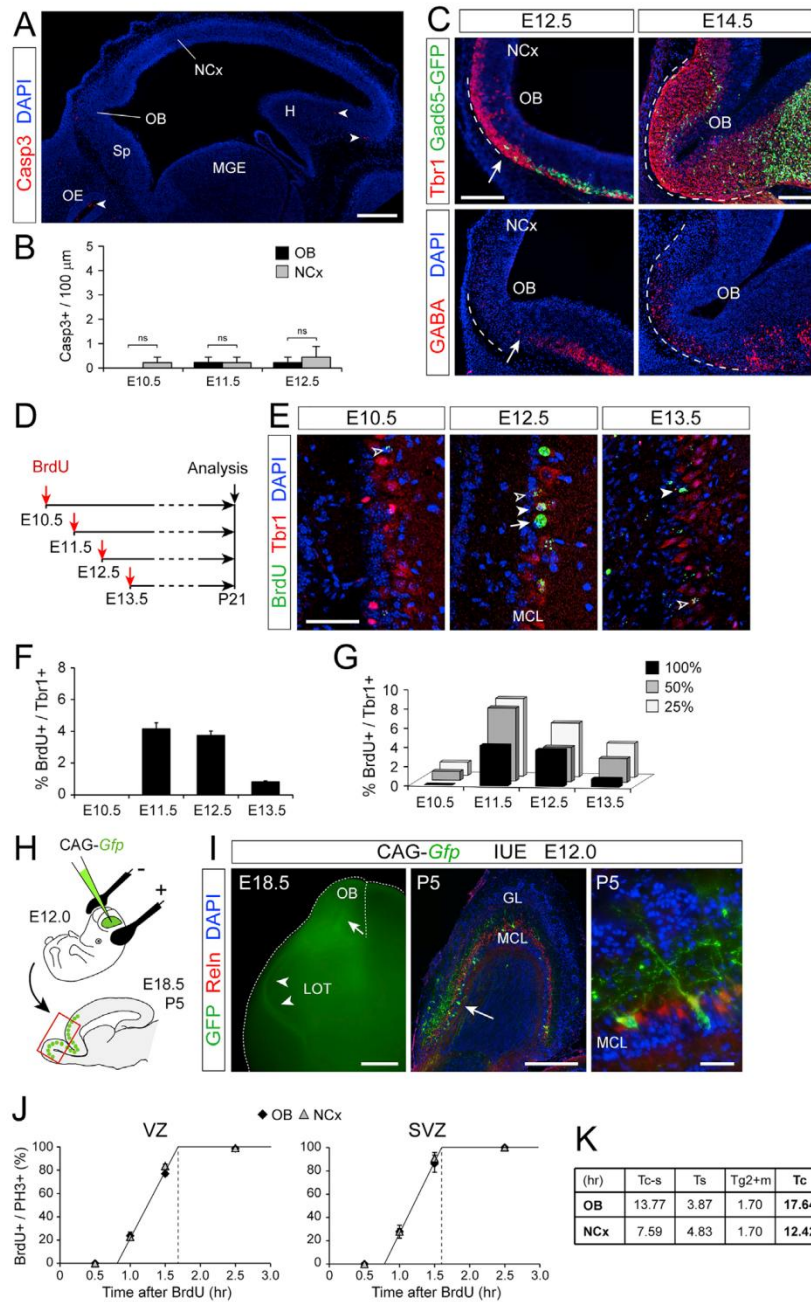


Figure S1. Differences between Early Growth of OB and NCx Correlate with Mitral Cell Generation, Not with Cell Death or Inhibitory Interneuron Accumulation, Related to Figure 1

(A) Sagittal section of mouse telencephalon at E12.5 stained for activated Caspase 3 and DAPI. Arrowheads indicate Casp3+ cells. H, hippocampus; MGE, medial ganglionic eminence; OE, olfactory epithelium; Sp, septum.

(B) Quantification of linear density of Casp3+ cells in OB and NCx at the indicated ages. Values are mean + SEM; n = 3 embryos per age; t tests, ns = not significant.

(C) Sagittal sections of the olfactory bulb primordium at E12.5 and E14.5 from a transgenic mouse expressing GFP in GAD65+ cells stained for Tbr1 or GABA. Dotted lines indicate the perimeter of the OB primordium. Arrows point at the leading edge of tangentially-migrating interneurons (GAD65+ or GABA+), which are just arriving to the OB primordium by E12.5.

(D) Experimental design for mitral cell birthdating by single BrdU injections and analyses at postnatal day (P) 21.

(E) Coronal sections of mouse OB at P21 after BrdU injections at the indicated ages, stained for Tbr1 to identify mitral cells retaining BrdU. Arrow indicates a cell retaining 100% BrdU, solid arrowheads indicate cells retaining 50% and open arrowheads indicate cells retaining only 25% of BrdU.

(legend continued on next page)

(F and G) Quantification of the proportion of mitral cells (Tbr1+) retaining full levels of BrdU (F), or 25%, 50% and 100% of BrdU (G). Values are mean + SEM; n = 3 embryos per stage.

(H) Experimental design to identify cell types produced by apical progenitors in the OB primordium.

(I) Images from brains electroporated with *Gfp*. Left, external view at E18.5 showing GFP+ mitral cell axons in the lateral olfactory tract (LOT); center and right, sagittal section through the OB at P5 showing GFP+ mitral cells. GL, granule layer; MCL, mitral cell layer.

(J and K) Measurement of the length of G2+M phase of the cell cycle in apical (VZ) and basal (SVZ) progenitors of OB and NCx at E12.5, as defined by the time for BrdU saturation of PH3+ cells after cumulative BrdU labeling (n = 3 embryos per group). Values for the duration of other cell cycle phases, and total cell cycle (Tc), are indicated in (K).

Scale bars: 200 μ m (A), 100 μ m (C), 50 μ m (E), 1 mm (E18.5 in I), 200 μ m (P5 in I), 10 μ m (P5 detail in I).

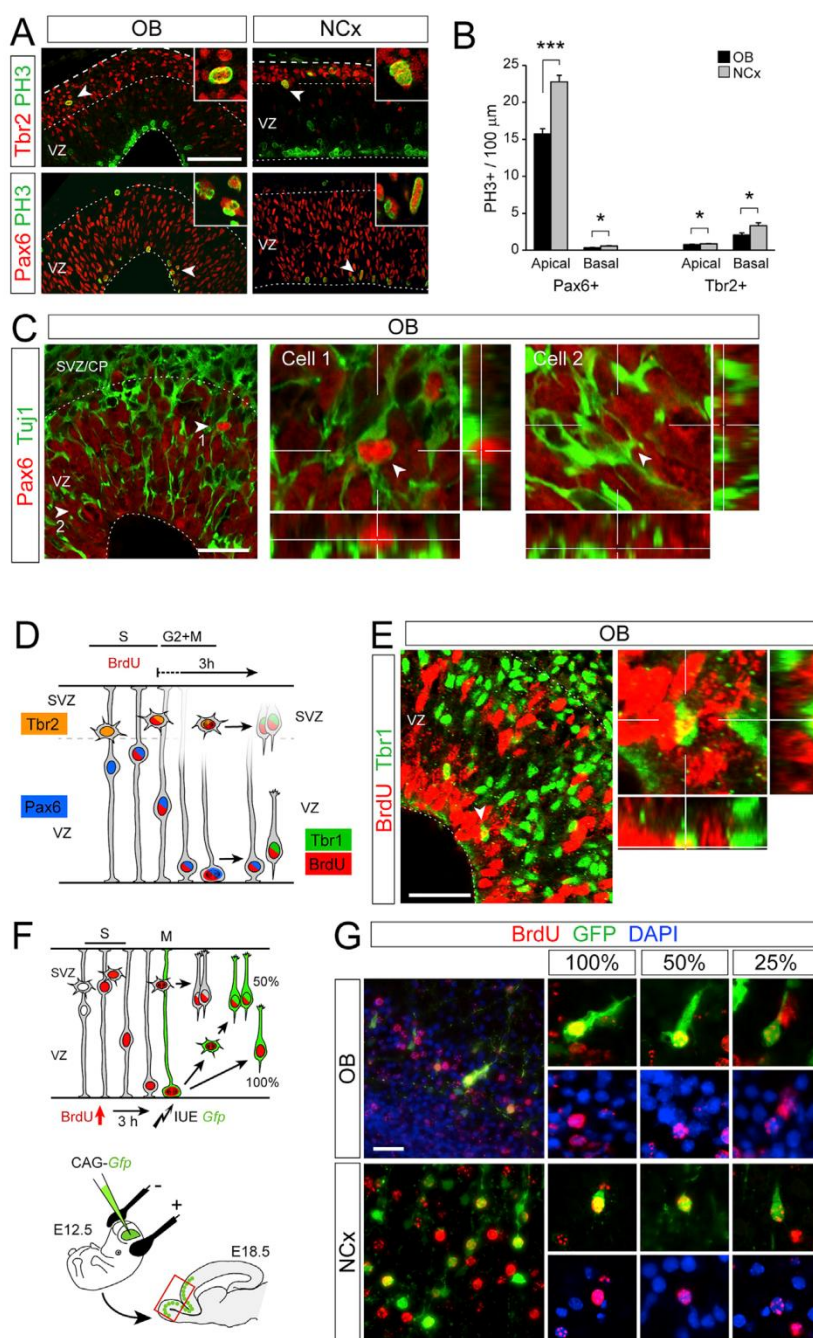


Figure S2. Evidence Supporting Abundant Direct Neurogenesis in OB, but Not NCx, at E12.5, Related to Figure 2

(A) Images from parasagittal sections of mouse OB and NCx at E12.5 stained for PH3 (mitoses), Pax6 (RGCs) and Tbr2 (IPC). Arrowheads point at double-positive nuclei shown at high magnification in the insets.

(B) Quantification of linear density of apical and basal PH3+ nuclei in OB and NCx positive for Pax6 or Tbr2. Values are mean + SEM; n = 4 embryos per group and 2-3 confocal planes for each embryo; t tests; *p < 0.05; ***p < 0.001.

(C) Single confocal plane images from a sagittal section of the OB at E12.5 stained for Pax6 and Tuj1. Cells 1 and 2 indicated by arrowheads co-express the two markers, as demonstrated by the high-magnification images including orthogonal planes at the levels indicated.

(D and E) Identification of neurons born from apical divisions *in vivo*. Experimental design used shown in (D). The timing for analysis after BrdU administration was defined following our previous measures of the duration of G2+M phases of the cell cycle. Images in (E) are from a sagittal section of the OB at E12.5 stained with BrdU and Tbr1. The arrowhead indicates the cell magnified to the right, with orthogonal views demonstrating co-localization. This cell is full of BrdU and expresses Tbr1 close to the ventricular border. Similar cells were never observed in NCx.

(F and G) Experimental design and examples of cells born directly or indirectly from VZ mitoses. Upon BrdU injection at E12.5, this is incorporated by RGCs and

(legend continued on next page)

IPCs in S-phase (F). BrdU+ cells start entering mitosis 3hr later, and then the ventricular side is electroporated, transducing RGC cell bodies next to the apical side but not IPCs in the SVZ, as these are distant from the electroporation surface. After allowing subsequent rounds of cell division, only neurons born by direct neurogenesis (not dividing again) will express GFP and contain 100% BrdU; cells with 50% BrdU or less are born after additional cell cycles, when direct versus indirect neurogenesis are indistinguishable by this method. (G) Examples of neurons in OB and NCx at E18.5 labeled as indicated in (F). High magnifications show examples of GFP+ cells retaining high (100%), medium (50%) or low (25%) levels of BrdU. Scale bars: 100 μ m (A), 25 μ m (C, E, and G).

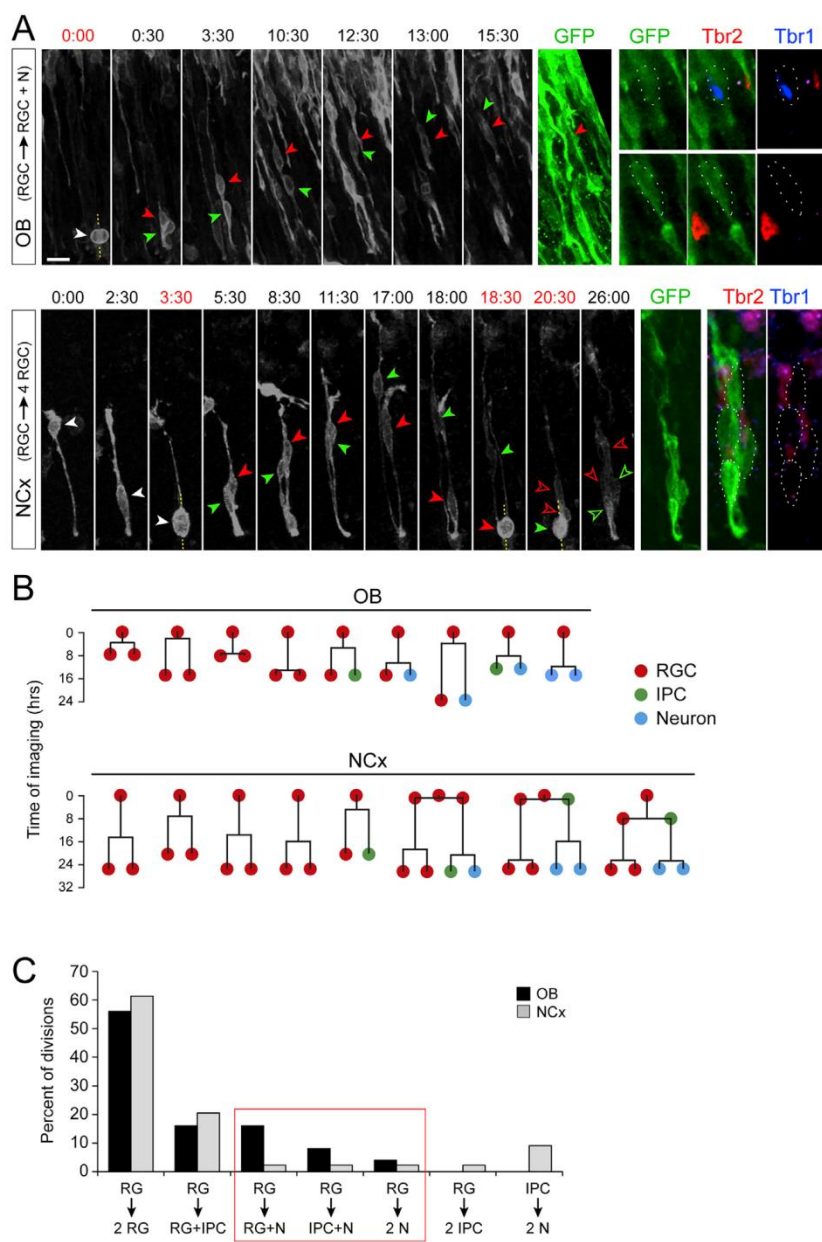


Figure S3. Videomicroscopy Analyses Demonstrating Abundant Direct Neurogenesis in the OB, but Not NCx, at E12.5, Related to Figure 2

(A) Individual frames from time-lapse videomicroscopy from OB (top) and NCx (bottom), imaged in brain slices 24hr after in utero electroporation of reporter plasmids at E12.5. Images from OB show one RGC (white arrowhead) dividing at $t = 0$ to generate one RGC (red arrowhead; Tbr1⁻, Tbr2⁻) and one neuron (green arrowhead; Tbr1⁺). Tbr1 and Tbr2 stain images are from a single confocal plane; dotted lines delimit the border of cells. Images from NCx show one RGC (white arrowhead) dividing at $t = 3:30$ hr to generate two more RGCs (solid green and red arrowheads), each inheriting an apical process and growing a basal process. These RGCs divide again at 18:30 and 20:30, respectively, to generate four RGCs (open green and red arrowheads; Tbr1⁻, Tbr2⁻). Scale bar: 15 μ m.

(B and C) Time plots from representative cell lineages starting as individual RGCs (B), analyzed by videomicroscopy as in (A), and frequency of cell division types observed (C). Three types of cells divisions produced direct neurogenesis (N from RG; red box), and the frequency of all three was much higher in OB than NCx. In contrast, indirect neurogenesis (N from IPC) was frequent in NCx but never observed in our OB imaging experiments. N = 44 divisions from 39 clones in NCx, 25 divisions from 25 clones in OB.

Scale bar: 10 μ m.

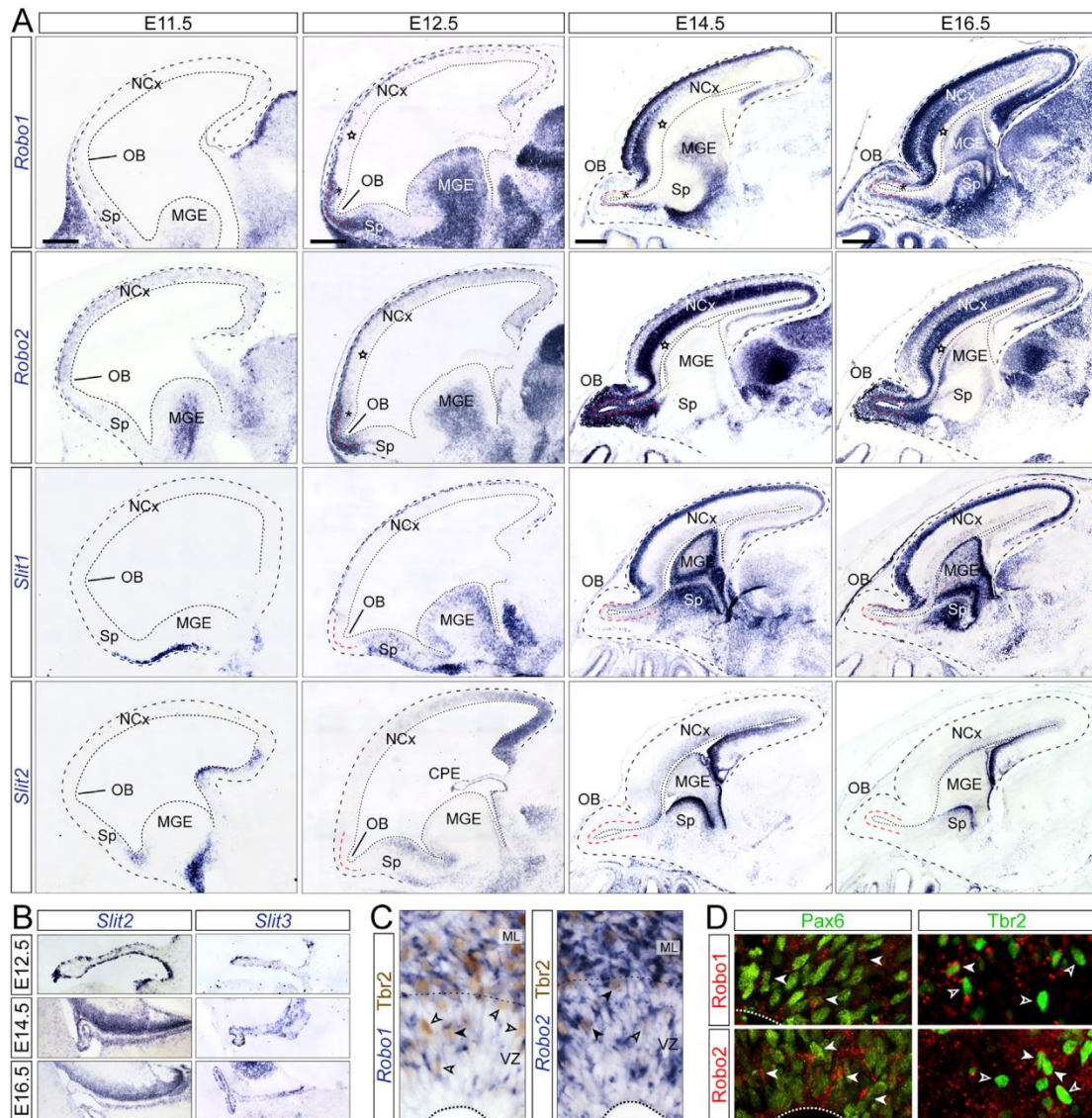


Figure S4. Robo Receptors and Slit Ligands Are Expressed in the Mouse Telencephalon during Embryonic Development, Related to Figure 3

(A and B) ISH for *Robo1*, *Robo2*, *Slit1*, *Slit2* and *Slit3* in the developing mouse telencephalon from E11.5 to E16.5. Stars indicate low expression of *Robo1* and 2 mRNA in the VZ of NCx, and asterisks indicate high expression of *Robo1* and 2 in the VZ of OB, between E12.5 and E16.5. *Slits* are expressed at moderate-low levels in the VZ of OB and NCx between E14.5 and E16.5. High-magnification details in (B) show strong expression of *Slit2* and *Slit3* mRNA in the choroid plexus epithelium (CPE) at E12.5, E14.5 and E16.5.

(C) ISH for *Robo1* and *Robo2* and immunostaining for *Tbr2* in OB, demonstrating co-expression in many *Tbr2*+ cells but not all (solid and open arrowheads, respectively).

(D) Single confocal plane images of double immunostains in E12.5 OB for *Robo1* and *Robo2*, with *Tbr2* and *Pax6*, demonstrating protein co-expression in many *Pax6*+ cells and some *Tbr2*+ cells (arrowheads). Dashed line indicates apical border of VZ.

Scale bars: 200 μ m (E11.5, E12.5), 500 μ m (E14.5, E16.5). MGE, medial ganglionic eminence; Sp, septum.

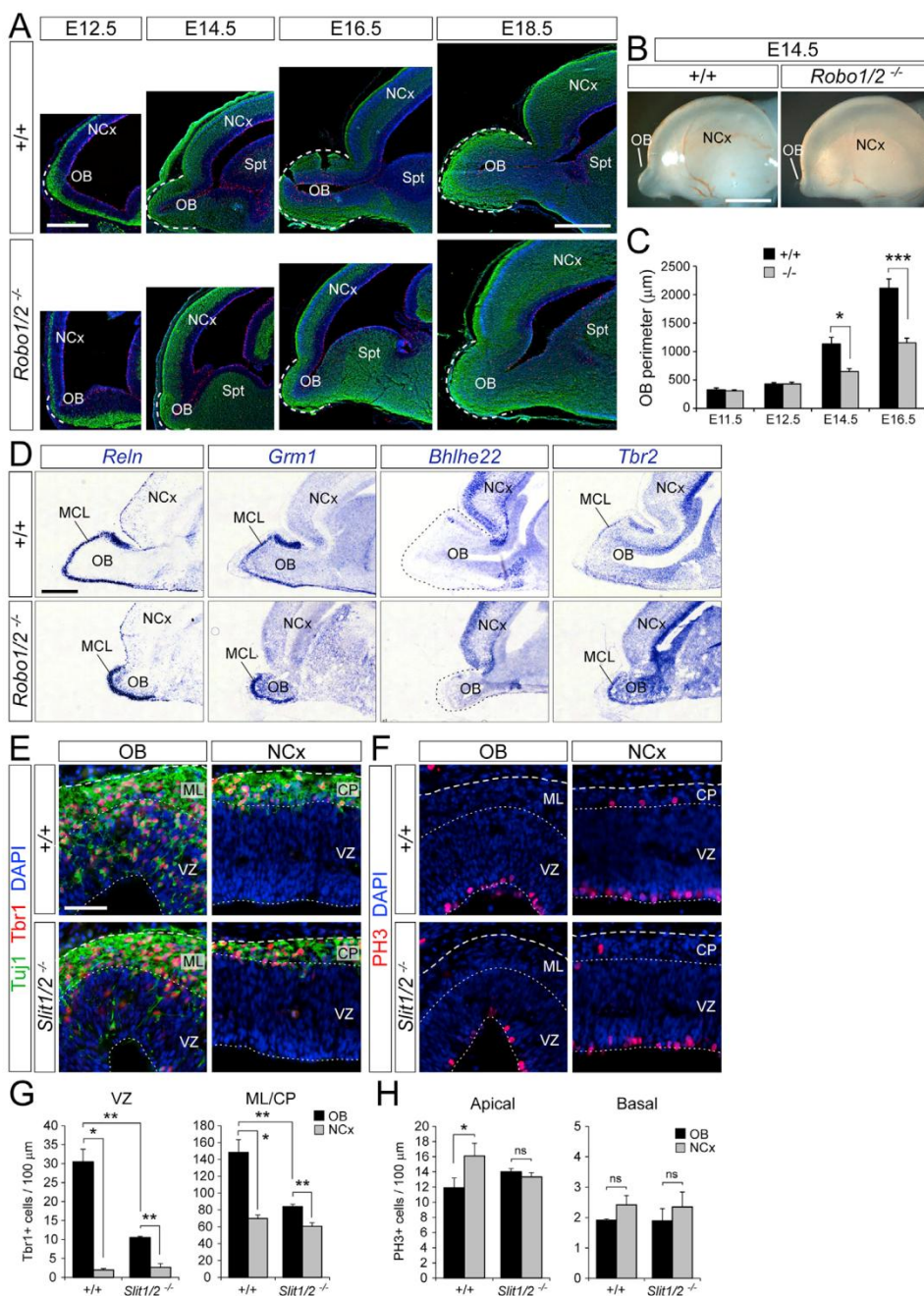


Figure S5. Regulation of OB Neurogenesis and Growth by Robo Receptors and Slit Ligands, Related to Figure 3

(A) Sagittal sections of the rostral telencephalon showing the growth and evagination of the OB in WT and mutant embryos from E12.5 to E18.5; dashed lines indicate OB perimeter.

(B) External lateral view of the brain in WT (+/+) and *Robo1/2*^{-/-} embryos.

(C) Measurement of the OB perimeter on sagittal sections from WT and *Robo1/2*^{-/-} embryos from E11.5 to E16.5 (n = 3-9 embryos per group).

(D) ISH on sagittal sections from WT and mutant embryos at E18.5 for the indicated genes, which delineate the extension of the OB by being either selectively expressed (*Reln*, *Grm1*, *Tbr2*) or selectively absent (*Bhlhe22*) in the mitral cell layer (MCL).

(E-H) Distribution and abundance of Tbr1+ and Tuj1+ neurons (E and G) and PH3+ apical and basal mitoses (F,H) in OB and NCx of WT and *Slit1/2*^{-/-} embryos at E12.5. Plots show density of cells per 100 µm of ventricular surface in the VZ (left) and mantle layer (ML) or cortical plate (CP) (n = 3 embryos per group).

Values are mean ± SEM; t tests, *p < 0.05, **p < 0.01, ***p < 0.001, ns = not significant. Scale bars: 200 µm (A: E12.5, E14.5), 500 µm (A: E16.5, E18.5; D), 1 mm (B), 50 µm (E and F).

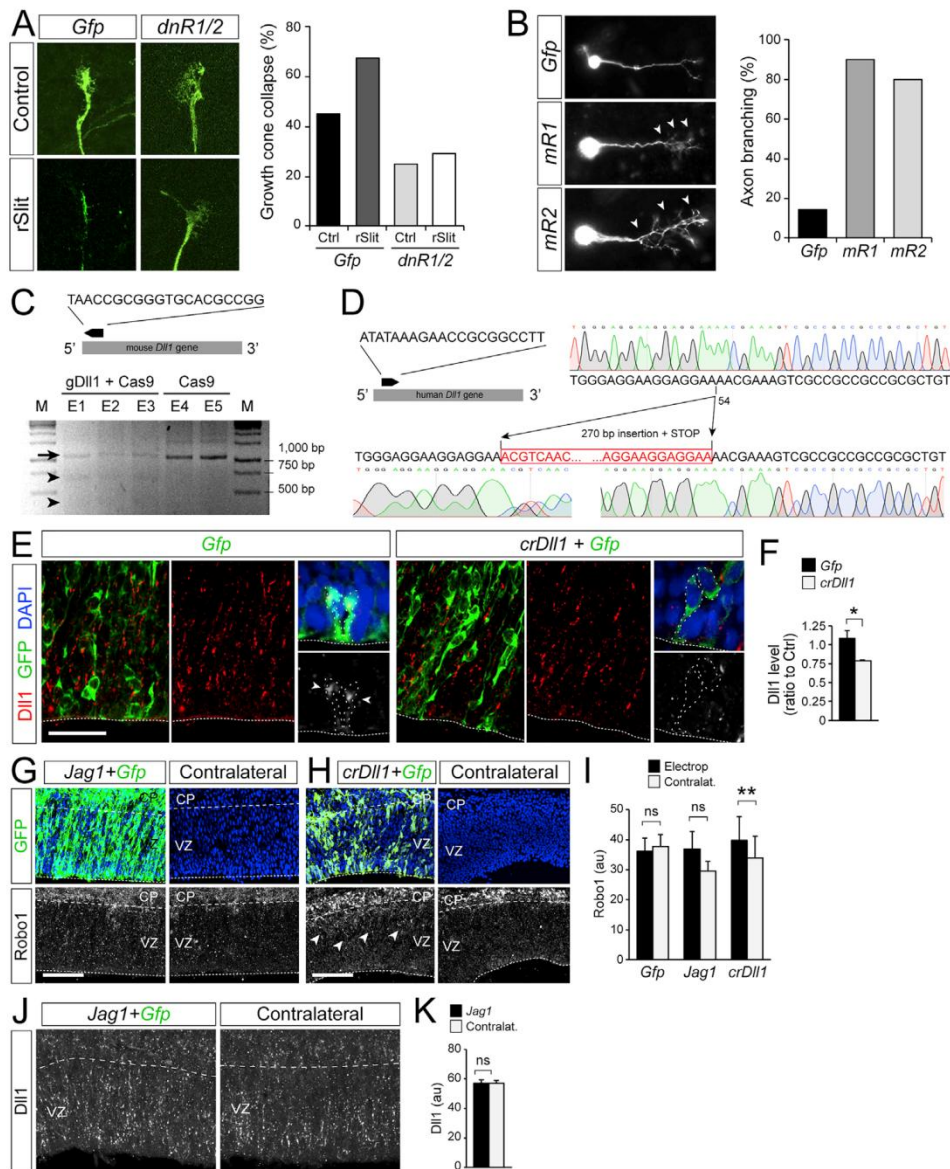


Figure S6. Functional Validation of Genetic Reagents and Test of Interaction between Robo and Notch Signaling, Related to Figures 4, 5, and 7

(A and B) Validation of dnRobo and myrRobo as dominant-negative and constitutively active for Robo signaling, respectively. In (A), growth cone collapse assay of growing axons from explants of embryonic mouse retinas, electroporated to express *Gfp* or *dnRobo* and exposed to recombinant Slit protein or vehicle solution. Failure of response to Slit upon dnRobo-overexpression demonstrates its dominant-negative effect ($n = 44\text{--}58$ growth cones per group, 3 independent experiments). In (B), branching assay of growing axons from single neurons of embryonic rat dorsal root ganglion, overexpressing *Gfp* alone or with myrRobo constructs as indicated. Exuberant axonal branching typically elicited by Slit-Robo signaling occurs in myrRobo-expressing neurons in the absence of Slit, demonstrating constitutive activation of Robo signaling ($n = 5\text{--}10$ neurons per group).

(C–F) Validation of crsp constructs for disruption of *Dll1* in mouse and human. (C) Top, sequence of the gRNA targeting *mouse Dll1*, and schematic of the orientation and location of the targeting site (black arrow) within the *mDll1* coding sequence (gray bar). Bottom, validation of Crispr-mediated editing of the *mDll1* locus upon electroporation with g*Dll1* plus Cas9, but not with Cas9 alone. Different lanes correspond to independent electroporated embryos. M, molecular weight marker. Arrow indicates 1,025 bp amplicon, arrowheads indicate the products of PCR amplicon digestion by Svrveyor Nuclease (656 + 368 bp), absent in the Cas9-alone lanes. (D) Left, sequence of the gRNA targeting *human Dll1*, and schematic of the orientation and location of the targeting site (black arrow) within the *hDll1* coding sequence (gray bar). Right, chromatograms for genome sequence validation of Crispr-mediated editing of the *hDll1* locus upon electroporation of cerebral organoid with g*Dll1* plus Cas9. A 270bp fragment was inserted at position 54 of the coding sequence, introducing a STOP codon in position 76. (E and F)

(legend continued on next page)

Effect of electroporating crDII1 in NCx (green cells) on the abundance of DII1 protein (red). Details are examples VZ cells loosing DII1 protein (arrowheads) from the cell surface upon crDII1 (n = 3 embryos per group).

(G–K) Antibody stain for GFP and Robo1 or DII1 in NCx at E13.5 upon electroporation of the indicated plasmid combinations at E12.5, and quantifications (paired t test). Arrowheads indicate area of increased Robo (n = 3 embryos per group).

Values are mean + SEM; paired or independent samples t tests; *p < 0.05; ns, not significant. Scale bars: 30 μ m (E), 50 μ m (G and H).

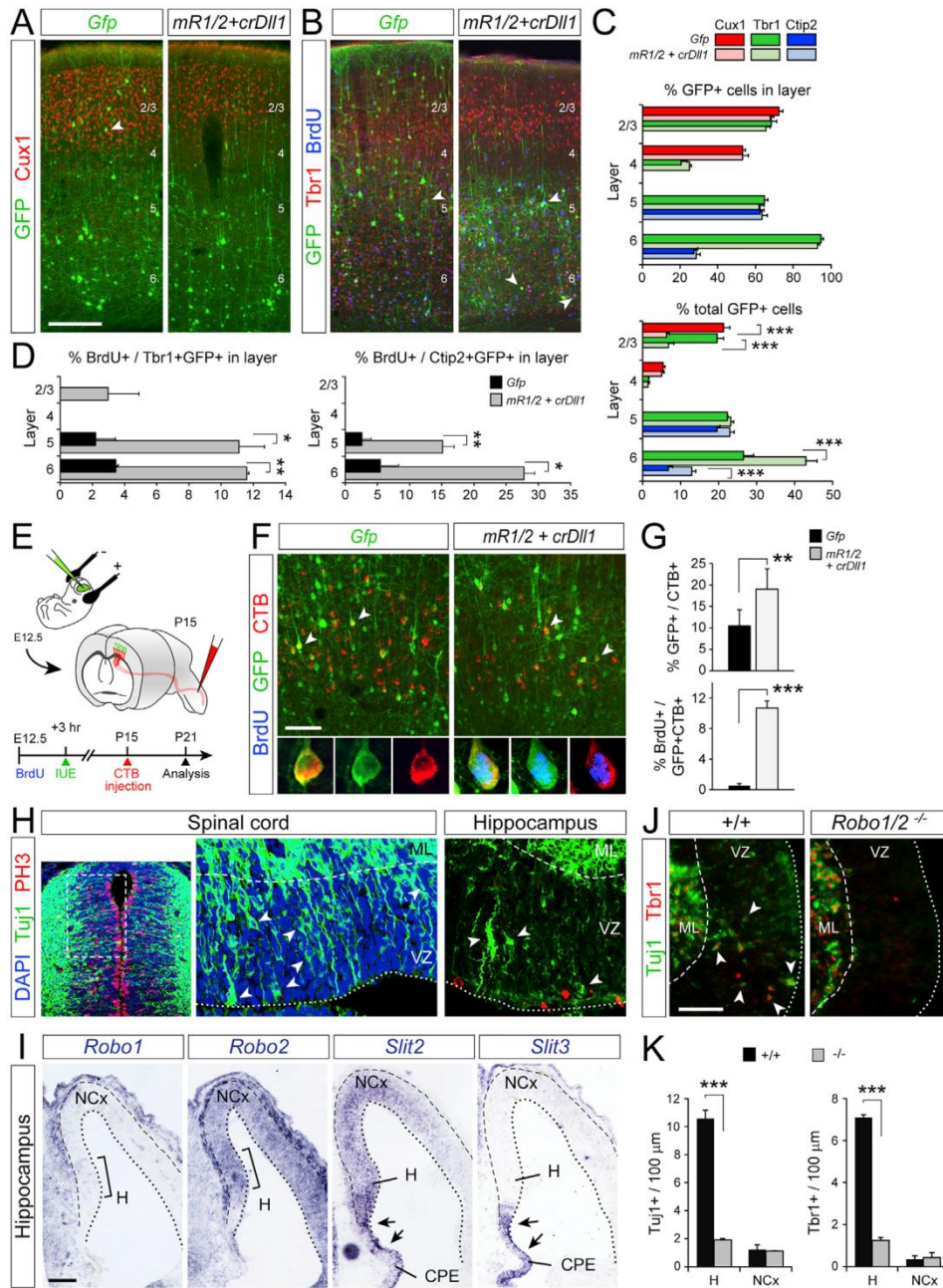


Figure S7. Robo/Dll1 Signaling Drives Direct Genesis of Deep-Layer Corticofugal Neurons and Regulates Direct Neurogenesis in Brain Regions with Ancestral Origin, Related to Figure 5

(A–D) Analysis of fate marker expression by directly generated neurons (arrowheads) upon electroporation with the indicated plasmid combinations. Plots in (C) show the proportion of GFP+ cells within each layer (top) and of all GFP+ cells in NCx (bottom) expressing each marker. Plots in (D) show the proportion of cells positive for GFP and Tbr1 (left), or Ctip2 (right), within each layer that retain 100% BrdU label ($n = 3-5$ animals per condition; one way ANOVA followed by χ^2 -test). (E) Experimental design to determine axonal projection identity of neocortical neurons born by direct neurogenesis at E12.5. (F and G) Retrograde labeling of corticospinal-projecting neurons generated directly upon electroporation with the indicated plasmid combinations, and analysis of abundance. Insets show soma of single CTB+GFP+ neurons. Plots in (G) show proportion of CTB-traced neurons expressing GFP (top; arrowheads in (F) and proportion of CTB+GFP+ neurons retaining 100% BrdU label (bottom) ($n = 3-4$ animals per condition; χ^2 -test). (H) Tuj1 and PH3 stains of the embryonic spinal cord and hippocampal primordium, showing that virtually all mitoses are apical and neurons are very abundant in the VZ of both regions, two traits indicative of direct neurogenesis.

(legend continued on next page)

(I) ISH in coronal sections of hippocampus and adjacent neocortex at E12.5. Expression of *Robo1*, *Robo2*, and of *Slit2* and *Slit3*, mRNAs is most prominent in hippocampus primordium (H) and choroid plexus epithelium (CPE), respectively.

(J and K) Distribution and abundance of Tuj1+ / Tbr1+ neurons (arrowheads) in hippocampal primordium and adjacent neocortex from control and *Robo1/2*^{-/-} mutants at E12.5 (n = 3 embryos per group; t tests).

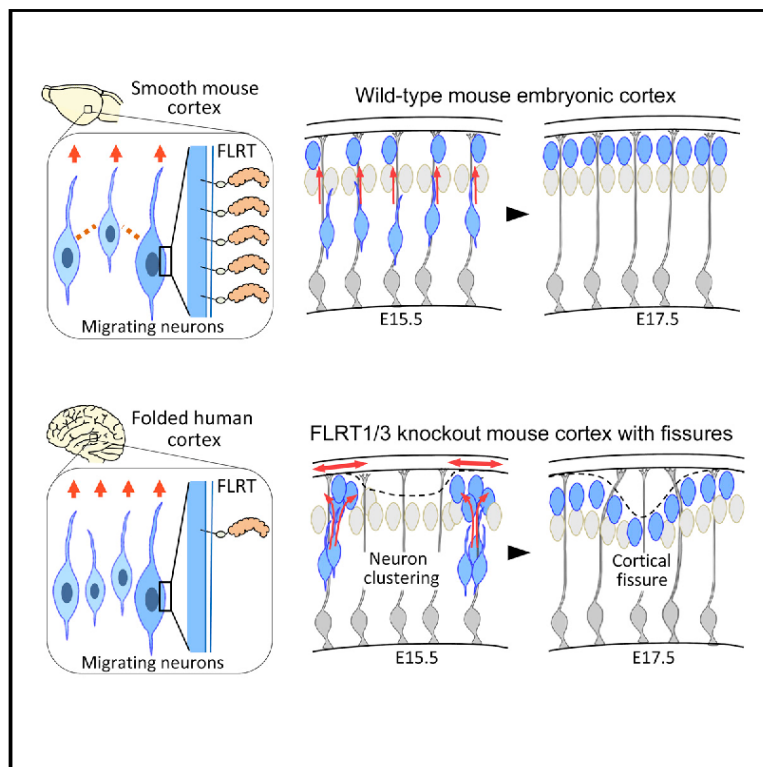
Values are mean + SEM; *p < 0.05; **p < 0.01; ***p < 0.001; ****p < 0.001. Scale bars: 200 μ m (A and B); 100 μ m (I), 50 μ m (F and J).

**Annex 2. Regulation of Cerebral Cortex Folding by Controlling
Neuronal Migration via FLRT Adhesion Molecules**

doi: [10.1016/j.cell.2017.04.012](https://doi.org/10.1016/j.cell.2017.04.012)

Regulation of Cerebral Cortex Folding by Controlling Neuronal Migration via FLRT Adhesion Molecules

Graphical Abstract



Authors

Daniel del Toro, Tobias Ruff, Erik Cederfjäll, Ana Villalba, Gönül Seyit-Bremer, Víctor Borrell, Rüdiger Klein

Correspondence

rklein@neuro.mpg.de

In Brief

Physical migration of neurons can create the folded cortical surface characteristic of primate brains.

Highlights

- *Flrt1/3* double-knockout mice develop macroscopic cortical sulci
- Cortex folding in mutant mice does not require progenitor cell amplification
- Absence of FLRT1/3 reduces intercellular adhesion and promotes immature neuron migration
- FLRT1/3 levels are low in the cortices of human embryos and future sulci of the ferret

Regulation of Cerebral Cortex Folding by Controlling Neuronal Migration via FLRT Adhesion Molecules

Daniel del Toro,^{1,4} Tobias Ruff,^{1,4} Erik Cederfjäll,¹ Ana Villalba,² Gönül Seyit-Bremer,¹ Víctor Borrell,² and Rüdiger Klein^{1,3,5,*}

¹Max Planck Institute of Neurobiology, Am Klopferspitz 18, 82152 Martinsried, Germany

²Instituto de Neurociencias, Consejo Superior de Investigaciones Científicas and Universidad Miguel Hernández, 03550 Sant Joan d'Alacant, Spain

³Munich Cluster for Systems Neurology (SyNergy), 80336 Munich, Germany

⁴These authors contributed equally

⁵Lead Contact

*Correspondence: rklein@neuro.mpg.de

<http://dx.doi.org/10.1016/j.cell.2017.04.012>

SUMMARY

The folding of the mammalian cerebral cortex into sulci and gyri is thought to be favored by the amplification of basal progenitor cells and their tangential migration. Here, we provide a molecular mechanism for the role of migration in this process by showing that changes in intercellular adhesion of migrating cortical neurons result in cortical folding. Mice with deletions of FLRT1 and FLRT3 adhesion molecules develop macroscopic sulci with preserved layered organization and radial glial morphology. Cortex folding in these mutants does not require progenitor cell amplification but is dependent on changes in neuron migration. Analyses and simulations suggest that sulcus formation in the absence of FLRT1/3 results from reduced intercellular adhesion, increased neuron migration, and clustering in the cortical plate. Notably, FLRT1/3 expression is low in the human cortex and in future sulcus areas of ferrets, suggesting that intercellular adhesion is a key regulator of cortical folding across species.

INTRODUCTION

The cerebral cortex is a central region in the brain that controls high-level cognitive functions (Geschwind and Rakic, 2013). During evolution, the cortex has undergone an enormous expansion that mostly accounts for the increase in brain size across mammalian species (Finlay and Darlington, 1995). Because the cerebral cortex is a laminar sheet of tissue, its expansion coincides with the formation of folds consisting of gyri and sulci. Based on cortical folding, mammals can be classified into gyrencephalic species (such as ferrets and most primates), which have folded brains, and lissencephalic species (such as mice), which have smooth-surfaced cortices.

Mechanistically, cortex folding is promoted by regional cortical growth together with tangential expansion (Borrell and Götz,

2014; Borrell and Reillo, 2012; Reillo et al., 2011). This model is based on the finding that one of the germinal zones of the cortex, the subventricular zone (SVZ), is subdivided into an inner (ISVZ) and outer (OSVZ) subventricular zone in gyrencephalic but not in lissencephalic species, (Reillo et al., 2011). The OSVZ is a proliferative region that contains transit-amplifying basal progenitors (BPs) that expands concomitant with the onset of cortical folding (Hansen et al., 2010; Lui et al., 2011). Recent observations have shown that local amplification of BPs can lead to gyrus formation in the smooth mouse cortex (Florio et al., 2015; Rash et al., 2013; Stahl et al., 2013; Wang et al., 2016), whereas a decrease of the BP pool reduces the gyrification index in the ferret (Reillo et al., 2011; Toda et al., 2016), indicating that expansion of BPs represents a key event to induce gyration of the mammalian brain. Interestingly, new findings have challenged this model regarding its predictive power on the gyration of the cortex. Recent studies have shown that increasing proliferation of BPs in the mouse SVZ per se increased the cortical thickness or surface but was not sufficient to cause gyrification (Nonaka-Kinoshita et al., 2013; Thomson et al., 2009; Wagenführ et al., 2015). Notably, the prevailing hypothesis proposes that it is the combination of BP amplification with divergent radial migration that contributes to the expansion of the cortex in radial and tangential axes and then its folding (Borrell and Reillo, 2012; Fernández et al., 2016; Lui et al., 2011; Reillo et al., 2011). According to this model, migrating neurons do not follow strictly parallel pathways but, instead, follow divergent trajectories, dispersing in the lateral axis, which leads to tangential cortical expansion and folding. Failure in neuronal migration causes severe abnormalities in cortical folding that result in human lissencephaly (Moon and Wynshaw-Boris, 2013). Moreover, recent findings directly support the radial divergence hypothesis by showing that, in the ferret cortex, migrating neurons do not follow strict radial pathways but, instead, follow more tortuous migration routes concomitant with the start of cortical folding (Gertz and Kriegstein, 2015). However, molecular mechanisms that affect neuronal migration and modulate this trajectory divergence, resulting in cortex folding, have not been found. Moreover, no mouse gene has yet been identified whose genomic or global modification (rather than acute and local) favors folding of the smooth mouse cortex.



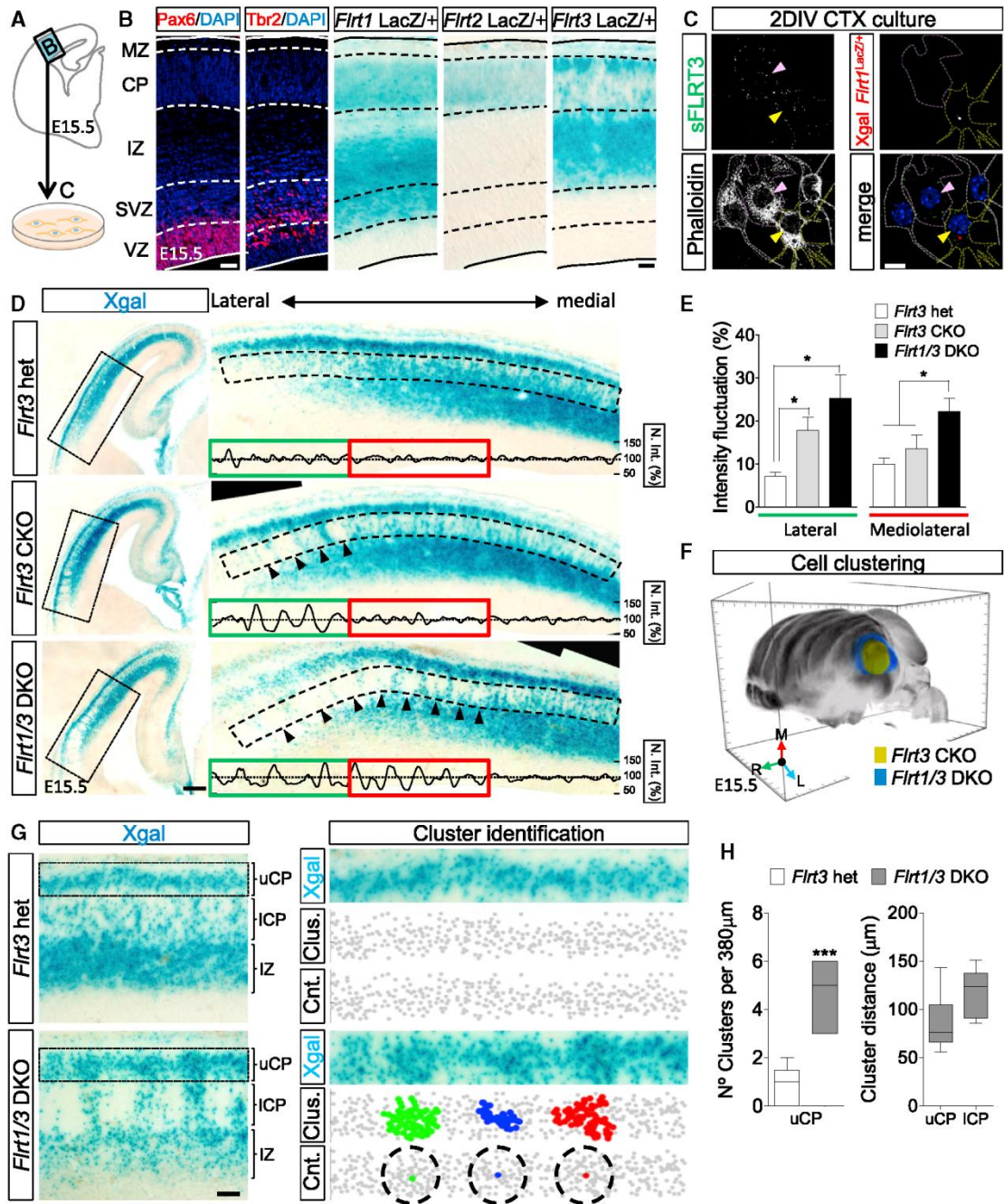


Figure 1. FLRT1 and FLRT3 Control Lateral Migration of Cortical Neurons

(A) Cortical region shown in (B) and source of cortical neurons shown in (C).
 (B) X-gal staining of FLRT1-3 expression on coronal sections of E15.5 cortex from *Firt1-3^{lacZ/lx}* reporter lines. Cortical layers were identified by DAPI and immunostained for Pax6 and Tbr2.
 (C) *Firt1^{lacZ/+}* cortical cultures at E15.5 (2 days in vitro), immunostained for FLRT3 (surface staining, green in merge), X-gal (for labeling Firt1+ cells, red in merge), and phalloidin. Yellow arrowheads/outlines indicate FLRT1/3 double-positive neurons. Magenta arrowheads/outlines show FLRT3 single-positive neurons. White outlines show FLRT3-negative neurons.
 (D) X-gal staining of coronal sections from E15.5 *Firt3* heterozygous (*Firt3^{lox/lacZ}*), *Firt3* CKO and *Firt1/3* DKO embryos. Areas in dashed rectangles are shown with higher magnification on the right. Normalized intensity plots are shown, obtained from the areas delineated with a dashed rectangle. Arrowheads indicate regions containing cell clusters, and green boxes highlight lateral and red boxes mediolateral portions of the cortex at intermediate-caudal levels.
 (E) Quantification of the intensity fluctuations in those portions of the neocortex; n = 3–5 mice/group, 2 sections/mouse; *p < 0.05, one-way ANOVA test with Tukey's post hoc analysis.

(legend continued on next page)

Previously, we have established that genetic ablation in mice of FLRT3, a member of the fibronectin leucine rich-repeat transmembrane protein (FLRT) family of cell adhesion molecules, leads to altered distribution of pyramidal neurons during cortical development, forming a repeated pattern of clusters along the tangential axis (Seiradake et al., 2014). FLRTs have the unique property of acting as adhesion molecules by homophilic and heterophilic binding to Latrophilin proteins and as repellents by binding to Unc5/Netrin receptors (Jackson et al., 2015, 2016; Yamagishi et al., 2011). Here we report that genetic ablation of FLRT1 and FLRT3 leads to the development of macroscopic cortical sulci during embryogenesis. Mechanistically, this process happens independent of progenitor cell amplification. Instead, we found that cortical neurons display reduced intercellular adhesion, faster neuronal migration, and clustering along the tangential axis, thereby leading to sulcus formation in the normally smooth mouse neocortex. Our results suggest that intercellular adhesion of migrating cortical neurons is a key factor underpinning folding of the cerebral cortex.

RESULTS

FLRT1 and FLRT3 Control the Lateral Dispersion of Pyramidal Neurons

Expression analysis of FLRTs in the developing cortex from embryonic day 13.5 (E13.5) to E17.5 (Figures 1A and 1B and Figures S1A–S1C and S1F) revealed a partial overlap between FLRT1 and FLRT3 in both the intermediate zone (IZ) and cortical plate (CP), whereas FLRT2 was confined to the CP. In cultures of dissociated cortical neurons from E15.5 embryos, approximately 30% were FLRT3-positive, and, among those, 35% co-expressed FLRT1 (Figure 1C). This finding was consistent with a molecular identity analysis from the E15.5 mouse cortex that also revealed strong enrichment of both FLRT1 and FLRT3 in migrating upper cortical neurons among other cell types (Figures S1D and S1G). To investigate whether FLRT1 plays a role in pyramidal neuron migration, possibly in a functionally redundant fashion with FLRT3, we generated double knockout mice lacking FLRT3 in developing neurons and progenitors and FLRT1 in all cells (*Flrt1*^{-/-}; *Flrt3*^{lox/lacZ}; *Nestin-Cre* mice; in short, *Flrt1/3* double knockout [DKO]) and compared them to the respective single mutants (*Flrt3*^{lox/lacZ}; *Nestin-Cre*; in short, *Flrt3* conditional knockout [CKO], and *Flrt1* knockout [KO] mice). In agreement with our previous work (Seiradake et al., 2014), we found that FLRT3-deficient (β -galactosidase [β -gal]⁺) neurons in *Flrt3* CKOs showed abnormal cell clustering in the lateral portion of the neocortex within the lower CP (Figures 1D and 1E; Figure S1I). Interestingly, this cell clustering effect was enhanced

in *Flrt1/3* DKO compared with *Flrt3* CKO mice, extending into medial and caudal regions of the cortex (Figures 1D–1F; Figure S1J; data not shown). To analyze the distribution of β -gal⁺ neurons, we calculated the normalized intensity profile of the X-gal staining in the lower half of the cortical plate (dashed region, Figure 1D), which revealed extended fluctuations in the density of *Flrt1/3* DKO neurons compared with *Flrt3* CKO and *Flrt3* heterozygous neurons (Figure 1E). To test whether the repeated pattern of cell clusters extended to the upper CP, we performed a distance-based clustering analysis, using as input the coordinates of X-gal-positive neurons populating the upper CP. We observed clustering of neurons in the upper CP of *Flrt1/3* DKO following a pattern of approximately 75- to 120- μ m intervals, in line with the pattern present in the lower CP (Figures 1G and 1H). This suggests that the altered localization and clustering of cells in the *Flrt1/3* DKO extended into the upper CP, where cells normally spread laterally to form cortical layers. Taken together, these results indicate partially redundant roles of FLRT1 and FLRT3 in controlling the tangential distribution of pyramidal neurons during cortical development.

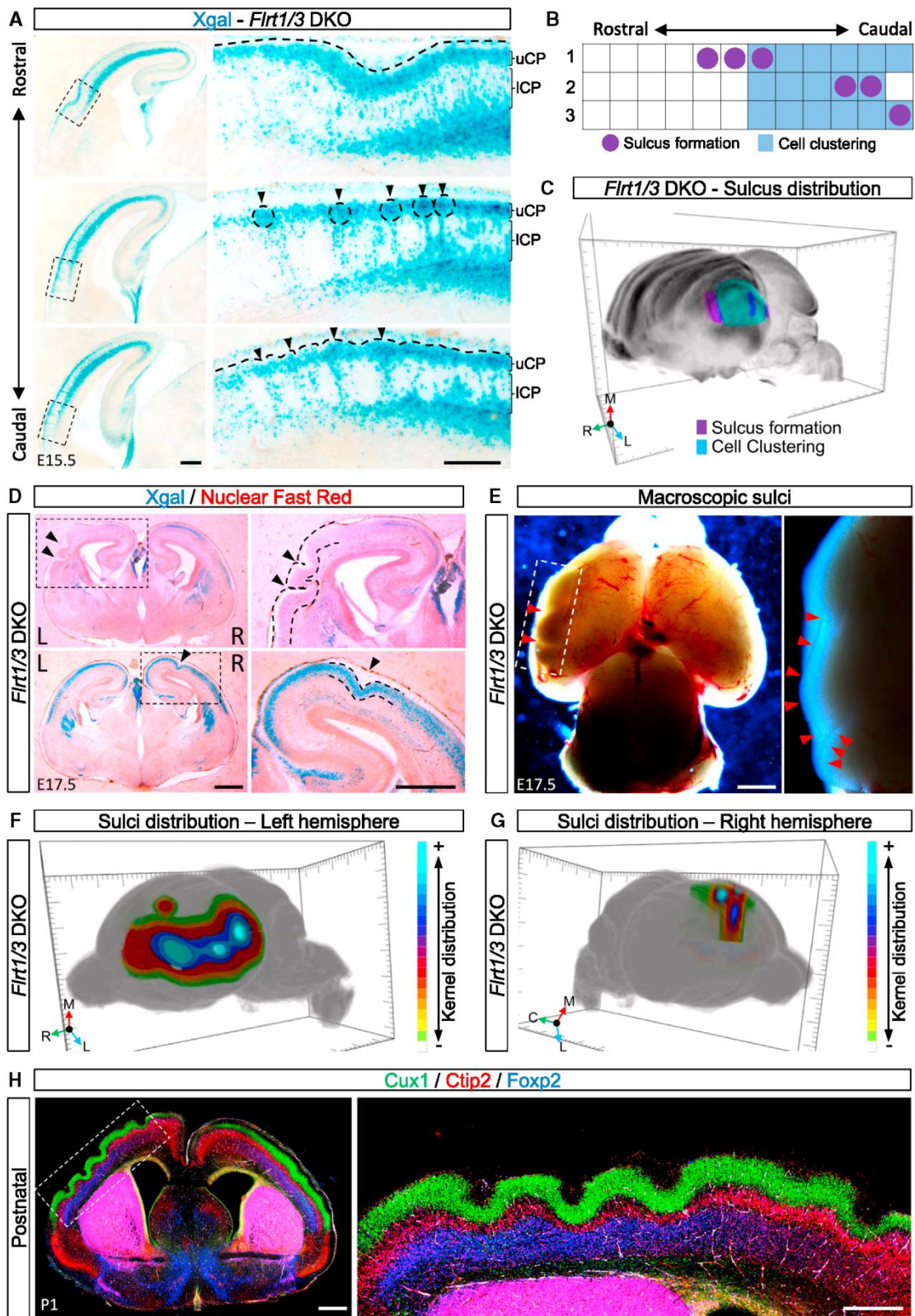
Flrt1/3 CKO Mice Develop Cortical Sulci

Upon further inspection of *Flrt1/3* DKO embryos, we found that, in 33% of the cases, the clustering of upper CP neurons at E15.5 correlated with the formation of an incipient sulcus in the otherwise smooth mouse neocortex (Figure 2A; Figures S2A and S2B). These cortical sulci developed on the lateral side of the cortex from intermediate to caudal levels where the repeated pattern of neuronal clusters was present in mutant embryos (Figures 2B and 2C), suggesting that these processes were causally linked. At later stages of cortical development (E17.5), cortical sulci were found in *Flrt1/3* DKO embryos, with a similar penetrance of 31% (Figure S2C). They showed considerable phenotypic variability between embryos, ranging from shallow to deep sulci that were easily visible in intact brains after removal of the meninges (Figures 2D and 2E).

Because cortical folding is not a random process but, rather, forms stereotyped patterns in gyrencephalic species (Borrell and Reillo, 2012), we determined the spatial distribution of sulci at E17.5. We used a kernel density estimator based on the location of sulci in coronal sections and plotted it onto a 3D mouse brain template. This analysis revealed that the left hemisphere had a higher probability of developing sulci and that they were mostly located between the perirhinal and postrhinal cortices of the mouse, close to the rhinal fissure (Beaudin et al., 2013; Figure 2F; Movie S1). In contrast, the right hemisphere developed sulci in rostral-medial cortical regions where clusters were not visible, suggesting that other mechanisms might also participate

(F) 3D mouse brain (template from the Allen Mouse Brain Atlas) with cortical areas displaying cell clustering in *Flrt3* CKO (green area) and *Flrt1/3* DKO (blue area) at E15.5.

(G) X-gal staining of coronal sections from E15.5 *Flrt3* heterozygous and *Flrt1/3* DKO embryos. Cell clusters in the upper CP were identified based on the position of individual X-gal⁺ neurons (areas in dashed rectangles are shown with higher magnification on the right) using a distance-based clustering method (a cluster was defined as a minimum of 25 cells spaced less than 20 μ m). Cluster identification is as follows. Neuron clusters in *Flrt1/3* DKO embryos are marked with different colors (red, green, and blue; "Clus"), and centroids of each cluster (cnt) are shown in the same color. Neurons that are not clustered are colored in gray. (H) Quantification of the number of clusters and the distance between them from the data shown in (G); n = 3–5 mice/group; ***p < 0.001, unpaired Student's t test. Whiskers in the box plot represent minimum and maximum. The data are presented as mean \pm SEM. Scale bars represent 150 μ m (B), 14 μ m (C), 300 μ m (D), and 50 μ m (G).



(legend on next page)

in this process (Figure 2G; Movie S1). The variability in sulcus location may have to do with the absence of gene expression microdomains. These structures play an important role in the generation of gyri/sulci at specific locations and are present in the developing cortex of gyrencephalic species such as the ferret but not in the lissencephalic mouse (de Juan Romero et al., 2015). Sulci were also found in postnatal stages of *Flrt1/3* DKO mice (penetrance, 24%) (Figure 2H; Figures S2D and S2E), indicating that these were not transient embryonic structures. The examination of single mutant brains revealed that *Flrt1* KO, but not *Flrt2* or *Flrt3* CKO, brains showed sulcus formation, albeit with lower penetrance (12%–16%; Figures S2C and S2D). In addition, *Flrt2/3* DKO brains rarely showed sulcus formation (1 in 13), suggesting that *Flrt1* plays a major role in the phenotype (Figures S2C and S2F). The morphologies of the sulci in *Flrt1* KO brains were comparable with those observed in *Flrt1/3* DKO brains (Figure S2G), suggesting that the underlying mechanisms were similar. These results indicate that FLRT1 and FLRT3 have partially redundant functions in the formation of a smooth neocortex.

Cortical Sulci Develop Independent of Cell Proliferation

As a first step toward understanding the mechanism involved in sulcus formation in *Flrt1/3* DKO brains, we analyzed cell proliferation in brain sections at different stages of cortical development by quantifying the numbers of apical (Pax6+) and basal (Tbr2+) progenitors (Englund et al., 2005). We also stained for the phosphorylated forms of vimentin (Pvim) and histone H3 (PH3) that label dividing radial glial (RG) and mitotic cells, respectively (Pilz et al., 2013). We did not find significant increases in mitotic and dividing RG cells in mutant embryos at different developmental stages and in different rostro-caudal regions, except for a small increase in intermediate cortical regions at E13.5 (Figures 3A–3C; Figures S3A–S3L). Moreover, the proportion of mitotic cells in basal versus apical germinal layers was unchanged in *Flrt1/3* mutant brains (Figure 3D; Figures S3D, S3H, and S3L), and the numbers of dividing basal RG cells were less than 5% in all experimental groups (data not shown). Quantification of total cell nuclei (stained with DAPI), Pax6+ and Tbr2+ progenitor cells, and short pulses of BrdU did not reveal significant increases in *Flrt1/3* mutant brains (Figure 3C; Figures S3C, S3G, S3K, and S3M–S3Q), suggesting that cortical sulci develop independent of changes in cell proliferation.

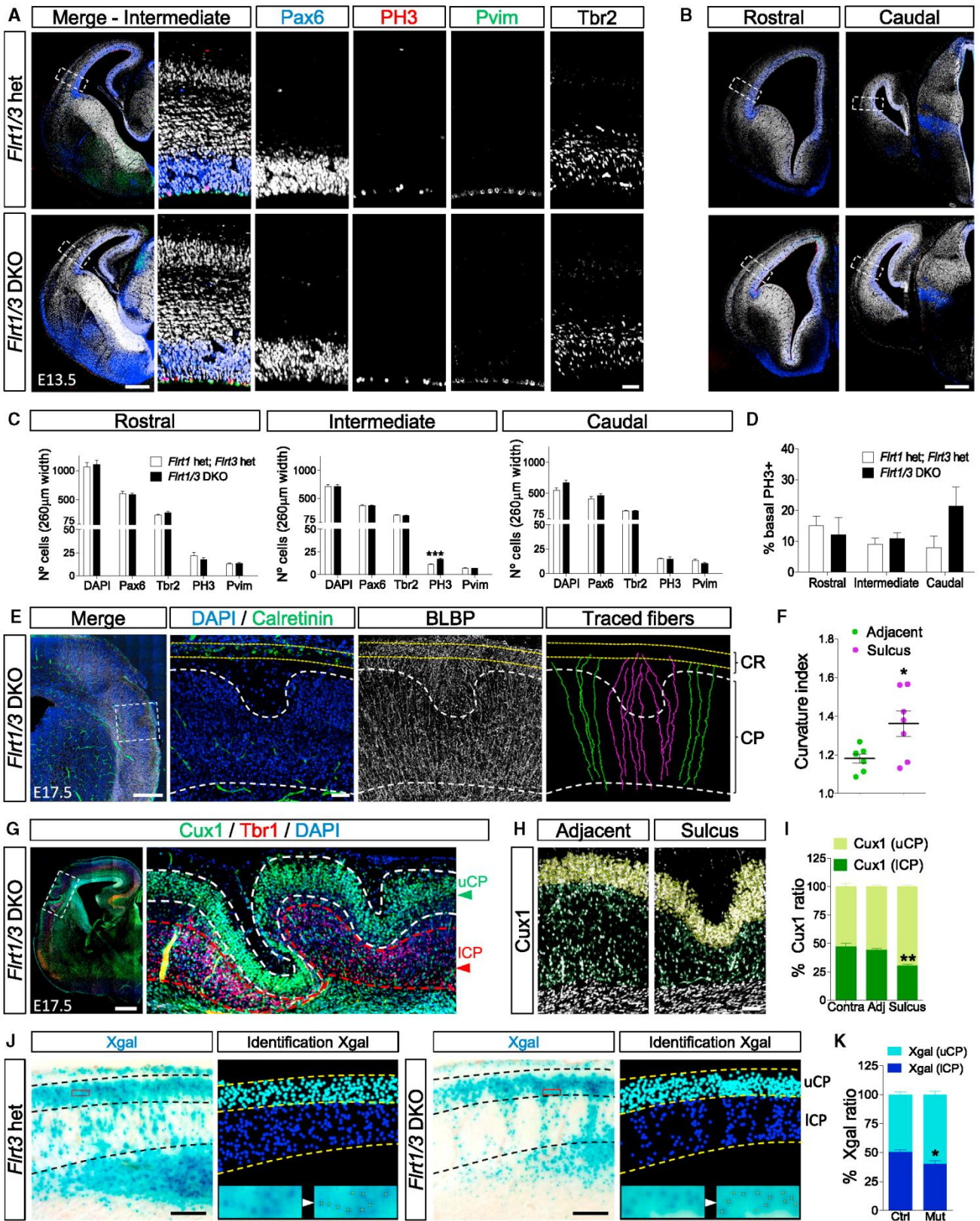
Next we explored alternative mechanisms underlying sulcus formation, such as alterations in the RG fiber scaffold, basement membrane formation, and Cajal-Retzius (CR) cell development. Tracing of individual RG fibers in *Flrt1/3* DKOs based on brain lipid-binding protein (BLBP) staining showed that RG processes located in sulcus areas reached the marginal zone (MZ), similar to control regions, even when sulci were very deep (Figure 3E; Figure S4A). The overall densities and lengths of RG processes in sulcus areas did not differ from adjacent regions (Figure S4B). The curvature index of RG processes was significantly higher in sulcus areas because of the convergence of fibers at sulcal pits (Figures 3E and 3F), similar to those reported in classic descriptions of gyrencephalic species such as ferrets and monkeys (Rakic, 1972; Smart and McSherry, 1986). Remarkably, the basal membrane was intact in seven of eight mutant brains (Figures S4C and S4D), suggesting that these sulci were not the result of neuronal ectopias as observed in cobblestone lissencephaly (Devisme et al., 2012). Because CR cells originating from the cortical hem (CH) express both FLRT1 and FLRT3 (Figures S4E–S4G), we also explored whether loss of FLRT1/3 affected CH-derived CR cell migration. We found that the distribution and density of CR cells in the MZ of sulcus areas in mutant brains appeared normal (Figure 3E), even in dramatic cases where the MZ followed the depth of the sulcus (Figure S4A). These results suggest that cortical sulci in *Flrt1/3* DKOs are not the result of alterations in RG scaffold, basal membrane formation, or CR cell development.

FLRT1/3-Deficient Pyramidal Neurons Reach Upper Cortical Layers Faster

Given the lack of strong alterations in progenitors and glial cells, we next asked whether sulcus formation correlated with changes in the migration and distribution of pyramidal neurons. Cortical layering seemed well preserved in sulcus areas of *Flrt1/3* DKO compared with controls (Figure 3G), but layer thickness was reduced, particularly in the lower CP (Figures S4H and S4I), similar to those reported in gyrencephalic species such as the ferret (Smart and McSherry, 1986). Notably, the proportion of Cux1+ neurons (Nieto et al., 2004) in the upper versus lower CP was significantly higher in sulci with respect to adjacent areas (Figures 3H and 3I). Similar results were obtained after bromodeoxyuridine (BrdU) pulse labeling of newborn pyramidal neurons at E14.5 and analyzing their distribution in the CP at E17.5

Figure 2. *Flrt1/3* CKO Mice Develop Cortical Sulci

(A) X-gal-stained serial coronal sections from the cortex of an E15.5 *Flrt1/3* DKO embryo. Areas in dashed rectangles are shown with higher magnification on the right. Dashed circles and arrowheads indicate prominent clustering of neurons in the upper CP, and horizontal dashed lines highlight incipient sulcus formation (top) and a wavy surface of the upper CP (bottom).
 (B) Twelve sections, rostral to caudal, of three *Flrt1/3* DKO brains (rows 1–3) at E15.5 were analyzed for the presence of sulci (circles) or cell clustering (blue squares).
 (C) 3D representation of the data shown in (B).
 (D) Coronal sections from two E17.5 *Flrt1/3* DKO brains with different degrees of sulcus formation in the cortical plate (arrowheads). Sections were stained with X-gal and nuclear fast red. Areas in dashed rectangles are shown with higher magnification on the right.
 (E) Macroscopic sulci in an E17.5 *Flrt1/3* DKO embryo. The area in the dashed rectangle is shown with higher magnification on the right, and sulci are indicated by arrowheads.
 (F and G) Sulcus distribution in the left (F) and right (G) hemispheres of all E17.5 *Flrt1/3* DKO embryos. The color bar indicates a higher (blue colors) or lower (green-white) density of sulci.
 (H) P1 FLRT1 KO brain section stained with Cux1, Ctip2, and Foxp2. Areas in dashed rectangles are shown with higher magnification on the right.
 Scale bars represent 300 μ m (A), 500 μ m (D), 1 mm (E), and 2.4 mm and 0.4 mm (H).



(legend on next page)

(Figures S4J and S4K). These results suggested that either FLRT1/3-deficient pyramidal neurons migrated faster through the cortical plate, thereby causing sulcification, or that sulcification provided a shorter migration distance compared with non-sulcus areas, resulting in a higher proportion of cells in the upper CP. Given that only a portion of migrating neurons expressed FLRT proteins, we next analyzed the distribution of FLRT3-deficient (β -gal⁺) neurons and compared non-sulcus areas of *Flrt1/3* DKO with controls. We found that the proportion of cells in the upper CP was higher in *Flrt1/3* DKO (Figures 3J and 3K). These results suggest that FLRT1/3-deficient pyramidal neurons migrate faster through the cortical plate than FLRT1/3-expressing neurons.

Lack of FLRT1/3 Increases Migration Speed

To obtain direct evidence for changes in the migration speed of cortical neurons, we performed live imaging of embryonic cortices *ex vivo*. Control and *Flrt1/3* DKO brains were sliced and imaged 48 hr after electroporation with pCAG-CRE and the Cre reporter pCALNL-DsRed to visualize migrating cells. This approach (Cre electroporation into *Flrt1/3* DKO embryos) was chosen over Cre electroporation into *Flrt1^{-/-}Flrt3^{lox/lox}* brains because the latter approach did not reliably induce sulci compared with control brains, presumably because of the low abundance of electroporated cells (data not shown). A caveat of the former approach was that only a subset of Cre reporter-positive cells expressed FLRT proteins because these brains also contain many non-FLRT-expressing cells (Figure 4A; Figures S5A and S5B). Hence, a large proportion of Cre reporter-positive cells in *Flrt1/3* DKO brains were not directly affected by the *Flrt1/3* mutations, thereby potentially masking subtle defects. Individual Cre reporter-positive neurons entering the CP from the IZ were tracked and processed using a custom Python algorithm that allowed us to quantify migration parameters and to color-code portions of each track based on migration speed (Figure 4B). Overall, Cre⁺ cells in *Flrt1/3* DKO neurons displayed parallel and straight paths (Figure S5C), except in rare cases when migrating through a forming sulcus, where they displayed convergent paths (Figure S5D; Movie S2). Similar to controls,

Cre⁺ neurons exhibited the stereotypic RG-based locomotor pattern with high speeds (>32 μ m/h) in the middle of the CP and decreasing speeds toward the upper CP (Kawauchi, 2015; Tabata and Nagata, 2016; Figure 4C). Given that Cre⁺ cells in *Flrt1/3* DKO neurons showed trends toward higher maximum speed and acceleration, we analyzed their speed profiles. These results revealed an increased proportion of high-speed segments (>58 μ m/h) in *Flrt1/3* DKO compared with control brains (Figure 4D; Figures S4E and S4F). Plotting the relative frequencies of the maximum migration speeds revealed that the fraction of cells reaching >70 μ m/h was significantly increased in *Flrt1/3* DKO brains compared with controls (19% versus 12%) (Figure 4E). These results suggest that *Flrt1/3* mutant neurons reached higher speeds more often than control neurons.

To assess the morphologies of individual *Flrt1/3* mutant neurons, we sparsely labeled *Flrt1/3* DKO neurons in an otherwise control background by introducing Cre and a Cre reporter into *Flrt1^{-/-}Flrt3^{lox/lox}* brains using the Supernova system, which makes use of a leaky Tet promoter driving Cre expression in few cells (Mizuno et al., 2014; Figure 4F). The general complexity of mutant neurons populating the lower CP appeared similar to those observed in control sections, as assessed by Sholl analysis (data not shown). When categorizing the neurons according to increasing maturity into multipolar, unipolar and bipolar neurons, and “bipolar branched” morphologies (Figure 4F), we observed a significant shift toward immature morphologies in the upper CP of Cre-induced *Flrt1/3* mutant neurons compared with controls (Figure 4G). Thus, ablation of FLRT1/3 increases the abundance of immature neurons in the upper cortical plate.

Modeling Clustering and Speed Profiles of *Flrt1/3* DKO Neurons

So far our analysis suggested a model in which increased migration speeds of *Flrt1/3* mutant neurons and/or the formation of cell clusters in the CP could be causal to sulcus formation (Figure 5A). To test this hypothesis, we performed data-driven computational modeling of neurons migrating through the CP. We took the following points into consideration. Both FLRT3 gain- and loss-of-function experiments *in vivo* revealed a repeated pattern

Figure 3. Pyramidal Neuron Distribution, but Not Cell Proliferation, Is Changed in Sulcus Areas

(A and B) E13.5 cortices from intermediate (A) and rostral, caudal regions (B) of control and *Flrt1/3* DKO embryos were labeled for the neuronal progenitors Pax6 (blue) and Tbr2 (white), mitotic cells (PH3, red), and dividing RG cells (Pvim, green). Areas in dashed rectangles in (A) are shown with higher magnification on the right.

(C) Quantification of the data shown in (A) and (B) ($n = 3-4$ mice/group). *** $p < 0.001$, unpaired Student's *t* test.

(D) Proportion of basal mitotic cells (PH3) ($n = 3-4$ mice/group; no significant changes between groups, unpaired Student's *t* test).

(E) *Flrt1/3* DKO section immunostained for BLBP (white), calretinin (green), and DAPI (blue). The area in the dashed rectangle is shown with higher magnification on the right. White dashed lines delineate sulci, and yellow dashed lines show the margins of the MZ where calretinin⁺ CR cells are located. Single traced RG processes are colored in magenta (in the sulcus region) or green (adjacent areas).

(F) Quantification of the curvature index of traced fibers shown in (E). $n = 7$ adjacent fibers, $n = 8$ sulcus fibers. * $p < 0.05$, unpaired Student's *t* test.

(G) E17.5 *Flrt1/3* DKO cortex immunostained for upper (Cux1, green) and deeper-layer (Tbr1, red) neurons and DAPI (blue).

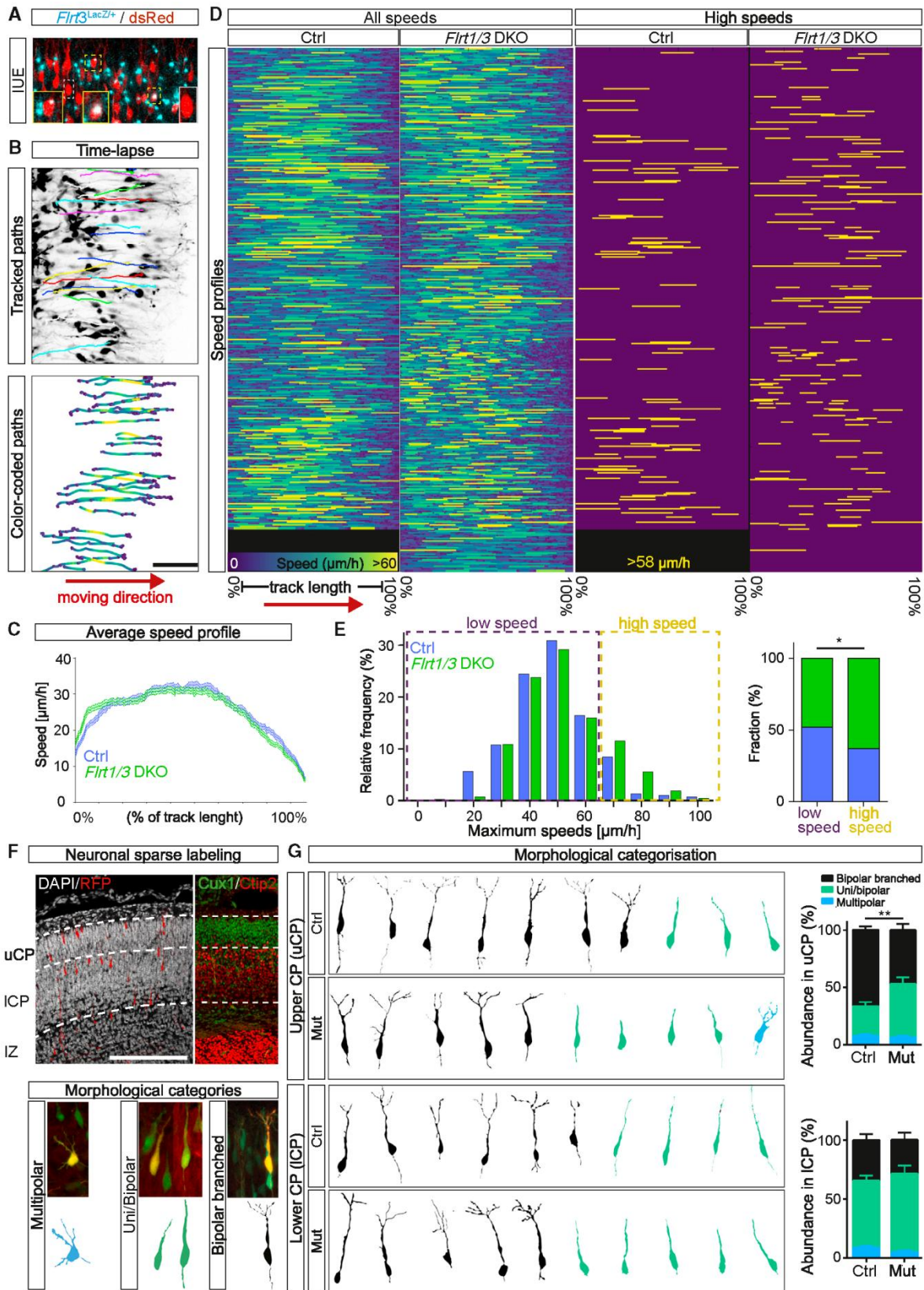
(H) Sulcus and adjacent region from an E17.5 *Flrt1/3* DKO section immunostained with Cux1 (white). Cux1⁺ cells in the upper CP are highlighted in light green, and Cux1⁺ cells still migrating in the lower CP are highlighted in dark green.

(I) Quantification of the data shown in (H) ($n = 12$ sections from a total of 5 mutant brains). ** $p < 0.01$, one-way ANOVA test with Tukey's post hoc analysis.

(J) X-gal staining of coronal sections from E15.5 *Flrt3* heterozygous and *Flrt1/3* DKO embryos. The CP was subdivided into upper and lower CP (Figure S11). The coordinates of X-gal precipitates (the red rectangle is shown with higher magnification on the right) were plotted as circles colored cyan (upper CP) and blue (lower CP).

(K) Quantification of the data shown in (J).

ICP, lower cortical plate (ICP). The data are represented as mean \pm SEM. Scale bars represent 400 and 150 μ m (A), 400 μ m (B), 600 and 100 μ m (E), 500 μ m (G), 90 μ m (H), and 120 μ m (J).



(legend on next page)

of cell clusters (Seiradake et al., 2014; Figure 1), which can be modeled as sine equations (Figure 5B). FLRTs act as cell adhesion molecules. This was shown for FLRT3 overexpression on cell clustering in vivo (Seiradake et al., 2014) and for FLRT-mediated cell aggregation in vitro (Figures S6A and S6B). The effects of *Flrt1/3* ablation on cell clustering in vivo are likely non-cell autonomous and may be the result of repulsive interactions with surrounding cells. Based on these considerations, we established two rules for the computational model: the sine equation modeled from gain-of-function experiments reflected the attraction forces of FLRT1/3+ neurons, and the sine equation from loss-of-function experiments represented the repulsion forces that FLRT1/3+ neurons are exposed to from surrounding cells. We distributed particles representing FLRT1/3-positive and -negative cells in a 2D grid, keeping equal distances and homogeneous distributions as observed in *Flrt1/3* heterozygous control sections. Particles representing FLRT1/3+ neurons showed attraction between them (first rule), whereas surrounding particles elicited repulsion toward them (second rule) (Figure 5C). To analyze the behavior of the particles during movement, particles were set to move along the z axis, and both speed and attraction-repulsion forces were random within a small range (ϵ) to mimic the fluctuations present in biological systems (Wilkinson, 2009). The attraction force was modulated by changing its amplitude and phase with respect to the repulsive force, which was kept constant under all conditions to reflect FLRT1/3 gain- and loss-of-function experiments (Figure S6C). Kernel distribution and minimum neighbor analysis of particles representing FLRT1/3+ neurons showed homogeneous distribution of particles when attraction and repulsion forces were balanced (Figures 5D and 5E). In contrast, particle clustering was observed when the attraction between particles was either high or low (Figures 5D and 5E; Figure S6D), which was consistent with the formation of neuronal clusters when FLRT1/3 were overexpressed or downregulated in vivo. Interestingly, the distribution of particles in the z axis was also influenced by attraction and repulsion forces. Under both high and balanced attraction conditions, the particles formed a smooth surface after moving along the z axis. Conversely, the low attraction paradigm resulted in a wavy surface because of an increased proportion of particles moving with high speed, reminiscent of the live imaging experiments with *Flrt1/3* DKO sections (Figures 5F and 5G).

Taken together, the low attraction paradigm of the computational model matched the experimental observations with *Flrt1/3* DKO mice rather well by generating particle clusters, increasing particle migration speed, and producing a wavy surface area.

FLRT Expression in Gyrencephalic Species

Given that FLRT1/3 ablation promoted sulcus formation in the normally smooth mouse neocortex, we set out to analyze endogenous FLRT1/3 expression in gyrencephalic species such as ferret and human. We hypothesized that FLRT1/3 expression levels may be generally low in gyrencephalic species to permit folding or relatively less abundant in sulcus than in gyrus areas. The ferret cortex is nearly lissencephalic at birth and undergoes complex and stereotyped postnatal folding (Reillo et al., 2011; Smart and McSherry, 1986). We analyzed ferret FLRT1/3 expression prior to morphological distinction of the prospective splenial gyrus and its adjacent lateral sulcus because previous studies have successfully identified genes involved in cortical folding in these regions (de Juan Romero et al., 2015; Figure S6E). In situ hybridization (ISH) for *Flrt1/3* revealed that both genes were mainly expressed in the CP, ISVZ, and OSVZ and, to a lesser extent, in the IZ at post-natal day 0 (P0) and P6 (Figures 6A and 6B; Figures S6F and S6G). Quantification of the expression levels revealed that both FLRT1 and FLRT3 were significantly less abundant in the cortical area that will form the lateral sulcus compared with the splenial gyrus (Figures 6C and 6D).

To study FLRT expression in human embryos, we used RNA sequencing (RNA-seq) data from three different sources. We first compared mouse FLRT1 and FLRT3 mRNA expression levels in E14 neocortex (subdivided into medial and lateral portions; (Wang et al., 2016) with RNA-seq data from human embryonic cortex at 12–19 post-conception weeks (pcw) (<http://www.brain-map.org>) normalized to the housekeeping gene GAPDH (Figures S6H and S6I). There were consistently higher levels in mouse cortex compared with a number of different cortical regions in human samples. Second, we analyzed mouse and human FLRT1 and FLRT3 normalized to GAPDH in different cortical layers (Fietz et al., 2012; Figures 6E and 6G). The abundance of mouse FLRT1 and FLRT3 mRNAs in the SVZ region ranged between 24%–49% of GAPDH, whereas the levels of human FLRT1 and FLRT3 ranged between 1%–3% of GAPDH (the human ISVZ

Figure 4. Faster Speed Profiles of *Flrt1/3* DKO Neurons

(A) *Flrt1/3* DKO embryos were electroporated at E13.5 with pCAG-Cre and the pCALNL-DsRed reporter plasmid (red staining; Figure S5). Yellow and white boxes indicate double dsRed/*Flrt3*+ and single dsRed+ cells, respectively.

(B) Time-lapse analysis of electroporated neurons migrating into the cortical plate in cultured E15.5 cerebral cortex slices. Migrating neurons were tracked (colored lines, top) and color-coded based on speeds in individual segments (bottom).

(C) Average speed profiles normalized to CP length of *Flrt1/3* DKO and littermate control embryos (from >400 tracked neurons).

(D) Color-coded speed profiles of >400 tracked neurons in controls and *Flrt1/3* DKO embryos normalized to total migration distance. Speeds higher than 58 $\mu\text{m}/\text{h}$ are highlighted in yellow on the right.

(E) Maximum speed frequency distribution of all tracked neurons in controls and *Flrt1/3* DKO embryos. Dashed rectangles indicate low (blue) and high (yellow) speed profiles, and their fraction is shown on the right. * $p < 0.05$, chi-square contingency analysis.

(F) Sparse cell labeling via electroporation at E13.5 of the Supernova vector system into either *Flrt1* $-/-$; *Flrt3lox/lox* (mutant) or *Flrt1* $+/-$; *Flrt3lox/lox* (control) littermates. At E16.5, Cre+ neurons were imaged and categorized according to their degree of maturity into multipolar, uni/bipolar, or bipolar branched phenotypes (example images are shown). The upper third portion of the CP was designated as upper CP based on the staining of *Cux1* (top, green) and *Ctip2* (bottom, red) markers.

(G) Abundance of each category of neurons in the lower and upper CP of mutant and control brains (representative images are shown; >150 neurons/group, * $p < 0.05$, chi-square contingency analysis).

IUE, in utero electroporation. The data bars are represented as mean \pm SEM. Scale bars represent 50 μm (B) and 200 μm (F).

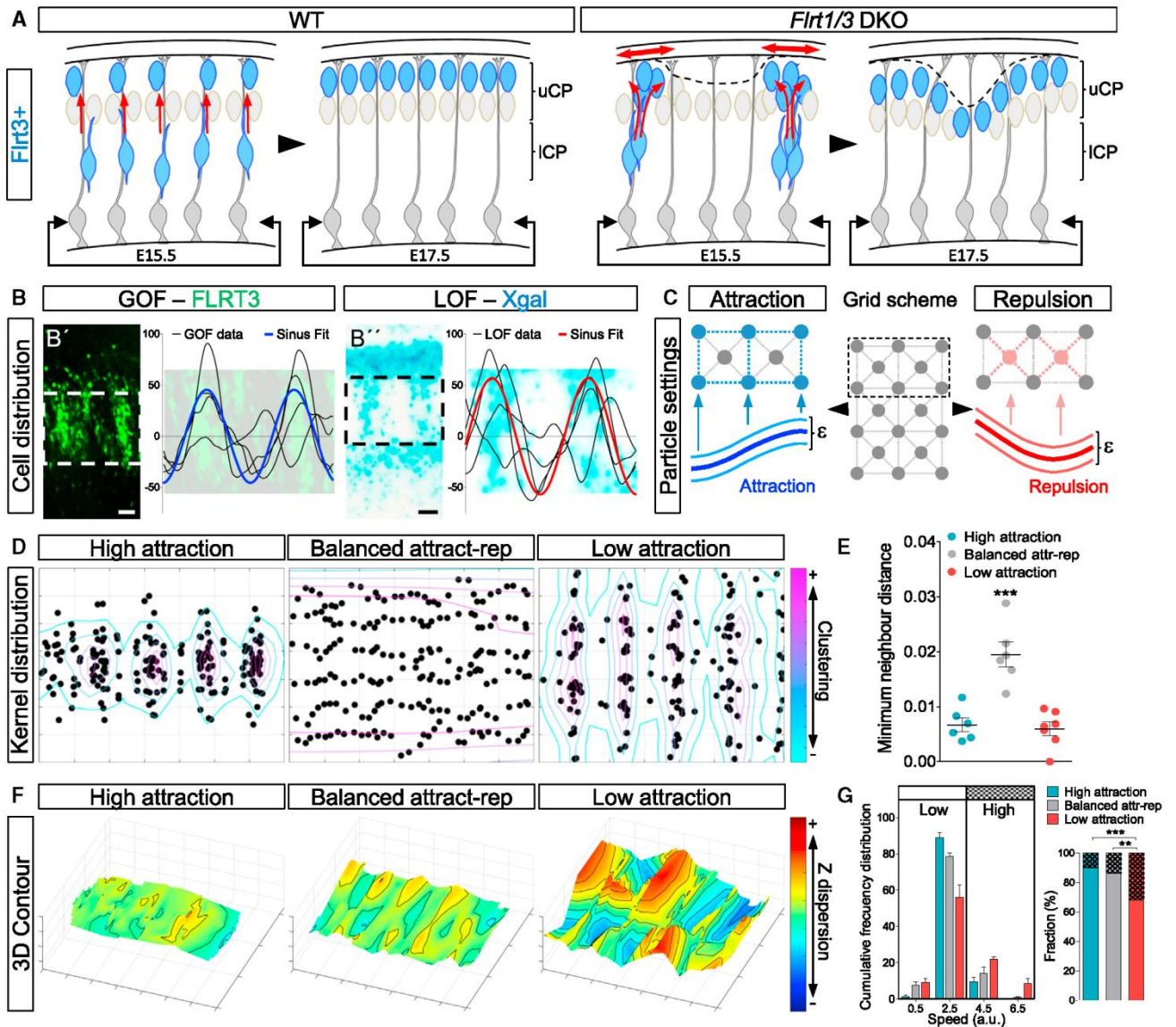


Figure 5. Computer Modeling Matches *Flrt1/3* DKO Experimental Observations

(A) Hypothetical model of sulcus formation in *Flrt1/3* DKO brains. In the wild-type (WT), *Flrt1/3*+ neurons show homogeneous distribution while migrating through the CP at E15.5 and form a uniform layer in the upper CP at E17.5. Loss of *FLRT1/3* induces cell clustering in the lower and upper CP, creating imbalanced tension forces, and loss of adhesion may increase tissue elasticity, ultimately leading to sulcus formation.

(B) *FLRT1/3* overexpression (GOF, B') or ablation (LOF, B'') alters the attraction-repulsion balance, resulting in the formation of neuronal cell clusters, which can be modeled as sinus equations. The graphs depict experimental data (black) and sinus fit (colored). The scale bar represents 40 μm .

(C) Scheme illustrating how particles representing *FLRT1/3*-positive (blue) and -negative neurons (red) are arranged. Blue particles show attraction between them. Red particles repel blue particles. Both attraction and repulsion forces are based on the sinus equation modeled (B). ϵ represents noise added to the system.

(D) Distribution of particles representing *FLRT1/3*+ neurons after computer simulations with high, balanced, or low attraction forces. The colored lines indicate a higher (magenta) or lower (cyan) density of particles based on their kernel distribution.

(E) Minimum neighbor distance of particles shown in (D). $n = 10$ computer simulations comprising 480 particles. *** $p < 0.001$, one-way ANOVA test with Tukey's post hoc analysis.

(F) Distribution of particles on the z axis after computer simulations. Note that both high and balanced attraction conditions result in a uniform surface, whereas low attraction conditions produce a wavy surface after computer simulations.

(G) Frequency distribution of speed profiles of particles shown in (F). Rectangles indicate low (plain) and high (pattern) speed profiles, and their relative fractions are shown on the right. ** $p < 0.01$, *** $p < 0.001$, chi-square contingency analysis.

The data are represented as mean \pm SEM.

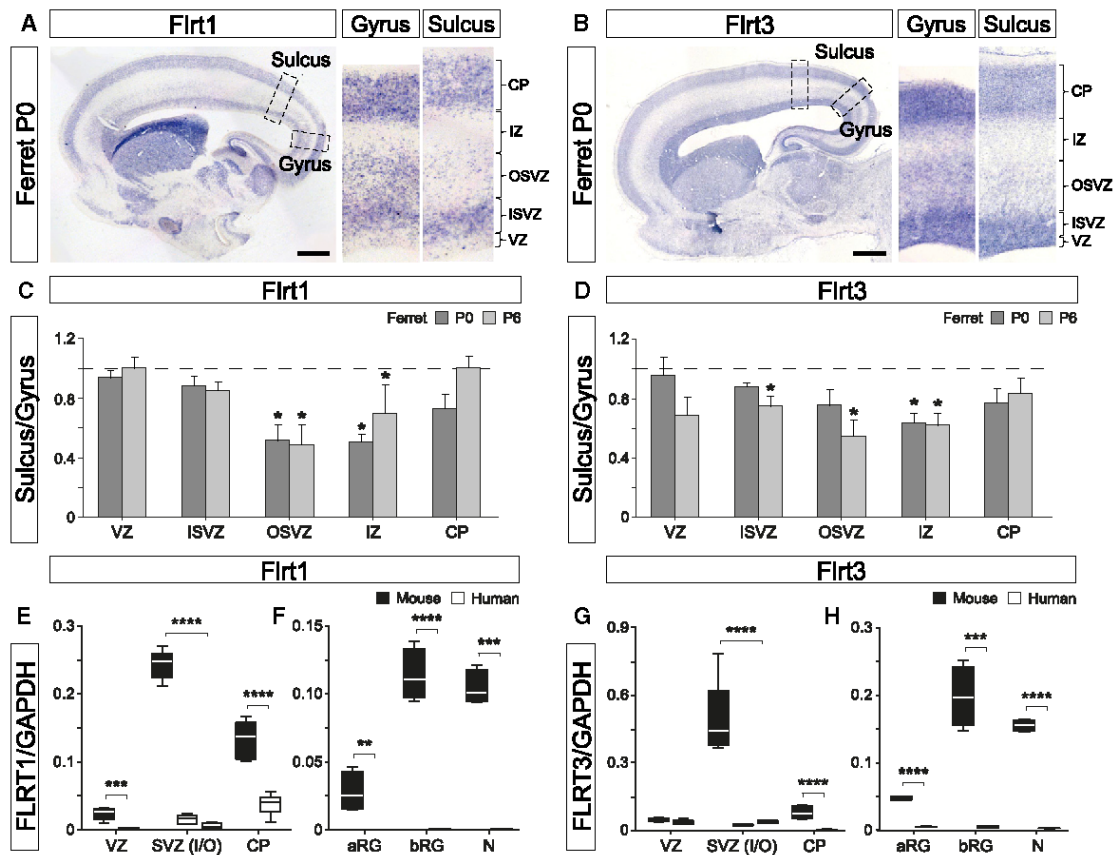


Figure 6. Low Endogenous Levels of FLRT1 and FLRT3 in a Future Sulcus Area of Ferret Cortex and in Specific Layers of Human Cortex

(A and B) ISH for FLRT1 (A) and FLRT3 (B) in sagittal sections of ferret cortex at P0. Regions marked by dashed rectangles delineate a prospective lateral sulcus (Sulcus) and splenial gyrus (Gyrus) and are shown with higher magnification on the right. The scale bars represent 1 mm.

(C and D) Intensity quantification of the images in (A) and (B) and Figures S6F and S6G, expressed as a ratio of sulcus/gyrus in different cortical layers at P0 and P6 ($n = 3$ separate ISH experiments for each group). * $p < 0.05$, unpaired Student's t test.

(E–H) Comparison of FLRT1 and FLRT3 expression between mouse and human with sequencing data from Fietz et al. (2012) (GEO: GSE38805) and Florio et al. (2015) (GEO: GSE65000). FLRT1 and FLRT3 mRNAs are more abundant in mouse compared with human when comparing different germinal layers (E and G) and specific cell types, including apical radial glia cells (aRG), basal radial glial cells (bRG), and migrating neurons (F and H).

FLRT sequencing data were normalized to housekeeping genes, including GAPDH (this figure) and PGK1 (Figures S6J–S6M). Whiskers in the boxplot represent minimum and maximum; unpaired Student's t test, ** $p < 0.01$, *** $p < 0.001$, **** $p < 0.0001$.

and OSVZ were combined). Relatively higher levels of mouse FLRT1 and FLRT3 were also seen in the CP. Higher levels of mouse FLRT1, but not FLRT3, were seen in the VZ. Normalizing FLRT1 and FLRT3 expression to another housekeeping gene (PGK1) gave similar results (Figures S6J and S6L). Third, we compared FLRT1/3 expression in apical and basal RG and migrating neurons in human and mouse (Florio et al., 2015; Figures 6F and 6H; Figures S6K and S6M). FLRT1 and FLRT3 expression in the mouse was highest in migrating neurons and basal RG cells, which are the mouse homologs of the outer RG cells found in gyrencephalic species (Borrell and Götz, 2014). Notably, FLRT1/3 levels in these cells were much higher in mouse than in human cortex. Given the high levels of FLRT1/3 in basal RG cells, we also asked whether the fraction of pvm-positive cells that display a basal radial glia-like morphology was altered in the FLRT1/3 DKO mice. This was not the case (Figures S6N and S6O), providing more evidence for lack of basal

radial glia involvement in the FLRT KO phenotype. Overall, these results revealed an inverse correlation between the presence of cortical folds/sulci and FLRT1/3 levels. Thus, the human neocortex expresses lower levels of FLRT1/3 compared with the mouse neocortex, and, in the ferret cortex, FLRT1/3 expression levels are less abundant in prospective sulcus than in gyrus areas.

DISCUSSION

In this study, we have identified FLRT1 and FLRT3 adhesion molecules as regulators of mammalian cortex folding. Genetic ablation of *Flrt1/3* in mice resulted in the formation of macroscopic cortical sulci that were maintained post-natally. These anatomical changes did not require progenitor cell amplification but, rather, correlated with changes in the behavior of migrating cortical neurons. Lack of FLRT1/3 reduced intercellular

adhesion, enhanced neuron clustering along the tangential axis, and mildly accelerated radial migration, resulting in a larger proportion of immature neurons reaching the upper cortical plate during late embryogenesis. These findings suggest that regulation of intercellular adhesion of migrating neurons is critical for sulcus formation in the cerebral cortex. Moreover, our expression analysis of FLRT1 and FLRT3 in gyrencephalic species revealed an inverse correlation between FLRT1/3 levels and sulcus formation, supporting a model by which increased abundance of FLRT1/3 levels during evolution led to the smoothing of an ancestral folded cortex. Therefore, *Flrt1/3* DKO mice are an interesting genetic model to study the cellular and molecular mechanisms of cortex folding induced by migrating neurons independent of progenitor amplification.

Mechanisms of FLRT1/3 Function

Flrt1/3 DKO mice are a unique genetic mouse model in which the cortex is folded without increases in neurogenic progenitor cells and basal radial glia. The lack of effects on neurogenic progenitor cells in *Flrt1/3* DKO is consistent with the lack of FLRT1/3 expression in apical or BPs (Figure 1; Figure S1; data not shown). Previous work in lissencephalic mice linked the expansion of the BP pool to gyrus formation (Florio et al., 2015; Ju et al., 2016; Rash et al., 2013; Stahl et al., 2013; Wang et al., 2016). In the gyrencephalic ferret, cortical regions with abundant BPs are more likely to develop into a gyrus than regions with fewer BPs (de Juan Romero et al., 2015; Reillo et al., 2011). Ectopic expansion of the BP pool in the ferret generates additional gyri (Masuda et al., 2015; Nonaka-Kinoshita et al., 2013), and its reduction has a stronger effect on cortical layering of gyri than sulci (Toda et al., 2016). The absence of BP pool expansion and of increases in neuron numbers in folded regions of *Flrt1/3* DKO mice suggests that the folds do not represent radial expansions and gyrus-like structures but, rather, furrows and sulcus-like structures.

FLRT1 and FLRT3 regulate the tangential distribution of cortical neurons. Lack of FLRT1/3 leads to transient neuron clustering in the embryonic cortical plate, and this process is spatially correlated with sulcus formation in early embryonic stages, suggesting that the two events are causally linked. Linking cortical folding to cell clustering and lowered intercellular adhesion may not be without precedent. Overexpression of the hominoid-specific gene *TBC1D3* in the mouse brain leads to cortical folding and increased generation of basal progenitors (Ju et al., 2016). *TBC1D3*-expressing cells show decreased levels of the adhesion protein N-cadherin and exhibit a clustered distribution reminiscent of cell clustering in *Flrt1/3* DKO brains. Although the authors of that study concentrated mainly on the link between cell proliferation and cortex folding, our computational model suggests that reduced intercellular adhesion and cell clustering may be a salient feature of *TBC1D3*-induced cortex folding.

The horizontal layers of the mammalian cortex are organized in cortical columns that contain closely related neurons. Clonal studies of cortical migration show that, in rodents, cortical neurons mostly migrate radially along a single parent RG fiber (Nocctor et al., 2001); however, in folded brains like those of the ferret or macaque, migrating neurons show increased cellular dynamics and exploratory behavior, including increased lateral

dispersion (Kornack and Rakic, 1995; Ware et al., 1999), but the mechanisms controlling this process are largely unknown. Our findings suggest that neuron clustering along the tangential axis in *Flrt1/3* DKO mice resembles the lateral dispersion observed in gyrencephalic species. This raises the interesting possibility that the underlying mechanisms may be similar. Neuron clustering in *Flrt1/3* DKO mice is likely the result of reduced intercellular adhesion, which alters the delicate balance of adhesion/repulsion required for cell migration (Cooper, 2013; Solecki, 2012). This conclusion is supported by our computational model, which shows that changes in the balance of adhesion/repulsion alter the distribution of cells from a uniform salt-and-pepper distribution to a clustered pattern. Hence, the increased lateral dispersion of cortical neurons in gyrencephalic brains may be the result of lowered intercellular adhesion.

The clustering mechanism alone is not likely to cause cortex folding because other mouse models with altered tangential neuron distribution do not show cortex folding (Dimidschstein et al., 2013; Torii et al., 2009). Our findings suggest that *Flrt1/3* DKO mice combine neuron clustering with increased migration speed and that this combination underlies sulcus formation. Similar to neuron clustering, increased migration speed may also be caused by reduced intercellular adhesion. This is suggested by our computational model, by previous mathematical models (DiMilla et al., 1991; Zaman et al., 2005), and by experimental studies (Lauro et al., 2006). A higher migration speed may increase the intercalation of neurons in local areas of the upper cortical plate (uCP), which, according to the radial intercalation hypothesis, increases tension and alters tissue elasticity, leading to sulcus formation (Striedter et al., 2015). We also find that the increased proportion of neurons reaching the upper CP of *Flrt1/3* DKO causes a shift toward more immature morphologies. Indeed, previous studies have shown that improper laminar position affects dendritic arborization of cortical neurons (Morgan-Smith et al., 2014). Whether this also contributes to sulcus formation will have to await further experimental analysis.

Evolutionary Considerations

The finding that lack of FLRT1/3 favors sulcus formation in the normally smooth mouse neocortex raised the question to what extent FLRT1/3 proteins are relevant for regulating cortical folding during evolution. Some studies suggest that the most recent common mammalian ancestor was gyrencephalic (Lewitus et al., 2014; O'Leary et al., 2013), and it was hypothesized that several transitions from gyrencephaly to lissencephaly occurred during mammalian evolution (Kelava et al., 2012; Lewitus et al., 2014). This conclusion is supported by the finding that the marmoset, despite being a lissencephalic species, retains neurogenic features characteristic of gyrencephalic neocortices (Kelava et al., 2012). Although these studies point out that lissencephaly has evolved from gyrencephaly, the mechanisms controlling this process are not known.

Our results suggest that FLRT1/3 expression levels might have participated in the transition from gyrencephaly to lissencephaly. In the wild-type mouse brain, high expression levels of FLRT1/3 promote adhesion between neurons, resulting in coordinated migration and little lateral dispersion, which favors the formation

of homogeneous and smooth cortical layers. Conversely, the absence of FLRT1/3 expression reduces adhesion between neurons, allowing them to acquire wide dynamic migratory profiles and a lateral distribution, which are features characteristic of neurons in the ferret at the onset of cortical folding (Gertz and Kriegstein, 2015). Interestingly, the gyrencephalic human neocortex expresses much lower levels of FLRT1/3 compared with the lissencephalic mouse neocortex, and regions in the ferret neocortex undergoing sulcus formation have lower levels of FLRT1/3 compared with regions developing into a gyrus. Notably, this markedly distinct expression pattern was mainly seen in the OSVZ, which is a key layer involved in cortical folding of gyrencephalic species (Borrell and Götz, 2014; Lui et al., 2011).

Our findings thus unraveled FLRT1/3 as key factors involved in the regulation of cortical migration and sulcus formation. Manipulations of their expression levels have a profound effect on the coordination of cortical migration and lateral dispersion of neurons, which, in turn, influences cortical folding. This scenario provides molecular and cellular insights into the evolution of neuronal migration from gyrencephalic to lissencephalic species.

STAR★METHODS

Detailed methods are provided in the online version of this paper and include the following:

- KEY RESOURCES TABLE
- CONTACT FOR REAGENT AND RESOURCE SHARING
- EXPERIMENTAL MODEL AND SUBJECT DETAILS
 - Mouse lines
 - Ferret
 - Primary cultures
- METHOD DETAILS
 - Immunohistochemistry and enzymatic staining
 - In utero electroporation assays
 - Time-lapse experiments
 - Nissl Staining
 - Cell morphology analysis
 - BrdU analysis
 - Computer modeling
 - in situ hybridization
 - RNaseq analysis
- QUANTIFICATION AND STATISTICAL ANALYSIS

SUPPLEMENTAL INFORMATION

Supplemental Information includes six figures and two movies and can be found with this article online at <http://dx.doi.org/10.1016/j.cell.2017.04.012>.

AUTHOR CONTRIBUTIONS

D.d.T. characterized the *Flrt1/3* DKO phenotype, performed neuronal cultures/explants, and designed the computational model. T.R. characterized the *Flrt1* KO and performed IUE and time-lapse and morphology analyses. E.C. performed bioinformatics analysis of RNA-seq data and analysis of the *Flrt2/3* DKO. G.S.B. characterized FLRT1-3 expression and assisted with IF assays. A.V. performed ISH on ferret sections. R.K. and V.B. supervised experiments. D.d.T. and R.K. wrote the manuscript with input from all other authors.

ACKNOWLEDGMENTS

We thank M. Götz for her insightful comments during the course of this study, R. Portugués and A. Boehm for help with the computational model, S. Falk for help with setting up time-lapse experiments, R. Kasper for technical help with gene expression analysis, A. Yeroslaviz and B. Habermann for help with the Supernova system, and H. Kucukdereli and A. Kist for help with Python programming. T.R., a member of the graduate program IMPRS-LS, was funded by a Boehringer Ingelheim Ph.D. fellowship. E.C. was supported by a postdoctoral research fellowship from the Alexander von Humboldt Foundation, and A.V. was supported by a predoctoral Severo Ochoa contract with the Spanish Ministry of Economy and Competitiveness (MINECO, SVP-2014-068671). This work was funded by the Max Planck Society and the Deutsche Forschungsgemeinschaft (Synergy) (to R.K.) and by the European Research Council (CORTEXFOLDING, 309633) and MINECO (SAF2015-69168-R to V.B.).

Received: October 6, 2016

Revised: February 9, 2017

Accepted: April 7, 2017

Published: May 4, 2017

REFERENCES

- Beaudin, S.A., Singh, T., Agster, K.L., and Burwell, R.D. (2013). Borders and comparative cytoarchitecture of the perirhinal and postrhinal cortices in an F1 hybrid mouse. *Cereb. Cortex* 23, 460–476.
- Borrell, V., and Götz, M. (2014). Role of radial glial cells in cerebral cortex folding. *Curr. Opin. Neurobiol.* 27, 39–46.
- Borrell, V., and Reillo, I. (2012). Emerging roles of neural stem cells in cerebral cortex development and evolution. *Dev. Neurobiol.* 72, 955–971.
- Bribián, A., Nocentini, S., Llorens, F., Gil, V., Mire, E., Reginensi, D., Yoshida, Y., Mann, F., and del Río, J.A. (2014). Sema3E/PlexinD1 regulates the migration of hem-derived Cajal-Retzius cells in developing cerebral cortex. *Nat. Commun.* 5, 4265.
- Buchholz, J. (2009). MATLAB Particles 2.0.
- Cooper, J.A. (2013). Cell biology in neuroscience: mechanisms of cell migration in the nervous system. *J. Cell Biol.* 202, 725–734.
- de Juan Romero, C., Bruder, C., Tomasello, U., Sanz-Anquela, J.M., and Borrell, V. (2015). Discrete domains of gene expression in germinal layers distinguish the development of gyrencephaly. *EMBO J.* 34, 1859–1874.
- Devisme, L., Bouchet, C., Gonzalès, M., Alanio, E., Bazin, A., Bessières, B., Bigi, N., Blanchet, P., Bonneau, D., Bonnières, M., et al. (2012). Cobblestone lissencephaly: neuropathological subtypes and correlations with genes of dystroglycanopathies. *Brain* 135, 469–482.
- Dimidschstein, J., Passante, L., Dufour, A., van den Areele, J., Tiberi, L., Hrechdakian, T., Adams, R., Klein, R., Lie, D.C., Jossin, Y., and Vanderhaeghen, P. (2013). Ephrin-B1 controls the columnar distribution of cortical pyramidal neurons by restricting their tangential migration. *Neuron* 79, 1123–1135.
- DiMilla, P.A., Barbee, K., and Lauffenburger, D.A. (1991). Mathematical model for the effects of adhesion and mechanics on cell migration speed. *Biophys. J.* 60, 15–37.
- Egea, J., Erlacher, C., Montanez, E., Burtscher, I., Yamagishi, S., Hess, M., Hampel, F., Sanchez, R., Rodriguez-Manzanera, M.T., Bösl, M.R., et al. (2008). Genetic ablation of FLRT3 reveals a novel morphogenetic function for the anterior visceral endoderm in suppressing mesoderm differentiation. *Genes Dev.* 22, 3349–3362.
- Englund, C., Fink, A., Lau, C., Pham, D., Daza, R.A.M., Bulfone, A., Kowalczyk, T., and Hevner, R.F. (2005). *Pax6*, *Tbr2*, and *Tbr1* are expressed sequentially by radial glia, intermediate progenitor cells, and postmitotic neurons in developing neocortex. *J. Neurosci.* 25, 247–251.
- Fernández, V., Llinares-Benadero, C., and Borrell, V. (2016). Cerebral cortex expansion and folding: what have we learned? *EMBO J.* 35, 1021–1044.

- Fietz, S.A., Lachmann, R., Brandl, H., Kircher, M., Samusik, N., Schröder, R., Lakshmanaperumal, N., Henry, I., Vogt, J., Riehn, A., et al. (2012). Transcriptomes of germinal zones of human and mouse fetal neocortex suggest a role of extracellular matrix in progenitor self-renewal. *Proc. Natl. Acad. Sci. USA* *109*, 11836–11841.
- Finlay, B.L., and Darlington, R.B. (1995). Linked regularities in the development and evolution of mammalian brains. *Science* *268*, 1578–1584.
- Florio, M., Albert, M., Taverna, E., Namba, T., Brandl, H., Lewitus, E., Haffner, C., Sykes, A., Wong, F.K., Peters, J., et al. (2015). Human-specific gene ARHGAP11B promotes basal progenitor amplification and neocortex expansion. *Science* *347*, 1465–1470.
- Gertz, C.C., and Kriegstein, A.R. (2015). Neuronal Migration Dynamics in the Developing Ferret Cortex. *J. Neurosci.* *35*, 14307–14315.
- Geschwind, D.H., and Rakic, P. (2013). Cortical evolution: judge the brain by its cover. *Neuron* *80*, 633–647.
- Gorski, J.A., Talley, T., Qiu, M., Puelles, L., Rubenstein, J.L., and Jones, K.R. (2002). Cortical excitatory neurons and glia, but not GABAergic neurons, are produced in the Emx1-expressing lineage. *J. Neurosci.* *22*, 6309–6314.
- Hansen, D.V., Lui, J.H., Parker, P.R.L., and Kriegstein, A.R. (2010). Neurogenic radial glia in the outer subventricular zone of human neocortex. *Nature* *464*, 554–561.
- Jackson, V.A., del Toro, D., Carrasquero, M., Roversi, P., Harlos, K., Klein, R., and Seiradake, E. (2015). Structural basis of latrophilin-FLRT interaction. *Structure* *23*, 774–781.
- Jackson, V.A., Mehmood, S., Chavent, M., Roversi, P., Carrasquero, M., Del Toro, D., Seyit-Bremer, G., Ranaivoson, F.M., Comoletti, D., Sansom, M.S.P., et al. (2016). Super-complexes of adhesion GPCRs and neural guidance receptors. *Nat. Commun.* *7*, 11184.
- Ju, X.-C., Hou, Q.-Q., Sheng, A.-L.S., Wu, K.-Y., Zhou, Y., Jin, Y., Wen, T., Yang, Z., Wang, X., and Luo, Z.-G. (2016). The hominoid-specific gene TBC1D3 promotes generation of basal neural progenitors and induces cortical folding in mice. *eLife* *5*, e18197.
- Kawauchi, T. (2015). Cellular insights into cerebral cortical development: focusing on the locomotion mode of neuronal migration. *Front. Cell. Neurosci.* *9*, 394.
- Kelava, I., Reillo, I., Murayama, A.Y., Kalinka, A.T., Stenzel, D., Tomancak, P., Matsuzaki, F., Lebrand, C., Sasaki, E., Schwamborn, J.C., et al. (2012). Abundant occurrence of basal radial glia in the subventricular zone of embryonic neocortex of a lissencephalic primate, the common marmoset *Callithrix jacchus*. *Cereb. Cortex* *22*, 469–481.
- Kornack, D.R., and Rakic, P. (1995). Radial and horizontal deployment of clonally related cells in the primate neocortex: relationship to distinct mitotic lineages. *Neuron* *15*, 311–321.
- Lauro, C., Catalano, M., Trettel, F., Mainiero, F., Ciotti, M.T., Eusebi, F., and Limatola, C. (2006). The chemokine CX3CL1 reduces migration and increases adhesion of neurons with mechanisms dependent on the beta1 integrin subunit. *J. Immunol.* *177*, 7599–7606.
- Lewitus, E., Kelava, I., Kalinka, A.T., Tomancak, P., and Huttner, W.B. (2014). An adaptive threshold in mammalian neocortical evolution. *PLoS Biol.* *12*, e1002000.
- Liao, Y., Smyth, G.K., and Shi, W. (2014). featureCounts: an efficient general purpose program for assigning sequence reads to genomic features. *Bioinformatics* *30*, 923–930.
- Love, M.I., Huber, W., and Anders, S. (2014). Moderated estimation of fold change and dispersion for RNA-seq data with DESeq2. *Genome Biol.* *15*, 550.
- Lui, J.H., Hansen, D.V., and Kriegstein, A.R. (2011). Development and evolution of the human neocortex. *Cell* *146*, 18–36.
- Masuda, K., Toda, T., Shinmyo, Y., Ebisu, H., Hoshiba, Y., Wakimoto, M., Ichikawa, Y., and Kawasaki, H. (2015). Pathophysiological analyses of cortical malformation using gyrencephalic mammals. *Sci. Rep.* *5*, 15370.
- Matsuda, T., and Cepko, C.L. (2007). Controlled expression of transgenes introduced by in vivo electroporation. *Proc. Natl. Acad. Sci. USA* *104*, 1027–1032.
- Mizuno, H., Luo, W., Tarusawa, E., Saito, Y.M., Sato, T., Yoshimura, Y., Itohara, S., and Iwasato, T. (2014). NMDAR-regulated dynamics of layer 4 neuronal dendrites during thalamocortical reorganization in neonates. *Neuron* *82*, 365–379.
- Moon, H.M., and Wynshaw-Boris, A. (2013). Cytoskeleton in action: lissencephaly, a neuronal migration disorder. *Wiley Interdiscip. Rev. Dev. Biol.* *2*, 229–245.
- Morgan-Smith, M., Wu, Y., Zhu, X., Pringle, J., and Snider, W.D. (2014). GSK-3 signaling in developing cortical neurons is essential for radial migration and dendritic orientation. *eLife* *3*, e02663.
- Nieto, M., Monuki, E.S., Tang, H., Imitola, J., Haubst, N., Khoury, S.J., Cunningham, J., Gotz, M., and Walsh, C.A. (2004). Expression of Cux-1 and Cux-2 in the subventricular zone and upper layers II–IV of the cerebral cortex. *J. Comp. Neurol.* *479*, 168–180.
- Noctor, S.C., Flint, A.C., Weissman, T.A., Dammerman, R.S., and Kriegstein, A.R. (2001). Neurons derived from radial glial cells establish radial units in neocortex. *Nature* *409*, 714–720.
- Nonaka-Kinoshita, M., Reillo, I., Artegiani, B., Martínez-Martínez, M.Á., Nelson, M., Borrell, V., and Calegari, F. (2013). Regulation of cerebral cortex size and folding by expansion of basal progenitors. *EMBO J.* *32*, 1817–1828.
- O’Leary, M.A., Bloch, J.I., Flynn, J.J., Gaudin, T.J., Giallombardo, A., Giannini, N.P., Goldberg, S.L., Kraatz, B.P., Luo, Z.-X., Meng, J., et al. (2013). The placental mammal ancestor and the post-K-Pg radiation of placentals. *Science* *339*, 662–667.
- Pilz, G.-A., Shitamukai, A., Reillo, I., Pacary, E., Schwausch, J., Stahl, R., Ninkovic, J., Snippert, H.J., Clevers, H., Godinho, L., et al. (2013). Amplification of progenitors in the mammalian telencephalon includes a new radial glial cell type. *Nat. Commun.* *4*, 2125.
- Rakic, P. (1972). Mode of cell migration to the superficial layers of fetal monkey neocortex. *J. Comp. Neurol.* *145*, 61–83.
- Rash, B.G., Tomasi, S., Lim, H.D., Suh, C.Y., and Vaccarino, F.M. (2013). Cortical gyrfication induced by fibroblast growth factor 2 in the mouse brain. *J. Neurosci.* *33*, 10802–10814.
- Reillo, I., de Juan Romero, C., García-Cabezas, M.Á., and Borrell, V. (2011). A role for intermediate radial glia in the tangential expansion of the mammalian cerebral cortex. *Cereb. Cortex* *21*, 1674–1694.
- Schindelin, J., Arganda-Carreras, I., Frise, E., Kaynig, V., Longair, M., Pietzsch, T., Preibisch, S., Rueden, C., Saalfeld, S., Schmid, B., et al. (2012). Fiji: an open-source platform for biological-image analysis. *Nat. Methods* *9*, 676–682.
- Seiradake, E., del Toro, D., Nagel, D., Cop, F., Härtl, R., Ruff, T., Seyit-Bremer, G., Harlos, K., Border, E.C., Acker-Palmer, A., et al. (2014). FLRT structure: balancing repulsion and cell adhesion in cortical and vascular development. *Neuron* *84*, 370–385.
- Smart, I.H., and McSherry, G.M. (1986). Gyrus formation in the cerebral cortex of the ferret. II. Description of the internal histological changes. *J. Anat.* *147*, 27–43.
- Solecki, D.J. (2012). Sticky situations: recent advances in control of cell adhesion during neuronal migration. *Curr. Opin. Neurobiol.* *22*, 791–798.
- Stahl, R., Walcher, T., De Juan Romero, C., Pilz, G.A., Cappello, S., Irmiler, M., Sanz-Aguela, J.M., Beckers, J., Blum, R., Borrell, V., and Götz, M. (2013). Trnp1 regulates expansion and folding of the mammalian cerebral cortex by control of radial glial fate. *Cell* *153*, 535–549.
- Striedter, G.F., Srinivasan, S., and Monuki, E.S. (2015). Cortical folding: when, where, how, and why? *Annu. Rev. Neurosci.* *38*, 291–307.
- Tabata, H., and Nagata, K. (2016). Decoding the molecular mechanisms of neuronal migration using in utero electroporation. *Med. Mol. Morphol.* *49*, 63–75.
- Thomson, R.E., Kind, P.C., Graham, N.A., Etherson, M.L., Kennedy, J., Fernandes, A.C., Marques, C.S., Hevner, R.F., and Iwata, T. (2009). Fgf receptor 3 activation promotes selective growth and expansion of occipitotemporal cortex. *Neural Dev.* *4*, 4.

- Toda, T., Shinmyo, Y., Dinh Duong, T.A., Masuda, K., and Kawasaki, H. (2016). An essential role of SVZ progenitors in cortical folding in gyrencephalic mammals. *Sci. Rep.* **6**, 29578.
- Torii, M., Hashimoto-Torii, K., Levitt, P., and Rakic, P. (2009). Integration of neuronal clones in the radial cortical columns by EphA and ephrin-A signalling. *Nature* **461**, 524–528.
- Trapnell, C., Roberts, A., Goff, L., Pertea, G., Kim, D., Kelley, D.R., Pimentel, H., Salzberg, S.L., Rinn, J.L., and Pachter, L. (2012). Differential gene and transcript expression analysis of RNA-seq experiments with TopHat and Cufflinks. *Nat. Protoc.* **7**, 562–578.
- Tronche, F., Kellendonk, C., Kretz, O., Gass, P., Anlag, K., Orban, P.C., Bock, R., Klein, R., and Schütz, G. (1999). Disruption of the glucocorticoid receptor gene in the nervous system results in reduced anxiety. *Nat. Genet.* **23**, 99–103.
- Wagenführ, L., Meyer, A.K., Braunschweig, L., Marrone, L., and Storch, A. (2015). Brain oxygen tension controls the expansion of outer subventricular zone-like basal progenitors in the developing mouse brain. *Development* **142**, 2904–2915.
- Wang, L., Hou, S., and Han, Y.-G. (2016). Corrigendum: Hedgehog signaling promotes basal progenitor expansion and the growth and folding of the neocortex. *Nat. Neurosci.* **19**, 1115.
- Ware, M.L., Tavazoie, S.F., Reid, C.B., and Walsh, C.A. (1999). Coexistence of widespread clones and large radial clones in early embryonic ferret cortex. *Cereb. Cortex* **9**, 636–645.
- Wilkinson, D.J. (2009). Stochastic modelling for quantitative description of heterogeneous biological systems. *Nat. Rev. Genet.* **10**, 122–133.
- Yamagishi, S., Hampel, F., Hata, K., Del Toro, D., Schwark, M., Kvachnina, E., Bastmeyer, M., Yamashita, T., Tarabykin, V., Klein, R., and Egea, J. (2011). FLRT2 and FLRT3 act as repulsive guidance cues for Unc5-positive neurons. *EMBO J.* **30**, 2920–2933.
- Zaman, M.H., Kamm, R.D., Matsudaira, P., and Lauffenburger, D.A. (2005). Computational model for cell migration in three-dimensional matrices. *Bio-phys. J.* **89**, 1389–1397.

STAR★METHODS

KEY RESOURCES TABLE

REAGENT or RESOURCE	SOURCE	IDENTIFIER
Antibodies		
Rabbit anti- β III Tubulin	Sigma-Aldrich	Cat#SAB4300623; RRID:AB_11128202
Rabbit anti-Cux1	Santa Cruz	Cat#SC-13024; RRID:AB_2261231
Rabbit anti-Tbr1	Abcam	Cat#AB31940; RRID:AB_2200219
Rabbit anti-Tbr2	Abcam	Cat#AB23345; RRID:AB_778267
Rabbit anti-laminin	Sigma-Aldrich	Cat#L9393; RRID:AB_477163
Rabbit anti-Pax6	BioLegend	Cat#901301; RRID:AB_2565003
Rabbit anti-BLBP	Millipore	Cat#ABN14; RRID:AB_10000325
Rabbit anti-Calretinin	Swant	Cat#7697; RRID:AB_2619710
Rat anti-Histone H3	Abcam	Cat#AB10543; RRID:AB_2295065
Rat anti-Ctip2	Abcam	Cat#18465; RRID:AB_2064130
Mouse anti-Pvim	Abcam	Cat#AB22651; RRID:AB_447222
Mouse anti-BrdU	Roche	Cat#11170376001; RRID:AB_514483
Mouse anti-Reelin	MBL	Cat#D223-3; RRID:AB_843523
Goat anti-FLRT1	R&D	Cat#AF2794; RRID:AB_2106598
Goat anti-FLRT3	R&D	Cat#AF2795; RRID:AB_2106855
Goat anti-FoxP2	Santa Cruz	Cat#SC-21069; RRID:AB_2107124
Anti-phalloidin-Cy3	Sigma-Aldrich	Cat#P5282
Chemicals, Peptides, and Recombinant Proteins		
BrdU	Sigma-Aldrich	B5002; CAS:59-14-3
Cresyl Violet acetate (for Nissl staining)	Sigma-Aldrich	C5042; CAS:10510-54-0
Deposited Data		
Mouse RNaseq data (lateral and medial cortex)	Wang et al., 2016	GEO: GSE80958
Human and mouse RNaseq data (cortical layers)	Fietz et al., 2012	GEO: GSE38805
Human and mouse RNaseq data (aRG, bRG and migrating neurons)	Florio et al., 2015	GEO: GSE65000
Human RNaseq data (different cortical regions)	Allan Brain Atlas	http://www.brain-map.org
Mouse reference genome, NCBI37	The Ensembl Project	http://may2012.archive.ensembl.org/Mus_musculus/
Human reference genome, GRCh37	Genome Reference Consortium	https://www.ncbi.nlm.nih.gov/grc/human
Experimental Models: Cell Lines		
Primary cell lines from FLRT1 lacZ mouse	EUCOMM	HEPD0528
Primary cell lines from FLRT3 lacZ mouse	Egea et al., 2008	N/A
Experimental Models: Organisms/Strains		
Mouse: FLRT1 null	Yamagishi et al., 2011	HEPD0528
Mouse: FLRT1 lacZ	EUCOMM	HEPD0528
Mouse: FLRT2 lox	EUCOMM	EPD0347
Mouse: FLRT2 null	Yamagishi et al., 2011	N/A
Mouse: FLRT2 lacZ	EUCOMM	EPD0347
Mouse: FLRT3 lox	Yamagishi et al., 2011	N/A
Mouse: FLRT3 null	Egea et al., 2008	N/A
Mouse: FLRT3 lacZ	Egea et al., 2008	N/A
Mouse: Nestin-Cre	Tronche et al., 1999	N/A

(Continued on next page)

Continued		
REAGENT or RESOURCE	SOURCE	IDENTIFIER
Mouse: EMX-Cre	Gorski et al., 2002	N/A
Pigmented ferrets (<i>Mustela putorius furo</i>)	Marshall Bioresources and Euroferret	N/A
Oligonucleotides		
ISH: Flrt1-forward TCAGCGTGCAGGTCATCTAC	This paper	N/A
ISH: Flrt1-reverse GCAGCCACAGGAGGTTACAG	This paper	N/A
ISH: Flrt3-forward TCTCCGACTGCTTTTCCTGT	This paper	N/a
ISH: Flrt3-reverse TATTCATTGCGTCCCCTGT	This paper	N/A
Recombinant DNA		
Plasmid: SUPERNOVA plasmid system	Mizuno et al., 2014	N/A
Plasmid: pCAG-Cre	Anjen Chenn lab	Cat#26647 (Addgene)
Plasmid: pCALNL-DsRed	Matsuda and Cepko, 2007	Cat#13769 (Addgene)
Software and Algorithms		
MATLAB, version R2015a	Mathworks Inc, USA	http://mathworks.com
MATLAB particles, version 2.1	Buchholz, 2009	N/A
Prism, version 5	Graphpad Software, USA	https://www.graphpad.com/
ImageJ (Fiji), version 2.0.0	Schindelin et al., 2012	https://imagej.net/Fiji
RStudio, version 0.98.1091	RStudio, USA	https://www.rstudio.com/
LAS software, version 4.7	Leica Microsystems, Germany	http://www.leica-microsystems.com/products/microscope-software/
Python, version 3.0	Python Software Foundation	https://www.python.org/
CellProfiler, version 2.2.0	CellProfiler, USA	http://cellprofiler.org
FASTX-Toolkit, version 0.0.13	Hannon lab	http://hannonlab.cshl.edu/fastx_toolkit/
TopHat, version 2.0.14	Trapnell et al., 2012	https://ccb.jhu.edu/software/tophat/
featureCounts, version 1.5.1	Liao et al., 2014	http://bioinf.wehi.edu.au/featureCounts/
DESeq2, version 3.4	Love et al., 2014	https://bioconductor.org/packages/release/bioc/html/DESeq2.html

CONTACT FOR REAGENT AND RESOURCE SHARING

Further information and request for resources and reagents should be directed to and will be fulfilled by the Lead Contact, Rüdiger Klein (rklein@neuro.mpg.de).

EXPERIMENTAL MODEL AND SUBJECT DETAILS

Mouse lines

Flrt3^{lacZ/lx} mice ([Egea et al., 2008](#)) carrying the floxed allele for *Flrt3* were crossed with Flrt1^{-/-} ([Yamagishi et al., 2011](#)) and the nervous system-specific Nestin-Cre ([Tronche et al., 1999](#)). Flrt2^{lacZ/lx} mice (line EPD0347 from EUCOMM) carrying the floxed allele for *Flrt2* were crossed with Flrt3^{-/lx} mice ([Egea et al., 2008](#)) and the nervous system-specific EMX-Cre ([Gorski et al., 2002](#)). More information is available in the [key resources table](#). All mice (C57BL/6 background) were housed with 12:12h light/dark cycle and food/water available ad libitum. All animal experiments were approved by the government of upper Bavaria.

Ferret

Pigmented ferrets (*Mustela putorius furo*) were obtained from Marshall Bioresources and Euroferret and kept on a 16:8h light:dark cycle at the Animal Facilities of the Universidad Miguel Hernández. Ferret were employed independently of their gender. Healthy animals postnatal day 0 had an average weight of 10 gr and postnatal day 6 animals weighed around 35 gr. Non previous procedures were performed in the animals used for tissue collection. All animals were treated according to Spanish and EU regulations, and experimental protocols were approved by the Universidad Miguel Hernández Institutional Animal Care and Use Committee (IACUC).

Primary cultures

Cortical neurons and hem explants were performed as described previously ([Bribián et al., 2014](#); [Seiradake et al., 2014](#); [Yamagishi et al., 2011](#)). Briefly, cortical hem explants from E12.5 Flrt3^{lacZ/+} embryos were dissected out and placed on 13 mm coverslips in

4 well-plate (Thermofisher, catalog 176740) coated with 0.5 $\mu\text{g}/\text{ml}$ Poly-D-Lysine (Sigma) and 20 $\mu\text{g}/\text{ml}$ laminin (Thermofisher). Neurons were dissociated from cortices of E15.5 Flrt1^{lacZ/+} embryos and cultured on coverslips coated with 0.5 $\mu\text{g}/\text{ml}$ Poly-D-Lysine in 24 well-plates (Thermofisher, catalog 140675). Explants and neurons were cultured for 1 day in vitro at 37°C, 5% CO₂ in Neurobasal medium supplemented with B27 (Invitrogen). Cultures were fixed with 4% Paraformaldehyde for 10 min and processed for immunostaining.

METHOD DETAILS

Immunohistochemistry and enzymatic staining

To stain for β -galactosidase activity, mouse brains were fixed for 1.5 hr in 0.2% glutaraldehyde and 1% PFA in PBS (containing 5 mM EGTA, 2 mM MgCl₂, and 0.02% NP40). Vibratome sections (50 μm) were stained for β -galactosidase activity by incubating them for 2–3 hr at 37°C in a 1 mg/ml X-gal solution (Invitrogen) containing 5 mM K₄Fe(CN)₆ and 5 mM K₃Fe(CN)₆. After rinsing, brain sections were counterstained with FastRed (Vector Laboratories).

For immunostaining, cultured cells, explants or embryonic brains were fixed in 4% PFA for ~15 min and over-night, respectively. For BrdU staining, sections were pretreated with 2N HCl for 30 min and subsequently neutralized with sodium-tetraborate (Na₂B₄O₇ 0.1M, pH: 8.5) for 2 \times 15 min. Cells and explants were incubated with primary antibodies after 10 min or 1 hr of permeabilization with 1% BSA, 0.1% Triton X-100/PBS, respectively. We used rabbit anti- β III Tubulin 1/1,000 (Sigma), rabbit anti-Cux1 antibody 1/300 (Santa Cruz), rabbit anti-Tbr1 and anti-Tbr2 1/300 (Abcam), rat anti-Ctip2 1/300 (Abcam), mouse anti-BrdU (Roche), goat anti-FLRT3 1/200 (R&D), anti-phalloidin-Cy3 1/100 (Sigma), goat anti-FoxP2 1/300 (Santa Cruz), mouse anti-Reelin 1/500 (MBL), rabbit anti-laminin 1/300 (Sigma), rabbit anti-Pax6 1/300 (BioLegend), rabbit anti-BLBP 1/300 (Millipore), rabbit anti-Histone H3 1/300 (Abcam), mouse anti-Pvim 1/300 (Abcam), rabbit anti-Calretinin 1/300 (Swant), goat anti-FLRT1/3 1/100 (R&D). The secondary antibodies were Alexa Fluor 488-, 555- and 647-conjugated goat or donkey anti-rabbit/mouse/goat (Molecular Probes 1:400). Samples were imaged using a SP8 laser scanning confocal spectral microscope (Leica Microsystems). Images were taken using a 20 \times (immunohistochemistry) or 40 \times (neuronal cultures, cortical explants) numerical aperture objective with a 1.5 \times digital zoom and 2 Airy disk pinhole.

In utero electroporation assays

In utero electroporation was performed at E13.5 as previously described (Seiradake et al., 2014) on Isoflurane anesthetized C57BL/6 control mice. DNA plasmids were used at 1 $\mu\text{g}/\mu\text{l}$ and mixed with 1% fast green (Sigma, final concentration 0.2%). 1 μl of plasmid solution were injected into the lateral ventricle with a pump-controlled micropipette (Picospritzer III). After injection, six 50ms (1 s interval) electric (30V) pulses were generated with electrodes confronting the uterus above the ventricle. The abdominal wall and skin were sewed and the mice were kept until the desired embryonic stage.

Time-lapse experiments

Embryos were electroporated at E13.5 using a combination of pCAG-Cre and pCALNL-DsRed plasmids (Matsuda and Cepko, 2007). pCALNL-DsRed was a gift from Connie Cepko (Addgene plasmid # 13769) and pCAG-Cre was a gift from Anjen Chenn (Addgene plasmid # 26647). After 48 hr, embryonic brains were dissected in ice cold sterile filtered and aerated (95% O₂/5% CO₂) dissection medium (15.6g/l DMEM/F12 (Sigma); 1.2g/l NaHCO₃; 2.9g/l glucose (Sigma); 1%(v/v) penicillin streptomycin (GIBCO)). Brains were embedded in 4% low melting agarose (Biozym) and cut into 300 μm thick sections using a vibratome (Leica, VT1200S). Sections were suspended in a collagen mix (64%(v/v) cell matrix type I-A, Nitta Gelatin; 24%(v/v) 5xDMEM/F12; 12%(v/v) reconstitution buffer (200mM HEPES; 50mM NaOH; 260mM NaHCO₃) and transferred onto a cell culture insert (Millicell; PICMORG50). Sections were incubated for 10 min at 37°C to solidify collagen. 1.5 mL slice medium (88%(v/v) dissection medium; 5%(v/v) horse serum; 5%(v/v) fetal calf serum; 2%(v/v) B27 supplement (GIBCO); 1%(v/v) N2 supplement (GIBCO)) was added into the dish surrounding the culture insert and incubated for 30 min at 37°C. Before start of time-lapse experiment, culture medium was added on top of the sections to allow objective immersion. Sections were imaged using a 20 \times water immersion objective on a Leica SP8 confocal microscope system equipped with a temperature-controlled carbon dioxide incubation chamber set to 37°C, 95% humidity and 5% CO₂. Sequential images were acquired every 20 min for 14–60 hr. After imaging slices were genotyped to identify Flrt1/3 DKO. Single cell movement was tracked using the Fiji plugin “Manual Tracking.” Only neurons entering the cortical plate were tracked. Single cell track analysis and plotting was carried out using homemade python scripts. All cells moving less than 4 $\mu\text{m}/\text{h}$ were considered as not moving.

Nissl Staining

Postnatal brains were fixed in 4% PFA over-night. Vibratome sections (50 μm) were dried on superfrost slides (Thermo Science) over-night at 42°C. Sections were incubated in 1:1 ethanol/chloroform for 2 hr and then rehydrated through 100%, 90%, 75%, 50% and 0% ethanol/distilled water (5min each step). Sections were stained in 0.1% cresyl violet solution for 5 min at 37°C and rinsed quickly in distilled water. Then sections were dehydrated from 0 to 100% ethanol/water (same steps as rehydration) and cleared in histo-clear (National diagnostics) before mounting with DPX mounting medium (Sigma-Aldrich). Images were acquired with Leica M205 FA stereomicroscope and processed with LAS software (version 4.7, Leica).

Cell morphology analysis

Flrt1^{-/-};Flrt3lx/lx (mutant) or Flrt1^{+/-};Flrt3lx/+ (control) embryos were electroporated at E13.5. For neuronal sparse labeling we used the SUPERNOVA plasmid system (1 µg/µl, pCAG-loxP-STOP-loxP-RFP-ires-tTA-WRPE; 300ng/µl, pTRE-Cre (Mizuno et al., 2014)). After 3 days, embryonic brains were collected, fixed in 4% PFA over-night and vibratome cut into 100µm sections. For single cell morphology analysis in the lateral cortex only posterior sections were used. Single cell morphology was reconstructed and analyzed using ImageJ (version 1.49) and RStudio (version 0.98.1091, RStudio).

BrdU analysis

Pregnant females were injected intraperitoneally with 0.15-0.2ml of 10mg/ml 5-bromo-2'-deoxyuridine (BrdU, Sigma-Aldrich) dissolved in PBS. This thymidine analog is incorporated during S-phase of the cell cycle. Pregnant females received a single injection of BrdU (final concentration 50 µg per g of mouse weight) at E14.5 and were sacrificed at E17.5, or at E12.5 (1.5 hr prior to sacrifice, short BrdU pulse analysis). Brains from the offspring were removed, fixed overnight with 4% PFA, and processed for immunohistochemistry.

Computer modeling

A sine curve was fitted to the normalized intensity profiles of GFP expression (GOF experiments overexpressing FLRT3 (Seiradake et al., 2014)) and Xgal staining (LOF experiments) after subtracting average intensity value (bs, basal subtraction) to center curves along the y axis at 0 position using the curve fitting tool from MATLAB (Mathworks, Inc). The sine equation contained one term as follows: Curve = A sin(λx + φ), where A is the amplitude, λ the frequency and φ the phase. Sine fitting revealed no statistically significance in the frequency (λ) between GOF and LOF fitted curves (λ, 0.55-0.12 range value) but a difference in their amplitude (A, GOF: 41.41, LOF: 56.74) from 4-6 independent experiments. The strength of both curves was adjusted with the term κ, which was 1/3 for the repulsion curve (LOF experiments) and from 1 to 1/5 for the attraction curve (GOF experiments) in order to mimic high attraction (1 and 1/2), balanced (1/3 equal to repulsion curve) and low attraction (1/4 and 1/5) conditions. The basal subtraction value (bs) used for fitting both curves was added to the equations together with the noise factor ε, which ranged randomly from -10 to 10. The complete equation for both curves used for particle simulation was:

$$\text{curve} = \kappa [A \sin(\lambda x + \phi)] + bs + \varepsilon.$$

Particle distribution and analysis was carried out in MATLAB using the particle system toolbox, MATLAB particles version 2.1 (Buchholz, 2009). Particles representing FLRT1/3+ cells were arranged in a matrix of 6 rows and 36 columns spaced by 0.2 units and were given an attraction toward neighboring particles in both axes based on their x axis position using the fitted attraction (GOF) curve. Particles representing FLRT1/3 negative cells were arranged in a matrix of 5 rows and 35 columns that were shifted 0.1 units in both X/y axis with respect to the previous matrix to keep the same distances between particles of both matrices. These particles were set to repel neighboring particles from the previous matrix (which represents FLRT1/3+ cells). Their repulsion force was set based on their x axis position using the fitted repulsion (LOF) curve and multiplying the result by -1 (negative force). All particles received random speed (ranging from 6 to 12 arbitrary units) for moving along the Z axis and were simulated during 100 frames (0.001 units step time). After simulation, the position of every particle representing FLRT1/3+ cells (first matrix) was retrieved and analyzed based on minimum neighbor distance and 2D kernel distribution which determines density of particles based on total counts per region (total area was divided in 4x4 regions). Particle speed was calculated based on number of frames and final position of each particle, which was also represented in 3D by using surface plot (MATLAB).

in situ hybridization

For ISH, new ferret probes were designed and cloned based on Flrt1/3 DNA sequences from Ensembl.org data. The designed primers to perform the PCR from ferret cDNA were the following: Flrt1-foward TCAGCGTGCAGGTCATCTAC, Flrt1-reverse GCAGC CACAGGAGGTTACAG, Flrt3-foward TCTCCGACTGCTTTCTGT and Flrt3-reverse TATTCATTGCGTCCCCTGT. Sense and anti-sense cRNA probes were synthesized and labeled with digoxigenin (DIG; Roche Diagnostics) according to the manufacturer's instructions. Briefly, 50 micron-thick frozen ferret brain sections were hybridized with DIG-labeled cRNA probes overnight in hybridization solution [50% formamide (Ambion), 10% dextran sulfate, 0.2% tRNA (Invitrogen), 1 × Denhardt's solution (from a 50 × stock; SIGMA), 1 × salt solution (containing 0.2 M NaCl, 0.01 M Tris, 5 mM NaH₂PO₄, 5 mM Na₂HPO₄, 5 mM EDTA, pH 7.5)]. After sections were washed, alkaline phosphatase-coupled anti-digoxigenin Fab fragments were applied. For visualization of the labeled cRNAs, sections were incubated in nitroblue tetrazolium (NBT)/5-bromo-4-chloro-3-indolyl phosphate (BCIP) solution [3.4 µl/ml from NBT stock and 3.5 µl/ml from BCIP stock in reaction buffer (100 mg/ml NBT stock in 70% dimethylformamide; 50 mg/ml BCIP stock in 100% dimethylformamide; Roche)]. Brain sections were processed for the detection of Flrt1 and Flrt3 mRNA using aforementioned probes, and developed in parallel and for an identical length of time. Digital images were obtained from equivalent rostro-caudal levels and latero-medial positions and with identical exposure settings. Color information was eliminated from images, and the brightness of signal above background noise was measured using ImageJ software. For each gene, 2 measurements per section, 3 sections per embryo were analyzed.

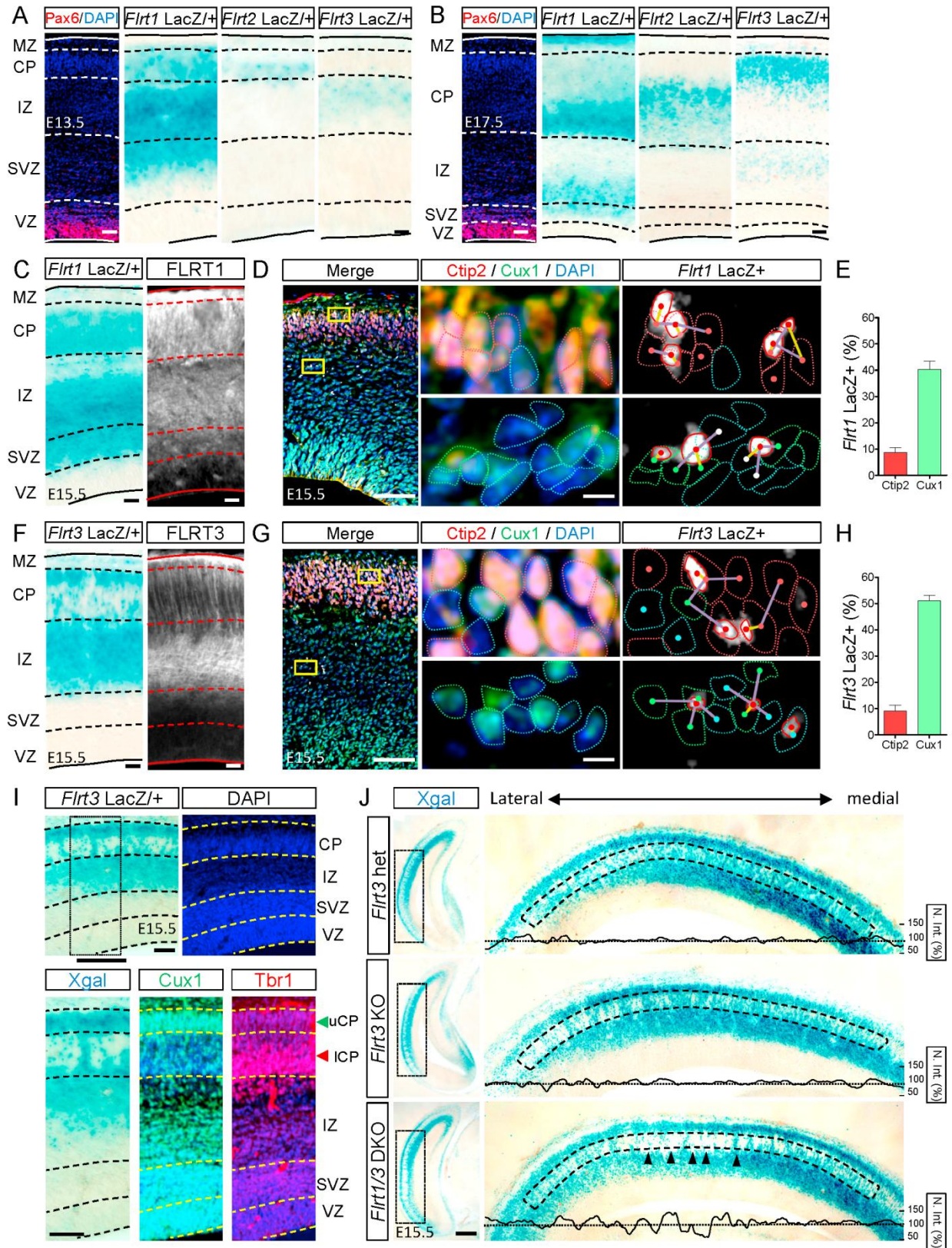
RNaseq analysis

RNaseq data were accessed from the NCBI Gene Expression Omnibus with accession numbers GEO: GSE80958 (Wang et al., 2016), GEO: GSE38805 (Fietz et al., 2012), GEO: GSE65000 (Florio et al., 2015) and the Allan Brain Atlas (<http://www.brain-map.org>) (Figure 6; Figure S6). Raw reads were processed with FASTX-Toolkit (http://hannonlab.cshl.edu/fastx_toolkit/) for initial quality control, where reads with a quality score > 20 and a nucleotide length > 20 were excluded. The processed reads were then mapped to Ensembl annotation files for human (GRCh37) and mouse (NCBIM37) genomes with TopHat (version 2.0.14) (Trapnell et al., 2012). Reads assigned to annotated genes were quantified with featureCounts (Liao et al., 2014) and used as input for DESeq2 (Love et al., 2014). The normalized output data were used to compare between orthologous genes of different length. Sequencing data of FLRTs relative to housekeeping genes is presented for cross-species comparisons (GAPDH in Figure 6 and PGK1 in Figure S6). For the regional cortical comparisons in Figure S6H,I, the same parameters described in Wang et al., 2016 were used. Briefly, RNA-seq data from early mid-trimester human fetuses at 12-19 pcw from the Allan Brain Atlas was compared to E14 mouse embryonic cortices. Values were log-transformed and expressed relative to GAPDH.

QUANTIFICATION AND STATISTICAL ANALYSIS

Statistical significance was determined using one-way ANOVA Tukey's post hoc test or unpaired Student's t test (for comparison between mutant and control mice) with the Prism version 5 (Graphpad Software). Statistical significance was defined as $p < 0.05$. All values in the text and in the figure legends indicate mean + SEM.

Supplemental Figures



(legend on next page)

Figure S1. Expression of FLRTs in the Developing Mouse Cortex and Cell Clustering Phenotype in *Flrt1/3* DKO Mice, Related to Figure 1

(A and B) Xgal staining showing FLRT1-3 expression on coronal sections of E13.5 (A) and E17.5 (B) cortex from individual *Flrt1-3^{lacZ/lx}* reporter lines. Cortical layers were identified by DAPI, and immunostaining for Pax6.

(C) Pattern of Xgal staining of FLRT1 at E15.5 (left image) in comparison to FLRT1 immunostaining (right image).

(D) Xgal staining of FLRT1 (white) on E15.5 coronal sections immunostained for upper layer (Cux1, green in merge) and lower layer (Ctip2, red) neuronal markers. Areas in yellow rectangles are shown with higher magnification on the right. Xgal precipitates were assigned to a particular cell based on the shortest distance between centers of mass. Centers of mass were calculated from the outlines of Xgal precipitates (red) and cells (dashed lines colored in pink for Ctip2, green for Cux1 or blue for remaining cells). Lines connecting the centers of mass are colored in magenta or yellow for the shortest one.

(E) Quantification of data shown in (D).

(F) Pattern of Xgal staining of FLRT3 at E15.5 (left image) in comparison to FLRT3 immunostaining (right image).

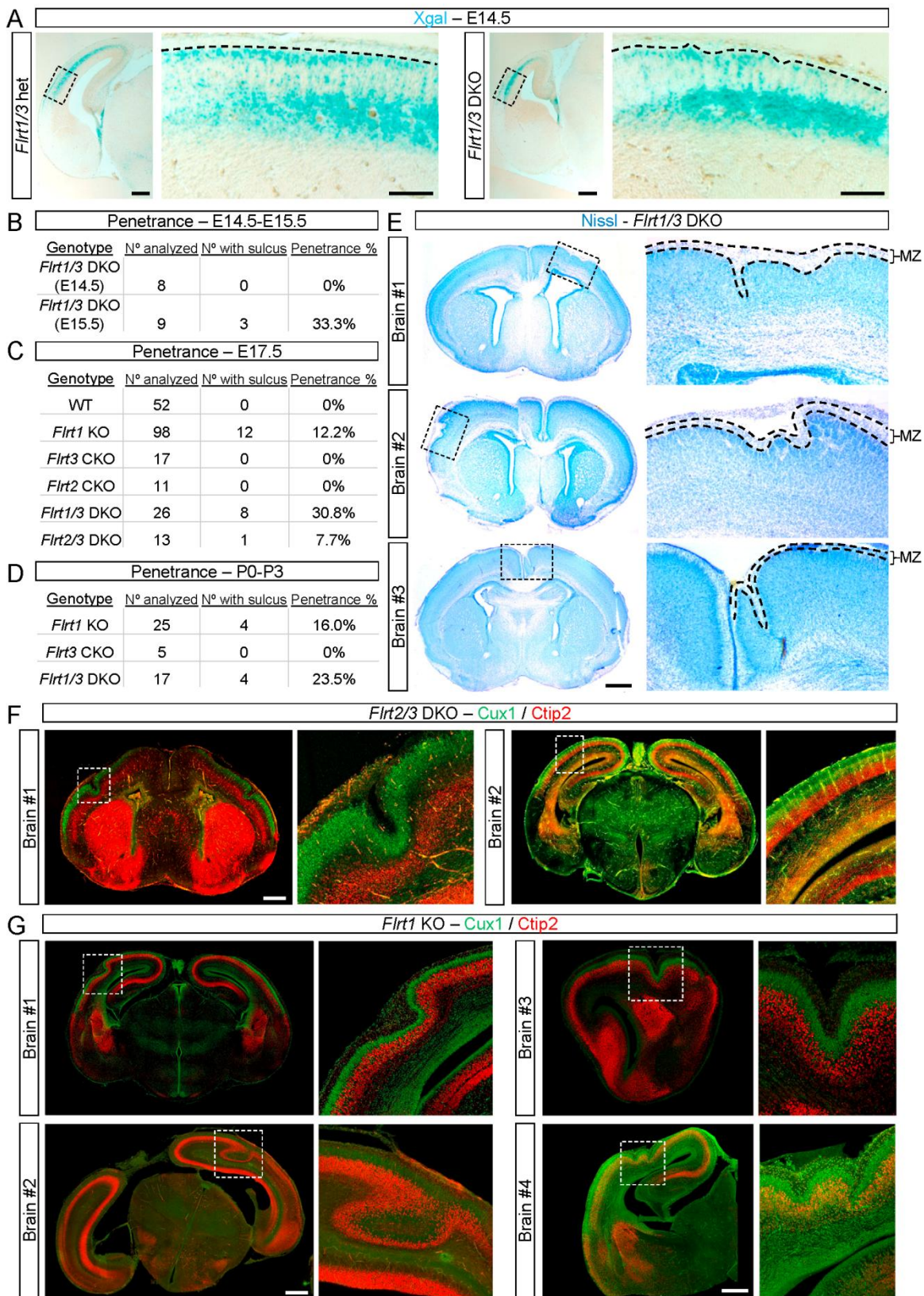
(G) Similar experiment as described in (D) except for FLRT3 expression.

(H) Quantification of data shown in (G).

(I) Xgal staining of FLRT3 on E15.5 coronal sections (left image) and DAPI staining (right image) to delineate cortical layers. Area in dashed rectangle is shown with higher magnification in lower panels. CP was subdivided into upper and lower CP based on Cux1 (upper) and Tbr1 (lower) staining of adjacent sections. Both regions were used to quantify *Flrt3* Xgal distribution (Figures 1D, 1G, and S1J).

(J) Xgal staining of caudal coronal sections from E15.5 *Flrt3* heterozygous *Flrt3^{lox/lacZ}* (het), *Flrt3* conditional KO and *Flrt1/3* double KO embryos. Areas in dashed rectangles are shown with higher magnification on the right. Normalized intensity plots (N. int.) are shown, obtained from the areas delineated with a dashed rectangle. Abbreviations: Marginal zone (MZ), cortical plate (CP), intermediate zone (IZ), subventricular zone (SVZ) and ventricular zone (VZ).

The data are represented as mean ± SEM. Scale bars represent 150 μm (A, B, C), 200, 15 μm (D), 150 μm (F), 200, 15 μm (G), 140 μm (I) and 300 μm (E).



(legend on next page)

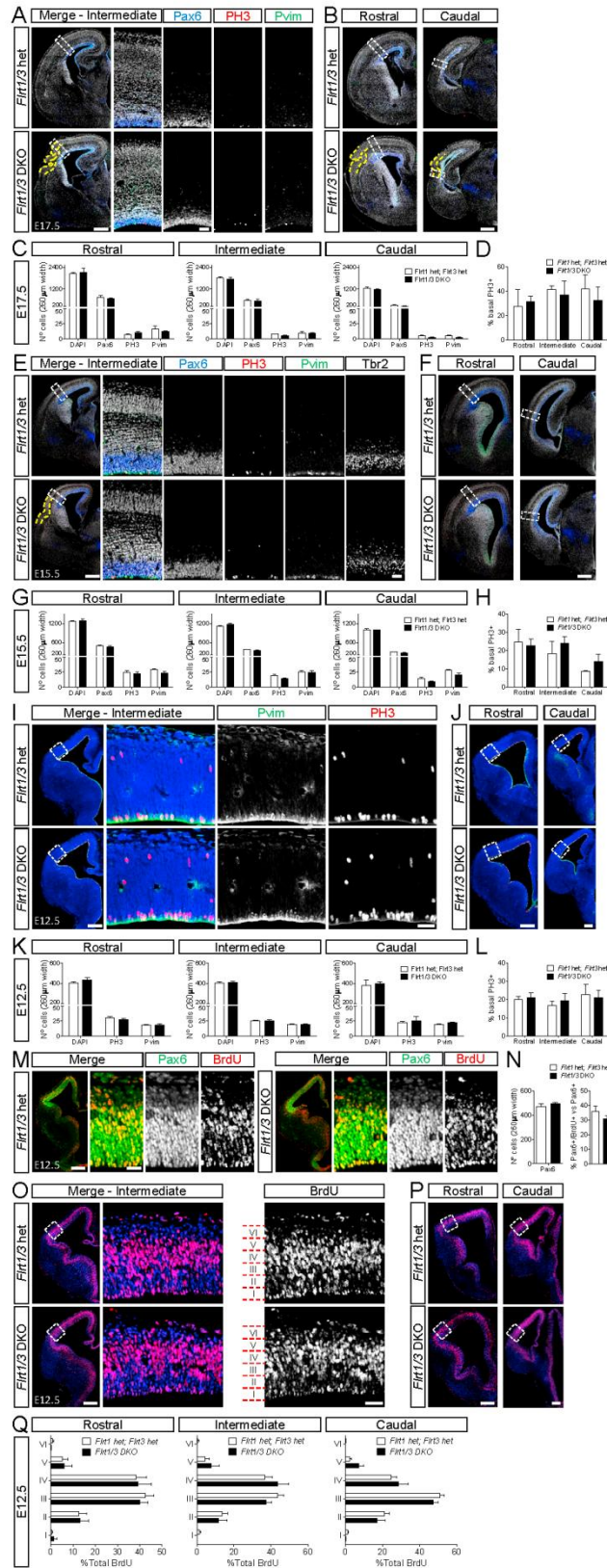
Figure S2. *Flrt1/3* CKO Mice Develop Cortical Sulci, Related to Figure 2

(A) Xgal staining of caudal coronal sections from E14.5 *Flrt1/3* heterozygous and *Flrt1/3* double KO embryos. Dashed line delineates the surface of the upper CP. (B–D) Cortical folding penetrance at embryonic and postnatal stages of the indicated genotypes. Brains were analyzed for the presence of one or more sulci as shown in Figure 2 and Figures S2 and S3.

(E) Nissl-stained postnatal brain sections from *Flrt1/3* DKO brains. Dashed rectangles are shown with higher magnification on the right and sulci are delineated by dashed lines.

(F) Coronal brain sections of *Flrt2/3* DKO brains at E17.5.

(G) Coronal brain sections of *Flrt1* single KO brains at E17.5. To distinguish upper and lower cortical plate, sections from panels F and G were immunostained with anti-Cux1 (upper, green) and anti-Ctip2 (lower, red) antibodies. Scale bars represent 150 μm (A), 800 μm (E) and 600 μm (F, G).



(legend on next page)

Figure S3. Cell Proliferation Is Unchanged in *Firt1/3* DKO Brains, Related to Figure 3

(A and B) E17.5 cortices from rostral to caudal regions were labeled for neuronal progenitors Pax6 (blue), mitotic cells (PH3, red), dividing RG cells (Pvim, green) and DAPI (white). Areas in dashed rectangles in (A) are shown with higher magnification on the right. Yellow stippled line delineates a sulcus in the E17.5 *Firt1/3* DKO section.

(C) Quantification of data shown in panels A,B (n = 3-6 mice per group. No significant changes between groups, unpaired Student's t test).

(D) Proportion of basal mitotic cells (PH3) from rostral to caudal regions (n = 3-6 mice per group. No significant changes between groups, unpaired Student's t test).

(E and F) Similar experiment as shown in panels A,B except for E15.5 cortices and including Tbr2 staining (white) .

(G) Quantification of data shown in panels E,F (n = 3-5 mice per group. No significant changes between groups, unpaired Student's t test).

(H) Proportion of basal mitotic cells (PH3) from rostral to caudal regions (n = 3-5 mice per group. No significant changes between groups, unpaired Student's t test).

(I and J) E12.5 cortices from rostral to caudal regions were labeled for mitotic cells (PH3, red) and dividing RG cells (Pvim, green). Areas in dashed rectangles in (I) are shown with higher magnification on the right.

(K) Quantification of data shown in (I) and (J) (n = 3-4 mice per group. No significant changes between groups, unpaired Student's t test).

(L) Proportion of basal mitotic cells (PH3) from rostral to caudal regions (n = 3-4 mice per group. No significant changes between groups, unpaired Student's t test).

(M) Control and mutant E12.5 cortices previously labeled with a short pulse (1.5h) of BrdU (red) were immunostained for neuronal progenitors (Pax6, green in the merge).

(N) Quantification of data shown in (M) (n = 3-4 mice per group. No significant changes between groups, unpaired Student's t test).

(O and P) Same experiment as in M except that BrdU-labeled brains (red) were counterstained with Dapi (blue).

(Q) Distribution of BrdU+ cells was quantified using a grid of 6 equal horizontal bins (I-VI) of data shown in (O) and (P) (n = 3-4 mice per group. No significant changes between groups, unpaired Student's t test).

The data are represented as mean \pm SEM. Scale bars represent 400, 150 μ m (A and B), 400, 150 μ m (E and F), 300, 100 μ m (I and J), 300, 100 μ m (M) and 300, 100 μ m (O).

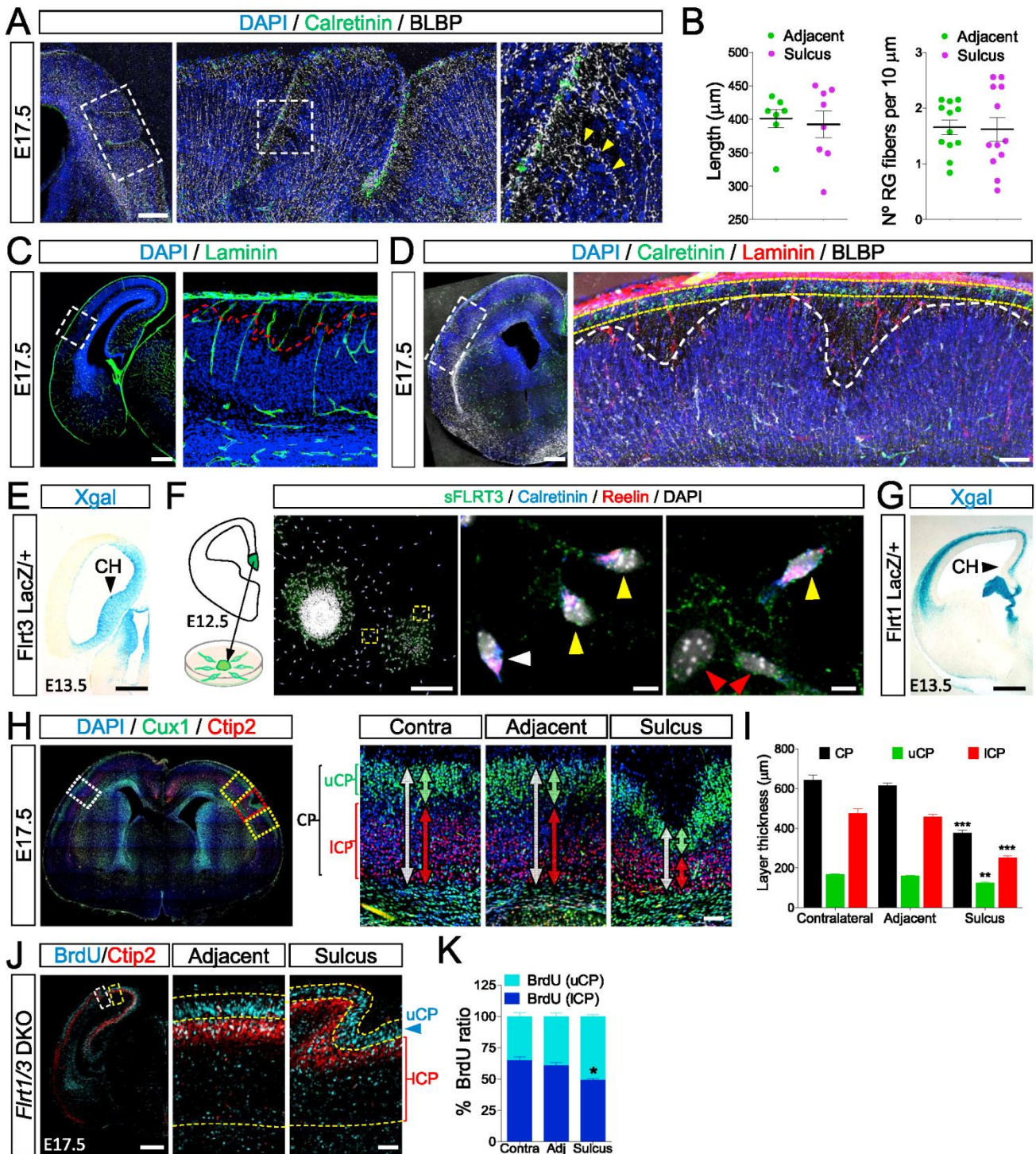


Figure S4. Radial Glia Fibers and the Basal Membrane are Unchanged in *Firt1/3* DKO Brains, Related to Figure 3

(A) E17.5 *Firt1/3* DKO cortex immunostained for BLBP (white) to visualize radial glia (RG) and for calretinin (green) a marker for Cajal-Retzius cells (CR). Nuclei are stained with DAPI (blue). Yellow arrows indicate RG fibers that converge to the sulcal pit. Note that CR cells follow the MZ into the sulcal pit.

(B) Quantification of the length of traced RG fibers (see example image in Figure 3D) and of the density of fibers, $n = 7$ adjacent fibers, $n = 8$ sulcus fibers (left graph) and $n = 12$ sections (right graph) from 5 *Firt1/3* DKO brains.

(C) E17.5 *Firt1/3* DKO cortex immunostained for laminin (green), a marker for basal membrane, and DAPI (blue). Dashed rectangle is shown with higher magnification on the right and the emerging sulcus is delineated by a red dashed line.

(legend continued on next page)

- (D) E17.5 *Flrt1/3* DKO cortex immunostained for laminin (red), calretinin (green), BLBP (white) and DAPI (blue). Dashed rectangle is shown with higher magnification on the right and sulci are delineated by a white dashed line. The MZ is outlined with a yellow dashed line. CR cells are within the MZ.
- (E) Xgal staining showing FLRT3 expression on sagittal sections of E13.5 cortex from *Flrt3^{lacZ/lox}* reporter line. Cortical hem (CH) position is indicated by black arrowhead.
- (F) Schematic representation of experimental design. E12.5 CH explants were cultured for 1 day and immunostained for FLRT3 (surface staining, green), calretinin (blue), reelin (red) and DAPI (white). Yellow arrowheads indicate CR cells expressing FLRT3, white arrowhead shows CR cell negative for FLRT3 and red arrowheads show FLRT3-positive cells which are not CR.
- (G) Xgal staining showing FLRT1 expression on coronal sections of E13.5 cortex from *Flrt1^{lacZ/lox}* reporter line. CH position is indicated by black arrowhead.
- (H) Coronal brain sections of *Flrt1/3* DKO brain at E17.5. To distinguish upper and lower cortical plate, sections were immunostained with anti-Cux1 (upper, green) and anti-Ctip2 (lower, red) antibodies. Dashed rectangles are shown with higher magnification on the right. Arrows indicate the thickness of CP (white), upper (green) and lower (red) CP.
- (I) Quantification of cortical thickness as shown in (H) (n = 12 sections from a total of 5 mutant brains). **p < 0.01, ***p < 0.001 one-way ANOVA test with Tukey's post hoc analysis.
- (J) E17.5 *Flrt1/3* DKO cortex labeled for BrdU (blue, E14.5 injection) and deeper layer neurons (Ctip2, red). Areas in dashed rectangles are shown with higher magnification on the right. Yellow dashed lines delineate the margins of upper and lower CP.
- (K) Quantification of data shown in (L). *p < 0.05, one-way ANOVA test with Tukey's post hoc analysis.
- The data are represented as mean ± SEM. Scale bars represent 400 μm (A), 300, 100 μm (C,D), 300 μm (E, G), 120, 15 μm (F), 300 μm (H) and 500 μm and 90 μm (J), 150 μm (J) and 120 μm (L).

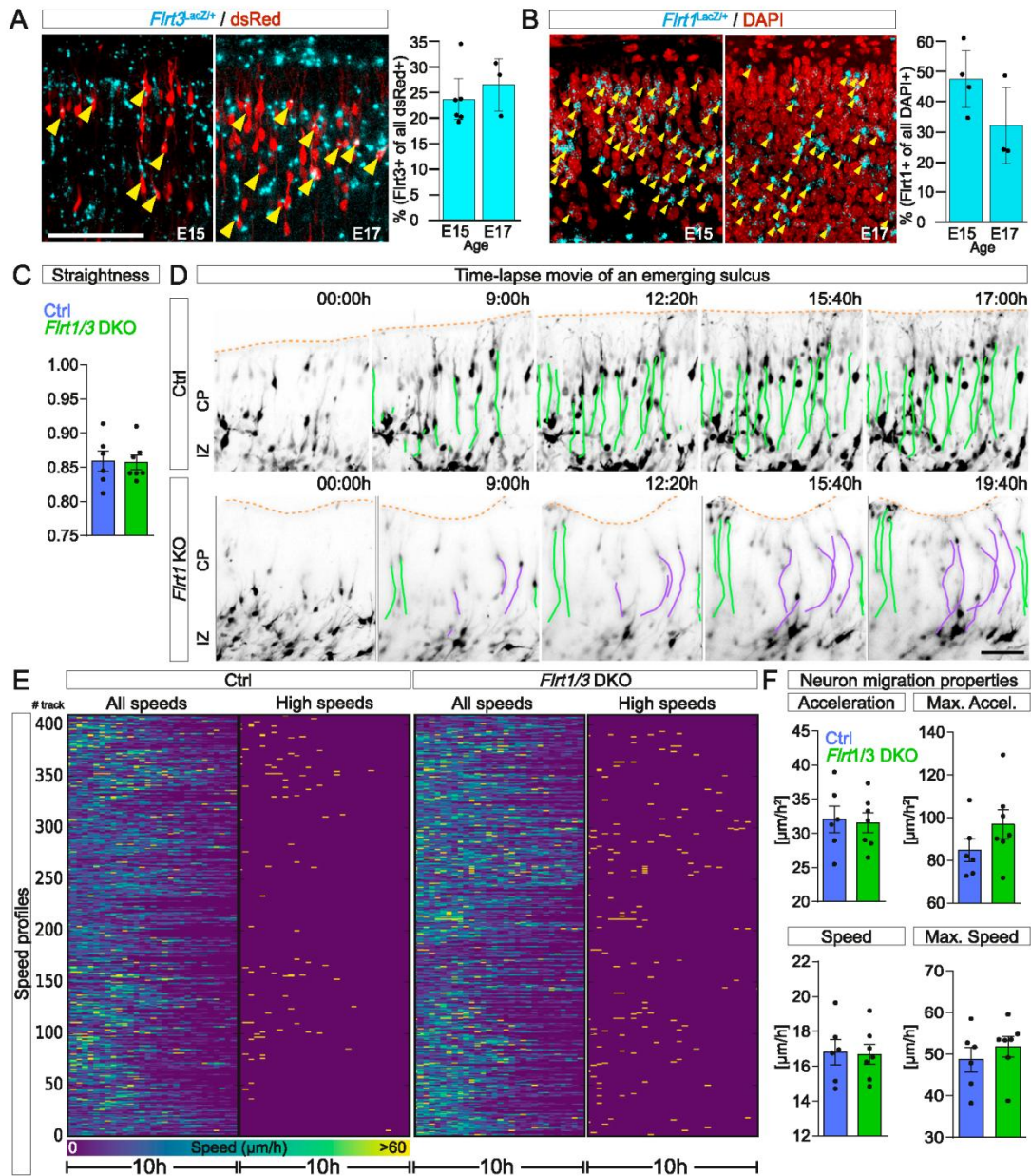


Figure S5. Faster Speed Profiles of *Flrt1/3* DKO Neurons, Related to Figure 4

(A) *Flrt3^{lacZ/+}* embryos were electroporated in utero at E13.5 using a combination of pCAG-Cre and the pCALNL-DsRed reporter plasmid (Red staining). Xgal staining (blue) performed at E15.5 or E17.5 revealed that approximately 25% of all electroporated neurons expressed FLRT3 (right graph, $n = 3-6$ brains).

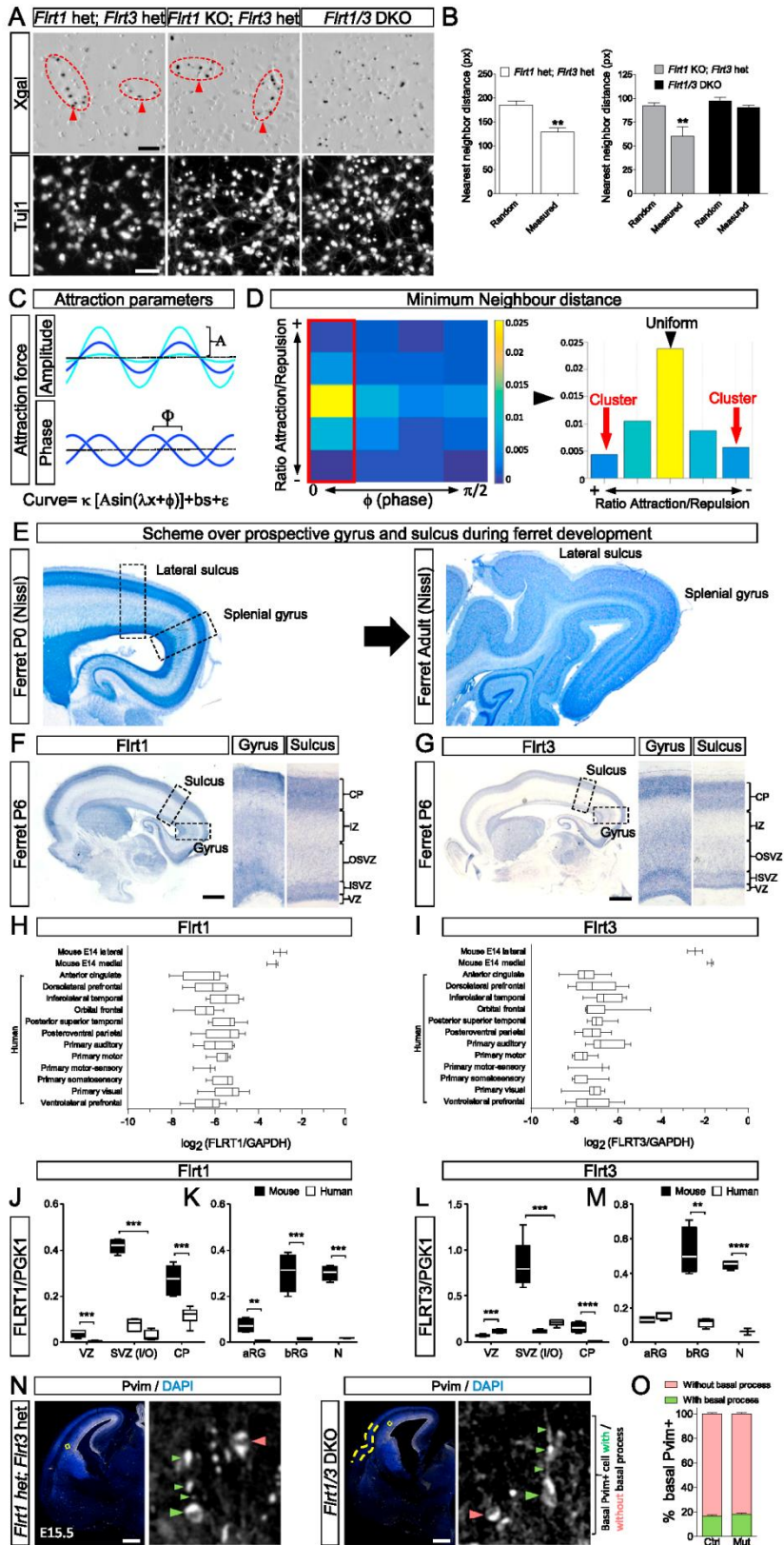
(B) Individual *Flrt1^{lacZ/+}* reporter line embryos stained for beta-galactosidase (blue) at E15.5 or E17.5 revealed that 32%–48% of all CP neurons expressed FLRT1 (right graph, $n = 3-4$ brains).

(C) Quantification of the average straightness of the paths of electroporated neurons migrating into the cortical plate in cultured E15.5 cerebral cortex slices from data shown in Figure 4.

(D) Still pictures of time-lapse movies of an emerging sulcus in a *Flrt1^{-/-}Flrt3^{lox/lox}* background electroporated with a combination of pCAG-Cre and pCALNL-DsRed plasmid (*Flrt1* KO, bottom) compared to electroporated controls. Live imaging shows that in the region of the sulcus neurons follow a curved track (purple) compared to straight tracks in adjacent regions (green) or control sections. Acquisition interval, 20min. Scale bar, 50 μ m.

(E) Color-coded speed profiles of > 400 tracked neurons from data shown in Figure 4 during time acquisition interval (10 h). Each speed segment represents 20min. High speeds, > 58 μ m/h.

(F) Quantification of average speed, acceleration and their maximum values from data shown in (C). $n \geq 6$ experiments per condition comprising 8-10 brains. The data are represented as mean \pm SEM. Scale bars represent 200 μ m (A), 60 μ m (D).



(legend on next page)

Figure S6. Clustering of *Flrt1/3*-Positive Neurons In Vitro and FLRT Expression in Gyrencephalic Species, Related to Figures 5 and 6

(A) Brightfield images of cortical neurons from heterozygous, *FLRT1* KO and *Flrt1/3* DKO embryos at E15.5 cultured for 2 days. FLRT3-expressing neurons are identified by Xgal staining (black dots). Neurons are identified by Tuj1 immunostaining.

(B) Quantification of the nearest neighbor distance between Xgal+ cells shown in A. $n = 3-5$ animals/cultures per group. ** $p < 0.01$, unpaired Student's t test.

(C) Parameters modulating the attraction force between particles representing FLRT1/3+ neurons. Amplitude (A) modulates the strength while phase (ϕ) reflects its position with respect to the repulsive force. κ and b_s (basal subtraction) are parameters used to modulate and fit both curves respectively, while ϵ represents the noise added to the system (see material and [STAR Methods](#)).

(D) Quantification of minimum neighbor distance between particles with different attraction amplitude and phase (as shown in [C]). Every square represents the average of 10 simulations comprising 480 particles with specific amplitude and phase. Red rectangle indicates the condition where particles clustered when attraction was high or low but showed uniform distribution when both forces were balanced. This condition requires similar phase for both attraction and repulsion. Quantification of this particular condition is shown on the right.

(E) Sagittal sections of ferret cortex at P0 and adult stained with Nissl. Dashed boxes indicate prospective lateral sulcus and splenial gyrus which are fully developed in the adult section on the right. Note the absence of cortical folding at P0.

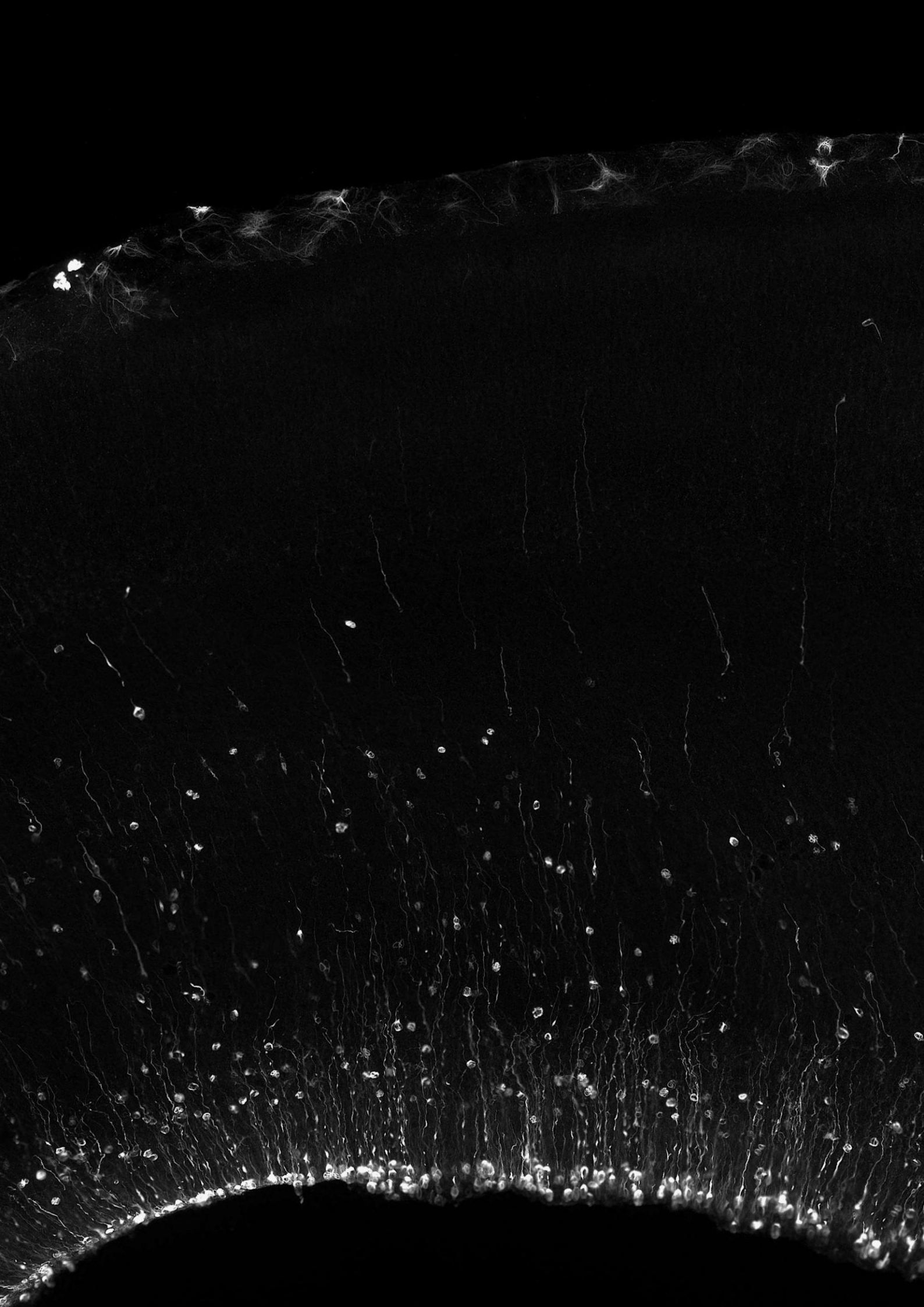
(F and G) In situ hybridization for FLRT1 and FLRT3 in sagittal sections of ferret at P6. Dashed rectangles delineate prospective lateral sulcus (Sulcus) and splenial gyrus (Gyrus). Quantification is shown in [Figure 6](#).

(H–M) Comparison of FLRT1 and FLRT3 expression between mouse and human with sequencing data from [Wang et al. \(2016\)](#) (GEO: GSE80958), [Fietz et al. \(2012\)](#) (GEO: GSE38805), [Florio et al. \(2015\)](#) (GEO: GSE65000) and the Allan Brain Atlas (<http://www.brain-map.org>). Expression normalized to housekeeping gene GAPDH (H and I) and PGK1 (J–M). Whiskers in boxplot represents min and max. Unpaired Student's t test where ** $p < 0.01$, *** $p < 0.001$, **** $p < 0.0001$.

(N) E15.5 control and *Flrt1/3* DKO sections immunostained for Pvim (white) and DAPI (blue). Dashed rectangle is shown with higher magnification on the right and sulci is delineated by a yellow dashed line. Basal Pvim-positive cells with and without a basal process are indicated with green and pink arrowhead respectively. Basal process is indicated with small green arrowheads.

(O) Quantification of the proportion of basal Pvim-positive cells with/without basal process as shown in (J) ($n = 4-5$ sections from each 4-5 mice per group). No significant changes between groups, unpaired Student's t test).

The data are represented as mean \pm SEM. Scale bars represent 50 μm (A), 1mm (F and G) and 300 μm (N).





7. References

"Si sigues las pisadas de un extraño verás cosas que jamás soñaste ver."

- Pocahontas

- Angevine, J.B., and Sidman, R.L. (1961). Autoradiographic study of cell migration during histogenesis of cerebral cortex in the mouse. *Nature* *192*, 766-768.
- Arai, Y., and Pierani, A. (2014). Development and evolution of cortical fields. *Neurosci Res* *86*, 66-76.
- Arai, Y., and Taverna, E. (2017). Neural Progenitor Cell Polarity and Cortical Development. *Frontiers in cellular neuroscience* *11*, 384-384.
- Bajjalieh, S.M., Frantz, G.D., Weimann, J.M., McConnell, S.K., and Scheller, R.H. (1994). Differential expression of synaptic vesicle protein 2 (SV2) isoforms. *J Neurosci* *14*, 5223-5235.
- Bajjalieh, S.M., Peterson, K., Shinghal, R., and Scheller, R.H. (1992). SV2, a brain synaptic vesicle protein homologous to bacterial transporters. *Science* *257*, 1271-1273.
- Barber, M., Arai, Y., Morishita, Y., Vigier, L., Causeret, F., Borello, U., Ledonne, F., Coppola, E., Contremoulins, V., Pfrieger, F.W., *et al.* (2015). Migration Speed of Cajal-Retzius Cells Modulated by Vesicular Trafficking Controls the Size of Higher-Order Cortical Areas. *Curr Biol* *25*, 2466-2478.
- Barnum, K.J., and O'Connell, M.J. (2014). Cell cycle regulation by checkpoints. *Methods in molecular biology (Clifton, NJ)* *1170*, 29-40.
- Bennett, M.K., Calakos, N., Kreiner, T., and Scheller, R.H. (1992). Synaptic vesicle membrane proteins interact to form a multimeric complex. *J Cell Biol* *116*, 761-775.
- Berezcki, E., Branca, R.M., Francis, P.T., Pereira, J.B., Baek, J.H., Hortobagyi, T., Winblad, B., Ballard, C., Lehtio, J., and Aarsland, D. (2018). Synaptic markers of cognitive decline in neurodegenerative diseases: a proteomic approach. *Brain* *141*, 582-595.
- Betizeau, M., Cortay, V., Patti, D., Pfister, S., Gautier, E., Bellemin-Menard, A., Afanassieff, M., Huissoud, C., Douglas, R.J., Kennedy, H., *et al.* (2013). Precursor diversity and complexity of lineage relationships in the outer subventricular zone of the primate. *Neuron* *80*, 442-457.
- Borrell, V. (2018). How Cells Fold the Cerebral Cortex. *J Neurosci* *38*, 776-783.
- Borrell, V., and Calegari, F. (2014). Mechanisms of brain evolution: regulation of neural progenitor cell diversity and cell cycle length. *Neurosci Res* *86*, 14-24.
- Borrell, V., Cardenas, A., Ciceri, G., Galceran, J., Flames, N., Pla, R., Nobrega-Pereira, S., Garcia-Frigola, C., Peregrin, S., Zhao, Z., *et al.* (2012). Slit/Robo signaling modulates the proliferation of central nervous system progenitors. *Neuron* *76*, 338-352.
- Borrell, V., and Gotz, M. (2014). Role of radial glial cells in cerebral cortex folding. *Curr Opin Neurobiol* *27*, 39-46.
- Borrell, V., and Marin, O. (2006). Meninges control tangential migration of hem-derived Cajal-Retzius cells via CXCL12/CXCR4 signaling. *Nat Neurosci* *9*, 1284-1293.
- Borrell, V., and Reillo, I. (2012). Emerging roles of neural stem cells in cerebral cortex development and evolution. *Dev Neurobiol* *72*, 955-971.

- Brodmann, K., ed. (1909). *Localization in the Cerebral Cortex* (London: Imperial College Press).
- Buckley, K., and Kelly, R.B. (1985). Identification of a transmembrane glycoprotein specific for secretory vesicles of neural and endocrine cells. *J Cell Biol* *100*, 1284-1294.
- Cappello, S., Attardo, A., Wu, X., Iwasato, T., Itohara, S., Wilsch-Brauninger, M., Eilken, H.M., Rieger, M.A., Schroeder, T.T., Huttner, W.B., *et al.* (2006). The Rho-GTPase *cdc42* regulates neural progenitor fate at the apical surface. *Nat Neurosci* *9*, 1099-1107.
- Cardenas, A., Villalba, A., de Juan Romero, C., Pico, E., Kyrousi, C., Tzika, A.C., Tessier-Lavigne, M., Ma, L., Drukker, M., Cappello, S., *et al.* (2018). Evolution of Cortical Neurogenesis in Amniotes Controlled by Robo Signaling Levels. *Cell* *174*, 590-606 e521.
- Caroline Crosby, E., and Humphrey, T. (1939). Studies of The Vertebrate Telencephalon. I. The nuclear configuration of the olfactory and accessory olfactory formations and of the nucleus olfactorius anterior of certain reptiles, birds, and mammals. *Journal of Comparative Neurology* *71*, 121-213.
- Celikyurt, I.K., Ulak, G., Mutlu, O., Akar, F.Y., Mulayim, S., Erden, F., and Komsuoglu, S.S. (2012). Positive impact of levetiracetam on emotional learning and memory in naive mice. *Life Sci* *90*, 185-189.
- Chan, J., Jones, N.C., Bush, A.I., O'Brien, T.J., and Kwan, P. (2015). A mouse model of Alzheimer's disease displays increased susceptibility to kindling and seizure-associated death. *Epilepsia* *56*, e73-77.
- Chang, W.P., and Sudhof, T.C. (2009). SV2 renders primed synaptic vesicles competent for Ca²⁺-induced exocytosis. *J Neurosci* *29*, 883-897.
- Chen, L., Tang, Y., Wang, J., Yan, Z., and Xu, R. (2013). miR-421 induces cell proliferation and apoptosis resistance in human nasopharyngeal carcinoma via downregulation of FOXO4. *Biochem Biophys Res Commun* *435*, 745-750.
- Chenn, A., and Walsh, C.A. (2002). Regulation of cerebral cortical size by control of cell cycle exit in neural precursors. *Science* *297*, 365-369.
- Chin, C.F., and Yeong, F.M. (2010). Safeguarding entry into mitosis: the antephase checkpoint. *Mol Cell Biol* *30*, 22-32.
- Cohen, J.E., Lee, P.R., Chen, S., Li, W., and Fields, R.D. (2011). MicroRNA regulation of homeostatic synaptic plasticity. *Proc Natl Acad Sci U S A* *108*, 11650-11655.
- Contreras-Garcia, I.J., Pichardo-Macias, L.A., Santana-Gomez, C.E., Sanchez-Huerta, K., Ramirez-Hernandez, R., Gomez-Gonzalez, B., Rocha, L., and Mendoza Torrealba, J.G. (2018). Differential expression of synaptic vesicle protein 2A after status epilepticus and during epilepsy in a lithium-pilocarpine model. *Epilepsy Behav* *88*, 283-294.
- Crevecoeur, J., Foerch, P., Doupagne, M., Thielen, C., Vandenplas, C., Moonen, G., Deprez, M., and Rogister, B. (2013). Expression of SV2 isoforms during rodent brain development. *BMC Neurosci* *14*, 87.

- Crowder, K.M., Gunther, J.M., Jones, T.A., Hale, B.D., Zhang, H.Z., Peterson, M.R., Scheller, R.H., Chavkin, C., and Bajjalieh, S.M. (1999). Abnormal neurotransmission in mice lacking synaptic vesicle protein 2A (SV2A). *Proc Natl Acad Sci U S A* *96*, 15268-15273.
- Cumbo, E., and Ligori, L.D. (2010). Levetiracetam, lamotrigine, and phenobarbital in patients with epileptic seizures and Alzheimer's disease. *Epilepsy Behav* *17*, 461-466.
- Custer, K.L., Austin, N.S., Sullivan, J.M., and Bajjalieh, S.M. (2006). Synaptic vesicle protein 2 enhances release probability at quiescent synapses. *J Neurosci* *26*, 1303-1313.
- Dale, J.M., Shen, H., Barry, D.M., Garcia, V.B., Rose, F.F., Jr., Lorson, C.L., and Garcia, M.L. (2011). The spinal muscular atrophy mouse model, SMADelta7, displays altered axonal transport without global neurofilament alterations. *Acta Neuropathol* *122*, 331-341.
- Dardou, D., Dassel, D., Cuvelier, L., Deprez, T., De Ryck, M., and Schiffmann, S.N. (2011). Distribution of SV2C mRNA and protein expression in the mouse brain with a particular emphasis on the basal ganglia system. *Brain Res* *1367*, 130-145.
- de Groot, J.F., Lamborn, K.R., Chang, S.M., Gilbert, M.R., Cloughesy, T.F., Aldape, K., Yao, J., Jackson, E.F., Lieberman, F., Robins, H.I., *et al.* (2011). Phase II study of aflibercept in recurrent malignant glioma: a North American Brain Tumor Consortium study. *J Clin Oncol* *29*, 2689-2695.
- De Juan Romero, C., and Borrell, V. (2015). Coevolution of radial glial cells and the cerebral cortex. *Glia* *63*, 1303-1319.
- de Juan Romero, C., Bruder, C., Tomasello, U., Sanz-Anquela, J.M., and Borrell, V. (2015). Discrete domains of gene expression in germinal layers distinguish the development of gyrencephaly. *EMBO J* *34*, 1859-1874.
- Dehay, C., Giroud, P., Berland, M., Killackey, H., and Kennedy, H. (1996). Contribution of thalamic input to the specification of cytoarchitectonic cortical fields in the primate: effects of bilateral enucleation in the fetal monkey on the boundaries, dimensions, and gyrification of striate and extrastriate cortex. *J Comp Neurol* *367*, 70-89.
- Dehay, C., Horsburgh, G., Berland, M., Killackey, H., and Kennedy, H. (1989). Maturation and connectivity of the visual cortex in monkey is altered by prenatal removal of retinal input. *Nature* *337*, 265-267.
- Del Toro, D., Ruff, T., Cederfjall, E., Villalba, A., Seyit-Bremer, G., Borrell, V., and Klein, R. (2017). Regulation of Cerebral Cortex Folding by Controlling Neuronal Migration via FLRT Adhesion Molecules. *Cell* *169*, 621-635 e616.
- Detrait, E., Maurice, T., Hanon, E., Leclercq, K., and Lamberty, Y. (2014). Lack of synaptic vesicle protein SV2B protects against amyloid-beta(2)(5)(-)(3)(5)-induced oxidative stress, cholinergic deficit and cognitive impairment in mice. *Behav Brain Res* *271*, 277-285.
- Devi, L., and Ohno, M. (2013). Effects of levetiracetam, an antiepileptic drug, on memory impairments associated with aging and Alzheimer's disease in mice. *Neurobiol Learn Mem* *102*, 7-11.

- Dong, M., Liu, H., Tepp, W.H., Johnson, E.A., Janz, R., and Chapman, E.R. (2008). Glycosylated SV2A and SV2B mediate the entry of botulinum neurotoxin E into neurons. *Mol Biol Cell* *19*, 5226-5237.
- Dong, M., Yeh, F., Tepp, W.H., Dean, C., Johnson, E.A., Janz, R., and Chapman, E.R. (2006). SV2 is the protein receptor for botulinum neurotoxin A. *Science* *312*, 592-596.
- Drago, J., Nurcombe, V., and Bartlett, P.F. (1991). Laminin through its long arm E8 fragment promotes the proliferation and differentiation of murine neuroepithelial cells in vitro. *Exp Cell Res* *192*, 256-265.
- Dunn, A.R., Stout, K.A., Ozawa, M., Lohr, K.M., Hoffman, C.A., Bernstein, A.I., Li, Y., Wang, M., Sgobio, C., Sastry, N., *et al.* (2017). Synaptic vesicle glycoprotein 2C (SV2C) modulates dopamine release and is disrupted in Parkinson disease. *Proc Natl Acad Sci U S A* *114*, E2253-e2262.
- Fatterpekar, G.M., Naidich, T.P., Delman, B.N., Aguinaldo, J.G., Gultekin, S.H., Sherwood, C.C., Hof, P.R., Drayer, B.P., and Fayad, Z.A. (2002). Cytoarchitecture of the human cerebral cortex: MR microscopy of excised specimens at 9.4 Tesla. *AJNR Am J Neuroradiol* *23*, 1313-1321.
- Feany, M.B., Lee, S., Edwards, R.H., and Buckley, K.M. (1992). The synaptic vesicle protein SV2 is a novel type of transmembrane transporter. *Cell* *70*, 861-867.
- Ferent, J., Giguere, F., Jolicoeur, C., Morin, S., Michaud, J.F., Makihara, S., Yam, P.T., Cayouette, M., and Charron, F. (2019). Boc Acts via Numb as a Shh-Dependent Endocytic Platform for Ptch1 Internalization and Shh-Mediated Axon Guidance. *Neuron* *102*, 1157-1171.e1155.
- Fernandez, V., Llinares-Benadero, C., and Borrell, V. (2016). Cerebral cortex expansion and folding: what have we learned? *EMBO J* *35*, 1021-1044.
- Fietz, S.A., Kelava, I., Vogt, J., Wilsch-Brauninger, M., Stenzel, D., Fish, J.L., Corbeil, D., Riehn, A., Distler, W., Nitsch, R., *et al.* (2010). OSVZ progenitors of human and ferret neocortex are epithelial-like and expand by integrin signaling. *Nat Neurosci* *13*, 690-699.
- Fietz, S.A., Lachmann, R., Brandl, H., Kircher, M., Samusik, N., Schroder, R., Lakshmanaperumal, N., Henry, I., Vogt, J., Riehn, A., *et al.* (2012). Transcriptomes of germinal zones of human and mouse fetal neocortex suggest a role of extracellular matrix in progenitor self-renewal. *Proc Natl Acad Sci U S A* *109*, 11836-11841.
- Fish, J.L., Kosodo, Y., Enard, W., Paabo, S., and Huttner, W.B. (2006). *Aspm* specifically maintains symmetric proliferative divisions of neuroepithelial cells. *Proc Natl Acad Sci U S A* *103*, 10438-10443.
- Florio, M., Albert, M., Taverna, E., Namba, T., Brandl, H., Lewitus, E., Haffner, C., Sykes, A., Wong, F.K., Peters, J., *et al.* (2015). Human-specific gene ARHGAP11B promotes basal progenitor amplification and neocortex expansion. *Science* *347*, 1465-1470.
- Florio, M., Heide, M., Pinson, A., Brandl, H., Albert, M., Winkler, S., Wimberger, P., Huttner, W.B., and Hiller, M. (2018). Evolution and cell-type specificity of human-specific genes preferentially expressed in progenitors of fetal neocortex. *Elife* *7*.

- Florio, M., and Huttner, W.B. (2014). Neural progenitors, neurogenesis and the evolution of the neocortex. *Development* *141*, 2182-2194.
- Freeman, S., and Hamilton, H. (2005). *Biological science* (Upper Saddle River, N.J.: Pearson Prentice Hall).
- Fujita, I., Shitamukai, A., Kusumoto, F., Mase, S., Suetsugu, T., Omori, A., Kato, K., Abe, T., Shioi, G., Konno, D., *et al.* (2020). Endfoot regeneration restricts radial glial state and prevents translocation into the outer subventricular zone in early mammalian brain development. *Nat Cell Biol* *22*, 26-37.
- Fukusumi, Y., Wakamatsu, A., Takashima, N., Hasegawa, E., Miyauchi, N., Tomita, M., and Kawachi, H. (2015). SV2B is essential for the integrity of the glomerular filtration barrier. *Laboratory investigation; a journal of technical methods and pathology* *95*, 534-545.
- Gal, J.S., Morozov, Y.M., Ayoub, A.E., Chatterjee, M., Rakic, P., and Haydar, T.F. (2006). Molecular and morphological heterogeneity of neural precursors in the mouse neocortical proliferative zones. *J Neurosci* *26*, 1045-1056.
- Garcia-Perez, E., Mahfooz, K., Covita, J., Zanduetta, A., and Wesseling, J.F. (2015). Levetiracetam accelerates the onset of supply rate depression in synaptic vesicle trafficking. *Epilepsia* *56*, 535-545.
- Garcia, K.E., Kroenke, C.D., and Bayly, P.V. (2018). Mechanics of cortical folding: stress, growth and stability. *Philos Trans R Soc Lond B Biol Sci* *373*.
- Gelman, D.M., and Marin, O. (2010). Generation of interneuron diversity in the mouse cerebral cortex. *Eur J Neurosci* *31*, 2136-2141.
- Geppert, M., Goda, Y., Hammer, R.E., Li, C., Rosahl, T.W., Stevens, C.F., and Sudhof, T.C. (1994). Synaptotagmin I: a major Ca²⁺ sensor for transmitter release at a central synapse. *Cell* *79*, 717-727.
- Gleeson, J.G., Lin, P.T., Flanagan, L.A., and Walsh, C.A. (1999). Doublecortin is a microtubule-associated protein and is expressed widely by migrating neurons. *Neuron* *23*, 257-271.
- Gordon Betts, P.D., Eddie Johnson, Jody E. Johnson, Oksana Korol, Dean H. Kruse, Brandon Poe. (2017). *Anatomy & Physiology*.
- Gotz, M., and Huttner, W.B. (2005). The cell biology of neurogenesis. *Nature Rev Mol Cell Biol* *6*, 777-788.
- Greig, L.C., Woodworth, M.B., Galazo, M.J., Padmanabhan, H., and Macklis, J.D. (2013). Molecular logic of neocortical projection neuron specification, development and diversity. *Nat Rev Neurosci* *14*, 755-769.
- Hansen, D.V., Lui, J.H., Parker, P.R., and Kriegstein, A.R. (2010). Neurogenic radial glia in the outer subventricular zone of human neocortex. *Nature* *464*, 554-561.
- Hao le, T., Burghes, A.H., and Beattie, C.E. (2011). Generation and Characterization of a genetic zebrafish model of SMA carrying the human SMN2 gene. *Mol Neurodegener* *6*, 24.

- Hebert, J.M., and Fishell, G. (2008). The genetics of early telencephalon patterning: some assembly required. *Nat Rev Neurosci* 9, 678-685.
- Heese, K., Nagai, Y., and Sawada, T. (2001). Identification of a new synaptic vesicle protein 2B mRNA transcript which is up-regulated in neurons by amyloid beta peptide fragment (1-42). *Biochem Biophys Res Commun* 289, 924-928.
- Hong, S.E., Shugart, Y.Y., Huang, D.T., Shahwan, S.A., Grant, P.E., Hourihane, J.O., Martin, N.D., and Walsh, C.A. (2000). Autosomal recessive lissencephaly with cerebellar hypoplasia is associated with human RELN mutations. *Nat Genet* 26, 93-96.
- Iezzi, M., Theander, S., Janz, R., Loze, C., and Wollheim, C.B. (2005). SV2A and SV2C are not vesicular Ca²⁺ transporters but control glucose-evoked granule recruitment. *J Cell Sci* 118, 5647-5660.
- Insausti, R. (1993). Comparative anatomy of the entorhinal cortex and hippocampus in mammals. *Hippocampus* 3, 19-26.
- Jahn, R. (2006). A Neuronal Receptor for Botulinum Toxin. *Science* 312, 540-541.
- Jakobsen, A.M., Ahlman, H., Wangberg, B., Kolby, L., Bengtsson, M., and Nilsson, O. (2002). Expression of synaptic vesicle protein 2 (SV2) in neuroendocrine tumours of the gastrointestinal tract and pancreas. *J Pathol* 196, 44-50.
- Janz, R., Goda, Y., Geppert, M., Missler, M., and Sudhof, T.C. (1999). SV2A and SV2B function as redundant Ca²⁺ regulators in neurotransmitter release. *Neuron* 24, 1003-1016.
- Janz, R., Hofmann, K., and Sudhof, T.C. (1998). SVOP, an evolutionarily conserved synaptic vesicle protein, suggests novel transport functions of synaptic vesicles. *J Neurosci* 18, 9269-9281.
- Janz, R., and Sudhof, T.C. (1999). SV2C is a synaptic vesicle protein with an unusually restricted localization: anatomy of a synaptic vesicle protein family. *Neuroscience* 94, 1279-1290.
- Johansson, P.A., Irmeler, M., Acampora, D., Beckers, J., Simeone, A., and Gotz, M. (2013). The transcription factor Otx2 regulates choroid plexus development and function. *Development* 140, 1055-1066.
- Johnson, M.B., Sun, X., Kodani, A., Borges-Monroy, R., Girskis, K.M., Ryu, S.C., Wang, P.P., Patel, K., Gonzalez, D.M., Woo, Y.M., *et al.* (2018). Aspm knockout ferret reveals an evolutionary mechanism governing cerebral cortical size. *Nature* 556, 370-375.
- Johnson, M.B., Wang, P.P., Atabay, K.D., Murphy, E.A., Doan, R.N., Hecht, J.L., and Walsh, C.A. (2015). Single-cell analysis reveals transcriptional heterogeneity of neural progenitors in human cortex. *Nat Neurosci* 18, 637-646.
- Jones, E.G. (2009). The origins of cortical interneurons: mouse versus monkey and human. *Cereb Cortex* 19, 1953-1956.

- Joo, J.-Y., Kim, B.-W., Lee, J.-S., Park, J.-Y., Kim, S., Yun, Y.-J., Lee, S.-H., Lee, S.-H., Rhim, H., and Son, H. (2007). Activation of NMDA receptors increases proliferation and differentiation of hippocampal neural progenitor cells. *Journal of Cell Science* 120, 1358-1370.
- Kandel, E.R., Schwartz, J.H., Jessell, T.M., and Mack, S. (2012). *Principles of neural scienc*, 5th ed. edn (McGraw-Hill).
- Kao, H.T., Li, P., Chao, H.M., Janoschka, S., Pham, K., Feng, J., McEwen, B.S., Greengard, P., Pieribone, V.A., and Porton, B. (2008). Early involvement of synapsin III in neural progenitor cell development in the adult hippocampus. *J Comp Neurol* 507, 1860-1870.
- Kaufman, K.R. (2011). Antiepileptic drugs in the treatment of psychiatric disorders. *Epilepsy Behav* 21, 1-11.
- Kawaue, T., Shitamukai, A., Nagasaka, A., Tsunekawa, Y., Shinoda, T., Saito, K., Terada, R., Bilgic, M., Miyata, T., Matsuzaki, F., *et al.* (2019). Lzts1 controls both neuronal delamination and outer radial glial-like cell generation during mammalian cerebral development. *Nat Commun* 10, 2780.
- Kelava, I., Lewitus, E., and Huttner, W.B. (2013). The secondary loss of gyrencephaly as an example of evolutionary phenotypical reversal. *Front Neuroanat* 7, 16.
- Knabbe, J., Nassal, J.P., Verhage, M., and Kuner, T. (2018). Secretory vesicle trafficking in awake and anaesthetized mice: differential speeds in axons versus synapses. *J Physiol* 596, 3759-3773.
- Knight, D., Tolley, L.K., Kim, D.K., Lavidis, N.A., and Noakes, P.G. (2003). Functional analysis of neurotransmission at beta2-laminin deficient terminals. *J Physiol* 546, 789-800.
- Kou, Z., Wu, Q., Kou, X., Yin, C., Wang, H., Zuo, Z., Zhuo, Y., Chen, A., Gao, S., and Wang, X. (2015). CRISPR/Cas9-mediated genome engineering of the ferret. *Cell Res* 25, 1372-1375.
- Krames, E., Peckham, P.H., and Rezai, A.R. (2018). *Neuromodulation : comprehensive textbook of principles, technologies, and therapies*.
- Krubitzer, L. (2007). The magnificent compromise: cortical field evolution in mammals. *Neuron* 56, 201-208.
- Kwon, H.J., Ma, S., and Huang, Z. (2011). Radial glia regulate Cajal-Retzius cell positioning in the early embryonic cerebral cortex. *Dev Biol* 351, 25-34.
- Kwon, S.E., and Chapman, E.R. (2012). Glycosylation is dispensable for sorting of synaptotagmin 1 but is critical for targeting of SV2 and synaptophysin to recycling synaptic vesicles. *J Biol Chem* 287, 35658-35668.
- Lazzell, D.R., Belizaire, R., Thakur, P., Sherry, D.M., and Janz, R. (2004). SV2B regulates synaptotagmin 1 by direct interaction. *J Biol Chem* 279, 52124-52131.

- Le Gros Clark, M.E. (1945). Deformation patterns on the cerebral cortex. In *Essays on Growth and Form*, W.E. Le Gros Clark, and P.B. Medawar, eds. (London: Clarendon), pp. 1-22.
- Liu, X., Hashimoto-Torii, K., Torii, M., Haydar, T.F., and Rakic, P. (2008). The role of ATP signaling in the migration of intermediate neuronal progenitors to the neocortical subventricular zone. *Proceedings of the National Academy of Sciences* *105*, 11802-11807.
- Llinares-Benadero, C., and Borrell, V. (2019). Deconstructing cortical folding: genetic, cellular and mechanical determinants. *Nat Rev Neurosci* *20*, 161-176.
- Long, K.R., and Huttner, W.B. (2019). How the extracellular matrix shapes neural development. *Open Biol* *9*, 180216.
- Long, K.R., Newland, B., Florio, M., Kalebic, N., Langen, B., Kolterer, A., Wimberger, P., and Huttner, W.B. (2018). Extracellular Matrix Components HAPLN1, Lumican, and Collagen I Cause Hyaluronic Acid-Dependent Folding of the Developing Human Neocortex. *Neuron* *99*, 702-719 e707.
- Loscher, W., Gillard, M., Sands, Z.A., Kaminski, R.M., and Klitgaard, H. (2016). Synaptic Vesicle Glycoprotein 2A Ligands in the Treatment of Epilepsy and Beyond. *CNS Drugs* *30*, 1055-1077.
- Löscher, W., Gillard, M., Sands, Z.A., Kaminski, R.M., and Klitgaard, H. (2016). Synaptic Vesicle Glycoprotein 2A Ligands in the Treatment of Epilepsy and Beyond. *CNS Drugs* *30*, 1055-1077.
- LoTurco, J.J., Owens, D.F., Heath, M.J., Davis, M.B., and Kriegstein, A.R. (1995). GABA and glutamate depolarize cortical progenitor cells and inhibit DNA synthesis. *Neuron* *15*, 1287-1298.
- Loulier, K., Lathia, J.D., Marthiens, V., Relucio, J., Mughal, M.R., Tang, S.C., Coksaygan, T., Hall, P.E., Chigurupati, S., Patton, B., *et al.* (2009). beta1 integrin maintains integrity of the embryonic neocortical stem cell niche. *PLoS Biol* *7*, e1000176.
- Lukas, J., Lukas, C., and Bartek, J. (2004). Mammalian cell cycle checkpoints: signalling pathways and their organization in space and time. *DNA Repair (Amst)* *3*, 997-1007.
- Lynch, B.A., Lambeng, N., Nocka, K., Kensel-Hammes, P., Bajjalieh, S.M., Matagne, A., and Fuks, B. (2004). The synaptic vesicle protein SV2A is the binding site for the antiepileptic drug levetiracetam. *Proc Natl Acad Sci U S A* *101*, 9861-9866.
- Lynch, B.A., Matagne, A., Brannstrom, A., von Euler, A., Jansson, M., Hauzenberger, E., and Soderhall, J.A. (2008). Visualization of SV2A conformations in situ by the use of Protein Tomography. *Biochem Biophys Res Commun* *375*, 491-495.
- Madeo, M., Kovács, A.D., and Pearce, D.A. (2014). The human synaptic vesicle protein, SV2A, functions as a galactose transporter in *Saccharomyces cerevisiae*. *The Journal of biological chemistry* *289*, 33066-33071.

- Maeder, C.I., San-Miguel, A., Wu, E.Y., Lu, H., and Shen, K. (2014). In vivo neuron-wide analysis of synaptic vesicle precursor trafficking. *Traffic* 15, 273-291.
- Martinez-Martinez, M.A., Ciceri, G., Espinos, A., Fernandez, V., Marin, O., and Borrell, V. (2018). Extensive branching of radially-migrating neurons in the mammalian cerebral cortex. *J Comp Neurol*.
- Martinez-Martinez, M.A., De Juan Romero, C., Fernandez, V., Cardenas, A., Gotz, M., and Borrell, V. (2016). A restricted period for formation of outer subventricular zone defined by *Cdh1* and *Trnp1* levels. *Nat Commun* 7, 11812.
- Migliore, M., and Shepherd, G.M. (2005). An integrated approach to classifying neuronal phenotypes. *Nature Reviews Neuroscience* 6, 810.
- Miyata, T., Okamoto, M., Shinoda, T., and Kawaguchi, A. (2015). Interkinetic nuclear migration generates and opposes ventricular-zone crowding: insight into tissue mechanics. *Frontiers in cellular neuroscience* 8, 473-473.
- Molyneaux, B.J., Arlotta, P., Menezes, J.R., and Macklis, J.D. (2007). Neuronal subtype specification in the cerebral cortex. *Nat Rev Neurosci* 8, 427-437.
- Mountcastle, V.B. (1997). The columnar organization of the neocortex. *Brain* 120 (Pt 4), 701-722.
- Mutch, S.A., Kensel-Hammes, P., Gadd, J.C., Fujimoto, B.S., Allen, R.W., Schiro, P.G., Lorenz, R.M., Kuyper, C.L., Kuo, J.S., Bajjalieh, S.M., *et al.* (2011). Protein quantification at the single vesicle level reveals that a subset of synaptic vesicle proteins are trafficked with high precision. *J Neurosci* 31, 1461-1470.
- Nagashima, F., Suzuki, I.K., Shitamukai, A., Sakaguchi, H., Iwashita, M., Kobayashi, T., Tone, S., Toida, K., Vanderhaeghen, P., and Kosodo, Y. (2014). Novel and robust transplantation reveals the acquisition of polarized processes by cortical cells derived from mouse and human pluripotent stem cells. *Stem Cells Dev* 23, 2129-2142.
- Nishiki, T., and Augustine, G.J. (2004). Synaptotagmin I synchronizes transmitter release in mouse hippocampal neurons. *J Neurosci* 24, 6127-6132.
- Nonaka-Kinoshita, M., Reillo, I., Artegiani, B., Martinez-Martinez, M.A., Nelson, M., Borrell, V., and Calegari, F. (2013). Regulation of cerebral cortex size and folding by expansion of basal progenitors. *Embo j* 32, 1817-1828.
- Nowack, A., Malarkey, E.B., Yao, J., Bleckert, A., Hill, J., and Bajjalieh, S.M. (2011). Levetiracetam reverses synaptic deficits produced by overexpression of SV2A. *PLoS One* 6, e29560.
- Nowack, A., Yao, J., Custer, K.L., and Bajjalieh, S.M. (2010). SV2 regulates neurotransmitter release via multiple mechanisms. *Am J Physiol Cell Physiol* 299, C960-967.
- O'Leary, D.D., Chou, S.J., and Sahara, S. (2007). Area patterning of the mammalian cortex. *Neuron* 56, 252-269.

- Ohno, Y., Ishihara, S., Terada, R., Kikuta, M., Sofue, N., Kawai, Y., Serikawa, T., and Sasa, M. (2009). Preferential increase in the hippocampal synaptic vesicle protein 2A (SV2A) by pentylentetrazole kindling. *Biochem Biophys Res Commun* 390, 415-420.
- Okamoto, M., Shinoda, T., Kawaue, T., Nagasaka, A., and Miyata, T. (2014). Ferret-mouse differences in interkinetic nuclear migration and cellular densification in the neocortical ventricular zone. *Neurosci Res* 86, 88-95.
- Peng, L., Tepp, W.H., Johnson, E.A., and Dong, M. (2011). Botulinum neurotoxin D uses synaptic vesicle protein SV2 and gangliosides as receptors. *PLoS Pathog* 7, e1002008.
- Pilz, D.T., Matsumoto, N., Minnerath, S., Mills, P., Gleeson, J.G., Allen, K.M., Walsh, C.A., Barkovich, A.J., Dobyns, W.B., Ledbetter, D.H., *et al.* (1998). LIS1 and XLIS (DCX) mutations cause most classical lissencephaly, but different patterns of malformation. *Hum Mol Genet* 7, 2029-2037.
- Pilz, G.A., Shitamukai, A., Reillo, I., Pacary, E., Schwausch, J., Stahl, R., Ninkovic, J., Snippert, H.J., Clevers, H., Godinho, L., *et al.* (2013). Amplification of progenitors in the mammalian telencephalon includes a new radial glial cell type. *Nat Commun* 4, 2125.
- Pollen, A.A., Nowakowski, T.J., Chen, J., Retallack, H., Sandoval-Espinosa, C., Nicholas, C.R., Shuga, J., Liu, S.J., Oldham, M.C., Diaz, A., *et al.* (2015). Molecular identity of human outer radial glia during cortical development. *Cell* 163, 55-67.
- Poluch, S., and Juliano, S.L. (2015). Fine-tuning of neurogenesis is essential for the evolutionary expansion of the cerebral cortex. *Cereb Cortex* 25, 346-364.
- Puelles, L., Harrison, M., Paxinos, G., and Watson, C. (2013). A developmental ontology for the mammalian brain based on the prosomeric model. *Trends Neurosci* 36, 570-578.
- Purves, D. (2011). *Neuroscience*, 5th Edition edn (Sinauer Associates Publishers).
- Radakovits, R., Barros, C.S., Belvindrah, R., Patton, B., and Muller, U. (2009). Regulation of radial glial survival by signals from the meninges. *J Neurosci* 29, 7694-7705.
- Radmanesh, F., Caglayan, A.O., Silhavy, J.L., Yilmaz, C., Cantagrel, V., Omar, T., Rosti, B., Kaymakcalan, H., Gabriel, S., Li, M., *et al.* (2013). Mutations in LAMB1 cause cobblestone brain malformation without muscular or ocular abnormalities. *American journal of human genetics* 92, 468-474.
- Rakic, P. (1972). Mode of cell migration to the superficial layers of fetal monkey neocortex. *J Comp Neurol* 145, 61-83.
- Rakic, P. (1974). Neurons in rhesus monkey visual cortex: systematic relation between time of origin and eventual disposition. *Science* 183, 425-427.
- Rakic, P. (1988). Specification of cerebral cortical areas. *Science* 241, 170-176.
- Rakic, P. (1995). Radial versus tangential migration of neuronal clones in the developing cerebral cortex. *Proc Natl Acad Sci U S A* 92, 11323-11327.

- Rakic, P. (2009). Evolution of the neocortex: a perspective from developmental biology. *Nat Rev Neurosci* 10, 724-735.
- Rash, B.G., Ackman, J.B., and Rakic, P. (2016). Bidirectional radial Ca(2+) activity regulates neurogenesis and migration during early cortical column formation. *Sci Adv* 2, e1501733.
- Reemst, K., Noctor, S.C., Lucassen, P.J., and Hol, E.M. (2016). The Indispensable Roles of Microglia and Astrocytes during Brain Development. *Frontiers in human neuroscience* 10, 566-566.
- Reillo, I., and Borrell, V. (2012). Germinal zones in the developing cerebral cortex of ferret: ontogeny, cell cycle kinetics, and diversity of progenitors. *Cereb Cortex* 22, 2039-2054.
- Reillo, I., de Juan Romero, C., Cardenas, A., Clasca, F., Martinez-Martinez, M.A., and Borrell, V. (2017). A Complex Code of Extrinsic Influences on Cortical Progenitor Cells of Higher Mammals. *Cereb Cortex* 27, 4586-4606.
- Reillo, I., de Juan Romero, C., Garcia-Cabezas, M.A., and Borrell, V. (2011). A role for intermediate radial glia in the tangential expansion of the Mammalian cerebral cortex. *Cereb Cortex* 21, 1674-1694.
- Reiner, O., Sapir, T., and Gerlitz, G. (2012). Interkinetic nuclear movement in the ventricular zone of the cortex. *J Mol Neurosci* 46, 516-526.
- Rice, D.S., and Curran, T. (2001). Role of the reelin signaling pathway in central nervous system development. *Annu Rev Neurosci* 24, 1005-1039.
- Sauerland, C., Menzies, B.R., Glatzle, M., Seeger, J., Renfree, M.B., and Fietz, S.A. (2018). The Basal Radial Glia Occurs in Marsupials and Underlies the Evolution of an Expanded Neocortex in Therian Mammals. *Cereb Cortex* 28, 145-157.
- Schivell, A.E., Batchelor, R.H., and Bajjalieh, S.M. (1996). Isoform-specific, calcium-regulated interaction of the synaptic vesicle proteins SV2 and synaptotagmin. *J Biol Chem* 271, 27770-27775.
- Schivell, A.E., Mochida, S., Kensel-Hammes, P., Custer, K.L., and Bajjalieh, S.M. (2005). SV2A and SV2C contain a unique synaptotagmin-binding site. *Mol Cell Neurosci* 29, 56-64.
- Scranton, T.W., Iwata, M., and Carlson, S.S. (1993). The SV2 protein of synaptic vesicles is a keratan sulfate proteoglycan. *J Neurochem* 61, 29-44.
- Serajee, F.J., and Huq, A.M. (2015). Homozygous Mutation in Synaptic Vesicle Glycoprotein 2A Gene Results in Intractable Epilepsy, Involuntary Movements, Microcephaly, and Developmental and Growth Retardation. *Pediatr Neurol* 52, 642-646.e641.
- Serrano, M.E., Bartholome, O., Van den Ackerveken, P., Ferrara, A., Rogister, B., Plenevaux, A., and Tirelli, E. (2019). Anxiety-like features and spatial memory problems as a consequence of hippocampal SV2A expression. *PLoS One* 14, e0217882.

- Shinmyo, Y., Terashita, Y., Dinh Duong, T.A., Horiike, T., Kawasumi, M., Hosomichi, K., Tajima, A., and Kawasaki, H. (2017). Folding of the Cerebral Cortex Requires Cdk5 in Upper-Layer Neurons in Gyrencephalic Mammals. *Cell reports* 20, 2131-2143.
- Siegenthaler, J.A., Ashique, A.M., Zarbalis, K., Patterson, K.P., Hecht, J.H., Kane, M.A., Folias, A.E., Choe, Y., May, S.R., Kume, T., *et al.* (2009). Retinoic acid from the meninges regulates cortical neuron generation. *Cell* 139, 597-609.
- Siwek, M.E., Muller, R., Henseler, C., Trog, A., Lundt, A., Wormuth, C., Broich, K., Ehninger, D., Weiergraber, M., and Papazoglou, A. (2015). Altered theta oscillations and aberrant cortical excitatory activity in the 5XFAD model of Alzheimer's disease. *Neural Plast* 2015, 781731.
- Smart, I.H., Dehay, C., Giroud, P., Berland, M., and Kennedy, H. (2002). Unique morphological features of the proliferative zones and postmitotic compartments of the neural epithelium giving rise to striate and extrastriate cortex in the monkey. *Cereb Cortex* 12, 37-53.
- Sola, I., Aso, E., Frattini, D., Lopez-Gonzalez, I., Espargaro, A., Sabate, R., Di Pietro, O., Luque, F.J., Clos, M.V., Ferrer, I., *et al.* (2015). Novel Levetiracetam Derivatives That Are Effective against the Alzheimer-like Phenotype in Mice: Synthesis, in Vitro, ex Vivo, and in Vivo Efficacy Studies. *J Med Chem* 58, 6018-6032.
- Son, Y.J., Scranton, T.W., Sunderland, W.J., Baek, S.J., Miner, J.H., Sanes, J.R., and Carlson, S.S. (2000). The synaptic vesicle protein SV2 is complexed with an alpha5-containing laminin on the nerve terminal surface. *J Biol Chem* 275, 451-460.
- Stahl, R., Walcher, T., De Juan Romero, C., Pilz, G.A., Cappello, S., Irmeler, M., Sanz-Aquela, J.M., Beckers, J., Blum, R., Borrell, V., *et al.* (2013). Trnp1 regulates expansion and folding of the mammalian cerebral cortex by control of radial glial fate. *Cell* 153, 535-549.
- Stenzel, D., Wilsch-Bräuninger, M., Wong, F.K., Heuer, H., and Huttner, W.B. (2014). Integrin α _v β ₃ and thyroid hormones promote expansion of progenitors in embryonic neocortex. *Development* 141, 795-806.
- Stockburger, C., Miano, D., Baeumlisberger, M., Pallas, T., Arrey, T.N., Karas, M., Friedland, K., and Muller, W.E. (2016). A Mitochondrial Role of SV2a Protein in Aging and Alzheimer's Disease: Studies with Levetiracetam. *J Alzheimers Dis* 50, 201-215.
- Stout, K.A., Dunn, A.R., Hoffman, C., and Miller, G.W. (2019). The Synaptic Vesicle Glycoprotein 2: Structure, Function, and Disease Relevance. *ACS Chem Neurosci* 10, 3927-3938.
- Stronati, E., Conti, R., Cacci, E., Cardarelli, S., Biagioni, S., and Poiana, G. (2019). Extracellular Vesicle-Induced Differentiation of Neural Stem Progenitor Cells. *Int J Mol Sci* 20.
- Sun, T., and Hevner, R.F. (2014). Growth and folding of the mammalian cerebral cortex: from molecules to malformations. *Nat Rev Neurosci* 15, 217-232.

- Takahashi, T., Misson, J.P., and Caviness, V.S., Jr. (1990). Glial process elongation and branching in the developing murine neocortex: a qualitative and quantitative immunohistochemical analysis. *J Comp Neurol* 302, 15-28.
- Tallinen, T., Chung, J.Y., Biggins, J.S., and Mahadevan, L. (2014). Gyrification from constrained cortical expansion. *Proc Natl Acad Sci U S A* 111, 12667-12672.
- Taverna, E., Gotz, M., and Huttner, W.B. (2014). The cell biology of neurogenesis: toward an understanding of the development and evolution of the neocortex. *Annu Rev Cell Dev Biol* 30, 465-502.
- Taverna, E., and Huttner, W.B. (2010). Neural progenitor nuclei IN motion. *Neuron* 67, 906-914.
- Taverna, E., Mora-Bermudez, F., Strzyz, P.J., Florio, M., Icha, J., Haffner, C., Norden, C., Wilsch-Brauninger, M., and Huttner, W.B. (2016). Non-canonical features of the Golgi apparatus in bipolar epithelial neural stem cells. *Scientific reports* 6, 21206.
- Toda, T., Shinmyo, Y., Dinh Duong, T.A., Masuda, K., and Kawasaki, H. (2016). An essential role of SVZ progenitors in cortical folding in gyrencephalic mammals. *Scientific reports* 6, 29578.
- Tsuda, S., Kitagawa, T., Takashima, S., Asakawa, S., Shimizu, N., Mitani, H., Shima, A., Tsutsumi, M., Hori, H., Naruse, K., *et al.* (2010). FAK-mediated extracellular signals are essential for interkinetic nuclear migration and planar divisions in the neuroepithelium. *J Cell Sci* 123, 484-496.
- Turrero Garcia, M., Chang, Y., Arai, Y., and Huttner, W.B. (2016). S-phase duration is the main target of cell cycle regulation in neural progenitors of developing ferret neocortex. *J Comp Neurol* 524, 456-470.
- Ueno, M., and Yamashita, T. (2014). Bidirectional tuning of microglia in the developing brain: from neurogenesis to neural circuit formation. *Curr Opin Neurobiol* 27, 8-15.
- Vaid, S., Camp, J.G., Hersemann, L., Eugster Oegema, C., Heninger, A.K., Winkler, S., Brandl, H., Sarov, M., Treutlein, B., Huttner, W.B., *et al.* (2018). A novel population of Hopx-dependent basal radial glial cells in the developing mouse neocortex. *Development* 145.
- Van Essen, D.C. (1997). A tension-based theory of morphogenesis and compact wiring in the central nervous system. *Nature* 385, 313-318.
- Vitali, I., Fievre, S., Telley, L., Oberst, P., Bariselli, S., Frangeul, L., Baumann, N., McMahon, J.J., Klingler, E., Bocchi, R., *et al.* (2018). Progenitor Hyperpolarization Regulates the Sequential Generation of Neuronal Subtypes in the Developing Neocortex. *Cell* 174, 1264-1276 e1215.
- Vogl, C., Tanifuji, S., Danis, B., Daniels, V., Foerch, P., Wolff, C., Whalley, B.J., Mochida, S., and Stephens, G.J. (2015). Synaptic vesicle glycoprotein 2A modulates vesicular release and calcium channel function at peripheral sympathetic synapses. *Eur J Neurosci* 41, 398-409.

- Vossel, K.A., Beagle, A.J., Rabinovici, G.D., Shu, H., Lee, S.E., Naasan, G., Hegde, M., Cornes, S.B., Henry, M.L., Nelson, A.B., *et al.* (2013). Seizures and epileptiform activity in the early stages of Alzheimer disease. *JAMA Neurol* *70*, 1158-1166.
- Wan, Q.F., Zhou, Z.Y., Thakur, P., Vila, A., Sherry, D.M., Janz, R., and Heidelberger, R. (2010). SV2 acts via presynaptic calcium to regulate neurotransmitter release. *Neuron* *66*, 884-895.
- Wang, D.D., and Kriegstein, A.R. (2009). Defining the role of GABA in cortical development. *The Journal of physiology* *587*, 1873-1879.
- Wang, L., Hou, S., and Han, Y.G. (2016). Hedgehog signaling promotes basal progenitor expansion and the growth and folding of the neocortex. *Nat Neurosci* *19*, 888-896.
- Wang, L., Shi, J., Wu, G., Zhou, F., and Hong, Z. (2014). Hippocampal low-frequency stimulation increased SV2A expression and inhibited the seizure degree in pharmacoresistant amygdala-kindling epileptic rats. *Epilepsy Res* *108*, 1483-1491.
- Watanabe, Y., Kawae, T., and Miyata, T. (2018). Differentiating cells mechanically limit the interkinetic nuclear migration of progenitor cells to secure apical cytotgenesis. *Development* *145*.
- Weissman, T., Noctor, S.C., Clinton, B.K., Honig, L.S., and Kriegstein, A.R. (2003). Neurogenic radial glial cells in reptile, rodent and human: from mitosis to migration. *Cereb Cortex* *13*, 550-559.
- Weissman, T.A., Riquelme, P.A., Ivic, L., Flint, A.C., and Kriegstein, A.R. (2004). Calcium waves propagate through radial glial cells and modulate proliferation in the developing neocortex. *Neuron* *43*, 647-661.
- Wonders, C.P., and Anderson, S.A. (2006). The origin and specification of cortical interneurons. *Nat Rev Neurosci* *7*, 687-696.
- Wong, F.K., Fei, J.F., Mora-Bermudez, F., Taverna, E., Haffner, C., Fu, J., Anastassiadis, K., Stewart, A.F., and Huttner, W.B. (2015). Sustained Pax6 Expression Generates Primate-like Basal Radial Glia in Developing Mouse Neocortex. *PLoS Biol* *13*, e1002217.
- Wu, T., Chen, C.C., Chen, T.C., Tseng, Y.F., Chiang, C.B., Hung, C.C., and Liou, H.H. (2009). Clinical efficacy and cognitive and neuropsychological effects of levetiracetam in epilepsy: an open-label multicenter study. *Epilepsy Behav* *16*, 468-474.
- Xu, G., Knutsen, A.K., Dikranian, K., Kroenke, C.D., Bayly, P.V., and Taber, L.A. (2010). Axons pull on the brain, but tension does not drive cortical folding. *J Biomech Eng* *132*, 071013.
- Xu, T., and Bajjalieh, S.M. (2001). SV2 modulates the size of the readily releasable pool of secretory vesicles. *Nat Cell Biol* *3*, 691-698.
- Yanagisawa, K. (2007). Role of gangliosides in Alzheimer's disease. *Biochim Biophys Acta* *1768*, 1943-1951.

- Yao, G., Zhang, S., Mahrhold, S., Lam, K.H., Stern, D., Bagramyan, K., Perry, K., Kalkum, M., Rummel, A., Dong, M., *et al.* (2016). N-linked glycosylation of SV2 is required for binding and uptake of botulinum neurotoxin A. *Nat Struct Mol Biol* 23, 656-662.
- Yao, J., and Bajjalieh, S.M. (2008). Synaptic vesicle protein 2 binds adenine nucleotides. *J Biol Chem* 283, 20628-20634.
- Yao, J., and Bajjalieh, S.M. (2009). SVOP is a nucleotide binding protein. *PLoS One* 4, e5315.
- Yao, J., de la Iglesia, H.O., and Bajjalieh, S.M. (2013). Loss of the SV2-like protein SVOP produces no apparent deficits in laboratory mice. *PLoS One* 8, e68215.
- Yao, J., Nowack, A., Kensel-Hammes, P., Gardner, R.G., and Bajjalieh, S.M. (2010). Cotrafficking of SV2 and synaptotagmin at the synapse. *J Neurosci* 30, 5569-5578.
- Yeh, F.L., Dong, M., Yao, J., Tepp, W.H., Lin, G., Johnson, E.A., and Chapman, E.R. (2010). SV2 mediates entry of tetanus neurotoxin into central neurons. *PLoS Pathog* 6, e1001207.
- Zhang, N., Gordon, S.L., Fritsch, M.J., Esoof, N., Campbell, D.G., Gourlay, R., Velupillai, S., Macartney, T., Pegg, M., van Aalten, D.M.F., *et al.* (2015). Phosphorylation of synaptic vesicle protein 2A at Thr84 by casein kinase 1 family kinases controls the specific retrieval of synaptotagmin-1. *The Journal of neuroscience : the official journal of the Society for Neuroscience* 35, 2492-2507.
- Ziyatdinova, S., Ronnback, A., Gurevicius, K., Mischczuk, D., Graff, C., Winblad, B., Pitkanen, A., and Tanila, H. (2016). Increased Epileptiform EEG Activity and Decreased Seizure Threshold in Arctic APP Transgenic Mouse Model of Alzheimer's Disease. *Curr Alzheimer Res* 13, 817-830.

